Aachener Verfahrenstechnik

RWTH AACHEN UNIVERSITY

Aachener Verfahrenstechnik Series
AVT.SVT – Process Systems Engineering
Volume 31 (2024)

Luise Friederike Kaven

In-Silico and In-Situ Optimization for Enhanced Synthesis of Functional Microgels

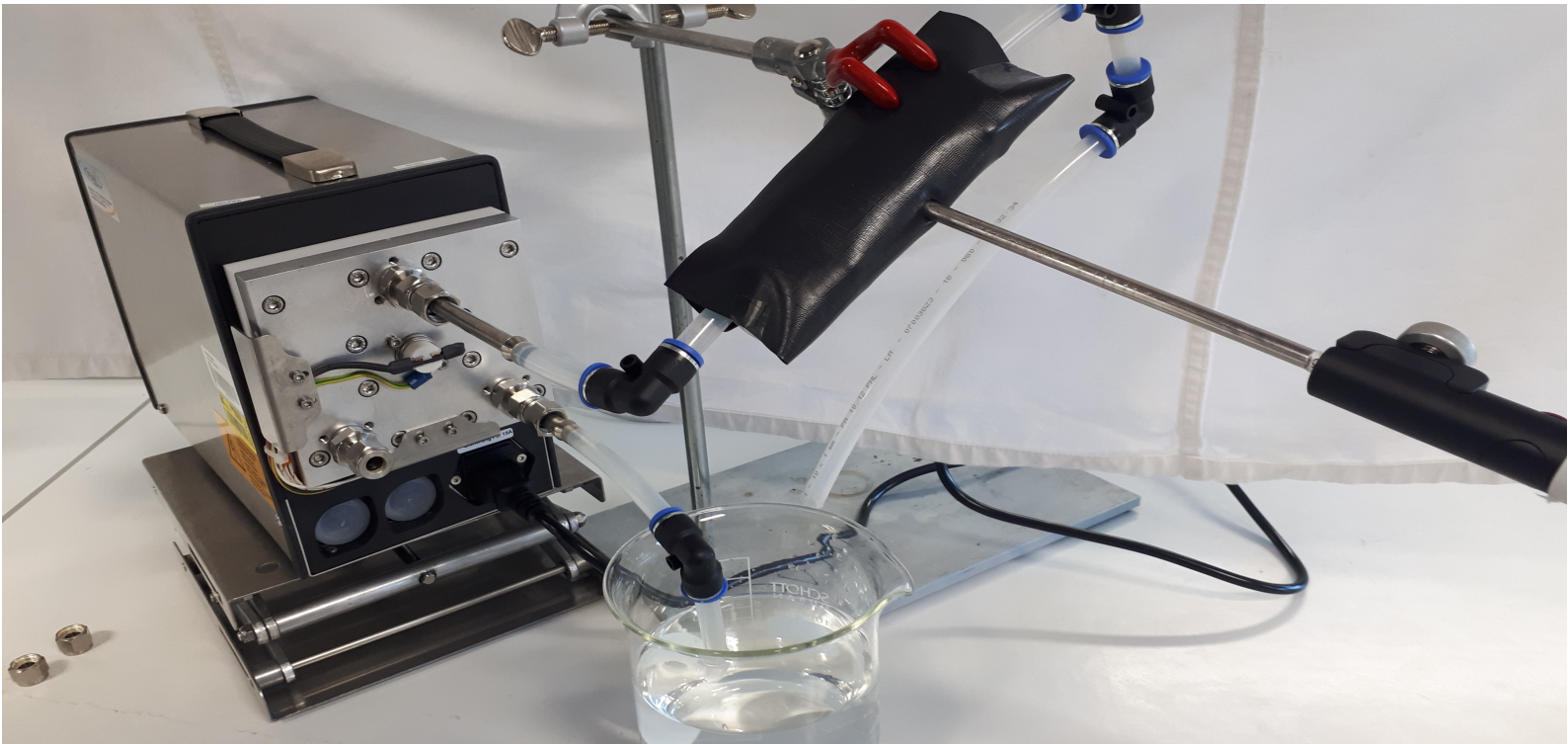

In-Silico and In-Situ Optimization for Enhanced Synthesis of Functional Microgels

In-Silico- und In-Situ-Optimierung für die verbesserte Synthese von funktionellen Mikrogelen

Von der Fakultät für Maschinenwesen der Rheinisch-Westfälischen Technischen Hochschule Aachen zur Erlangung des akademischen Grades einer Doktorin der Ingenieurwissenschaften genehmigte Dissertation

vorgelegt von

Luise Friederike Kaven, geb. Bering

Berichter: Universitätsprofessor Alexander Mitsos, Ph.D.
Universitätsprofessor Dr.-Ing. Matthias Wessling

Tag der mündlichen Prüfung: 25.04.2024

Diese Dissertation ist auf den Internetseiten der Universitätsbibliothek online verfügbar.

Titel: In-Silico and In-Situ Optimization for Enhanced Synthesis of Functional Microgels

Autor: Luise Friederike Kaven, geb. Bering

Reihe: Aachener Verfahrenstechnik Series
AVT.SVT - Process Systems Engineering
Band 31 (2024)

Herausgeber: Aachener Verfahrenstechnik
Forckenbeckstraße 51
52074 Aachen
Tel.: +49 (0)241 80 97717
Fax.: +49 (0)241 80 92326
E-Mail: secretary.svt@avt.rwth-aachen.de
http://www.avt.rwth-aachen.de

Acknowledgements

This thesis was developed during my time as a research associate at the Aachener Verfahrenstechnik, Chair of Process Systems Engineering (AVT.SVT) of RWTH Aachen University. I am extremely grateful to my doctoral advisor Prof. Alexander Mitsos, Ph.D. for his exceptional support, academic guidance, and role model function for integrity. In addition, I thank Prof. Dr.-Ing. Matthias Wessling for the co-examination of my thesis, Prof. Dr.-Ing. Heinz Günter Pitsch for chairing the examination committee, and Prof. Kai Leonhard for his contribution as assessor.

My research project was funded by the Collaborative Research Centre 985 "Functional Microgels and Microgel Systems" (SFB 985) by the German Research Foundation, which I gratefully acknowledge. In particular, I thank Falco Jung, Agnieszka Ksiazkiewicz, Prof. Kai Leonhard, Prof. Adel Mhamdi, Thomas Nevolianis, Prof. Andrij Pich, Jörn Viell, Prof. Matthias Wessling, Hanna Wolff, and Nadja Wolter for the very pleasant collaborations. Furthermore, I would like to thank Franca Janssen and Julian Meyer-Kirschner for valuable guidance, and Fabian Fink and Moritz Becker for strategic support. Moreover, I would like to thank my external collaborators Eleni Koronaki, Ph.D., Prof. Yannis Kevrekidis, Dr. Shaghayegh Hamzehlou, and Dr. Nicholas Ballard for fruitful collaborations.

I would also like to thank my extremely bright SVT colleagues for the great time we spent together and your endless unconditional support. Wonderful memories include sharing an office with various colleagues, fantastic times in the Simtech team, eventful traveling to conferences, rebellious laboratory group meetings, numerous coffee breaks, sailing trips, AVT rockt participations, a trip to Bad Dürkheim, and too many nights in Apollo or Kaktus. I would like to extend my deepest gratitude to all of you: Adrian Caspari, Alexander Echtermeyer, Alexandra Weber-Bernard, Andrea König, Andreas Bremen, Anita Ziegler, Aron Zingler, Artur Schweidtmann, Caroline Marks, Chrysanthi Papadimitriou, Chryssa Kappatou, Clara Witte, Daniel Jungen, Dominik Bongartz, Eike Cramer, Georgianna Prokopou, Jan Pyschik, Jan Rittig, Jan Schulze, Jannik Burre, Jannik Lüthje, Johannes Faust, Katharina Ebeling, Luisa Brée, Marc-Daniel Stumm, Marco Langiu, Marian Panofen, Michael Rix, Mohammad El Wajeh, Moritz Begall, Pascal Schäfer, Philipp Ackermann, Raphael Seidenberg, Simone Mucci, Tobias Ploch, Wolfgang Huster, and Yannic Vaupel.

I had the pleasure to work with a large number of students and I would like to thank all of them for their excellent performance and exemplary commitment contributing to the successful completion of many tasks in projects and general laboratory operations. In particular, I thank Jan Keil who supported me and my students for many years, and Lukas Wille and Jana Israel for their exceptional contributions. Furthermore, I would like to extend my thanks to Jutta Friedrich, Sascha Gerhards, Didem Uslu, Wanda Frohn, and Petra Eissa for their comprehensive organizational support and commitment. Also, I was lucky to receive support from my girls squad - some organized and some at chance. Special thanks goes to my fellow *female network Melaten* women and my friends Johanna Arenhoevel, Marlena Just, and Nicole Weber. I can always count on you.

Finally, my deepest thanks go to my family. I would like to thank my parents, my sister Henriette, my grandmother Christa, and my bonus sister Maximilia for their continued support and encouragement in all phases of my studies and doctorate and, last but not least, my husband Lennard and my children Emil and Mathilde: You mean the world to me. Thank you for your understanding patience and loving support!

Aachen, July 2024 *Luise F. Kaven*

Contents

Notation

Abbreviations

AA	acrylic acid
AEMH	amine 2-aminoethylmethacrylate hydrochloride
AFM	atomic force microscopy
AltDMAPs	alternating diffusion maps
AMPA	2,2'-azobis(2-methylpropanimidamide)dihydrochloride
ANN	artificial neural network
APMH	amine N-(3-aminopropyl)methacrylamide hydrochloride
APS	ammonium persulfate
AVT	Aachener Verfahrenstechnik
BIS	*N*,*N'*-methylene bis(acrylamide)
CANN	conformal autoencoder neural network
CHM	complemental hard modeling
CTAB	hexadecyltrimethylammonium bromide
CV	cross-validation
D_2O	deuterium oxide
DFT	density functional theory
DLS	dynamic light scattering
DMAPs	diffusion maps
EGDMA	ethylene glycol dimethylacrylate
EPDM	ethylene propylene diene monomer
FMU	functional mock-up unit
FTIR	Fourier-transform infrared
GMA	glycidyl methacrylate
GP	Gaussian process

H_2O	water
HCl	hydrochloric acid
HM	hard model
HWHM	half-width at half maximum
IHM	indirect hard modeling
IRC	intrinsic reaction coordinate
KPS	potassium persulfate
LHS	latin hyper-cube sampling
MAA	methacrylic acid
MAA^-	dissociated methacrylic acid
MAiNGO	McCormick-based algorithm for mixed-integer nonlinear global optimization
MAPE	mean absolute percentage error
MCR-ALS	multivariate curve resolution-alternating least squares
MEHQ	4-methoxyphenol
MeLOn	machine learning models for optimization
NaOH	sodium hydroxide
NIPAM	*N*-isopropylacrylamide
NIR	near-infrared
NMR	nuclear magnetic resonance
NN	neural network
PAT	process analytical technology
PCA	principal component analysis
PCM	pure component model
PLS	partial least squares
PNIPAM	poly *N*-isopropylacrylamide
PTFE	polytetrafluoroethylene
PVC	poly vinyl chloride
PVCL	poly *N*-vinylcaprolactam

rpm	rotations per minute
RRHO	rigid rotor harmonic oscillator
SDS	sodium dodecyl sulfate
SEM	scanning electron microscopy
SNR	signal-to-noise ratio
SNV	standard normal variate
SVT	process systems engineering
TEM	transmission electrion microscopy
TS	transition state
TS-EMO	Thompson sampling efficient multi-objective optimization
UV	ultraviolet
VCL	*N*-vinylcaprolactam
VFc	vinylferrocene
VPTT	volume phase transition temperature

Symbols

B	baseline function	–
c	molar concentration	$\mathrm{mol\,m^{-3}}$
ΔH_R	polymerization enthalpy	$\mathrm{J\,mol^{-1}}, \mathrm{kJ\,mol^{-1}}$
$\mathbf{D}$	diagonal matrix	–
D_H	hydrodynamic diameter	nm
E	activation energy	$\mathrm{J\,mol^{-1}}$
F	volumetric flow rate	$\mathrm{mL\,min^{-1}}$
f	initiator efficiency	–
F_I	volumetric flow rate of initiator solution	$\mathrm{mL\,min^{-1}}$
F_M	volumetric flow rate of monomer solution	$\mathrm{mL\,min^{-1}}$
F_product	volumetric flow rate of microgel product solution	$\mathrm{mL\,min^{-1}}$
$\mathbf{K}$	Markov matrix	–
k_d	initiator decomposition rate coefficient	$\mathrm{s^{-1}}$

$k_{\mathrm{d},0}$	initiator decomposition pre-exponential factor	s^{-1}
$k_{\mathrm{p}ij}$	propagation rate coefficient of an active polymer chain with end type i with a monomer type j	$\mathrm{m}^3\,\mathrm{mol}^{-1}\,\mathrm{s}^{-1}$
k_{t}	termination rate coefficient	$\mathrm{m}^3\,\mathrm{mol}^{-1}\,\mathrm{s}^{-1}$
$\mathbf{p}$	vector of model parameters	–
r	reactivity ratio	–
R^2	coefficient of determination	–
RMSE	root mean squared error	–
RMSECV	root mean squared error of cross-validation	–
r_{H}	hydrodynamic radius	nm
$R_{\mathrm{p}ij}$	propagation rate of an active polymer chain with end type i with a monomer type j	$\mathrm{mol}\,\mathrm{m}^{-3}\,\mathrm{s}^{-1}$
$R_{\mathrm{R}j}$	reaction rate of an initiator radical with a monomer type j	$\mathrm{mol}\,\mathrm{m}^{-3}\,\mathrm{s}^{-1}$
$R_{\mathrm{t}i}$	termination rate of an active polymer chain with end type i	$\mathrm{mol}\,\mathrm{m}^{-3}\,\mathrm{s}^{-1}$
s	standard deviation	wt%, W
T	temperature	$°C$, K
t	time	s, min
t_j	discrete time points	s, min
V	reactor volume	m^3, mL
w	weight fraction	wt%
$\mathbf{W}$	Gaussian kernel matrix	–
$\widetilde{\mathbf{W}}$	normalized Gaussian kernel matrix	–
$\mathbf{x}$	vector of inputs	–
$\mathbf{y}$	vector of outputs	–
y	mole fraction	mol%
z	output measurement for parameter estimation	–

Greek Letters

α	maximum spectral intensity	–
α^{diss}	dissociation degree	–
β	fraction of Gaussian part	–
γ	half-width at half maximum	–
δ	spectral position	–
ϵ	epsilon constraint	–
ν	latent variable of autoencoder	–
ϕ_i	eigenvector	–
ϕ_k	diffusion maps coordinate	–
Σ_{R}	enthalpy transfer rate	W, kW
τ	mean residence time	s, min
ω	weights in mixture hard model	–

Subscripts

0	initial
f	final
k	component

Superscripts

avg	average
CV	cross-validation
L	lower bound
meas	measured
min	minimal
pred	model-predicted
t	time
target	target
U	upper bound

Physical constants

R_{gas}	ideal gas constant	$8.314\,\mathrm{J\,mol^{-1}\,K^{-1}}$

Reactants

CL	cross-linker
I	initiator
M	monomer
M_j	monomer of type j
P^n	polymer chains of length n
PDB	pendant double bond
$\mathrm{R}^0_\bullet$	initiator radical
R^n_i	active polymer chain of length n with end group i
X	cross-link

Kurzfassung

Mikrogele sind funktionelle Polymere mit dem Potenzial für vielseitige Anwendungen. Jede Anwendung erfordert maßgeschneiderte Eigenschaften der Mikrogele. Um eine maßgeschneiderte Produktion zu ermöglichen, sind Einblicke während der Reaktion durch Prozessanalytik sowie mathematische Modellierung zur computergestützten Vorhersage und Optimierung der Mikrogeleigenschaften unerlässlich. In dieser Arbeit werden daher Fortschritte bei der Mikrogelsynthese hinsichtlich Analytik, Modellierung und Optimierung erzielt, um das volle Potenzial dieser vielseitigen Polymere zu erschließen.

Zunächst wird die Konzentrationsbestimmung mittels Raman-Spektroskopie für die kontinuierliche Mikrogelproduktion eingeführt. Die Übertragung dieser Messtechnik von Batch- auf kontinuierliche Durchflussanlagen birgt Herausforderungen, die systematisch angegangen werden. Es wird ein Qualitätskriterium für Raman-Spektren abgeleitet, das die Erkennung von Ausreißern während der kontinuierlichen Synthese ermöglicht. Insgesamt wird damit ein Leitfaden für die Übertragung von Inline-Analytik erstellt.

Zweitens werden die Möglichkeiten der Raman-Spektroskopie erweitert, indem eine Methode zur Bestimmung der Mikrogelgröße aus Raman-Messungen vorgestellt wird. Dabei werden fortschrittliche Entwicklungen im Bereich des maschinellen Lernens genutzt, um die Qualität der Größenvorhersage zu verbessern. Die daraus resultierende Vorhersagegenauigkeit ist mit den etablierten Offline-Messtechniken vergleichbar. Die Kombination von Raman-Spektroskopie und maschinellem Lernen ist somit ein vielversprechender Ansatz für die Inline-Partikelgrößenbestimmung.

Drittens ist die Raman-Spektroskopie auch für die Überwachung der geladenen Mikrogelsynthese geeignet. Modell-basierte Auswertung bewältigt dabei die Komplexität, die durch die Multikomponentenlösungen mit dissoziierten und undissoziierten Zuständen verursacht wird. Dadurch wird ein detaillierter Einblick in die Reaktionsphänomene während der Synthese geladener Mikrogele ermöglicht.

Viertens wird die Erweiterung eines mechanistischen, dynamischen Modells um die Einbeziehung von funktionellen Epoxidgruppen in der Synthese von Mikrogelen vorgestellt. Unbekannte Parameterwerte werden mittels Parameterschätzung berechnet. Durch die strategische Einbeziehung quantenmechanisch berechneter Parameterwerte kann die Übereinstimmung zwischen Modellvorhersage und experimentellen Messungen bei geringem Rechenaufwand präzisiert werden. Das identifizierten Synthesemodell prädiziert die Verteilung der funktionellen Epoxidgruppen innerhalb des Mikrogels.

Fünftens wird die Erweiterung eines mechanistischen, dynamischen Modells für die Synthese von geladenen Mikrogelen unter Berücksichtigung von pH-Einfluss vorgestellt. Auch hier werden fehlende Parameterwerte mittels Parameterschätzung berechnet und quantenmechanisch berechnete Werte dabei eingebunden. Das entwickelte Modell ermöglicht die Vorhersage und Optimierung geladener Mikrogele für die effiziente Entwicklung maßgeschneiderter Systeme.

Sechstens wird ein datengetriebener Hardware-in-the-Loop-Ansatz zur erfolgreichen Synthese von Mikrogelen einer gewünschten Größe präsentiert. Dabei wird Bayes'sche Optimierung eingesetzt für die gleichzeitige Verbesserung der Mikrogelsynthese hinsichtlich Produkt- und Prozesseigenschaften. Der vorgeschlagene Ansatz ermöglicht eine effiziente Mikrogelentwicklung, indem die Anzahl der erforderlichen Experimente minimiert werden.

Die Arbeit vereint Fortschritte in den Bereichen Prozessanalytik, mathematische Modellierung und datengetriebene Optimierung und kombiniert experimentelle Entwicklungen (in-situ) mit theoretischen Überlegungen (in-silico). Daher stellen die Ergebnisse dieser Arbeit einen wichtigen Schritt in Richtung der Synthese von maßgeschneiderten Mikrogelen mit spezifischen Zusammensetzungen oder Funktionalitäten in einem größeren Produktionsmaßstab dar. Schließlich sind viele Erkenntnisse dieser Arbeit nicht nur für andere Polymersysteme relevant, sondern auch für die Methodenentwicklung im Bereich der spektroskopiebasierten Größenvorhersage oder der Hardware-in-the-Loop-Optimierung für alle Arten von (chemischen) Systemen.

Summary

Microgels are functional polymers with the potential for versatile applications. Each application requires tailored properties of the functional microgels. To enable a tailor-made production, insights during the reaction via process monitoring are essential, as well as mathematical modeling for predicting and optimizing microgel properties. Thus, this thesis provides advancements in microgel synthesis regarding monitoring, modeling, and optimization to unlock the full potential of these versatile polymers.

First, concentration monitoring via Raman spectroscopy is established for the continuous microgel production mode. Transferring this monitoring technique from batch to continuous flow setups poses challenges that are systematically addressed. A quality criterion for Raman spectra is derived to allow functional outlier detection during continuous synthesis. Hence, overall, a guideline for in-line monitoring transfer is established.

Second, the capabilities of Raman spectroscopy are enhanced by presenting a method to determine the microgel size from Raman measurements. Recent developments in machine learning are leveraged to improve size determination quality. The resulting accuracy is comparable with state-of-the-art off-line analysis tools. Thus, combining Raman spectroscopy and advanced machine learning methods is a promising approach for in-line polymer size determination.

Third, Raman spectroscopy is also enabled for monitoring the charged microgel synthesis. Applying indirect spectral hard modeling resolves the complexities caused by the multi-component solutions with dissociated and undissociated states. Therefore, a detailed insight into the reaction phenomena during the charged microgel synthesis is enabled.

Fourth, a mechanistic, dynamic model for the synthesis of microgels is extended to account for integration of functional epoxy groups. Unknown parameter values are calculated within a parameter estimation. By strategically including quantum mechanically calculated parameter values, the fit between model prediction and experimental measurements can be improved while reducing the calculational effort. By applying the identified synthesis model, the distribution of functional epoxy groups within the microgel is predicted.

Fifth, a mechanistic, dynamic model is enhanced to capture the synthesis of charged microgels with regard to pH changes during the process. Again, missing parameter values are calculated within a parameter estimation, including quantum mechanically computed values strategically. The developed model presents a robust framework for predicting and optimizing the performance of charged microgels in diverse scenarios, paving the way for designing more efficient and tailored microgel-based systems.

Sixth, a data-driven hardware-in-the-loop approach is presented to synthesize microgels of a desired size successfully. Data-driven approaches, particularly Bayesian optimization, are employed for microgel synthesis optimization for multiple objectives regarding product and process properties simultaneously. The proposed framework includes global deterministic optimization and has the potential for efficient microgel development by minimizing the number of experiments and modeling efforts needed.

The thesis brings together advancements in the fields of process analytical technology, mathematical modeling, and data-driven optimization while combining experimental real-world development (in-situ) with theoretical considerations (in-silico). Therefore, this thesis's findings provide one step toward synthesizing tailored microgels with specific compositions or functionalities at increased production scale. Finally, many findings of this thesis are relevant not only for other polymer systems but also for method development in the field of spectroscopy-based size determination and hardware-in-the-loop optimization for all kinds of (chemical) systems.

Publications and Copyrights

This thesis is a result of the research executed by the author during her time at the Chair of Process Systems Engineering (AVT.SVT) between 2017 and 2023. Parts of this thesis have already been published or submitted as peer-reviewed journal articles. The publications originate from collaborative research projects and are integrated in the thesis chapters as described below. In addition, the author contributions for the respective publications are explicitly listed. Alexander Mitsos and Jörn Viell provided ideas, guidance, and edits to these publications and this dissertation.

- [1] **L. F. Kaven**, H. J. M. Wolff, L. Wille, M. Wessling, A. Mitsos, and J. Viell. In-line Monitoring of Microgel Synthesis: Flow versus Batch Reactor. *Organic Process Research & Development*, 2021, **25**(9), 2039–2051. Copyright © 2021 American Chemical Society. Reprinted (adapted) with permission from Organic Process Research & Development.

  Content of this publication has also been presented at scientific conferences [2–4].

  This journal article is partially reproduced in Chapter 3. The according supplemental information is partially incorporated in Appendix A.

  Authors contributions:
  L. F. Kaven: Measurement cell design; design of experiments; indirect hard modeling (IHM) and calibration; development of quality criterion; evaluation of synthesis spectra.
  H. J. M. Wolff: Experimental setup; assistance for measurement cell design; scientific support and discussion on microgels and flow reactor.
  L. Wille: Assistance for experimental setup; synthesis conduction; Raman spectra acquisition.
  M. Wessling: Scientific support and discussion on continuous synthesis; advice on structure and presentation of this work.
  A. Mitsos Design of the project; scientific support and discussion on interpretation of batch comparison; advice on structure and presentation of this work.
  J. Viell: Design of the project; scientific support and discussion on experimental and analytical methods; advice on structure and presentation of this work.
  All authors contributed to writing, reviewing and editing the article.

- [5] E. D. Koronaki, **L. F. Kaven**, J. M. M. Faust, Y. G. Kevrekidis, A. Mitsos. Nonlinear Manifold Learning Determines Microgel Size from Raman Spectroscopy. *AIChE Journal*, 2024, e18494. Copyright © 2024 The Author(s). AIChE Journal published by Wiley Periodicals LLC on behalf of American Institute of Chemical Engineers. Open access publication, permission is not required for (adapted) reprint.

  Content of this publication has also been presented at a scientific conference [6].

  This article is partially reproduced in Chapter 4. The content of this article is currently undergoing the patent application process in the drafting phase, with legal professionals

preparing the patent claim.

Authors contributions:
E. D. Koronaki: Developed, implemented and applied the diffusion maps (DMAPs), alternating diffusion maps (AltDMAPs), and Y-shaped autoencoder frameworks, developed the heuristic pre-processing, wrote initial draft.
L. F. Kaven: Experimental design, pre-processing of data, implemented applied partial least squares (PLS) regression and hybrid PLS regression with IHM method, wrote initial draft.
J. M. M. Faust: Performed preliminary numerical experiments with DMAPs, guided analysis, reviewed and edited the manuscript.
Y. G. Kevrekidis: Guided the DMAPs, AltDMAPs and Y-shaped autoencoder frameworks, reviewed and edited the manuscript.
A. Mitsos: Conceived the idea, initiated project, supervising L. F. Kaven and J. M. M. Faust, wrote initial draft.

- [7] **L. F. Kaven**, J. Keil, N. Wolter, T. Nevolianis, A. Pich, K. Leonhard, A. Mhamdi, A. Mitsos. Dynamic Modeling and Identification of Microgel Synthesis with Charged Domains. *Industrial & Engineering Chemistry Research*, 2024, **63**(17), 7727–7742. Copyright © 2024 American Chemical Society. Reprinted (adapted) with permission from Industrial & Engineering Chemistry Research.

  This article is partially reproduced in Chapters 5 and 7. The according supplemental information is partially incorporated also in Chapter 5 and in Appendix B.

  Authors contributions:
  L. F. Kaven: IHM development, supervising J. Keil, Raman spectra and calorimetry data evaluation, synthesis modeling, parameter estimation, model simulations, writing original draft, reviewing and editing, visualization.
  J. Keil: Assistance for experimental setup, synthesis conduction, Raman spectra acquisition, assistance in IHM development, reviewing the article.
  N. Wolter: Investigation of experiments with calorimetry, formal analysis, reviewing and editing.
  T. Nevolianis: Investigation of thermochemical and kinetic properties via computational chemistry methods, formal analysis, reviewing and editing.
  A. Pich: Design of the project, scientific support and discussion, supervising N. Wolter, reviewing and editing.
  K. Leonhard: Design of the project, scientific support and discussion, supervising T. Nevolianis, reviewing and editing.
  A. Mhamdi: Design of the project, scientific support and discussion, reviewing and editing.
  A. Mitsos: Design of the project, scientific support and discussion especially for parameter estimation setup, supervising L. F. Kaven.

- [8] **L. F. Kaven**, T. Nevolianis, N. Wolter, A. Mhamdi, A. Pich, A. Mitsos, K. Leonhard. Identification of a dynamic model of the *N*-vinylcaprolactam-co-glycidyl methacrylate microgel synthesis. *Proceedings of the 33rd European Symposium on Computer Aided Process Engineering*, 2023, 807–812. Copyright © 2023 Elsevier. Reprinted (adapted) with permission from Elsevier.

Content of this publication has been presented at a scientific conference [9].

This publication is partially reproduced in Chapter 6.

Authors contributions:
L. F. Kaven: Methodology, investigation of the process model, parameter estimation, validation, formal analysis, writing original draft, visualization.
T. Nevolianis: Methodology, investigation of thermochemical and kinetic properties with computational chemistry methods, formal analysis, sensitivity analysis.
N. Wolter: Methodology, investigation of experiments, formal analysis.
A. Mhamdi: Design of the project, scientific support and discussion.
A. Mitsos: Design of the project, scientific support and discussion, supervising L. Kaven.
A. Pich: Design of the project, scientific support and discussion, supervising N. Wolter.
K. Leonhard: Design of the project, scientific support and discussion, supervising T. Nevolianis.
All authors contributed to reviewing and editing the article.

- [10] **L. F. Kaven**, A. M. Schweidtmann, J. Keil, J. Israel, N. Wolter, A. Mitsos. Data-driven Product-Process Optimization of *N*-isopropylacrylamide Microgel Flow-Synthesis. *Journal of Chemical Engineering*, 2024, **479**, 147567. Copyright © 2023 Elsevier. Reprinted (adapted) with permission from Elsevier.

  Content of this publication has also been presented at a scientific conference [11].

  This journal article is partially reproduced in Chapter 8. The according supporting information is partially incorporated in Appendix C.

  Authors contributions:
  L. F. Kaven: Conceptualization, methodology, Raman spectra evaluation, dynamic light scattering (DLS) measurement interpretation, designing experimental studies, TS-EMO and MAiNGO optimization configuration, graphic design, writing original draft.
  A. M. Schweidtmann: TS-EMO optimization configuration, scientific support and discussion on interpretation of computational results, reviewing and editing the article.
  J. Keil: Assistance for experimental setup, synthesis conduction, Raman spectra acquisition, reviewing the article.
  J. Israel: Synthesis conduction, Raman spectra acquisition, conducting DLS measurements, reviewing the article.
  N. Wolter: Conducting DLS measurements, reviewing and editing the article.
  A. Mitsos: Design of the project, scientific support and discussion on interpretation of computational results, and advice on the structure and presentation of this work, reviewing and editing the article.

The author supervised and co-supervised the student theses of Emna Aidi, Jonas Derichs, Sebastian Prenger, Ahmed Salah Ben Letaief, Thomas Pütz, Sami Ghori, Felix Terhürne, and Luca Fehler. The valuable work of all students is strongly acknowledged as they assissted in generating data and performing exploratory work that supported the research presented in this dissertation. None of these

theses are part of this dissertation explicitly. Involvement of student workers (Lukas Wille, Jan Keil, and Jana Israel) is credited with co-authorships in the according journal publications and included in the previously stated author contributions.

Additionally, the following publications were submitted during the author's time at AVT.SVT and contain contributions by the author but are not part of this thesis:

- [12] A. N. Ksiazkiewicz, **L. F. Bering**, F. Jung, N. A. Wolter, J. Viell, A. Mitsos, A. Pich. Closing the 1–5 µm size gap: Temperature-programmed, fed-batch synthesis of µm-sized microgels. *Chemical Engineering Journal*, 2020, **379**, 1385–8947.

- [13] P. Schäfer, **L. F. Bering**, A. Caspari, A. Mhamdi, A. Mitsos. Nonlinear Dynamic Optimization for Improved Load-Shifting Agility of Cryogenic Air Separation Plants. *Proceedings of the 13th International Symposium on Process Systems Engineering*, 2018, 547–552.

- [14] T. Nevolianis, N. Wolter, **L. F. Kaven**, A. Mhamdi, A. Pich, A. Mitsos, K. Leonhard. Kinetic Modeling of a Poly(N-vinylcaprolactam-co-glycidyl methacrylate) Microgel Synthesis: A Hybrid In Silico and Experimental Approach. *Industrial & Engineering Chemistry Research*, 2023, **62**(2), 893–902.

1 Introduction

Microgels are cross-linked polymer networks in the size range between 0.1 µm to 100 µm in the swollen state [15]. These microgels inhibit the unique characteristic that they react reversibly upon specific triggers in their surrounding medium (such as temperature [16], pH [17, 18], electrochemical potential [19–21], and ultraviolet (UV) irradiation [22–25]). The most studied microgels are thermo-responsive and based on the monomers *N*-isopropylacrylamide (NIPAM) [26, 27] and *N*-vinylcaprolactam (VCL) [28, 29]. Upon reaching a certain threshold in temperature, the so-called volume phase transition temperature (VPTT), thermo-responsive microgels collapse and thus change their size. This collapse is fully reversible when cooling below the VPTT, making microgels attractive for switchable systems. The VPTT is approximately 32°C for NIPAM [26, 30, 31] and 31°C to 38°C for VCL [32], thus, close to physiological temperature. It is possible to enhance the microgel's functionality beyond thermo-responsiveness by adding co-monomers to the synthesis, e.g., pH-responsive groups such as methacrylic acid (MAA) or other functional units such as glycidyl methacrylate (GMA). The multi-responsive functionality, relatively small size, and the VPTT close to physiological temperature make microgels interesting for many applications. Microgels with single or dual stimuli swelling response are relevant, e.g., for medical applicationss [33–40], catalysis [41–44], enzyme immobilization [45], sensing [46], phase separation [47–49], and membranes [22].

Scientific research on microgel synthesis is versatile. To structure the scope of this thesis, the following paragraphs focus on three research topics regarding the synthesis of microgels: process monitoring, mechanistic modeling, and data-driven optimization. The literature gaps are highlighted for each topic. Furthermore, a thorough literature review is included in each of the subsequent chapters separately.

Microgels are synthesized via precipitation polymerization [26, 50]. In the past, synthesis in batch reactors has been the established production mode [12, 50–53]. Recently, production in continuous flow reactors has gained more attention [54–56]. Each production mode holds benefits, e.g., continuous production facilitates scale-up and reaction control, while batch reactors enable more flexibility and process optimization at an early development stage. Synthesis monitoring via suitable process analytical technology (PAT) is crucial for process control and identifying reaction phenomena. Raman spectroscopy is an established and reliable tool for in-line concentration monitoring of the microgel synthesis [57, 58]. The term *in-line* refers to a measurement probe positioned directly inside the reactor as opposed to automatic *on-line* measurements using a bypass [59]. Both measurement types do not require sample drawing. In-line monitoring of polymerization via Raman spectroscopy is standard for batch reactors but is yet to be manifested for flow reactors. Maintaining the measurement precision is critical when transferring the in-line Raman spectroscopy from batch to flow reactors. A systematic approach for transferring Raman monitoring from batch to continuous flow setups is yet to be established. At the same time, process analytical investigation of multi-component solutions that occur in the synthesis of microgels is challenging, especially when charged species such as MAA occur. Therefore, a suitable evaluation procedure is needed to determine the content of all participating components during the synthesis of charged microgels. Furthermore, the polymer size also constitutes a crucial characteristic for product quality in the polymerization of microgels. Recent approaches [58, 60–64] and some theoretical considerations show a correlation between Raman signals and particle sizes but do not determine polymer size from Raman spectroscopic measurements

accurately and reliably. Hence, recent developments of machine learning are expected to enable a better size determination quality.

To tailor microgels with defined composition or functionality, model-based approaches are suitable. As microgels are considered products by process [65], the synthesis conditions directly determine the functionality of the produced microgel. The detailed insight into the occurring reactions during the microgel synthesis derived from computational models enables the precise control of the microgel properties. However, modeling approaches for synthesizing charged microgels include steady-state models exclusively, while the kinetic parameter values still need to be fully understood. Hence, a model accounting for pH changes during the synthesis of charged microgels is needed. For applications with specified requirements regarding size, producing tailored microgels in a continuous flow reactor is advantageous because the microgel properties can be controlled tightly. However, no fully specified mechanistic models are available for continuous microgel synthesis, as the physical properties of the included components are only studied partly. Also, the microgel growth has been modeled only semi-empirically so far [66]. Thus, data-driven approaches can optimize microgel synthesis without needing a mechanistic system representation.

In this thesis, the production of functional microgels is enhanced in multiple ways. The focus is on the three aspects of the microgel synthesis mentioned previously (process monitoring, extending mechanistic models, and data-driven hardware-in-the-loop optimization). Monitoring via Raman spectroscopy is enhanced in three ways: conversion monitoring in continuous flow reactors, conversion monitoring of charged microgels, and microgel size determination. Further, dynamic modeling approaches are extended to cover pH changes during the synthesis and to predict reaction progression for novel functional co-monomers. Finally, a data-driven approach is applied to conduct a product-process optimization of the microgel synthesis using Bayesian optimization.

As an underlying theme, this thesis combines in-silico and in-situ optimization of the microgel synthesis. Conducting experiments (in-situ) contributes to the generation of new knowledge and insights, that support the understanding of fundamental principles in the synthesis of microgels. Furthermore, experimental validation is essential to test theoretical concepts and to confirm or challenge existing theories. In addition, in-silico studies involving mathematical modeling and computational simulations are particularly helpful to reduce experimental effort, cost, and time. This thesis bridges the gap between purely experimental and theoretical studies by exploiting the complementary advantages of both approaches.

The following thesis is structured as described below. Chapter 2 gives background information on microgel synthesis focusing on materials, batch production, monitoring via Raman spectroscopy, and mechanistic modeling approaches.

Chapters 3, 4, and 5 deal with synthesis monitoring, in particular with the transfer from batch to continuous processing, monitoring charged species, and exploiting the Raman signal for particle size determination. Chapter 3 presents a customized Raman measurement cell for in-line monitoring in a tubular flow reactor and a systematic accuracy analysis of the obtained measurement. Also, an accuracy analysis comparing three calibration models and measurements of flowing solvent, monomer solution, and microgel solution is included. In Chapter 4, a machine learning workflow leveraging diffusion maps (DMAPs), a nonlinear manifold learning technique, and conformal autoencoder neural networks is presented for microgel size determination from Raman spectra. The workflow is applied to a data set of Raman spectra with associated size measured via dynamic light scattering of 47 microgel samples in a diameter range of 208 nm to 483 nm and compared to state-of-the-art methods. Lastly, in Chapter 5, Raman spectroscopy and indirect hard modeling (IHM) are used to monitor the synthesis of charged microgels and thereby predict the monomer contents.

Chapters 6 and 7 deal with synthesis modeling and subsequent parameter estimation. In both

chapters, the presented models are based on previous modeling approaches by Jung et al. [66–69] and extended to account for addition of functional co-monomers. In Chapter 6, a kinetic model of the co-polymerization of VCL-based microgels with functional GMA monomers and cross-linked with *N*,*N'*-methylene bisacrylamide (BIS) is identified. For that, propagation reaction rates calculated via quantum chemical methods are incorporated. Subsequently, the five most sensitive propagation and initiation and termination rates using the enthalpy transfer rate from real-time reaction calorimetry experiments are estimated. For the parameter estimation, the quantum chemically calculated values act as start values, and the determined error scopes function as bounds in the optimization. Finally, the developed approach of incorporating computed parameter values is compared to variations of the procedure. In Chapter 7, a dynamic synthesis model for the polymerization of charged microgels, including pH dependency, is derived. Based on the reaction monitoring results from Raman spectroscopy, and real-time reaction calorimetry, and quantum chemical computations, missing parameter values are estimated to obtain a complete set of reaction parameter values for synthesizing NIPAM-*co*-MAA microgels. The proposed model allows simulating the microgel synthesis concerning changes in pH and its implications.

Chapter 8 deals with data-driven synthesis optimization, particularly microgel product-process optimization in a continuous flow reactor via Bayesian optimization. To accelerate tailor-made microgel development, a data-driven optimization in a hardware-in-the-loop approach is proposed to efficiently synthesize microgels with defined sizes. The synthesis is optimized regarding conflicting objectives (maximum production efficiency, minimum energy consumption, and the desired microgel radius) by applying Bayesian optimization via the solver *Thompson sampling efficient multi-objective optimization* (TS-EMO). The optimization is validated using the deterministic global solver *McCormick-based algorithm for mixed-integer nonlinear global optimization* (MAiNGO), and three computed Pareto optimal solutions are verified via experiments.

The thesis ends with a summary of the key results, derived conclusions, and perspectives for further research in Chapter 9.

2 Background Information on Microgel Synthesis

This chapter outlines background knowledge about the main topics of microgel synthesis covered within this dissertation at a high-level description to provide a general introduction. In addition, each of the following chapters includes a literature review that explores the specific aspects in more depth. For more detailed information, the reader is referred to the literature cited below. First, the basic procedure for synthesizing thermo-responsive microgels is outlined focusing on the chemicals used (see Section 2.1) and the general setup in batch production mode (see Section 2.2). Next, the synthesis monitoring via Raman spectroscopy and the evaluation of detected spectra via indirect hard modeling is shown (see Section 2.3). Subsequently, the current approaches in microgel synthesis modeling are summarized (see Section 2.4).

2.1 Materials

For synthesizing microgels, the experimental procedure relies on the following reactants:

- **Solvent:** Throughout the thesis deionized water is used as the exclusive solvent. The deionized water (referred to as "water" in the following chapters) is produced in-house (conductivity 0.8 $\mu S\ cm^{-1}$ at 25°C). All other reactants are dissolved in water, but the solvent does participate in the polymerization reaction. For microgels, the solvent is highly relevant, as the solvent influences the gel properties [70, 71].

- **Main monomer:** The main monomer is added in high concentration to form the body of the microgel. This thesis focuses on *N*-isopropylacrylamide (NIPAM) as the main monomer, but also covers a synthesis involving *N*-vinylcaprolactam (VCL) as the main monomer (see Chapter 6). NIPAM (97%, Acros Organics for Chapter 3 and TCI Chemicals for Chapters 5 and 8) is recrystallized from hexane. Microgels based on VCL and NIPAM exhibit similar response temperatures, but VCL-based microgels have the advantage of biodegradability [72] and reduced reaction times compared to NIPAM. VCL (98%, Sigma Aldrich) is distilled under vacuum and recrystallized from hexane for purification.

- **Cross-linker:** As cross-linker only *N*,*N*'-methylenebis(acrylamide) (BIS, 99%, Sigma-Aldrich) is considered in this thesis. BIS is used as received. The cross-linker creates connections (so-called cross-links) between polymer chains and thereby generates a polymer network.

- **Functional co-monomer:** Functional co-monomer is incorporated in the synthesis at low concentration to enable a targeted functionality. This dissertation concentrates on the functional co-monomers methacrylic acid (MAA) and glycidyl methacrylate (GMA). MAA (>99%, stabilized with 4-methoxyphenol (MEHQ), TCI Chemicals) is used as received. Adding MAA to the thermo-responsive microgel synthesis extends the functionality to pH-responsiveness. GMA (97%, Sigma Aldrich) is distilled for purification. The reactive epoxy group of GMA is versatile in subsequent reactions.

- **Initiator:** Two initiators are considered in the context of this thesis, namely 2,2'-azobis(2-methylpropionamidine)dihydrochloride (AMPA, 97%, Sigma-Aldrich) and potassium persulfate (KPS, ≥99.0%, Sigma-Aldrich). Both initiators decompose thermally, meaning that above a defined temperature, they start to decompose by forming two initiator radicals. They are both used as received in the synthesis.

- **Surfactant:** Hexadecyltrimethylammonium bromide (CTAB, ≥97%, Merck) and sodium dodecyl-sulfate (SDS, 99%, Acros Organics) are considered as surfactants in this thesis. Both chemicals are used as received. Surfactants ensure colloidal stability but do not influence the reaction kinetic of the microgel synthesis.

Note that not all reactants need to be part of the microgel synthesis. Surfactant is only added for colloidal stability, which is not needed in all applications. Also, the co-monomers pose as optional additives. Finally, occasionally no cross-linker is needed to produce ultra-low cross-linked microgels [73]. Each chapter outlines the involved reactants and the respective amount in the microgel synthesis under investigation.

2.2 Batch Synthesis

To this day, most microgels are synthesized in (fed-)batch reactor setups. Therefore, the following paragraph highlights the general experimental procedure for batch synthesis. For details on continuous production, the reader is referred to Section 3.2 and supporting literature sources [54, 55]. The polymerization of NIPAM with BIS is depicted exemplarily in a reaction scheme in Figure 2.1.

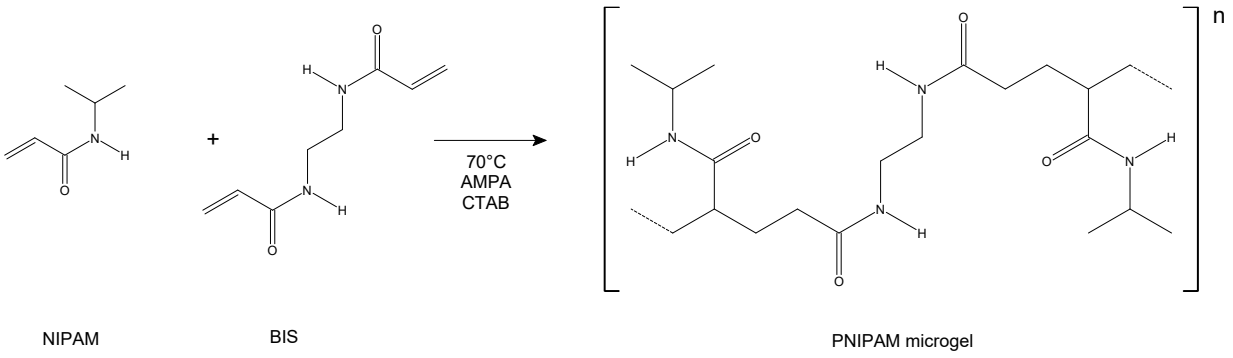

Figure 2.1: Schematic representation of the NIPAM-based microgel synthesis.

First, all partaking reactants except the initiator are dissolved. The reaction mixture is then heated to reaction temperature under constant degassing using nitrogen to repress all oxygen from the system. Oxygen inhibits the reaction, as it bonds to the radicals in the system and prevents the continuation of the polymerization. After approximately 30 min of degassing, the initiator is added (usually in dry form). The initiator decomposes and thereby forms primary radicals. The formed radicals build chains by propagating with monomer, cross-linker, or functional co-monomer. Here, the terminal end of the growing radical chains determines the kinetics of the propagation reaction. Therefore, different reaction kinetics are valid. While adding a monomer to the chain extends the chain, adding a cross-linker attaches a second double bond, thus enabling a three-dimensional network formation. As the solubility in water decreases with longer chains, the polymers start to precipitate from the water upon reaching a critical length. The propagation reactions continue until all monomers are fully converted to polymer chains. The synthesis ends with a termination reaction of two polymer

chains. The reaction setup permits several degrees of freedom, including the initial concentration of all components, temperature, stirring, and feeding of additional reactants during the synthesis. The reaction temperature is usually between 60°C to 80 °C, as a minimum temperature is needed for the decomposition of the initiator to set in, and water evaporation limits the maximum temperature. Generally, a higher temperature speeds up the reaction kinetics and thus decreases the overall reaction time [57]. For the experiments conducted within this thesis, the stirring speed is set to 300 rpm if not stated otherwise. It is well known that the stirring speed influences the microgel size [66] but does not affect the reaction kinetics. Note that microgels are not considered particles [74], and thus, the term *microgel size* or *polymer size* is used throughout this thesis instead of the more common *particle size*. Also, various contributions of experimental [51, 53, 54, 75] and simulation [76] analysis regarding the microgel growth indicate that the microgel growth is homogeneous, resulting in monodispers microgels.

2.3 Process Monitoring via Raman Spectroscopy

For polymerization processes, the time scales of change are usually in the order of minutes [77]. Precipitation polymerization of VCL-based microgels at 80°C reaches a final conversion already after 5 min to 8 min after addition of the initiator [57]. Monitoring the synthesis adequately requires measurements of a suitable, relatively high frequency. Here, in-line monitoring with low acquisition times enables the acquisition of the desired information on the analyte. As mentioned before, the term *in-line* refers to a measurement probe positioned directly inside the reactor as opposed to automatic *on-line* measurements using a bypass [59]. Off-line methods that require sampling or even further sample preparation before measurement cause long delays in the processing and are, therefore, not the first choice for high-resolution microgel synthesis monitoring.

For concentration monitoring, Raman spectroscopy is established as a suitable in-line process analytical tool for microgel synthesis [57, 58]. Raman spectroscopy is an optical method for identifying and quantifying components in samples of all physical states. In general, optical methods inherit the benefit of nondestructive measurements. For Raman spectroscopy, a monochromatic light source (laser) is used to excite the molecules in the analyte, and the scattered photon radiation is detected subsequently [78]. The inelastically scattered photons from the molecules inhibit a lower frequency than the excitation. These frequencies shifted from the excitation (also called Raman-shifted) are characteristic for each molecule. A measurement device collects the scattering intensities for these shifted wavelengths.

For the Raman spectra recorded within this dissertation, an RXN2 Raman Analyzer (Kaiser Optical Systems) is used. The Raman spectra are recorded in HoloGRAMS (Kaiser Optical Systems, Ann Arbor, Michigan, USA) with cosmic ray correction. The RXN2 operates at 785 nm with 400 mW excitation power. Depending on the reaction system, a short (0 mm) or long focus (3 mm) immersion probe (both Kaiser Optical Systems) is employed. The respective focus length is indicated in each chapter. The total detectable wavenumber range of the RXN2 Raman Analyzer used is between $100\,\mathrm{cm}^{-1}$ to $3450\,\mathrm{cm}^{-1}$. The acquisition time interval applied is adjusted to the specific system and described in each chapter separately.

For the evaluation of Raman spectra, indirect hard modeling (IHM) using the software PEAXACT (S-Pact GmbH, Germany, 2018) is applied. As the software evolves, the version varies between 4.5 to 5.8 in the following chapters. However, the main functionality of the software remains the same throughout. IHM is a physically justified, multivariate regression method that allows analysis of mixtures with overlapping component peaks and accounting for nonlinear spectral effects [79, 80], while relying on relatively small calibration data sets [79, 81]. For IHM, pure component models

(PCMs) are used to construct a mixture hard model (HM). The general procedure is visualized in Figure 2.2 [82]. To derive the PCM for each component in the reaction system, a spectrum of the pure component is collected. Subsequently, pseudo-Voigt peaks are fitted to the characteristic spectrum of the component within a certain spectral range, the so-called fingerprint range. Each peak is comprised of four parameters: the maximum intensity (α), the position (δ), the half-width at half maximum (HWHM, γ), and the fraction of the Gaussian part (β). For species that occur in mixtures, such as the dissolved monomers for the microgel synthesis, complemental hard modeling (CHM) [80] is applied. For CHM, the PCM of the known component and additional pseudo-Voigt peaks are fitted to the mixture spectra.

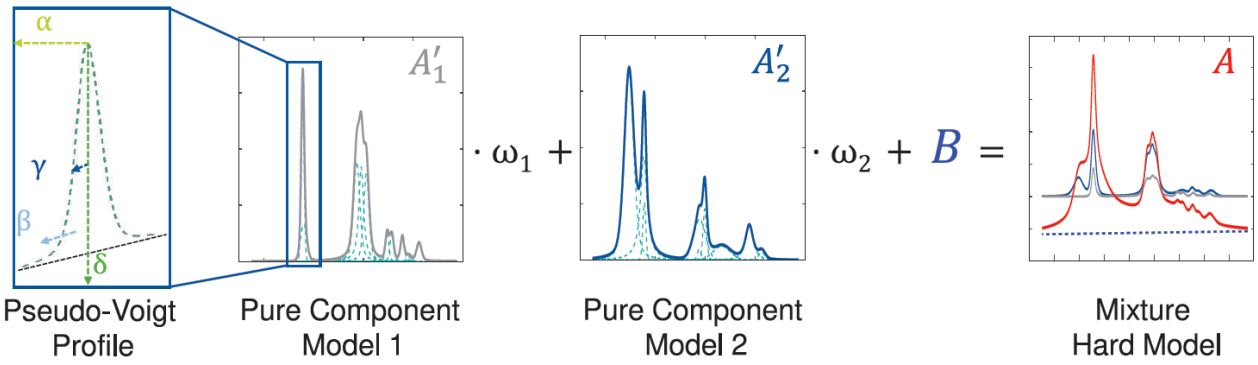

Figure 2.2: Indirect hard modeling procedure (Graphic taken from [82] and adapted).

Next, the PCM is subtracted so that only the peaks related to the other component remain. All PCM together, in Figure 2.2 they correspond to A_1' and A_2', are combined by linear weighting (ω_1, ω_2) and a baseline (B) is added to build the mixture HM A. To calibrate the mixture HM, Raman spectra of samples with known concentrations of all components are used. After calibration, the mixture HM can predict concentrations of known composition. For that, the mixture HM is adjusted to the spectrum of unknown composition within PEAXACT. The individual HM for evaluating the different microgel systems are described in the respective chapters. The settings for acquisition time interval, finger print region, excluded ranges, applied spectral pre-treatment, base line parameter, and additional peak constraints are also presented in each chapter separately.

To evaluate the model performance, qualitative and quantitative assessments occur. For qualitative considerations, the overall fit of mixture HM to the spectrum under evaluation is examined. For quantitative analysis, the following figures of merit for validation are applied: root mean squared error (RMSE) and RMSE of cross-validation (RMSECV), standard deviation of multiple measurements (s), and coefficient of determination (R^2). Each figure of merit is a measure to assess the model prediction performance.

The RMSE is calculated from the difference of the measured $y_{k,i}^{\text{meas}}$ and model-predicted $y_{k,i}^{\text{pred}}$ mole fraction of each species (k) based on a single measurement or multiple calibration measurements (N^{cal}):

$$\text{RMSE}_k = \sqrt{\frac{\sum_{i=1}^{N^{\text{cal}}} \left(y_{k,i}^{\text{meas}} - y_{k,i}^{\text{pred}}\right)^2}{N^{\text{cal}}}}. \tag{2.1}$$

The RMSE value can be interpreted as a measure of how spread the predicted values are on average from the measured sample concentrations. Another measure for the quality of the calibration model is the RMSECV, which is also calculated for each chemical species k in the analyte individually:

$$\text{RMSECV}_k = \sqrt{\frac{\sum_{i=1}^{N^{\text{CV}}} \left(y_{k,i}^{\text{meas}} - y_{k,i}^{\text{pred,CV}}\right)^2}{N^{\text{CV}}}}. \tag{2.2}$$

Here, the calibration is conducted with a subset of the whole calibration sample set, and the remaining samples are used for validation. This procedure is repeated until all subsets have been left out once. The additional index CV denotes that the values are predicted by an IHM calibrated on the subset of calibration samples N^{CV} of the experimental data set N. To access how spread the Raman spectra (N^{spectra}) of the same sample are, the sample standard deviation (s) for each species k is calculated as:

$$s_k = \sqrt{\frac{\sum_{i=1}^{N^{\mathrm{spectra}}} \left(y_{k,i}^{\mathrm{pred}} - y_k^{\mathrm{pred,avg}}\right)^2}{N^{\mathrm{spectra}} - 1}}. \tag{2.3}$$

Here, $y_k^{\mathrm{pred,avg}}$ accounts for the mean of the $y_{k,i}^{\mathrm{pred}}$ values.

Finally, the R_k^2 value represents the fraction of variance in the calibration for each species k explained by the regression model:

$$\mathrm{R}_k^2 = 1 - \frac{\sum_{i=1}^{N^{\mathrm{cal}}} \left(y_{k,i}^{\mathrm{meas}} - y_{k,i}^{\mathrm{pred}}\right)^2}{\sum_{i=1}^{N^{\mathrm{cal}}} (y_{k,i}^{\mathrm{meas}} - y_{k,i}^{\mathrm{meas,avg}})^2}. \tag{2.4}$$

Here, the total number of calibration samples is given by N^{cal} and $y_{k,i}^{\mathrm{meas,avg}}$ accounts for the mean of the calibration samples. The R^2 value is not exceeding 1, indicating a high prediction performance.

2.4 Microgel Synthesis Modeling

Modeling the conversion of reactants during polymerization has been a key topic of research for numerous decades. Owing to the similar structures and assumptions employed by kinetic models for general polymer synthesis and microgel synthesis, modeling approaches for microgel synthesis frequently derive from general models for radical polymerization. Odian presents a comprehensive summary of various polymerization types and modeling approaches, highlighting prevalent assumptions in the context of radical polymerization. In past studies, modeling approaches have been applied and presented for the synthesis of microgels in different microgel systems [14, 66–68, 76, 83–88].

Hoare et al. [83] derived a solely propagation-based steady-state terminal co-polymerization model accounting for the simultaneous reaction of four separate monomers. They applied the model for synthesizing microgels containing NIPAM, cross-linker, and up to two functional monomers. To estimate the required reactivity ratios, they used the Price-Alfrey scheme [89]. Subsequently, Hoare et al. [84] observed a sufficient accuracy of their model prediction of the chain and radial functional group distribution with experimentally observed data.

Janssen et al. [85] presented an elaborate dynamic co-polymerization model for the VCL-based microgel synthesis accounting for initiation, distinguishing between liquid and gel phase reaction, and including disproportionation and recombination as termination mechanisms. They applied quantum mechanical calculations and parameter estimation to determine unknown reaction parameter values. Subsequently, Janssen et al. [86] extended the model to account for the terpolymerization of NIPAM- and VCL-based microgels. In addition, Janssen et al. [76] later formulated the model as a pseudo-bulk model to describe the particle growth and particle size distribution during the microgel synthesis. The model showed good agreement in comparison with experimental data from calorimetry and dynamic light scattering.

Virtanen et al. [87] used in situ small-angle neutron scattering to monitor the formation of NIPAM-based microgels and developed a single exponential equation for the average particle volume from the experimentally observed values. The derived equation entails that the particle growth rate depends only on monomer concentration. The developed correlation was successfully applied by Nishizawa et

al. [88], who used temperature-controlled high-speed atomic force microscopy to monitor the NIPAM-based microgel synthesis.

Jung et al. [66] simplified the dynamic model by Janssen et al. [85] by assuming a pseudo-homogeneous phase, accounting only for diffusion-limited termination and excluding chain-transfer reactions. Next, they conducted a parameter identifiability analysis to increase the reliability of the estimated parameter values. Also, Jung et al. [67] modeled the impact of reactor type, reactor temperature, monomer-to-initiator ratio, cross-linker concentration, and surfactant concentration on the hydrodynamic radius of collapsed VCL- and NIPAM-based microgels. In experimental validation, they showed a suitable quantitative alignment of model predictions and various experimental data. Furthermore, Schneider et al. [68] extended their simplified dynamic model to account for the co-polymerization of NIPAM-based microgel with functional vinyl ferrocene (VFc) co-monomers. They used the enhanced model to simulate feeding strategies to modify the localization of the functional co-monomer within the particle and were able to experimentally validate the proposed strategies.

In the following, the underlying general reaction mechanisms are described based on the assumptions and derivations developed by Jung et al. [66].

- **Initiator Decomposition:** $\mathrm{I} \xrightarrow{k_\mathrm{d}} 2f\mathrm{R}_\bullet^0$
  Within the initiator decomposition, the initiator (I) decays to initiator radicals $\mathrm{R}_\bullet^0$. For this reaction, two main factors are relevant for the kinetics of the subsequent polymerization reactions: the decomposition rate coefficient (k_d) and the initiator efficiency (f). The rate coefficient depends on the type of initiator that is used in the synthesis. The decomposition rate also depends on the reaction temperature. The initiator efficiency for polymerization reactions ranges in the literature between 2 % and 99 % [90].

- **Chain initiation:** $\mathrm{R}_\bullet^0 + \mathrm{M}_j \xrightarrow{k_{\mathrm{p}11}} \mathrm{R}_j^{n+1}$
  Once initiator radicals $\mathrm{R}_\bullet^0$ are formed, they begin attacking monomers M of all types j (here, j also includes cross-linker monomers). The initiation kinetic coefficient is assumed to be equal to the propagation reaction (described below) coefficient $k_{\mathrm{p}11}$ of an active polymer chain with the main monomer (index 1) as the end type with another main monomer.

- **Propagation of monomer:** $\mathrm{R}_i^n + \mathrm{M}_j \xrightarrow{k_{\mathrm{p}ij}} \mathrm{R}_j^{n+1}$
  The propagation reactions of monomer M describe the chain growth of an active polymer chain R of length n. The kinetics of these reactions are assumed to only depend on the radical type i at the end of the active polymer chain and the attaching monomer j. This method is called terminal approach [91].

- **Propagation of cross-linker:** $\mathrm{R}_i^n + \mathrm{CL} \xrightarrow{k_{\mathrm{p}i\mathrm{CL}}} \mathrm{R}_\mathrm{CL}{}^{n+1} + \mathrm{PDB}$
  The propagation reactions of cross-linker CL with an active polymer chain R are similar to the propagation of monomer. However, since the cross-linker has two double bonds that allow a chain connection, a pendent double bond PDB is formed whenever a cross-linker is incorporated into the active polymer chain. This PDB enables another possibility for a monomer radical to attach.

- **Cross-linking:** $\mathrm{R}_i^n + \mathrm{PDB} \xrightarrow{k_{\mathrm{p}i\mathrm{CL}}} \mathrm{R}_i^{n+1} + X$
  Cross-linking occurs when a PDB attaches another active radical. A cross-link X is created that establishes the three-dimensional network formation of the microgel. The cross-linking kinetic coefficient is assumed to be the same as for the propagation of cross-linker.

- **Termination:** $\mathrm{R}_i^n + \mathrm{R}_j^m \xrightarrow{k_\mathrm{t}} \mathrm{P}^n + \mathrm{P}^m$
  In the termination reaction, two active polymer chains R_i^n and R_j^m convert to inactive polymer chains P^n and P^m. The termination reaction is assumed to be diffusion-limited, as the longer polymer chains lack mobility [90, 92]. Thus, the kinetic coefficient of the termination reactions k_t does not depend on the active polymer chain type i or j. This approach reduces the model complexity and the number of parameters and facilitates parameter identification.

3 In-line Monitoring of Microgel Synthesis: Flow versus Batch Reactor

Data Repository: *The Raman spectra acquired and the indirect hard modeling evaluation models developed in this chapter are published and available for free download via RWTH Publications [93].*

3.1 Motivation for In-line Monitoring of Continuous Flow Microgel Synthesis

The use of flow reactors continuously gains interest for polymer synthesis. Reis et al. [94] provide a detailed review of recent advances in flow polymerization. Flow reactors facilitate quasi-isothermal reaction control due to a high surface area to volume ratio, which is beneficial for quality control despite the exothermic polymerization. Flow reactors can be used for enhanced generation of reaction knowledge at the lab-scale when sufficient in-line monitoring is integrated. The term *in-line* implies that the immersion probe is inserted into the process stream, and the analysis is performed in situ [95]. In-line measurements via Raman spectroscopy are non-destructive, need no preparation, and are only slightly affected by scattering of water below a Raman shift of $2750\,\mathrm{cm}^{-1}$. Thus, Raman spectroscopy represents an established process analytical technology (PAT) tool for various applications in polymerization, most prominently in emulsion polymerization [96–100] and precipitation polymerization [57, 101].

From the PAT perspective, flow processing in a tube reactor enables the transfer from the time to the space domain when the reactor is operated at steady-state conditions. In an ideal flow reactor operated at steady-state, the composition of the analyte is constant over time at any location. Then, the acquisition time of the PAT is independent of the elapsed reaction time, thus the acquisition time is no longer a limiting factor for high-resolution measurements. In flow reactors, measurements over long periods improve the signal-to-noise ratio (SNR) and enable satisfying Raman spectroscopy measurements, which commonly experience low sensitivity [102]. Thus, flow reactors enable reaction monitoring at a higher SNR thus higher resolution than batch reactors, at least in principle. An improved resolution is valuable, especially for polymer synthesis, where complex chain-growth kinetics and rapid reaction rates occur. Yet, to benefit from the advantages of a flow reactor system, a high measurement accuracy of the Raman signal is essential.

Recently, Wolff et al. [54] successfully demonstrated the use of a flow reactor system. During precipitation polymerization, the reactants are dissolved in water and homogeneously mixed when the initiator is added to start the synthesis. The polymer chains build a colloidal network, transform into a collapsed state, and precipitate from the solution [50]. The precipitation of microgels is associated with rising turbidity towards the end of the fast reaction progress, making monitoring the synthesis demanding towards PAT.

In this chapter, the challenges associated with the integration of Raman spectroscopy into the flow reactor for the microgel synthesis are addressed. In particular, a measurement cell for monitoring in flow reactors is developed, potential measurement errors are systematically excluded, and Raman measurements in flow and batch reactors are compared. Below, each of these aspects is discussed in

detail concerning the literature and the approach applied in this work.

Generally, there are examples for the integration of Raman spectroscopy in continuous flow, as outlined in the review by Sans et al. [103]. It is stated that integration approaches at the lab-scale usually encounter difficulties in incorporating the spectrometer into the flow reactor without affecting the reaction system. When using a commercial spectrometer for in-line monitoring in flow reactors, the development of customized flow cells and analytical probes to integrate into the reactor entails a challenging task [103]. Flow cell development aims at minimizing the distance between reactor position and measurement cell position, which otherwise causes a significant dead volume. Despite the challenging conditions for in-line monitoring via Raman spectroscopy in flow reactors, some reactions have already been monitored inside continuous micro-reactors. Prominent applications of Raman spectroscopy in micro-reactors include the works of Mozharov et al. [102, 104], Leung et al. [105], Schwolow et al. [106], Rinke et al. [107], and Cao et al. [108].

Monitoring of polymerization is particularly challenging due to the rapid kinetics and turbidity. So far, exclusively Barnes et al. [109] monitored a polymeric system in flow via Raman spectroscopy. Barnes et al. measured the content of the monomer and the conversion of droplet phase fluids inside a microfluidic device during photo-polymerization. In contrast to micro-reactors, the in-line analysis via Raman spectroscopy in the milliscale, also called mesoscale, flow reactors is less studied [110]. Hamlin et al. [110, 111], Chaplain et al. [112], and Feidl et al. [113] propose approaches for flow syntheses in mesoscale reactors.

In terms of the **measurement cell design**, Hamlin et al. [110, 111] present a flow cell (width: 6.5 mm, height: 20 mm, length: 5 mm) connected to the reactor via tubes with an inner diameter of 1 mm. Therefore, the flow cell has a different geometry and size than the reactor tubes where the reaction under investigation occurs. Chaplain et al. [112] present a custom-built polytetrafluoroethylene (PTFE) in-line flow cell with a quartz window and a diameter of 10 mm. Here, the focus of the Raman laser points axially into the channel, and the fluid orthogonally exits the cell; thus, the direction of flow is suddenly changed. Feidl et al. [113] developed an in-house measurement cell for assistance in chromatography. The cell consists of a non-contact objective, a flow cuvette, and a concave mirror. The measurements occur in a cubic cuvette, which does not have the same geometric properties as the in-coming tube. At laboratory scale, Raman probe integration via simple union tees shows a sufficient performance for in-line monitoring as influence of the cell material is avoided. In this chapter, a 3d-printed measurement cell is proposed made of polyamide with a customized geometry for Raman measurements, thereby overcoming substantial alterations between reactor and measurement cell geometry. The cell allows measurements at two positions along the reactor tube. In this work, the measurement cell and reactor are similarly structured, as the tube geometry and magnitude of the diameter are equivalent. The developed cell presents an alternative to union tees and can be used in applications where steel is not inert.

For a **systematic elimination of measurement errors**, the identification of sources for measurement errors is essential. Here, the interface of the sample, the measurement settings, and the environmental conditions influence the method's accuracy [114] and need to be carefully studied when applying Raman spectroscopy. Also, inherent reactor dynamics are caused by rheology effects in the reactor or by short-term fluctuations of the included pumps, which are often impacted by pulsation [104]. In heterogeneous fluid systems, the pulsation of multiple pumps can cause an unstable flow. The unstable flow can impact the distribution of the components within the reactor and, hence, impede the synthesis's reproducibility. As reactor dynamics can affect the accuracy of the measurements, these dynamics need to be considered. For example, Mozharov et al. [102] assessed the flow conditions for their micro-reactor setup qualitatively and reported that the spectral noise is smaller than pumping-related noise. However, so far, for flow reactors, the influence of sample presentation on measurement accuracy has not been systematically studied in a quantitative assessment. Thus, a

systematic approach for studying and analyzing the factors impacting the Raman method accuracy in a tubular flow reactor is presented. Specifically, individual factors are investigated such as the evaluation model calibration, the flow of the solvent in the reactor, the position of the measurement along the length of the flow reactor, the influence of particular solutions, and the cumulative accuracy in detail. Overall, different calibration strategies for the evaluation model are compared, and a quality criterion for the Raman measurements in the flow reactor is derived to allow outlier detection.

High accuracy monitoring of the microgel synthesis in flow enables **comparing Raman measurements in the flow and batch reactors**. Meyer-Kirschner et al. [57, 101] showed that Raman spectroscopy adequately monitors the monomer and the polymer content during the microgel synthesis in batch reactors. Fandrich et al. [55] measured the continuous synthesis of *N*-isopropylacrylamide (NIPAM)-based microgels via in-situ Fourier-transform infrared (FTIR) spectroscopy. Since the water signal strongly influences infrared spectroscopy, Raman spectroscopy appears to be the more suitable PAT for monitoring the microgel synthesis. However, in-line Raman spectroscopy is yet to be transferred to the tubular flow reactor. Herein, the poly *N*-isopropylacrylamide (PNIPAM) microgel synthesis is measured via in-line Raman spectroscopy, integrating the probe via the customized measurement cell, and apply the developed quality criterion. Finally, the trajectories of the reaction conversion over the mean residence time from batch and flow experiments of the PNIPAM synthesis are compared. For validation, the in-line FTIR measurements of the continuous microgel synthesis [55] are compared with the Raman measurements of this chapter.

3.2 Experimental

3.2.1 Flow Reactor

The microgel synthesis in the flow reactor is carried out similar to previous works by Wolff et al. [54], using two stock solutions, the monomer and the initiator stock solution. The stock solution of the monomer contains 12.52 g of the monomer NIPAM, 0.42 g of the cross-linker *N*,*N*'-methylenebis(acrylamide) (BIS), and 0.15 g of the surfactant hexadecyltrimethylammonium bromide (CTAB) dissolved in 1000 mL of water. The stock solution of the initiator contains 0.4 g of the initiator 2,2'-azobis(2-methylpropionamidine)dihydrochloride (AMPA) dissolved in 50 mL of water. The stock solution of the monomer is stirred and heated to 70°C while constantly being degassed with nitrogen for 30 minutes before the reaction start. For the initiator solution, pure water is degassed with nitrogen for 30 minutes at 70°C. The initiator is added after cooling the degassed water to ambient temperature in a vacuum.

A schematic representation of the experimental setup is shown in Figure 3.1. To start the reaction, two pumps (LabDos P100, HiTec Zang, Herzogenrath, Germany and ISMATEC MCP Standard with Easy-Load II pump head, Wertheim, Germany) transport the stock solutions of the initiator and the monomer. Both solutions are mixed in a Y-connector and a subsequent static PTFE mixer (24 mixing elements, total length: 150 mm, outer diameter: 6.35 mm; ESSKA, Hamburg, Germany) with a volume ratio of 19 to 1 of the heated monomer solution to initiator solution at ambient temperature, respectively. An increased concentration in the stock solution of the initiator compared to previous works [54] is introduced to minimize the temperature loss in the Y-connector due to the ambient temperature of the initiator solution. Nevertheless, the overall concentrations in the flow reactor still match those previously reported in recipes for batch reactions [101]. Subsequently, the reaction solution flows into two sequential tubular glass reactors with an inner diameter of 4 mm (customized production by Seele Glasapparatebau & Laborservice, Swisttal-Straßfeld, Germany). The reactor coil is embedded in a 70°C tempered fluid controlled by an external heating bath (MGW Lauda C6 with

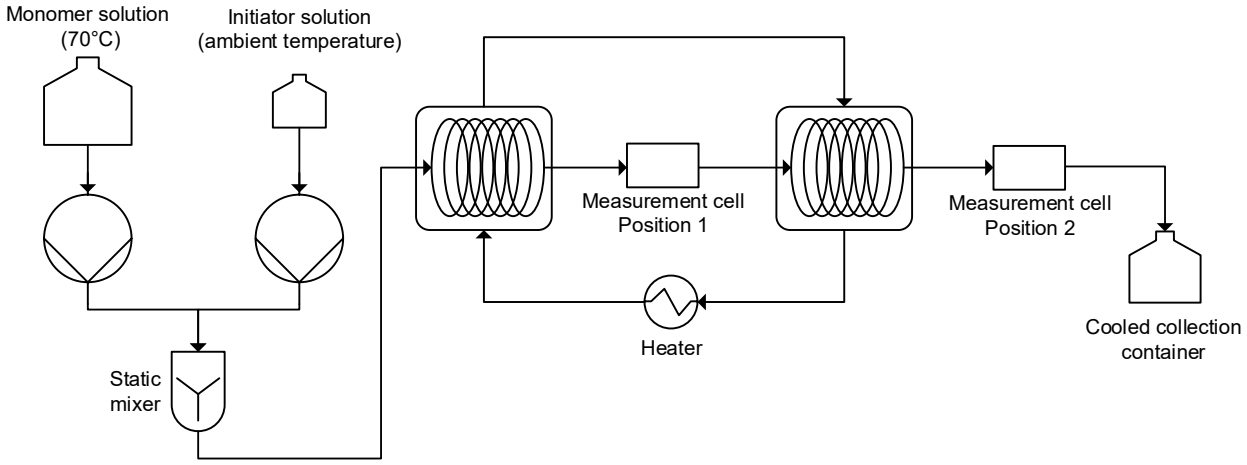

Figure 3.1: Schematic representation of the experimental setup for the PNIPAM synthesis in flow including equipment and material flows.

a control unit CS, Lauda, New Jersey, USA). The use of glass reactors enables the visualization of the reaction progress from a transparent to a turbid appearance from the growing microgels. Unlike high-temperature plastic materials such as polycarbonates, the glass construction hinders oxygen diffusion through the reactor walls and comprises higher heat transfer coefficients. Thus, oxygen inhibition during the microgel synthesis and temperature loss are avoided inside the glass reactors. At the end of the second tubular glass reactor, the polymerization is stopped by cooling the reaction fluid in an ice bath.

3.2.2 Raman Measurements

3.2.2.1 Evaluation Models

The Raman spectra for calibration are collected using a 60 s acquisition time interval. A Raman shift from 800 cm^{-1} to 1850 cm^{-1} is considered, as this range covers the so-called fingerprint region of the monomer and the polymer [101]. The atmospheric oxygen signal between 1552 cm^{-1} to 1560 cm^{-1} is excluded for the model generation. The pure component model of water is directly determined, while the pure component models of NIPAM and PNIPAM are derived using complemental hard modeling (CHM) [80]. Pure component models are then used to build a mixture model. A linear baseline is employed in every evaluation model.

The mixture model with the integrated linear baseline is calibrated using ratiometric regression and leave-10%-out cross-validation. Samples of aqueous mixtures containing up to 1.5 wt% NIPAM and up to 1.5 wt% PNIPAM span the calibration range (see Tables A.1 and A.2 in Appendix). Measurements of the calibration samples are recorded by applying three different strategies. Firstly, measurements are acquired via a standard procedure with single measurements inside glass flasks. This procedure is usually conducted for batch monitoring and is abbreviated as *in glass flask*.Among the considered strategies, the *in glass flask* strategy is the least time-consuming, as the effort to prepare calibration samples in glass flasks is low. The standard procedure is extended to multiple measurements of the same calibration sample inside a glass flask as the second strategy. This second procedure is referred to as *multiple in glass flask*. The *multiple in glass flask* takes notably longer, as the time for multiple measurements linearly scales with the number of measures. Lastly, calibration measurements are carried out inside the novel measurement cell (abbreviated *in cell*) to avoid any

influence of the transfer between calibration and measurement setup. The *in cell* model ultimately requires the highest effort, as the measurement cell has to be prepared to conduct measurements. For the *in cell* procedure, the weighting of samples takes place in glass flasks, and the content is afterward transferred into the cell. The procedure comes along with significant effort for cleaning the measurement cell for proper calibration measurements. However, the evaluation model calibrated by applying the *in cell* strategy is expected to outperform the other models in terms of accuracy when evaluating measurements inside the measurement cell. Here, the calibration environment and the measurement environment are identical; thus, no structural offset occurs concerning the transfer from calibration to measurement setup.

By applying the indirect hard modeling (IHM) evaluation models to measurements of pure solvent inside the reactor setup, the suitability of the calibration methods in terms of accuracy and effort is analyzed. The prediction accuracy of the developed calibration models is evaluated based on the root mean squared errors of cross-validation (RMSECV) and the coefficients of determination (R^2).

3.2.2.2 Synthesis Conditions

In-line Raman measurements during the microgel synthesis are conducted at two positions at the reactor setup (see Figure 3.1) using different settings of the volume flow rates of the stock solutions. The spectrum acquisition interval starts when continuous Raman measurements of 10 s acquisition time per spectrum show no longer a gradient in intensity.

For synthesis monitoring, larger acquisition time intervals generally yield higher SNRs and thus measurements of higher quality, but the gain of the SNR is limited. Meyer-Kirschner et al. [58] found the SNR to be constant above an acquisition time interval of 40 s for off-line measurements of a similar microgel system. Therefore, a time interval of 40 s is applied in all experiments for Raman signal acquisition as a trade-off between maximizing SNR and minimizing effort in time.

3.2.2.3 Measurement Accuracy

The accuracy of the Raman measurements is analyzed via a variety of measurements inside the novel measurement cell. Thereby the influence of several aspects is analyzed, which are listed below and visualized in Figure 3.2.

1. The calibration method of the IHM evaluation model
2. The flow of the solvent water
3. The flow of the monomer NIPAM and the flow of PNIPAM microgels with turbid conditions
4. The complete setup
5. The position of the measurement cell

The investigated analytes comprise pure water and mixtures of water with NIPAM or PNIPAM. First, the analyte is in stagnation for analyzing the influence of the reactor environment and for comparing differently calibrated evaluation models. The subsequent measurements for the analysis of the accuracy are conducted with flowing analytes. If not stated otherwise, the measurements are conducted at the reaction temperature of 70°C. The effects of temperature on the measurement accuracy are not studied in depth in this work, as previous studies by Meyer-Kirschner et al. [57] show that the Raman peaks of microgel solutions at different temperatures not exhibit nonlinear effects. Furthermore, Meyer-Kirschner et al. quantified the effects of temperature changes on the microgel spectra as a relative error of 1.8%. Also, temperature has the most significant impact on Raman OH-stretching in the spectrum of water. This stretching occurs at frequencies outside the considered spectral range of this work. Hence, the role of temperature effects are negligible in this work.

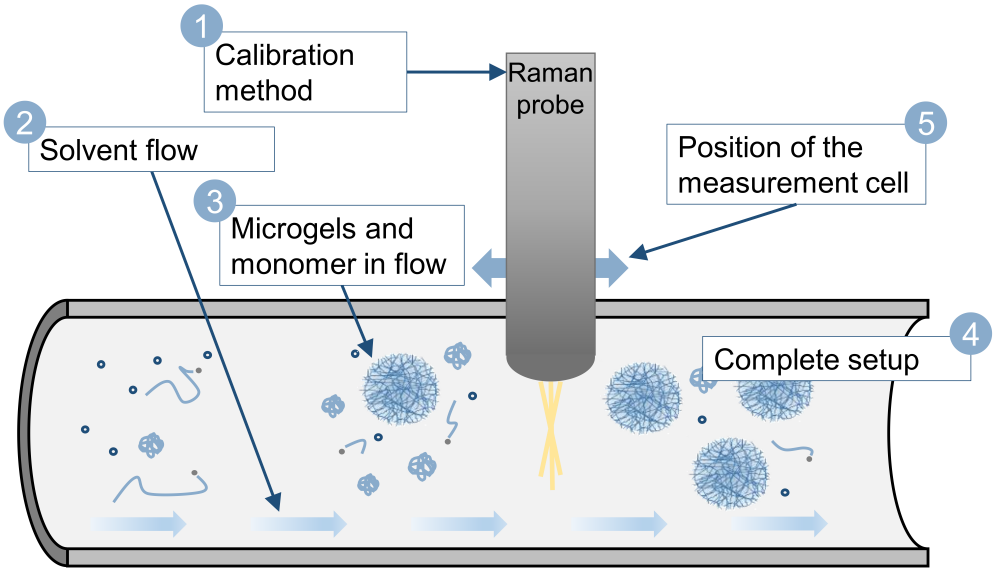

Figure 3.2: Graphical representation of the aspects of interest of the measurement accuracy analysis.

The measurements are evaluated using a calibrated evaluation model (see Section 3.2.2.1). Then error-values are calculated like the root mean squared error (RMSE) and standard deviations of the sample (s) for the NIPAM prediction as measures for the measurement accuracy. The NIPAM content is most reliable to predict due to a strong double-bond signal.

The RMSE is calculated from the predictions of multiple measurements (see Equation (2.1)).The RMSE value can be interpreted as a measure of how spread the predicted values are from the true sample concentrations (determined via weighting). During the synthesis, the aims is to determine the concentration from samples of unknown composition, thus the RMSE can not be calculated under these conditions. In this case, the sample standard deviation (s) is calculated (see Equation (2.3)).

3.3 Results and Discussion

The results of this chapter comprise the development of an adequate measurement cell, the comparison of calibration strategies for the development of an evaluation model, and the systematic analysis of the accuracy of the Raman measurements in the flow reactor. The comparison of different calibration strategies allows the analysis of the suitability of the calibrated evaluation models. From the systematic analysis of the accuracy in the flow reactor, a quality criterion is derived for outlier detection during synthesis monitoring. This quality criterion is applied to in-line measurements of the PNIPAM microgel synthesis. Additionally, the results include the comparison of Raman measurements in the carried-out synthesis in flow with a batch synthesis [101] and a FTIR approach in a flow reactor [55] from the literature. The comparison to batch measurements shows the impact of the synthesis transfer to batch. The comparison to FTIR measurements enables the validation of the Raman synthesis measurements in flow reactors.

3.3.1 Measurement Cell

The customized measurement cell enables in-line Raman measurements during the synthesis in flow with reduced velocity variations and flexible positioning (see Figure 3.1). The cell consists of three main components shown in Figure 3.3: a flow channel with an open slot, a cover with a bore for the Raman immersion probe head, and a sealing plate. Additionally, two metal tube connectors are attached to the flow channel, one on each side.

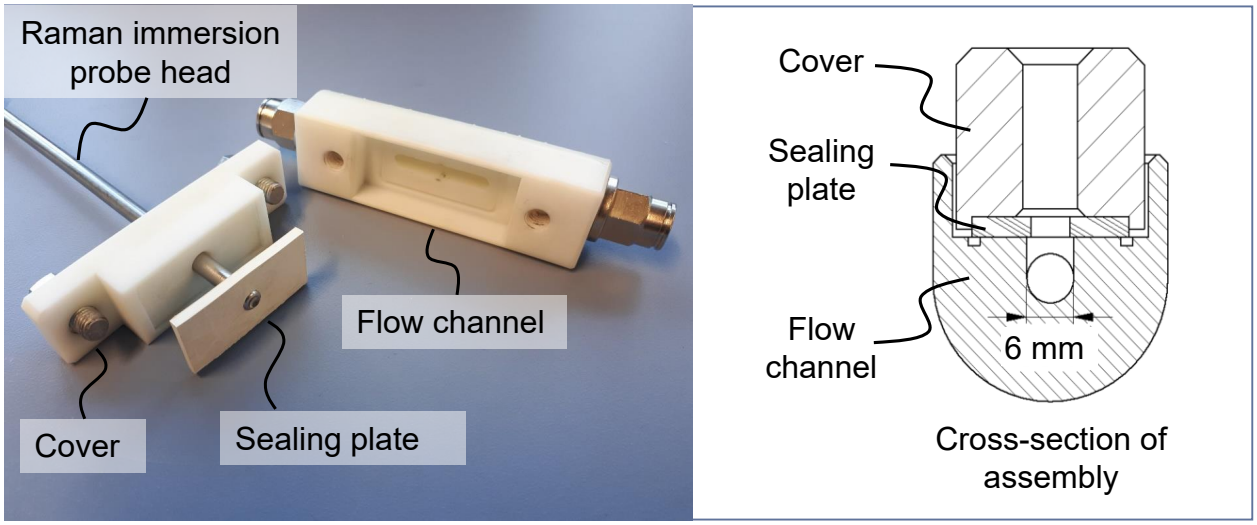

Figure 3.3: Measurement cell consisting of flow channel and cover with sealing plate and Raman immersion probe head.

The connectors allow a quick assembly of the measurement cell with the reactor system and enable flexibility in positioning the cell along the tubular flow reactor (see Figure 3.1). The 3d-printed flow channel and the cover are made from polyamide, whereas the sealing plate is made of a 3 mm ethylene propylene diene monomer (EPDM) rubber plate. The reaction fluid enters the cell via the connector on one side. Subsequently, the fluid runs through a 6 mm diameter circular channel until it reaches the open slot where the channel becomes semi-circular (see cross-section depicted in Figure 3.3) and the Raman immersion probe head is positioned perpendicular to the direction of flow.

During all measurements, the backside of the channel is lined with aluminum foil to minimize the influence on the Raman spectra caused by the cell's material. Furthermore, all ambient light is excluded during data acquisition by placing an opaque polyvinyl chloride (PVC) cover around the cell. For synthesis execution, the cell is tilted upward in the direction of flow to prevent gas bubbles from getting stuck inside the cell.

3.3.2 Evaluation Models

Three calibration models are developed for the Raman spectroscopy in the flow reactor: *in cell*, *in glass flask*, and *multiple in glass flask*. The calibration results show that all three models perform with high accuracy. The calibration models consist of the priorly developed pure component models for NIPAM and PNIPAM. The pure component models agree with previously published models [101, 115]. The Raman measurements of calibration samples in the measurement cell containing water and NIPAM are shown in Figure 3.4. Figure 3.5 illustrates the Raman measurements of calibration samples in the measurement cell containing water and PNIPAM. All spectra are treated with a linear fit subtraction for visualization. The characteristic peaks are described in detail in Appendix A.1.

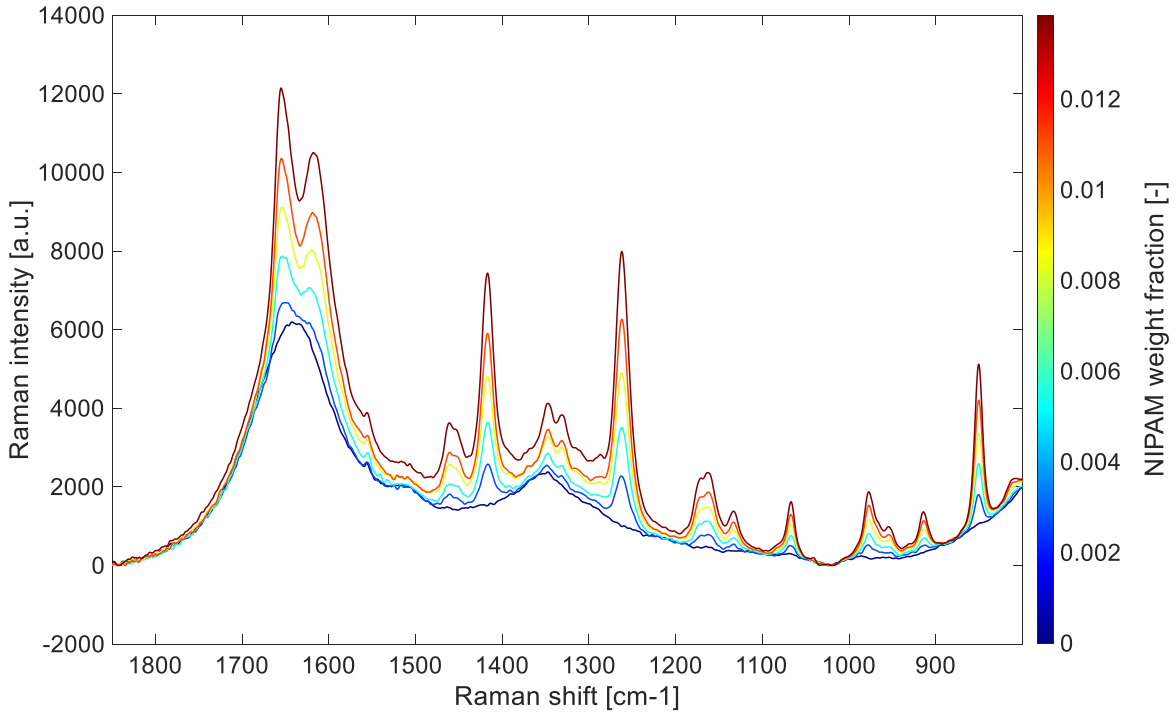

Figure 3.4: Raman spectra of the *in cell* calibration measurements containing NIPAM and water. The spectra are treated with a linear fit subtraction.

The calibration results are illustrated as parity plots in Figure 3.6 for the three alternative calibration models. The parity plots indicate that all evaluation models predict the calibration measurement composition precisely. Yet, for all evaluation models, the prediction for NIPAM consistently is more accurate than for PNIPAM. The corresponding RMSECV and R^2 values for the prediction of NIPAM and PNIPAM for the three calibration models are shown in Table 3.1. For the *in cell* calibration, the RMSECV value for NIPAM is 0.037 wt% and for PNIPAM 0.157 wt%, while the R^2 values of NIPAM and PNIPAM are 0.998 and 0.954, respectively. For the calibration in the glass flasks, the RMSECV values result in 0.040 wt% for NIPAM and 0.434 wt% for PNIPAM. The according R^2 values are 0.996 and 0.613. Finally, for the calibration *multiple in glass flasks*, the RMSECV values for NIPAM and PNIPAM yield 0.026 wt% and 0.269 wt%, whereas the R^2 values yield 0.998 and 0.758. All of these values are equivalent to previously published IHM models for similar systems [57, 101]. Thus, the results confirm that predictions of the monomer content tend to be the most reliable.

Table 3.1: RMSECV and R^2 values for the NIPAM and PNIPAM prediction of the three alternative calibration strategies.

Component	Evaluation model	RMSECV [wt%]	R^2
NIPAM	*in cell*	0.037	0.998
	in glass flask	0.040	0.996
	multiple in glass flask	0.026	0.998
PNIPAM	*in cell*	0.157	0.954
	in glass flask	0.434	0.613
	multiple in glass flask	0.269	0.758

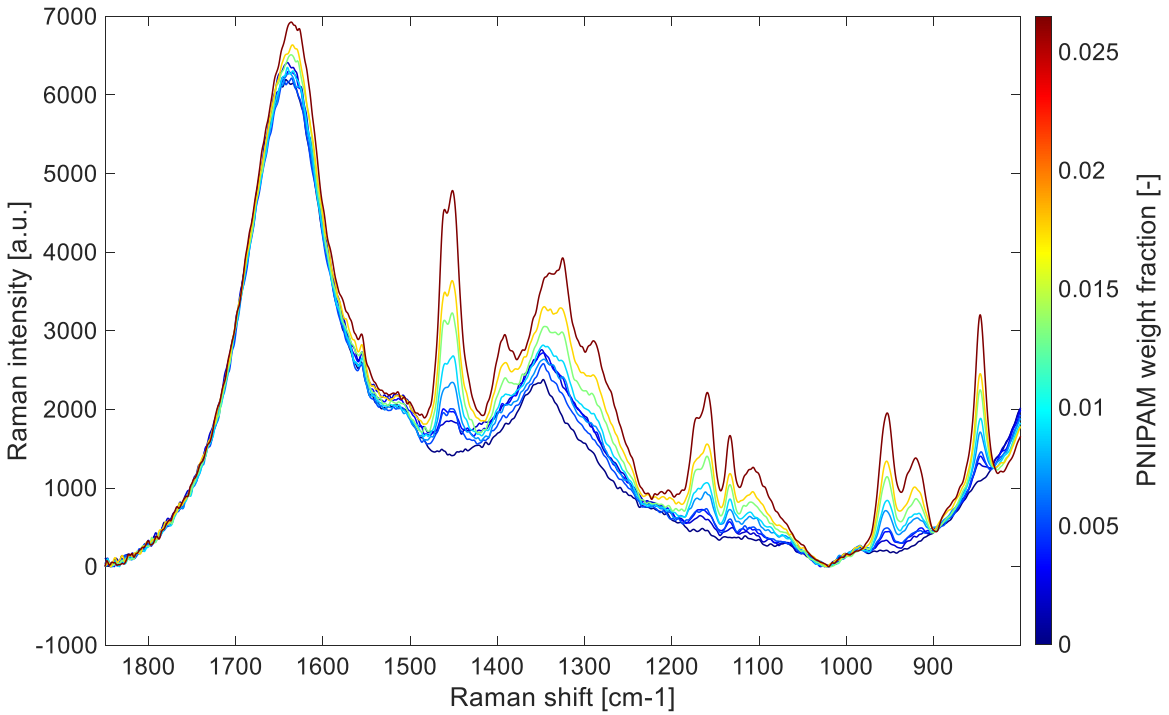

Figure 3.5: Raman spectra of the *in cell* calibration measurements containing PNIPAM and water. The spectra are treated with a linear fit subtraction.

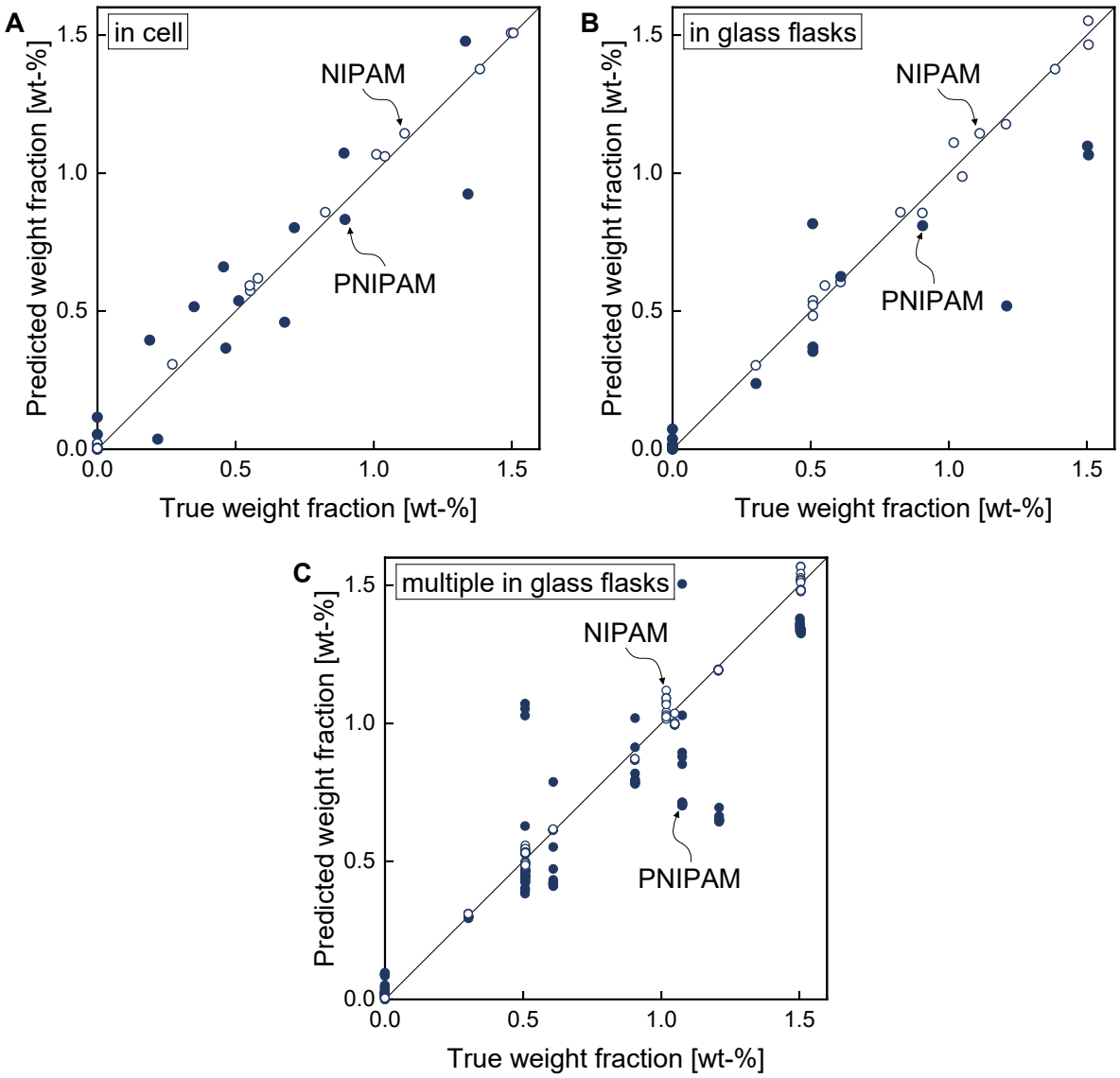

Figure 3.6: Parity plots of the three evaluation models with different calibration strategies: (A) *in cell*, (B) *in glass flasks*, and (C) *multiple in glass flasks*. Open circles denote NIPAM predictions and filled circles denote PNIPAM predictions.

Comparing the three calibration strategies yields that the *in cell* and *multiple in glass flask* methods are most appropriate. For NIPAM predictions, the comparison of the RMSECV and the R^2 values in Table 3.1 validates a high prediction accuracy of the NIPAM content for all presented models. Still, these coefficients indicate an improved prediction accuracy for the *in cell* and the *multiple in glass flask* calibration strategy. Thus, both calibration strategies constitute sufficiently accurate methods for the generation of the evaluation model.

3.3.3 Systematic Elimination of Measurement Errors

To systematically eliminate measurement errors, the accuracy analysis is carried out for the influencing parameter. The accuracy analysis yields that the influence of a multi-molecular analyte determines the quality criterion. When transferring PAT from batch to continuous mode, the influence of the monomer and microgel flow, the precision of the complete reactor setup, and the measurement cell position (see Figure 3.1) need to be considered in detail to maintain high accuracy quantification. The RMSE values for the NIPAM prediction are calculated to quantitatively assess the influence of the analyzed factors. The RMSE indicates how much NIPAM content the model predicts even when the analyte contains no NIPAM. For measurements, which contain an unknown amount of NIPAM, the standard deviation of the sample is calculated from the NIPAM predictions to estimate the pertaining measurement accuracy.

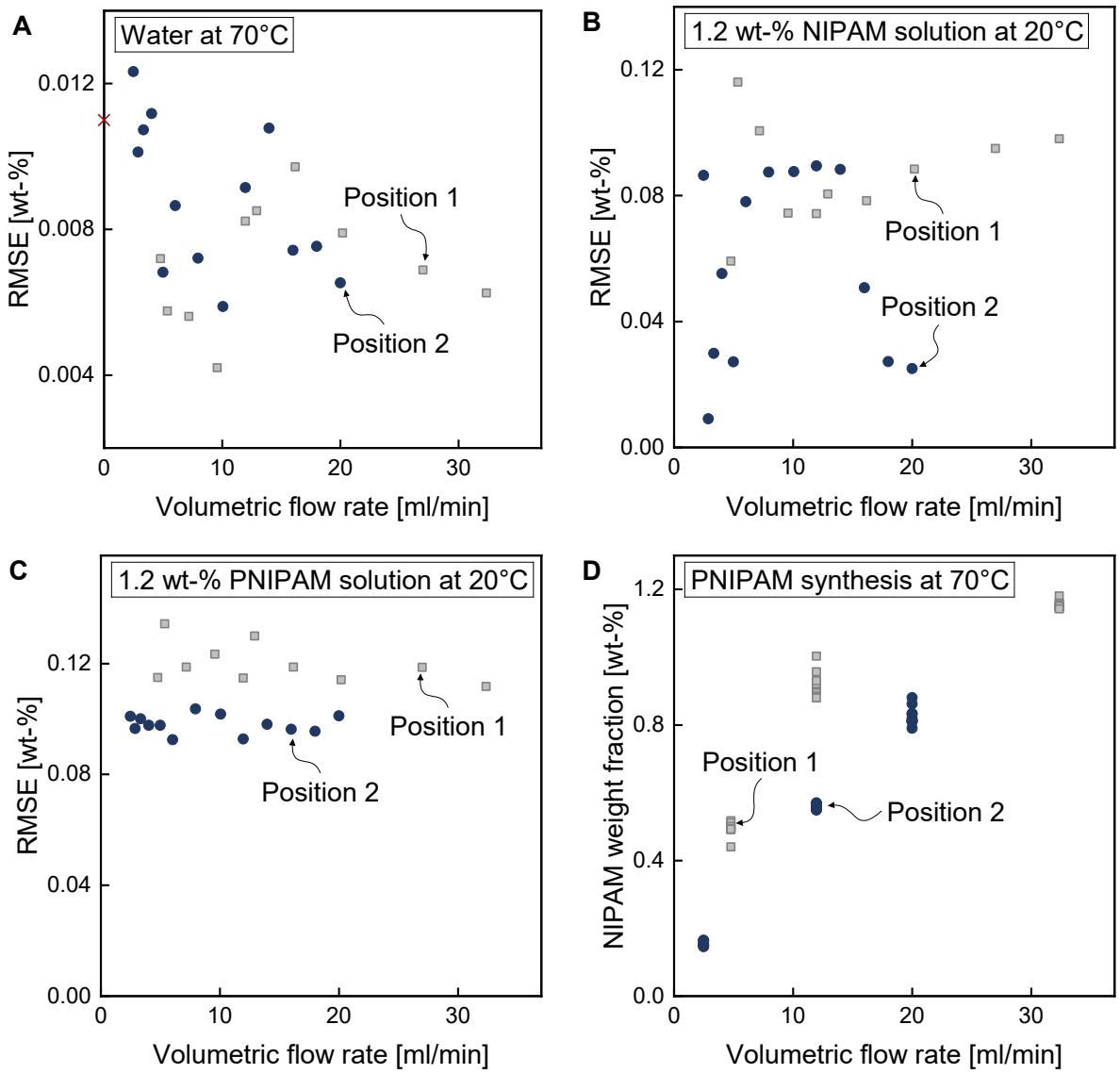

Figure 3.7: RMSE of the NIPAM prediction for different flow rates for measurements of (A) pure water at 70°C, (B) 1.2 wt% NIPAM solution at 20°C, and (C) 1.2 wt% PNIPAM solution at 20°C; (D) predicted NIPAM content for different flow rates during the microgel synthesis at 70°C. Grey boxes and blue circles denote measurements at Position 1 and 2, respectively. Red x represents the RMSE of the NIPAM prediction at stagnation.

3.3.3.1 Calibration Method

Although the calibration of the *in cell* evaluation model is the most laborious among the studied calibration methods, it suits the application most accurately. The comparison of RMSE values from the evaluation using different calibration models yields that the *in cell* model performs more accurately than the models calibrated *in glass flasks*. The calculated RMSE value for ten repeated measurements is 0.011 wt% for 70°C using the *in cell* evaluation model. This value is significantly smaller than the correlated RMSECV error value 0.037 wt% of the *in cell* model, which indicates that the measurement variations of the solvent in the cell are negligible compared to the inherent evaluation model deviation. Thus, the *in cell* model represents the reactor environment with sufficient precision.

As deviations resulting from the transfer from calibration to reactor setup are expected, the *in cell* model expectedly outperforms all other considered evaluation models. Nonetheless, all models are discussed below. The RMSE value of the *in glass flask* model evaluation is 0.061 wt% at 70°C and thus larger than the RMSECV value 0.040 wt% of the model itself. A similar phenomenon applies for the *multiple in glass flask* model, where the RMSECV value 0.026 wt% is smaller than the RMSE value of 0.061 wt% at 70°C. Hence, deviations in measurement evaluation are notable at 70°C but still range in a similar magnitude to the inherent model error for both models calibrated in glass flasks. Thus, the prediction resulting from a model not calibrated at ideal environment conditions is still relatively accurate and could be acceptable depending on the application. Therefore, the needed accuracy for the individual application must first be defined to choose the most suitable calibration strategy for effort and preciseness. The *in cell* evaluation model is applied to generate reaction data knowledge, as most precise measurements are targeted.

3.3.3.2 Solvent in Flow

The measurement accuracy from flowing solvent water shows no identifiable dependency on the magnitude of the volumetric flow rate. Furthermore, the accuracy at Position 2 is slightly better than at Position 1. The RMSE of the NIPAM prediction under changing volume flow rates of the solvent water is shown in Figure 3.7(a) for both measurement cell positions at 70°C. On average, the RMSE values calculated from ten measurements are lower at Position 1 with 0.0070 wt% than at Position 2 with 0.0088 wt%. At Position 1, the measurements exhibit a maximum RMSE value of 0.0097 wt% and a minimum of 0.0042 wt%, while for Position 2 the maximum RMSE value is 0.0123 wt% and the minimum is 0.0059 wt%. The RMSE values of Positions 1 and 2 are still in a similar range. They show that overall the deviations resulting from the impact of the solvent flow are negligible compared to the inherent error from the evaluation model itself. This finding suggests that for transferring the PAT, a closer analysis of the impact of the solvent flow is not recommended considering the effort and time of the transfer.

3.3.3.3 NIPAM in Flow

The presence of multi-molecular systems in the reactor impacts the quantification accuracy. Here, the actual NIPAM content of the analyte is known from the weighing during the preparation of the solution. Thus, the actual content is used for the calculation of the RMSE. The impact of flowing NIPAM on the measurement accuracy can be analyzed only at ambient temperature because an increase to reaction temperature could initiate the polymerization and falsify the real NIPAM content. Furthermore, omitting AMPA in the analyte solution ensures that no PNIPAM is formed during the measurements.

Figure 3.7(b) shows the RMSE values of the NIPAM prediction at Position 1 and 2 for a 1.2 wt%

NIPAM solution in flow at ambient temperature. At Position 1, the average RMSE is 0.0865 wt%, with a maximum of 0.1161 wt% and minimum of 0.0591 wt%. For Position 2, the values are given by an average RMSE of 0.0571 wt% and the maximum and maximum of 0.0894 wt% and 0.0091 wt%, respectively. The comparison shows that the prediction at Position 2 is slightly better than Position 1, but the accuracy range is similar. The RMSE values are significantly higher for the measurements including NIPAM than for pure water at ambient temperature. Measurements of flowing water at ambient temperature have an average RMSE value of 0.0110 wt% at Position 1 and 0.0092 wt% at Position 2. Therefore, the presence of NIPAM monomers impairs the accuracy significantly. The magnitude of the deviations resulting from the NIPAM influence hence considerably dictates the best possible accuracy.

3.3.3.4 Microgels in Flow

The turbidity from the presence of PNIPAM microgels in the solution reduces the measurement accuracy further. The RMSE values of the NIPAM prediction over different flow rates of measurements of a 1.2 wt% PNIPAM microgel solution inside the reactor at ambient temperature are depicted in Figure 3.7(c). The analyte solution contains PNIPAM microgels which have been dialyzed for multiple days against water to remove unreacted substances and freeze-dried to remove the water content. For the measurements at Position 1, the maximum RMSE value is 0.1343 wt% and the minimum is 0.1117 wt% with an average value of 0.1199 wt%. For the measurements at Position 2, the maximum RMSE value is 0.1036 wt% and the minimum is 0.0925 wt% while the average value is at 0.0980 wt%. Thus, the accuracy at Position 2 is slightly better than at Position 1.

The comparison of the PNIPAM microgel and NIPAM solution measurements in the flow reactor yields that the accuracy is in the same order of magnitude. This similarity indicates that the increasing turbidity caused by the PNIPAM microgels does not influence the preciseness as much as solely the multi-molecular system. Yet, the average RMSE values for the NIPAM solution at Position 1 and Position 2 are lower than for the PNIPAM microgel solution by 0.0334 wt% and 0.0409 wt%, respectively. However, conducting measurements of PNIPAM microgels comes along with increased effort, as the PNIPAM microgels either have to be synthesized, filtered, and freeze-dried or have to be bought, which is relatively expensive. Both ways to receive PNIPAM microgels are cumbersome. Thus, it is suggested that generally the accuracy range achievable with NIPAM molecules flowing through the reactor is applied as the limit on feasible accuracy for synthesis measurements. However, considering the quality criterion in the context of this work, the RMSE values of the PNIPAM microgel measurements are applied subsequently.

3.3.3.5 Precision of Complete Setup

Variations between multiple microgel synthesis measurements at the same reactor setting are larger for Position 1 than for Position 2. Still, overall the variations range in an insignificant magnitude compared to the formerly analyzed factors, like flowing NIPAM or PNIPAM microgel solution. Reactor dynamics can only be analyzed when varying composition occurs. Also, the RMSE of the NIPAM prediction can not be calculated as the population mean (meaning the true NIPAM content) is unknown. Consequently, the reactions are measured ten times to calculate the standard deviation of the sample. The prediction of the NIPAM content for the different volumetric flow rates is depicted in Figure 3.7(d). The resulting values of the standard deviation are presented in Table 3.2. The variation of multiple synthesis measurements at Position 1 is overall higher than at Position 2. However, the largest measured standard deviation is only 0.0334 wt%. Thus, the inaccuracies from the inherent reactor dynamics are negligible compared to the influence of flowing NIPAM molecules or PNIPAM

microgels in the reactor. The small standard deviation values indicate a sufficient reproducibility of the synthesis in the flow reactor.

Table 3.2: Sample standard deviation for the NIPAM prediction of reaction measurements at 70°C at Position 1 and 2.

	Volumetric flow rate [mL min^{-1}]	Standard deviation [wt%]
Position 1	4.8	0.0204
	11.97	0.0334
	32.4	0.0108
Position 2	2.5	0.0075
	12.0	0.0076
	20.0	0.0270

3.3.3.6 Measurement Position

The review of the results from the previous sections, which are graphically summarized in Figure 3.7, indicates that the measurements at Position 2 mainly have a lower RMSE or standard deviation and, hence, a higher precision. However, the results do not explicitly show a clear trend towards one position over the other. To further elucidate the relevance of the cell position on the measurement accuracy, the relation between RMSE and mean residence time is plotted in Figure 3.8. The mean residence time is linked to the volumetric flow rate by the correlation provided in Appendix Figure A.3. In Figure 3.8, the RMSE is lower for most measurements acquired at a similar mean residence time for Position 2 than for Position 1. The only exception occurs for the flow of the NIPAM solution at around 436 s mean residence time. The results indicate that overall the measurements at Position 2 tend to be more precise. The accuracy of measurements at Position 1 or 2 range in a similar order of magnitude, thus not allowing for a final recommendation on optimal position of the measurement cell. Nevertheless, Position 2 of the measurement cell is slightly favored regarding measurement accuracy. Hence, if feasible, measurements should preferably be conducted at Position 2 of the proposed reactor setup at higher volumetric flow rates.

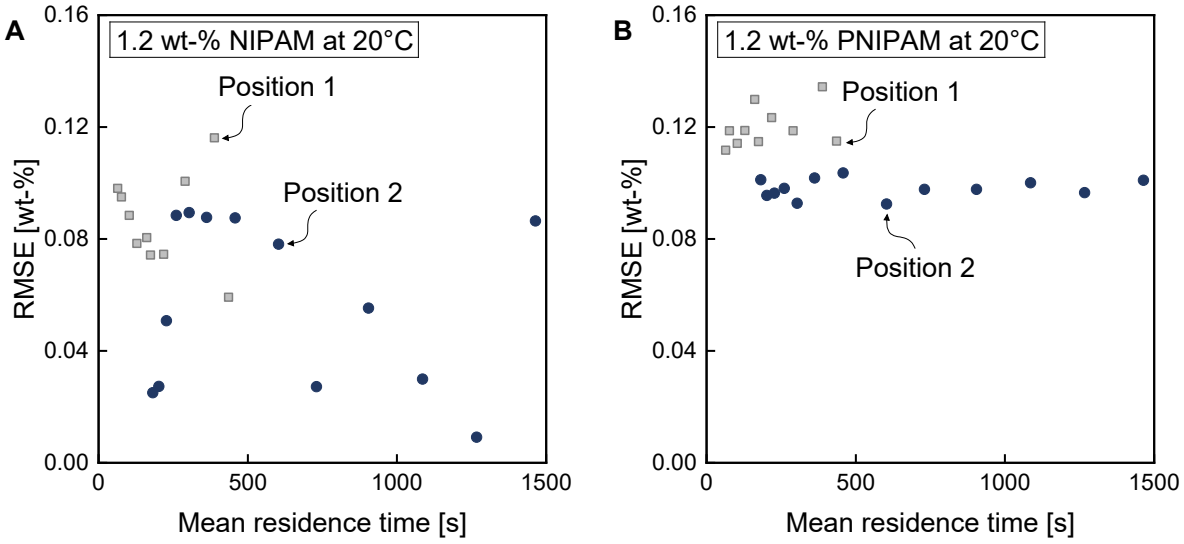

Figure 3.8: RMSE of measurements of (A) the NIPAM solution and (B) the PNIPAM microgel solution at Position 1 and 2 for various mean residence times. Grey boxes and blue circles denote measurements at Position 1 and 2, respectively.

3.3.4 Synthesis Conditions

In-line monitoring of the microgel synthesis via Raman spectroscopy in the tubular reactor yields satisfying results of high accuracy when using the manufactured measurement cell and the developed quality criterion. If the sample standard deviation of the synthesis measurements exceeds the average RMSE error value of the flowing PNIPAM microgels (see Figure 3.7(c)), the measurement data of the synthesis is discarded, and the experiment is repeated. This procedure enables reliable outlier detection and ensures measurements of sufficient precision. Consequently, if the measurements quality is acceptable, the measurements can be used for generating reaction knowledge or estimating kinetic parameters. Raman spectra are taken at different volume flow rates inside the developed measurement cell during the continuous reaction. Qualitatively, the results show successfull monitoring of the microgel synthesis reaction (see Figure 3.9). The Raman intensity of the prominent monomer double peak at approximately $1550\,\mathrm{cm}^{-1}$ to $1700\,\mathrm{cm}^{-1}$ diminishes (yellow to dark blue curve) as the volume flow rate decreases. Similarly, the characteristic polymer peak at $950\,\mathrm{cm}^{-1}$ increases with lower volume flow rates.

The quantitative evaluation of the Raman measurements in Figure 3.8(b) shows that the predictions for Position 1 and 2 coincide. The predicted weight fraction of NIPAM with the associated standard deviation of the measurements over the mean residence time is shown in Figure 3.10. At least six measurements are taken into account to calculate the average NIPAM prediction and the standard deviation for each set of volumetric flow rates. The measurements at Position 1 tend to have a lower standard deviation than the measures at Position 2. However, only one set of synthesis measurements at a volumetric flow rate of $14.0\,\mathrm{mL\,min}^{-1}$ had to be repeated from all conducted experiments, as the standard deviation exceeded the applied quality criterion. Overall, the progress of the NIPAM content over the mean residence time meets the expectations.

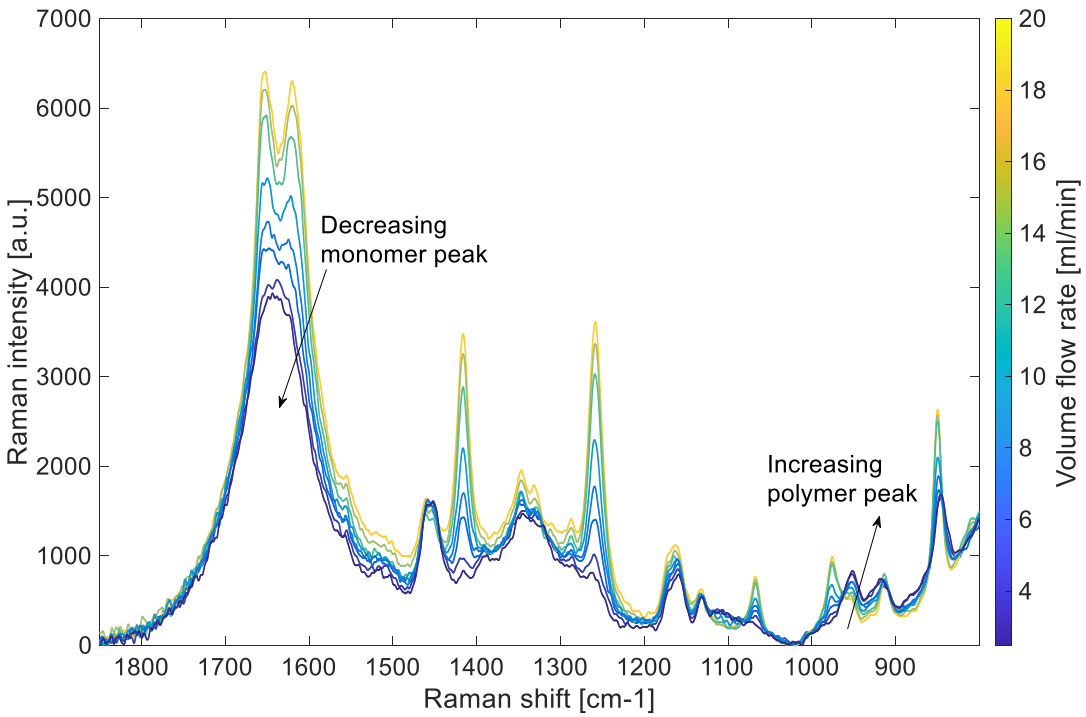

Figure 3.9: Raman intensity over Raman shift pretreated with a linear fit baseline subtraction for synthesis measurements at 70°C at volume flow rates between 2.5 mL min^{-1} to 18 mL min^{-1} in the flow reactor.

3.3.5 Comparison to Batch Reactor

The comparison of synthesis measurements via in-line Raman spectroscopy in batch and flow reactor diverge significantly, especially in the first seconds of the residence time. Figure 3.11 compares the NIPAM conversion measurements from the batch [101] and the flow reactor obtained in this work. The recipe of the batch reference [101] is transferred identically to the flow reactor so that the initial concentrations of the components and the reaction temperature of 70°C are the same. However, when transferring the synthesis, the flow regime changes from turbulent conditions in the batch reactor to laminar conditions in the flow reactor.

In both reactor types the change in conversion of the monomer NIPAM (see Figure 3.11) can be monitored, but the progress of the predictions from the batch reactor and the flow reactors are not congruent. In the early reaction stages, up to about 700 s mean residence time, the deviation between batch and flow synthesis is most significant. The Raman measurements of the flow and the batch reactor agree in a final conversion of about 85%. Fandrich et al. [55] ascribed the delayed beginning of the reaction in the flow reactor to non-ideal mixing, which leads to a laminar flow regime and a diffusion-limited reaction. However, from the conducted accuracy analysis and the comparison with batch measurements in this chapter, solely measurement inaccuracies can be excluded as the cause for the deviation between batch and flow. The deviations seem to be caused by an initial inhibition of the reaction, visible for short mean residence times in Figure 3.11. Such an inhibition can stem from multiple factors. For example, remaining or diffusing oxygen in the reaction solution, temperature loss in the tubing from the reservoir to the reactor, and a necessarily present reduced initial temperature in the reactor due to mixing the initiator phase. Further, the deviations could occur because of the different hydrodynamics in the reactors. Hence, a model-based analysis is necessary to account for the described phenomena and to precisely explain the differences between batch and flow reactions.

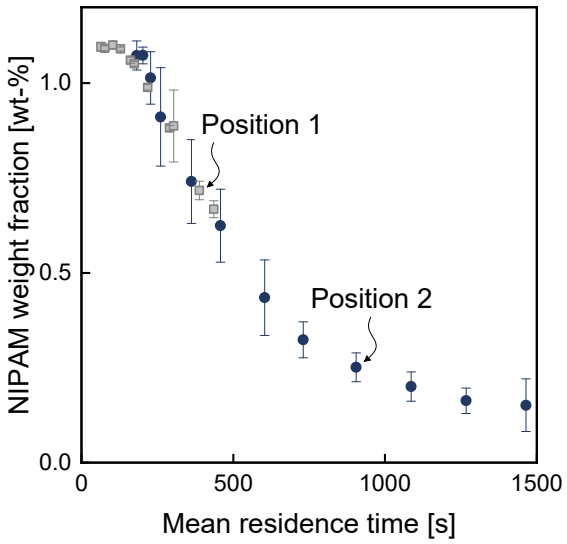

Figure 3.10: Prediction of NIPAM weight fraction and standard deviation of synthesis measurements at Position 1 and 2 for different mean residence times at 70°C. Grey boxes and blue circles denote measurements at Position 1 and 2, respectively.

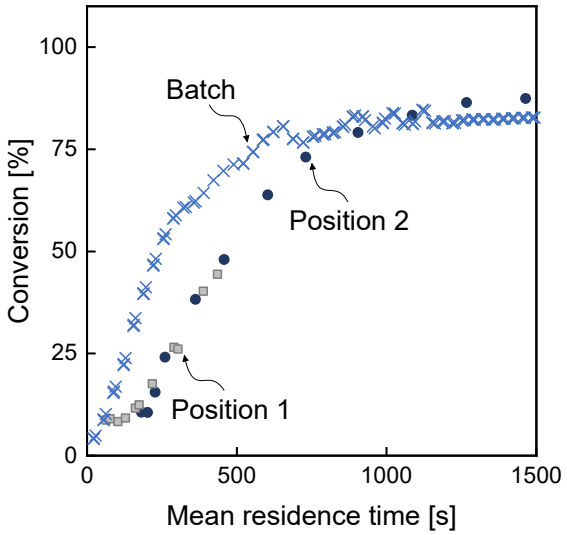

Figure 3.11: Comparison of the NIPAM conversion over the mean residence time during the synthesis of PNIPAM microgels at 70°C: blue x indicate Raman measurements from a batch reactor, grey boxes and blue circles indicate Raman measurements in the proposed flow cell at Position 1 and 2, respectively. The conversion data of the reference batch reactor measured via Raman spectroscopy is taken from Meyer-Kirschner et al. [101].

3.3.6 Measurement Validation

To validate the results, the Raman measurements are compared with flow reactor FTIR measurements by Fandrich et al. [55]. To this end, the reaction recipe is changed from the original recipe presented in Section 3.2.1 to match the concentrations from the literature [55]. Initial concentrations of $0.07\,\mathrm{mol\,L^{-1}}$ NIPAM and $3.7\,\mathrm{mol\,L^{-1}}$ BIS are applied and ammonium persulfate (APS) is used as the reaction initiator. The recipe yields microgels with a 5% BIS fraction. The reported FTIR measurements were carried out with deuterium oxide (D_2O) as the solvent. For the synthesis monitored via Raman spectroscopy in this thesis, water (H_2O) is used. Although the solvents are different, the

difference in dielectric constants of the solvents which is relevant for the reactivity can be regarded negligible in this context [116, 117].

As a result, Raman measurements match FTIR measurements (see Figure 3.12). FTIR measurements (green triangles) agree with Raman measurements (blue circles) sufficiently under the same reaction conditions using APS as initiator with the most considerable difference at approximately 900 s of 13% conversion. However, both methods exhibit a mean absolute error of 8% conversion at the analyzed residence times. Therefore, the Raman measurements from this chapter are validated effectively.

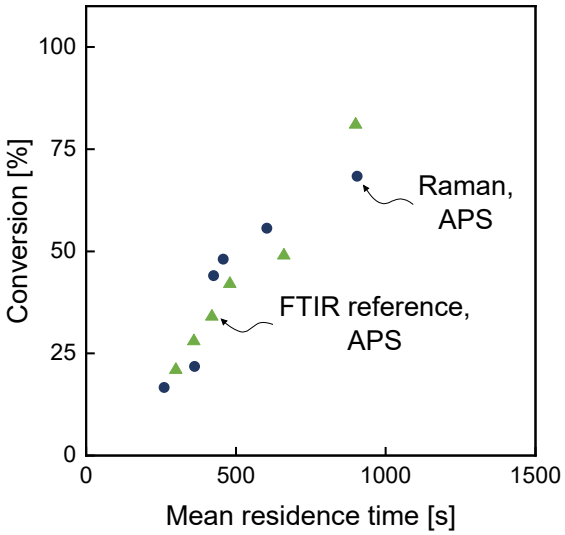

Figure 3.12: Comparison of the NIPAM conversion over the mean residence time during the synthesis of PNIPAM microgels at 70°C without stabilizer: Green triangles indicate FTIR spectroscopy in a flow reactor, blue circles indicate Raman measurements in the proposed flow cell at Position 2 with initiator APS. The conversion data of the reference flow reactor measured via FTIR is taken from Fandrich et al. [55].

3.4 Conclusions

Precise synthesis monitoring via Raman spectroscopy is essential for reaction understanding yet challenging to implement into small-scale flow reactors. In-line Raman spectroscopy is integrated into a tubular flow reactor to monitor precipitation polymerization of PNIPAM microgels. Using a 3d-printed measurement cell to conduct in-line measurements and to calibrate the evaluation model enabled a high quality of the Raman measurements. Furthermore, an increased acquisition time interval of the Raman spectroscopy to 40 s ensured measurements with low SNRs. Several potential measurement errors are eliminated systematically and the RMSE of multiple measurements of flowing PNIPAM microgels is applied as a quality criterion for the synthesis measurements. That way, the detection of outliers is enabled and reliable and accurate insights into the reaction progress are proffered. These insights are valuable, especially at the early reaction stages, where fast changes occur. The comparison of Raman measurements in the flow and batch reactor shows that the progress of the measurement predictions is not congruent. With this work, the measurement deviations are reduced and potential measurement errors are eliminated as the cause for divergent results of batch and flow reactors. The comparison of Raman measurements and FTIR measurements allows the validation of the proposed measurement setup. Furthermore, the advantage of Raman spectroscopy

is underlined as it does not require expensive D_2O as a solvent for high quality measurements.

Altogether, this contribution illustrates the advantages of suitable measurement cells for in-line monitoring and exposes the potential of integrating powerful analytical technology into flow reactor systems with a systematic quality assessment. The proposed method for outlier detection applies to other spectroscopic techniques and can thus be extended for further applications. Further study is recommended to address the model-based analysis of the synthesis in flow reactors. The flow phenomena and the influence of possible oxygen diffusion or heating phenomena in the reactor setup are of interest to fully understand the differences between the microgel synthesis in batch and flow reactors. Particularly, the non-ideal velocity, concentration, and temperature profile caused by the dimensions and modularity of the reactor need to be elucidated. Regarding synthesis monitoring, a further investigation of the measure in the radial direction is relevant to determine whether the detected intensity originates from the (weighted) average or a portion of the radial intensity profile.

4 Nonlinear Manifold Learning Determines Microgel Size from Raman Spectroscopy

Data Repository: *The acquired raw Raman spectra, the pre-treated Raman spectra, and the derived IHM parameters thereof are published and available for free download via RWTH Publications [118].*

4.1 Motivation for Polymer Size Determination from Raman Spectra

Process analytical methods are crucial for optimizing process performance and product properties, especially in polymerization. In-line spectroscopic methods are advantageous, and, in particular, near-infrared (NIR) and Raman spectroscopy are widely applied spectroscopic methods [119–122]. Evaluation methods for concentrations from spectroscopic data are established and comprise regression models, such as univariate peak integration based on the Beer-Lambert law [123], multivariate partial least squares (PLS), or artificial neural networks (ANNs) [124], and physically supported strategies such as multivariate curve resolution-alternating least squares (MCR-ALS) [125] or indirect hard modeling (IHM) [79].

Size is a crucial product feature in several processes, e.g., polymerization and crystallization. In contrast to concentrations, determination of size from spectroscopic data remains a major challenge. As mentioned earlier, the here analyzed microgels are not considered particles [74], and thus the term *microgel size* or *polymer size* is used throughout, instead of the more common *particle size*. The fact that particles such as polymers influence spectroscopic measurements by light scattering is well established [126], and experimental evidence of the correlation between Raman scattering and polymer size has been presented [60], even for relatively large particles [61]. However, only a few approaches attempt to determine polymer sizes from Raman spectra [58, 60–64]. These approaches rely on relatively small sets of data points and focus on training data-driven models. The accuracy of these approaches needs improvement compared to established methods such as dynamic light scattering (DLS). An overview of the state-of-the-art work on polymer size determination from Raman spectra is presented in Table 4.1. Most of these methods are based on the linear methods PLS or principal component analysis (PCA), which reduce the predictors to a smaller set of uncorrelated components and perform least squares regression on these components instead of on the original data.

Each spectral measurement consists of many measured intensities at different wavelengths, resulting in large dimensionality of the input vector. However, the measured intensities are not independent and ideally depend on a small number of meaningful properties, e.g., concentration and size. When the available data live in a low-dimensional, yet nonlinear manifold, linear methods often fail to capture the majority of the variance of the data, even with an increased number of principal components. Hence, in this chapter, nonlinear manifold learning approaches are proposed to achieve significant

Table 4.1: Overview of state-of-the-art approaches and the proposed method (last row) to determine polymer sizes from Raman spectra. The number of data points refers to the amount of samples measured via Raman spectroscopy.

Ref.	Method	Polymer system	Size [nm]	# points	Spectrum [cm^{-1}]
[62]	PLS	styrene, butadiene, methyl methacrylate, acrylonitrile	80-200	47	100-4000
[61]	Focal depth	styrene	42-210	6	3200-3800
[60]	PLS	styrene, acrylic acid	55-150	23	400-4000
[63]	PLS	styrene, butyl acrylate, acrylic acid, methyl acrylate	20-200	N.S.	150-400, 150-1800
[64]	PLS	styrene	50-400	40	150-400, 0-4000
[58]	IHM+PLS	styrene	23-60	21	1020-2000
Nonlinear manifold learning		*N*-isopropylacrylamide	208-483	47	100-3425

dimensionality reduction, replacing extensive data sets with few latent variables and, more importantly, to identify latent variables possessing certain desired (predictive) properties. For the former, diffusion maps (DMAPs) [127–129] are employed, to derive a parsimonious reduced description of the Raman spectra. Subsequently, an ensemble of concurrently trained neural networks (NNs) is proposed, named Y-shaped conformal autoencoders, introduced by Evangelou et al. [130] in the context of parameter non-identifiability.

The proposed workflow is particularly appropriate for measurements that depend on various combinations of factors, the effect of which is not readily quantifiable. Herein, the workflow is employed to identify the changes in the spectra explicitly attributed to the polymer sizes since the samples are not pretreated, and several factors beyond the size influence them: specifically, the concentrations of monomer, inhibitor, surfactant, and other species that participate in the reaction. In essence, the proposed method acts as a nonlinear filter that isolates or rather disentangles the changes in the spectra that are attributed to the differences in polymer size.

The starting point for the machine learning approach proposed in this chapter addresses the reduction of the high dimensionality of spectra, here achieved with DMAPs. The DMAPs algorithm is based upon (mathematical) diffusion processes on the data, and facilitates discovering meaningful low-dimensional intrinsic geometric descriptions of data sets, even when the data is high-dimensional, nonlinear, and/or corrupted by (relatively small) noise. The DMAPs framework has been shown to facilitate the discovery of meaningful low-dimensional intrinsic geometric descriptions of data sets (dimensionality reduction) [131–133]. For a detailed description of the method, the interested reader is referred to the seminal papers [127, 129, 131, 132, 134, 135].

The algorithm is used as an effective dimensionality reduction of full spectra, consisting of $\sim$11 000 wavenumbers. This reduction enables efficient interpolation and regression since much fewer (typically $<$10) variables are involved. Once the low-dimensional representation of the spectra is determined, it is possible to translate between coordinates in the ambient (spectra) and the reduced space (DMAP coordinates). The mapping from high to low dimension is achieved with the Nyström extension [136,

137]. Accurate reconstruction of the data set from the selected DMAP coordinates indicates that the latter is an adequate low-dimensional parameterization.

After the dimensionality reduction, the machine learning workflow begins. Here, recent advances in conformal autoencoder neural network (CANN) techniques are exploited. The DMAP coordinates are used as inputs (and also outputs) to a Y-shaped autoencoder to disentangle the dependencies of the latent variables discovered by a traditional autoencoder architecture and define the desired output, i.e., the polymer size, as a function of a single latent variable. Ultimately, given a new set of DMAPs, this CANN determines the corresponding polymer size and reconstructs the DMAPs themselves.

The proposed workflow is compared with state-of-the-art techniques, demonstrating it is important to not only find **a generic** parsimonious low-dimensional parameterization of the data (here achieved with DMAPs) but, more importantly, to find the **appropriate one**, i.e., the one that possesses a component that the polymer size can be writen as a function of. It is demonstrated that although the number of pairs of microgel size and spectral measurements is moderate (47, i.e., at least as high as in previous works, Table 4.1), the workflow is a promising direction in deducing polymer size in-line from Raman spectra.

The remainder of this chapter is structured as follows: First, the process of data collection is presented along with an overview of the state-of-the-art methods for polymer size determination from spectra. Subsequently, the DMAPs method is summarized, followed by a detailed description of the CANN architecture. Finally, results and conclusions are drawn from the proposed implementation.

4.2 Methods

The following sections include the description of the data set used in this contribution (Section 4.2.1) and the applied methods for size determination: benchmark methods in Section 4.2.2, and the proposed workflow in Section 4.2.3, including the DMAPs approach (Section 4.2.3.1), and the CANN (Section 4.2.3.2).

4.2.1 Data

The considered microgels here are based on *N*-isopropylacrylamide (NIPAM) and cross-linked via *N*,*N*'-methylenebis(acrylamide) (BIS). The reactor and measurement setup for the continuous synthesis are explained in Chapter 3. Using the continuous flow reactor, microgels of different sizes are synthesized by changing the reactor temperature and flow rates and the initiator and surfactant concentration. As microgels are known to have uniform size [51, 54, 76], they represent an excellent system to study polymer size deduction from Raman spectroscopy. In previous works presented in Chapter 8, in-line Raman spectra at reaction temperature at 60°C to 80°C and DLS measurements at 50°C were conducted. In contrast, in this chapter, additional off-line Raman measurements of the same samples but at 20°C and restricted conditions are acquired. The restrictions include measuring the samples all within a small amount of time (over two experimentation days) and in glass vials filled to the exact same fluid level to ensure equal conditions for the acquisition of all spectra and to eliminate external influences on the measurements. Consequently, further DLS measurements at 20°C are also conducted.

The data consist of Raman spectra and DLS measurements of microgel samples. The samples are taken from the output of the continuous flow reactor, which runs at different experimental conditions for each sample. The samples are measured off-line without further treatment, e.g., filtration or dialysis. In total, the data comprises 47 samples at different microgel sizes in the range of 208 nm to

483 nm in diameter.

Microgels have a different size depending on a threshold in temperature: above approximately 32°C, they occur in a collapsed state, and below the threshold temperature, they occur in a swollen state. Hence, the microgel sizes at 20°C are almost twice as big as at the reaction temperature. Each sample is measured three times via Raman spectroscopy. Raman spectra are taken with an acquisition time of 40 s. DLS measurements of the samples diluted in ultrapure water are conducted via the Zetasizer Ultra (Malvern Panalytical, Malvern, UK) at 20°C with a scattering angle of 90°. Each DLS measurement is repeated four times, and the software ZS Xplorer analyzes the scattering intensities.

The Raman spectra comprise the Raman intensity measured over a range of wavelengths. The global range is between $100\,\mathrm{cm}^{-1}$ to $3425\,\mathrm{cm}^{-1}$ correlating to 11 084 wavelengths per spectrum. Different spectra pretreatment methods can be applied to the spectral data. Using raw spectra and spectra with a linear fit or rubber band baseline correction in combination with standardization in the form of either standard normal variate (SNV) or min-max normalization are compared. The experimental data set is published open access [118] and comprises raw and pretreated Raman and evaluated DLS data.

The same data set is applied for all subsequently described methods to determine microgel size from Raman spectra. Out of the 47 pairs of microgel size and Raman spectra, 40 are used for training and 7 for testing. The same split is applied to quantify the performance of each considered method (state-of-the-art methods and the proposed workflow with nonlinear methods). The training for each method is conducted with 10-fold cross-validation, which involves splitting the training set into ten smaller sub-sets and using nine for training and one for testing. By repeating this process, using a different collection of sub-sets for training and validation each time, it is possible to define the best possible model hyper-parameters without sacrificing a lot of data. The number of hyper-parameters varies depending on the method. Hence, the set of hyper-parameters for the individual method is described for each method separately in the following sections. The performance of each method is evaluated based on commonly applied metrics: coefficiant of determination (R^2), root mean squared error (RMSE), and mean absolute percentage error (MAPE) for training and testing.

The accuracy is reflected in the %-error calculated as:

$$\%-\text{error} = 100 \cdot \frac{D_\mathrm{H}^\mathrm{pred} - D_\mathrm{H}^\mathrm{meas}}{D_\mathrm{H}^\mathrm{meas}}, \tag{4.1}$$

where D_H is the microgel's hydrodynamic diameter. Based on the %-error the MAPE is calculated as the sum of the %-errors divided by the number of observations.

4.2.2 Benchmark Methods for Polymer Size Determination from Raman Spectra

To benchmark the proposed method, it is compared against two state-of-the-art methods. These methods include the direct application of PLS to the spectral intensities (Section 4.2.2.1) and the application of PLS to fitted IHM parameters (Section 4.2.2.2).

4.2.2.1 Partial Least Squares Regression of Spectral Intensities

As conducted in the literature [60, 62, 64, 100], a PLS model regression is directly applied to the spectral data as first introduced by [62]. Different spectral ranges for the calibration of the PLS models are considered. These ranges include the global range and the so-called fingerprint region

between 850 cm^{-1} to 1800 cm^{-1}. Also, pretreatment methods are applied, combining two different types of baseline subtractions (linear fit and rubber band) and two normalization approaches (min-max and SNV). Further, the data is normalized using the `zscore` function in Matlab. The results are analyzed based on the metrics R^2, RMSE, and MAPE for calibration and validation. Based on the mean squared error (MSE) for cross-validation, the number of components (latent variables) for the PLS regression is determined.

4.2.2.2 Regression of Hard Model Parameters

The regression of fitted hard model parameters for determining microgel sizes is conducted, as proposed by Meyer-Kirschner et al. [58]. First, an indirect hard model (IHM) [79] is developed. For that model, the spectral range of the so-called fingerprint region between 800 cm^{-1} to 1850 cm^{-1} is considered. The range between 1552 cm^{-1} to 1560 cm^{-1} is excluded as it is attributed to an atmospheric oxygen signal. Besides the range restrictions, no further pretreatment is usually applied [58]. However, the PLS performance of the IHM parameters is compared with and without pretreatment for a comprehensive comparison. The applied pretreatment for the comparison is min-max or SNV normalization and linear fit or rubber band baseline subtraction. The IHM evaluation model is calibrated using calibration measurements from [93].

The model includes component hard models for the monomer, polymer, and water and a linear baseline. The hard model of each component consists of multiple characteristic peaks. The individual peaks are characterized by four parameters (see Figure 2.2): position δ, maximum intensity α, shape (fraction of the Gaussian part) β, and half-width at half maximum (HWHM) γ. The complete IHM combines the component models with their distinctive peaks. The indirect hard model parameters are adjusted to suit the spectra of interest within the fitting process. The applied fitting mode constitutes a medium interaction method, where the weights of the components, the baseline, and the peak positions are varied. The weights of the components represent the magnitude of the individual component in the spectra. Each component (monomer, polymer, water) is accredited with one weight parameter during the model fitting process. The incorporated linear baseline is fitted with regard to its offset and slope. In this context, component shifts are restricted to avoid ambiguities due to overlapping spectral peak positions. The fitting mode follows previous works by Meyer-Kirschner et al. [58]. The medium interaction fitting mode results in 49 modified parameter values (intercept and slope of the baseline, one weight for each of the three components, 23 monomer peak positions, 17 polymer peak positions, and four water peak positions) that serve as the input variables to the PLS regression model.

In addition, the medium fitting mode is compared with the fitting mode with high interaction. For the high interaction, in addition to the changes in the medium interaction, all peak parameters can be varied within the fitting process. Thus, the high interaction method results in 181 modified parameter values (intercept and slope of the baseline, one weight for each of the three components, 23 monomer peaks, 17 polymer peaks, and four water peaks, where each peak is characterized by the four parameters described previously).

The fitted IHM parameter values serve as input to the subsequent PLS regression. Again, the data is normalized using the `zscore` function in Matlab. The results of the PLS regression are also analyzed based on the R^2, RMSE, and MAPE values for the hybrid modeling approach, combining IHM and PLS. Based on the MSE for cross-validation, the number of components for the PLS regression is chosen.

4.2.3 Nonlinear Manifold Learning Workflow

The following section outlines the proposed nonlinear manifold learning workflow. First, the functionality of DMAPs for dimensionality reduction is highlighted. Subsequently, the Y-shaped CANN is introduced. Figure 4.1 shows a schematic representation of the entire workflow.

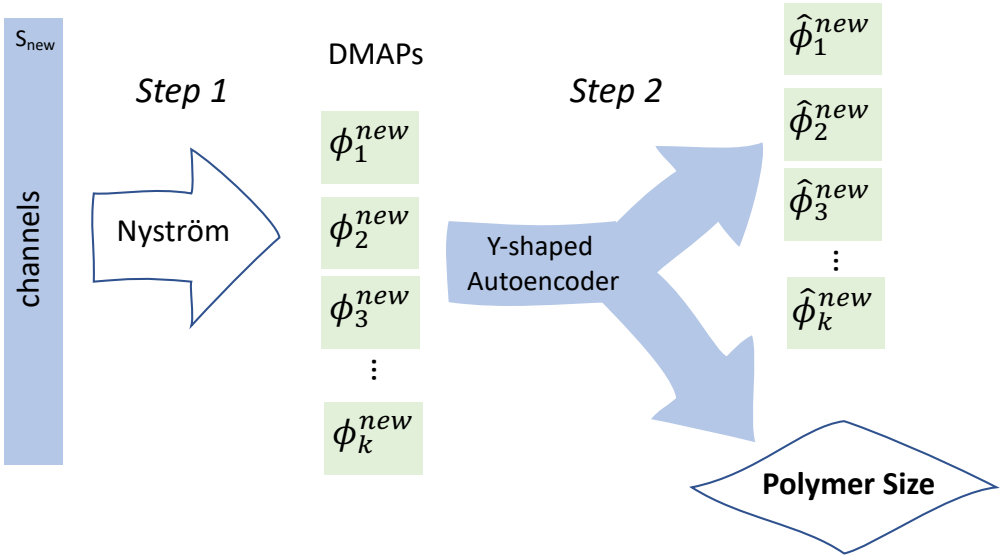

Figure 4.1: Schematic representation of the proposed workflow including the DMAPs algorithm and Y-shaped CANN architecture.

4.2.3.1 Diffusion Maps for Dimensionality Reduction

The DMAPs algorithm discovers the dimensionality of the manifold that contains a collection of Raman spectra of microgel samples. Furthermore, DMAPs discover data-driven coordinates on the low-dimensional manifold. These coordinates are a few of the leading eigenvectors, ϕ_i, of a scaled affinity matrix, which contains the Euclidean distances between all the pairs of available data points.

Discovering which eigenvectors parameterize independent directions and do not span the same direction with different frequencies (harmonics) is essential. To achieve this distinction, the so-called local linear regression algorithm is used as proposed by Dsliva et al. [138] and summarized here. Each DMAP coordinate is fit as a function of the previous ones. To select DMAP coordinates that are independent, the "goodness of fit" of this function is used. A good fit is associated with a specific eigenvector, ϕ_k, that is a harmonic function of the previous eigenmodes, whereas a bad fit signifies that ϕ_k is a new, independent direction on the data manifold.

An important ingredient of the proposed approach includes the reverse mapping from the DMAP coordinates to the variables in ambient space, which allows for the translation between the high and low-dimensional data description. To this end, geometric harmonics are proposed, introduced originally in [127], as a scheme for extending functions defined on data $\mathbf{X}$, $f(\mathbf{X}) : \mathbf{X} \rightarrow \mathbf{R}$, for $x_{new} \notin \mathbf{X}$. Here, the DoubleDMAPs [132] algorithm, a particular implementation of geometric harmonics, is selected. DoubleDMAPs are suitable in cases where the data are low-dimensional and can be parameterized by a few non-harmonic eigenvectors. Generally, geometric harmonics construct an input-output mapping between the ambient coordinates $\mathbf{X}$ and a function of interest f defined on $\mathbf{X}$ by operating directly on the non-harmonic DMAP coordinates.

The DMAPs algorithm starts with a data set of N individual points (represented as d-dimensional real vectors, $x_1,...,x_N$). A similarity measure between each pair of vectors (x_i,x_j), is computed

based on the standard Euclidean distance, based on which an affinity matrix is constructed. A popular choice is the Gaussian kernel $w(i,j) = \exp\left[-\left(\frac{||x_i - x_j||}{\epsilon}\right)^2\right]$ where ϵ is a hyper-parameter that quantifies the kernel's bandwidth. To recover a parameterization insensitive to the sampling density, the normalization

$$\widetilde{\mathbf{W}} = \mathbf{P}^{-1}\mathbf{W}\mathbf{P}^{-1}$$

is performed, where $P_{ii} = \sum_{j=1}^{N} W_{ij}$ and W_{ij} the elements of the matrix $\mathbf{W}$. A second normalization applied on $\widetilde{\mathbf{W}}$,

$$\mathbf{K} = \mathbf{D}^{-1}\widetilde{\mathbf{W}} \tag{4.2}$$

gives a $N \times N$ Markov matrix $\mathbf{K}$; here $\mathbf{D}$ is a diagonal matrix, collecting the row sums of the matrix $\widetilde{\mathbf{W}}$ eigenvectors ϕ_i.

In an offline step, the dimensionality reduction of the original collection of spectra, consisting of around 11 000 wavenumbers via DMAPs, is conducted. The goal is to reduce the number of variables to ideally < 10 and thus to re-state the high-dimensional data set in a low-dimensional coordinate system, parameterized by a small number of selected eigenvectors of the kernel matrix defined in Equation (4.2). The eigenvectors are selected with the help of the local linear regression algorithm. Having established a reduced representation of the spectra, the online steps for a new spectrum follows. In the online step, the DMAP coordinates of a new spectrum are computed using the Nyström extension (see Figure 4.1).

4.2.3.2 Y-shaped CANNs

The proposed workflow to determine polymer sizes from Raman spectra involves an ensemble of concurrently trained NNs, called Y-shaped CANNs. These Y-shaped CANNs are applied to determine polymer sizes based on DMAP coordinates. The schematic representation of the workflow including the Y-shaped CANN is presented in Figure 4.1. The Y-shaped autoencoder scheme, initially proposed by Nikolaos et al. [130], is summarized here as it is adjusted for the current application. For more details on the implementation and training of this machine learning technology, the reader is referred to the original work of Nikolaos et al. [130]. At the core of the scheme lies a regular autoencoder, i.e., a NN where the inputs and outputs are the same, with the addition of an extra side NN component, as explained below. Overall, the Y-shaped scheme can be broken down into three connected subnetworks (illustrated in Figure 4.2):

- Encoder, NN1, which maps the DMAP coordinates, ϕ_k, to the autoencoder latent variables, ν_i:
  $(\phi_1, \phi_2, \phi_3, \phi_4, \phi_5) \mapsto (\nu_1, \nu_2, \nu_3, \nu_4, \nu_5)$

- Decoder, NN2, which can be thought of as the inverse transformation from the latent space of the autoencoder (ν_i) back to the DMAP coordinates ϕ_k:
  $(\nu_1, \nu_2, \nu_3, \nu_4, \nu_5) \mapsto (\hat{\phi}_1, \hat{\phi}_2, \hat{\phi}_3, \hat{\phi}_4, \hat{\phi}_5)$

- Polymer size estimator, NN3, which maps *the right number* of autoencoder latent variables, here one of them, ν_1, to the observed output data, here the polymer size D_{H}:
  $(\nu_1) \mapsto D_{\mathrm{H}}$

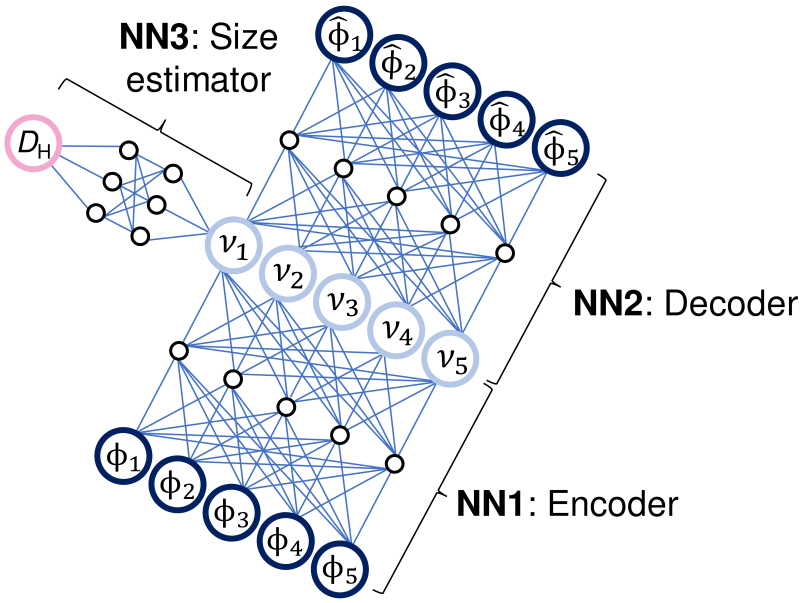

Figure 4.2: Schematic breakdown of the Y-shaped CANN architecture: NN1 is the encoder that maps the DMAP coordinates to the latent variables of the autoencoder; NN2 is the inverse transformation, from the latent space back to the DMAP coordinates; NN3 maps one of the latent variables to the output of interest: polymer size D_H.

The key feature is the loss function, consisting of several parts. The first part is the successful reconstruction of the input original parameters (the autoencoder part). Next comes the ability of NN3 to reproduce the observed output, i.e., the polymer size. The polymer size becomes a funstion of a single input ν_1. To concurrently train the different NNs, an additional component to the loss function becomes necessary, which results from further imposing an orthogonality constraint on the conformal autoencoder's latent coordinates:

$$\langle d\nu_i, d\nu_j \rangle = 0, \forall i \neq j.$$

Here, $d\nu_i$ indicates the vector of partial derivatives of the latent coordinate ν_i with respect to of the input parameters ϕ_k and $\langle \cdot, \cdot \rangle$ indicates the inner product. This constraint is imposed using the automatic differentiation capabilities of the relevant code libraries and aims to disentangle the combination of features that matters to the output from those combinations of features that do not affect it, making the architecture a conformal autoencoder.

4.3 Results and Discussion

The results comprise the analysis of the size determination from the benchmark methods in Section 4.3.1 and 4.3.2, and the developed workflow based on the Y-shaped CANN in Section 4.3.3. The Raman spectra and size measurements from DLS of microgel samples are available for trans-

parency [118]. The codes implementing the different workflow steps can be found in the GitLab repository [139].

4.3.1 Partial Least Squares Regression of Spectral Intensities

The exhaustive evaluation of various combinations of pretreatment methods for Raman spectra as the basis for PLS regression is summarized in Table 4.2. Overall, the direct application of PLS regression to the spectral intensities results in poor performances for any pretreatment method. The poor performance is indicated by the R^2 values significantly lower than 1 for the training and testing. Comparing the performance of spectra in the fingerprint and global spectral region yields that the performance is slightly better when using models in the fingerprint region. Interestingly, the number of latent variables needed for the fingerprint region is consistently higher than for the global region, although the global region comprises more predictive variables.

Table 4.2: Performance of PLS regression on Raman spectra with different pretreatment methods. The values for RMSE are given in nm and for MAPE in %.

Pretreatment	Spectral region	Training			Testing			# latent variables
		R^2	RMSE	MAPE	R^2	RMSE	MAPE	
Linear fit	Fingerprint	0.759	31.200	7.013	0.535	39.350	10.105	4
Linear fit	Global	0.283	53.820	12.876	0.584	37.240	8.915	2
min-max, linear fit	Fingerprint	0.780	29.790	6.558	0.336	47.050	11.298	6
min-max, linear fit	Global	0.412	48.730	11.255	0.735	29.690	7.173	3
min-max, rubber band	Fingerprint	0.753	31.570	6.773	0.084	55.260	14.736	5
min-max, rubber band	Global	0.421	48.340	11.116	0.732	29.880	7.350	3
Raw	Fingerprint	0.961	12.570	2.884	0.596	36.680	10.574	7
Raw	Global	0.495	45.170	10.635	0.160	52.920	14.233	4
Rubber band	Fingerprint	0.801	28.320	6.834	0.461	42.400	11.962	4
Rubber band	Global	0.613	39.530	9.430	0.484	41.470	10.795	4
SNV, linear fit	Fingerprint	0.751	31.710	7.481	0.545	38.930	10.993	4
SNV, linear fit	Global	0.275	54.110	12.941	0.608	36.150	9.168	2
SNV, rubber band	Fingerprint	0.766	30.720	7.142	0.430	43.580	11.727	4
SNV, rubber band	Global	0.275	54.110	12.940	0.609	36.120	9.157	2

In summary, determination of microgel sizes using raw spectra with no pretreatment in the fingerprint region perform best in training and testing. Also, the determination based on spectra in the fingerprint region pretreated via SNV and a linear fit subtraction shows a relatively good performance. Thus, the parity plot for these most promising configurations is shown in Figure 4.3 in comparison. Here, the gray circles represent the training data, and the red circles represent the test data. Over-fitting is precluded sufficiently, as the discrepancy between actual and deduced size is in the same range for the training and the test data set. Furthermore, comparing the PLS results based on the pretreated spectra (left) and raw spectra (right) shows no significant improvement for the pretreated spectra in the PLS performance.

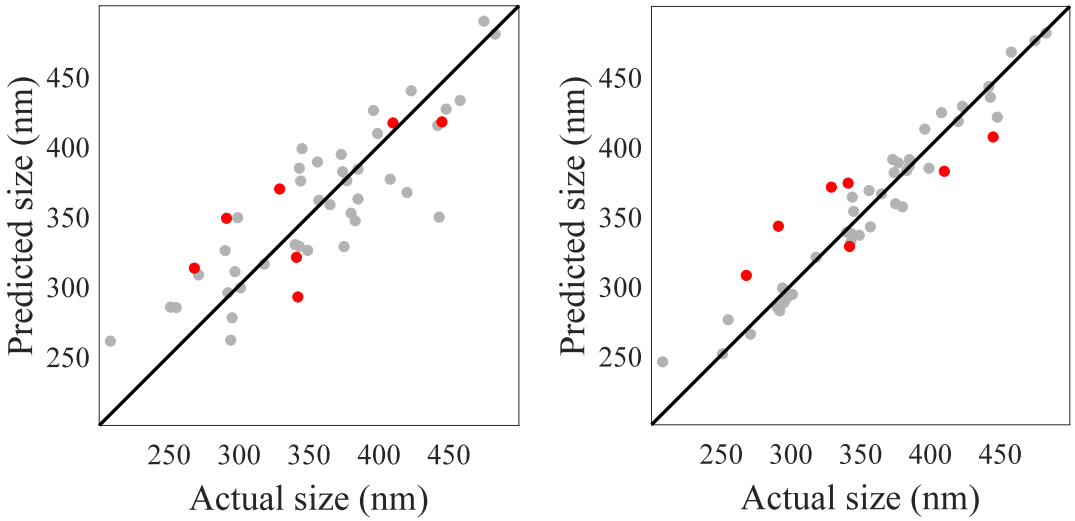

Figure 4.3: Parity plots of microgel size determination via PLS regression of spectra in the fingerprint region. Left: pretreated via SNV normalization and linear fit baseline subtraction. Right: Raw spectra. Gray circles represent the training data and red circles indicate the test data.

4.3.2 Regression of Hard Model Parameters

Table 4.3 shows the overview of different pretreatment methods in the indirect hard modeling step. The fitted parameter values from the IHM are subsequently used in the PLS regression. A high and medium fitting mode are considered corresponding to more or less degrees of freedom for fitting the IHM evaluation model to the experimental spectra. Similarly to the direct regression on spectral intensities, the overall performance is unsatisfying. Again, the determined R^2 values are significantly lower than 1 for the training and even below zero for testing in some cases. Note that R^2 values below zero imply that the size determination would be more accurate using the mean value than the value determined by the regression model. Overall, the medium fitting mode shows a poorer performance than the high fitting mode. However, the high fitting mode necessitates more latent variables, as a larger space of predictive variables needs to be reduced. Furthermore, no clear trend exists that one pretreatment method performs better than the other.

Figure 4.4 presents the results of the PLS regression based on IHM parameters from Raman spectra pretreated via SNV and rubber band baseline subtraction and high interaction during the fitting, as this configuration yields the relatively best performance according to Table 4.3. Also, the second best performing configuration is shown, namely regression based on spectra pretreated with a linear fit subtraction and high interaction fitting. Similarly to the results from Section 4.3.1, the distribution of gray circles (training data) and the red circles (test data) here shows that over-fitting is suppressed. In addition, the comparison of the PLS results based on the IHM parameter values from SNV plus linear fit pretreated spectra (left) and spectra only pretreated with a linear fit subtraction (right) shows a notable improvement for the spectra additionally pretreated via SNV in the PLS performance. However, the resulting performance does not indicate reliable accuracy.

Table 4.3: Performance of PLS regression on IHM parameters from Raman spectra with different pretreatment methods. The values for RMSE are given in nm and for MAPE in %.

Pretreatment	Fitting mode	Training R^2	Training RMSE	Training MAPE	Testing R^2	Testing RMSE	Testing MAPE	# latent variables
Linear fit	High	0.734	32.770	7.264	0.286	48.780	9.908	5
Linear fit	Medium	0.211	56.450	14.184	0.260	49.660	12.108	1
Raw	High	0.921	17.850	4.281	-0.515	71.070	19.052	9
Raw	Medium	0.212	56.420	14.142	0.276	49.140	11.965	1
Rubber band	High	0.647	37.750	8.566	0.346	46.690	11.745	6
Rubber band	Medium	0.359	50.900	11.921	-0.144	61.750	12.369	3
min-max, linear fit	High	0.739	32.500	7.201	0.280	49.000	9.974	5
min-max, linear fit	Medium	0.506	44.650	10.667	-0.430	69.050	18.194	5
min-max, rubber band	High	0.682	35.850	7.766	0.335	47.080	12.032	6
min-max, rubber band	Medium	0.384	49.900	11.443	-0.173	62.540	11.966	3
SNV, linear fit	High	0.743	32.250	7.239	0.235	50.500	10.730	5
SNV, linear fit	Medium	0.499	44.970	10.725	-0.438	69.240	18.220	5
SNV, rubber band	High	0.584	40.990	9.520	0.636	34.840	8.573	4
SNV, rubber band	Medium	0.382	49.970	11.492	-0.183	62.790	12.004	3

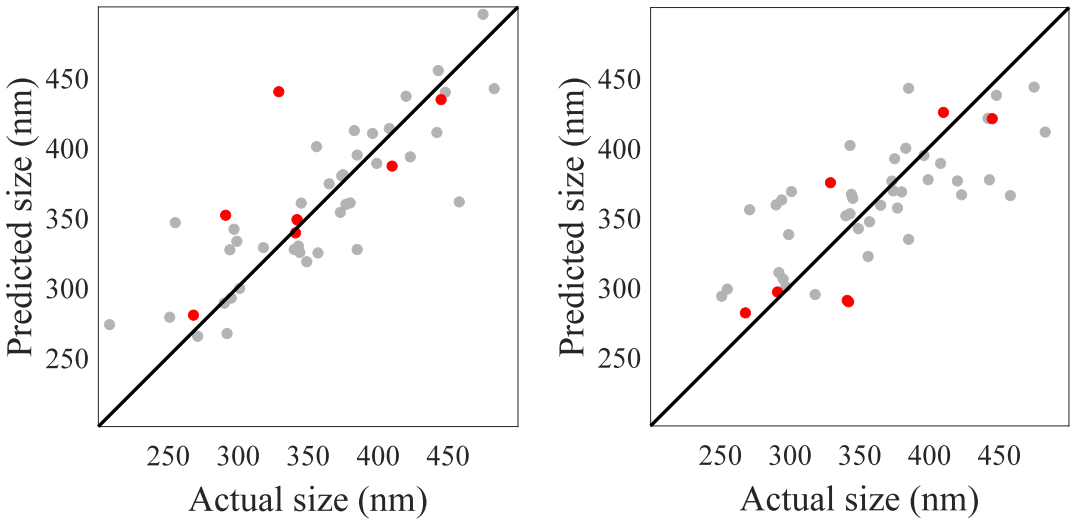

Figure 4.4: Parity plots of microgel size determination via PLS regression of IHM parameters from spectra fitted via high interaction. Left: pretreated via SNV normalization and rubber band baseline subtraction. Right: pretreated via linear fit subtraction only. Gray circles represent the training data and red circles indicate the test data.

4.3.3 Nonlinear Manifold Learning Workflow

Firstly, the DMAPs algorithm is implemented, and six DMAP coordinates, ϕ_1, ϕ_2, ϕ_3, ϕ_4, ϕ_5, and ϕ_6 are selected to parsimoniously represent the spectra that live in a high-dimensional ambient space. These are selected based on how accurately the original data can be reconstructed from those latent variables. Following the computation of diffusion coordinates, it is possible to proceed directly with the determination of the polymer size via the Y-shaped CANN.

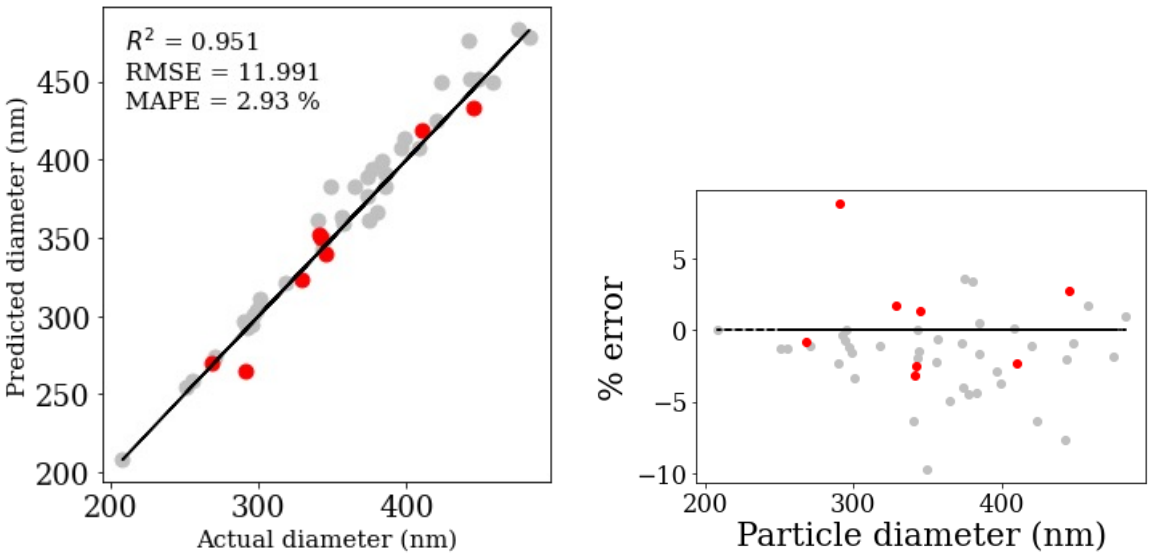

Figure 4.5: Size determination from Y-shaped autoencoder architecture: (a) Actual versus predicted polymer size, and (b) % error for each one of the data points in the test set. Red points correspond to the test set and gray points correspond to the training set values. The R^2, RMSE, and MAPE reported correspond to the test data.

The CANN architecture described in Section 4.2.3.2 is trained with the DMAP coordinates $(\phi_1,...,\phi_6)$ corresponding to the training set as the input to the encoder network NN1. These values are also the target values for the decoder network NN2. Six latent variables are set in the bottleneck layer, and the polymer size is required to be defined as a function of ν_1, by concurrently training the neural network NN3.

The proposed method shows a superior performance with R^2= 0.951 and MAPE= 2.93% for the test set. Assumably, the reason for the enhanced performance lies in the fact that the Y-shaped architecture not only finds the latent variables of the data set, as do DMAPs, but with the second NN, specific properties are explicitly imposed on one of them: the polymer size must be a function of one latent variable, which *it must also be orthogonal to all other latent variables*. The latter property implies that *only* this one latent variable correlates to the particle diameter.

4.3.4 Comparison of Presented Methods

Table 4.4 compares the results from the state-of-the-art to the proposed method. The results using the state-of-the-art methods are described in detail in Section 4.3.1 and 4.3.2. Here, solely the best-forming configuration of pretreatment and spectral range for the direct PLS regression on Raman spectra and PLS regression on IHM parameters are presented. Finally, the in-depth results regarding the size determination from DMAP coordinates via Y-shaped autoencoder are presented in Section 4.3.3.

For the collection of Raman spectra studied here, the Y-shaped CANN outperforms the other state-of-the-art methods indicated by the only R^2 value considerably close to 1. Also, the low RMSE values of the Y-shaped autoencoder, being approximately a third of the values of the compared methods, indicate the improved performance. Lastly, the MAPE value of the autoencoder-based method ranges at 2.930 %, which approximates the precision range of around 2 % expected from DLS [140], the established size measurement device. Thus, even though the evaluation is based on a data set with limited size, for the first time, a purely data-driven evaluation method based on Raman

Table 4.4: Testing performance of all considered methods within this work. The values for RMSE are given in nm and for MAPE in %.

Cluster	Method	R^2	RMSE	MAPE	# latent variables
State-of-the-art	Best configuration based on PLS regression directly to Raman spectra	0.596	36.668	10.574	7
	Best configuration based on PLS regression on IHM parameters	0.636	34.840	8.573	4
Determination from DMAP coordinates	Y-shaped autoencoder	0.951	11.991	2.930	1

spectra advances the accuracy capability of the established size determination device.

Further, it is worth looking into the number of latent variables required (see the last column of Table 4.4). DMAPs is able to meaningfully embed the high dimensional data using six coordinates. Even though a parsimonious embedding of the data is achieved, which is key in making machine learning tasks computationally tractable, it is not a quantitatively accurate predictor. This is where the CANN becomes relevant for the polymer size determination. Consequently, it is possible to reduce even further the variables that are meaningful for the specific task of determining polymer size to a single latent variable, on the data. It becomes clear that designed latent spaces, i.e., ones with specific desired characteristics, become useful in disentangling the data features and creating latent variables that specifically map to the observable quantity of choice, here polymer size. This is precisely the motivation for the proposed CANN architecture: it manages to identify a single latent variable, which not only maps to the size, but in addition is independent of other data features by design (by imposing an orthogonality condition in the loss function of the neural network). This trait of the CANN architecture enables the minimal accurate determination of polymer size here.

4.4 Conclusions

In this contribution, the important open problem of determining particle sizes online is considered. A data-driven approach is proposed to determine polymer sizes from Raman spectra. This approach is applied the acquired open-access data set of continuous microgel synthesis and demonstrate its capability. Further, the proposed approach is compared against two state-of-the-art benchmark methods to underline the excellent performance of the nonlinear approach.

The proposed nonlinear approach relies on nonlinear manifold learning, more precisely dimensionality reduction via DMAP coordinates combined with recent advances of Y-shaped autoencoder. The proposed workflow outperforms the state-of-the-art linear methods significantly. The Y-shaped autoencoder approach based on determination from DMAP coordinates enables drastically better accuracy, similar to the established size measurement methods such as DLS.

Determining polymer sizes directly from Raman spectra taken directly from untreated samples and not manipulated by spectral pretreatment constitutes a substantial advantage. Compared to the established particle determination via DLS, Raman spectra can now be acquired in-line and evaluated directly online, circumventing the labor-intensive DLS processing and allowing online reaction monitoring for closed-loop control. Furthermore, the ability to handle noise in the form of information included in the spectra, such as chemical composition, irrelevant for size determination, makes the proposed workflow superior. Compared to state-of-the-art Raman methods, the workflow is advantageous for determining polymer sizes, as no spectral pretreatment and, thus, no expert knowledge

is necessary. In addition, the workflow typically relies on less than ten coordinates in the reduced component space. Here, only the first six DMAP coordinates enable us to use the entire wavelength spectrum without exclusions, which would require problem-specific intuition.

Future works include the application of the proposed workflow to determine polymer concentrations and sizes simultaneously to highlight the application of the proposed readily available analysis tool. The simultaneous determination allows a more comprehensive characterization via a single in-line process analytical tool. In addition, future considerations involve extending the workflow to other systems beyond the presented application. Additional types systems to consider in the future can involve crystallization processes, amongst others.

5 Raman Spectroscopy and Indirect Hard Modeling for Microgel Synthesis with Charged Domains

Data Repository: *The Raman spectra acquired and the indirect hard modeling evaluation models developed in this chapter are published and available for free download via RWTH Publications [141].*

5.1 Motivation for Monitoring the Synthesis of Microgels with Charged Domains

Microgels ungergo a volume phase transistion in response to external stimuli. The most studied stimulus constitutes temperature but pH-responsiveness has gained a lot of interested over the years as well [142–145]. By adding functional carboxylic acids such as methacrylic acid (MAA) or acrylic acid (AA) to thermo-responsive microgels such as *N*-isopropylacrylamide (NIPAM)- or *N*-vinylcaprolactam (VCL)-based microgels, dual-responsive microgels are created. These microgels with dual stimulus swelling response are especially relevant for applications in drug delivery [33–36], catalysis [42, 43], sensing [46], and membranes [22]. For each application, tailored properties are desired for optimal microgel functionality. Therefore, the production process of these charged microgels needs to be fully understood and optimally controlled.

For improved insight into the charged microgel synthesis, process monitoring via analytical technology is needed. So far, most work studying the synthesis of microgels with carboxylic acids focuses on the examination of the final microgel product. For investigating these completed microgels, process analytical studies involve mostly size measurements via dynamic light scattering (DLS) [143, 146–149], determination of the polymerization conversions by gravimetric analysis [148] or Fourier transform infrared (FTIR) microscopy [146, 147], scanning electron microscopy analysis [146–148], morphology analysis via atomic force microscopy (AFM) [146], or (time-lapse) nuclear magnetic resonance (NMR) [150] to evaluate the microgel's swelling response. Monitoring of conversion or size during the synthesis has not been the research focus.

For monitoring of charged species, Echtermeyer et al. [81] showed that via Raman spectroscopy monitoring of the dissociated states of an acidic component is possible. In this chapter, an analysis of the capabilities of Raman spectroscopy to monitor the synthesis of charged microgels at the example of NIPAM-*co*-MAA microgels is presented. For the analysis of the Raman spectra, indirect hard modeling (IHM) is applied, as this methods yields sufficient predictions for multi-component systems with many overlapping component peaks [79, 80] while necessitating only a small calibration data set [79, 81].

The chapter is structured as follows. First, the experimental methods, including the microgel synthesis settings, and Raman spectroscopy with indirect hard modeling, are presented in Section 5.2. Subsequently, in Section 5.3, the results are highlighted with focus on the Raman evaluation model and the synthesis monitoring outcome. Finally, conclusions from the work are drawn in Section 5.4.

5.2 Experimental

In the following sections, first the setup of the synthesis of charged microgels in batch is described in Section 5.2.1. The NIPAM-*co*-MAA synthesis is conducted with varying MAA content. By taking samples during polymerization, measuring them via Raman spectroscopy, and evaluating the measurements via IHM, the species concentrations are infered (Section 5.2.2). For the evaluation of the measurements, the IHM is calibrated (Section 5.2.3).

5.2.1 Experimental Procedure For Microgel Synthesis and Sampling

Three different compositions of microgels with varying molar fractions of the MAA monomer within the microgel are synthesized within this work. For that, molar MAA fractions of 5, 10, and 15 mol% are targeted. For the synthesis of NIPAM-*co*-MAA microgels, an aqueous solution of the monomer NIPAM, the functional carboxylic co-monomer MAA, the surfactant sodium dodecyl-sulfate (SDS), the cross-linker *N*,*N*'-methylenebis(acrylamide) (BIS), and deionized water is prepared in a glass flask. The composition of the initial synthesis solution is presented in Table 5.1. The cross-linker content of the microgel is fixed at 1.0 mol-% while the composition of NIPAM to MAA varies.

Table 5.1: Recipe of the NIPAM-*co*-MAA synthesis.

Component	5 mol%	10 mol%	15 mol%
Deionized water	184.65 g	184.65 g	184.65 g
MAA	0.12 g	0.24 g	0.36 g
NIPAM	2.95 g	2.80 g	2.64 g
BIS	43 mg	43 mg	43 mg
SDS	80 mg	80 mg	80 mg
KPS	150 mg	150 mg	150 mg

The reactor head has multiple openings for the Raman probe, pH and temperature sensors (SenTix 940 from WTW), mechanical stirrer (RZR 2102 control from Heidolph), and access for the addition of the initiator and the withdrawal of samples. The reaction solution is heated to the reaction temperature of 70°C, stirred at 300 rpm, and continuously purged with nitrogen for the entire duration of the synthesis to prevent oxygen inhibition. After the system reaches a steady state with constant temperature, the initiator potassium persulfate (KPS) is added in dry form to start the polymerization. Samples are drawn directly before initiation and 1, 3, 5, 7, 10, 15, 20, 30, 60, and 120 minutes after initiation. The withdrawn samples are shock-cooled in an iced water bath to terminate the polymerization. Subsequently, the samples are investigated off-line via Raman spectroscopy.

After two hours of reaction time, the product solution is collected and cooled for storage. The remaining solution is filtered through glass wool and dialyzed against deionized water using Spectra/Por dialysis membranes (ZelluTrans MWCO of 12000 to 14000 from Carl Roth). The deionized water is changed daily for four to six days. Afterwards, the dialyzed solution is freeze-dried under a vacuum to receive the pure microgel. The freeze-dried microgel is then weighted to determine the conversion of reactants.

5.2.2 Raman Spectroscopy of Reaction Samples and Indirect Hard Modeling

Raman measurements are taken with two accumulations of a time interval of 30 s and assessed using the software PEAXACT to apply IHM [80]. For the IHM, a Raman shift from 1025 cm^{-1} to 1850 cm^{-1} is considered. The atmospheric oxygen signal between 1552 cm^{-1} to 1560 cm^{-1} is included as a dummy peak for the model generation. Also, the remaining signal of the device is derived from a measurement in the empty dark chamber and is modeled as a combination of dummy peaks spanning the entire considered wavenumber range. The pure component model (PCM) of water is directly determined, while the PCMs of KPS, NIPAM, MAA, and the respective microgel are derived using complemental hard modeling (CHM) [80]. Within the PCM of each species, characteristic peaks are merged into peak groups, which are fitted coherently. The fitting of peak groups has been shown to decrease confusion between neighboring peaks of different components during the model fitting process. PCMs are then used to build a mixture model for the aqueous NIPAM-BIS-MAA system. The mixture model utilizes a linear fit baseline subtraction and SNV normalization. The applied fitting mode for a component evaluation encompasses medium interaction, no component shift, and ten considered component peaks with a 0.001 component weight threshold. The relative parameter constraints comprise variations in position δ $\pm$10, maximum intensity α $\pm$20%, half-width at half maximum (HWHM) γ $\pm$10%, and the Gaussian part β $\pm$0.5 (see Figure 2.2).

5.2.3 Calibration of the Raman Evaluation Models

IHM evaluation models need calibration for each component of the respective system to predict concentrations of an unknown sample. For IHM of multi-component systems, calibrating the pure components is sufficient to measure the mixture spectra thereof. Also, relatively few calibration samples are needed for a suitable model calibration enabled by the physical justification of the IHM method. For the IHM calibration for the NIPAM-BIS-MAA system, aqueous mixtures of monomers and microgels are prepared in 4 mL glass vials. The calibration set contains nine aqueous mixtures of NIPAM (0.2 wt% to 1.8 wt%), and MAA (0.05 wt% to 0.45 wt%). For the microgel calibration, the calibration samples contain three aqueous mixtures of NIPAM-MAA-based microgels (0.2 wt% to 1.8 wt%). For calibration of the initiator KPS, two samples are used (0.008 wt% to 0.08 wt%). Each calibration sample is measured ten times. Finally, the evaluation model is calibrated using ten measurements per calibration sample and ratiometric regression with 10-fold cross-validation.

5.3 Results and Discussion

The results comprise the IHM evaluation model of the Raman measurements (Section 5.3.1) and the resultant outcomes (Section 5.3.2). The presentation of the IHM evaluation model comprises the consideration of neglected components (Section 5.3.1.1), the influence of pH on the Raman spectra (Section 5.3.1.2), the developemnt of different IHM evaluation models depending on the content of MAA during the synthesis (Section 5.3.1.3), and the calibration metrices (Section 5.3.1.4). The outcomes involve the Raman spectra during the synthesis, the weight fraction predictions thereof, and the NIPAM and MAA conversion determined.

5.3.1 Raman IHM Evaluation Model

The synthesis of cross-linked microgels with pH-responsive functional groups results in a complex system to monitor, as it comprises many components. For developing the Raman evaluation model via IHM, ratiometric calibration is applied since all components of the analyte are known. However, some components present during the synthesis are neglected in the evaluation model due to low Raman activity or initial concentration.

5.3.1.1 Neglected Components

Within the Raman evaluation model based on IHM, a few components of the complex system are neglected. These components include the crosslinker BIS and the stabilizer SDS. BIS is excluded from the peak modeling and calibration because of the low concentration during the synthesis. Furthermore, the contribution of the stabilizer SDS to the spectral signal is negligible due to the low Raman activity of the component.

In Figures 5.1(a) and 5.1(b), the Raman spectra of pure deionized water are compared to the Raman spectra of aqueous solutions of BIS and SDS at synthesis conditions, respectively. For the BIS solution, two BIS characteristic peaks can be differentiated at around $1259\,\mathrm{cm}^{-1}$ and $1413\,\mathrm{cm}^{-1}$. These peaks are relatively small and overlap with characteristic peaks of the monomer NIPAM, which exhibit a significantly higher intensity. Hence, the weight fraction of BIS cannot be reliably quantified during the microgel synthesis. For the SDS solution a similar phenomenon occurs. Here, the two SDS characteristic peaks at around $1062\,\mathrm{cm}^{-1}$ and $1442\,\mathrm{cm}^{-1}$ exhibit an even lower signal intensity in the aqueous solution. Hence, the SDS weight fraction is also not quantifiable during the synthesis. Also, technically there is no need to determine the SDS content during the synthesis, as SDS is not expected to take part in the polymerization reactions.

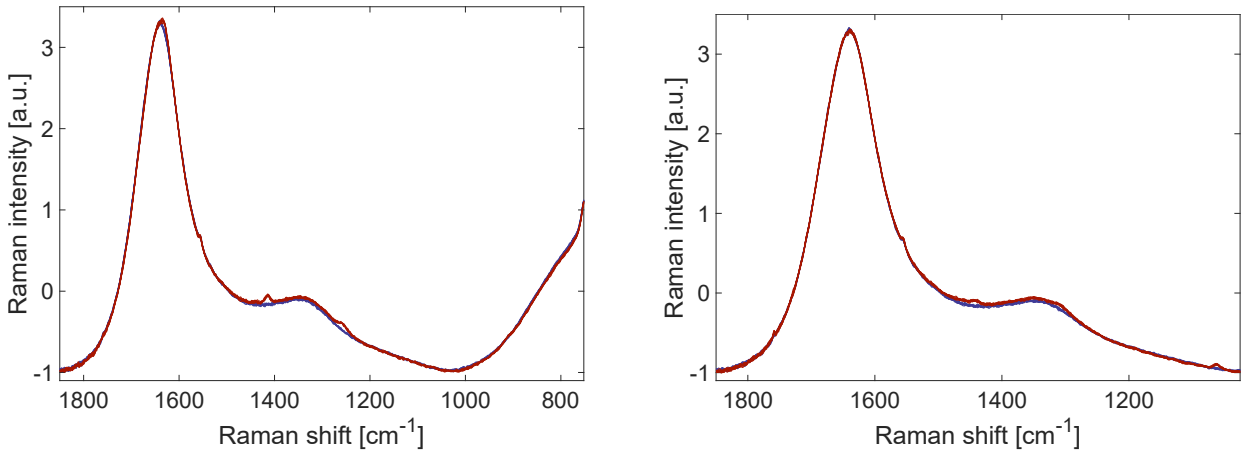

(a) BIS (b) SDS

Figure 5.1: Comparison of Raman spectra of deionized water (blue spectra) and other components (red spectra). (a) 0.023 wt% BIS in deionized water, and (b) 0.044 wt% SDS in deionized water. Spectra are recorded at 25°C and pretreated with linear fit subtraction and SNV standardization for visualization.

5.3.1.2 pH Influence on Raman Signal

The Raman spectra of MAA solutions are analyzed at different pH values to analyze the impact of the dissociation of the carboxylic groups on the Raman signal.

For the development of the Raman evaluation model, the detectability of the monomer MAA and its charged state MAA^- in Raman spectra is investigated. Both monomers contain carboxylic groups that enable the monomers to switch between the charged and uncharged state. Changing the pH value of the monomer solution influences the charge of the monomers. For a pH value below the so-called pKa value, the monomers are mostly protonated (MAA). Whereas, for a pH value above the pKa value, the monomers are mostly negatively charged (MAA^-). The pKa value of MAA at 20°C is 4.65 [151]. Since modifications of the charge involves changes of the molecular structure in the form of loosing a hydrogen atom, a spectral change is expected to be visible via Raman measurements.

To visualize the influence of pH change on the MAA Raman spectra, titration experiments are conducted. In these experiments, the pH value of the monomer solution is gradually changed and the Raman signal is recorded at each step. The experimental setup (Figure 5.2) and protocol for the titration are adapted from Echtermeyer at al. [81]. The titration is conducted at constant temperature in a three-neck flask with a RXN2 Raman Analyzer probe and a pH electrode (SenTix 940) with pH meter (Multi 3420, WTW, Weilheim, Germany) including a thermometer. To adjust the pH value of the solution, sodium hydroxide (NaOH, $1\,\mathrm{mol\,L^{-1}}$, VWR Chemicals) and hydrochloric acid (HCl, $1\,\mathrm{mol\,L^{-1}}$, Carl Roth) as received are used. The solution is heated by a water bath. A non-transparent black PVC liner is installed around the setup to exclude ambient light. The analyte solution contains MAA in deionized water at different concentrations.

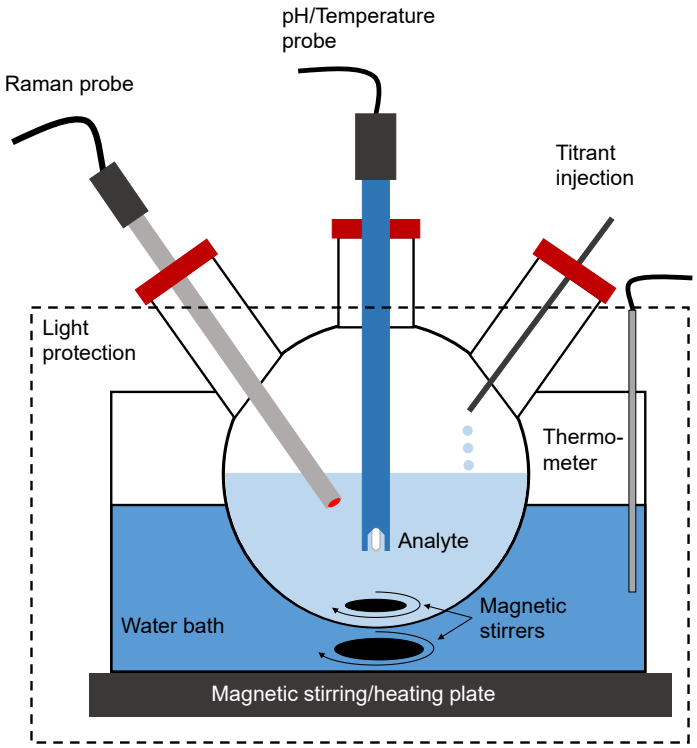

Figure 5.2: Setup for titration experiments including three-neck flask with a pH/temperature probe and Raman immersion probe. Schematic drawing adapted from Echtermeyer et al. [81].

The analyte concentrations studied and the concentration and volume of the titration steps are presented in Table 5.2. The molar concentrations for MAA in the analyte are $0.5\,\mathrm{mol\,L^{-1}}$ and

$0.05\,\mathrm{mol\,L^{-1}}$. The monomer concentration of $0.05\,\mathrm{mol\,L^{-1}}$ corresponds to the same order of magnitude as the initial reaction composition of 15 mol% microgel synthesis ($0.022\,\mathrm{mol\,L^{-1}}$). Titrations with $0.5\,\mathrm{mol\,L^{-1}}$ of MAA are carried out at 25°C and 70°C. Titrations with $0.05\,\mathrm{mol\,L^{-1}}$ of MAA are conducted only at 25°C. If not noted otherwise, the pH of the solution is titrated to an acidic pH using $1\,\mathrm{mol\,L^{-1}}$ HCl to ensure full dissociation of MAA. However, due to the low concentration in reaction conditions, the acid is practically fully deprotonated without the use of acidic titrants. A NaOH solution as titrant is injected step-wise to the stirred analyte solution. During the titration, the pH value of the aqueous acid mixture is monitored. For the titration with $0.05\,\mathrm{mol\,L^{-1}}$ MAA, smaller and less concentrated titrant steps are chosen due to the low concentration of MAA and related sensitivity of the protonation state. During the titration, Raman spectra of the solution are taken at every titration step.

Table 5.2: Concentration and volume of titration steps.

	c_{MAA} [$\mathrm{mol\,L^{-1}}$]	c_{NaOH} [$\mathrm{mol\,L^{-1}}$]	V_{Titrant} [mL]
Reference concentration	0.5	1	1.5
Synthesis concentration	0.05	0.05	0.25 - 1.5

Figures 5.3 to 5.4 show the resulting Raman spectra from the titration experiments. First, in Figure 5.3(a) the influence of pH variation on the Raman spectra of a $0.5\,\mathrm{mol\,L^{-1}}$ MAA solution is examined. The most prominent peaks with associated molecular groups of MAA are found at $800\,\mathrm{cm^{-1}}$ (COOH group), $850\,\mathrm{cm^{-1}}$ (COO^- group), $1400\,\mathrm{cm^{-1}}$ (CO and OH group) and $1690\,\mathrm{cm^{-1}}$ (C=O group). An evolution of those peaks with regards to the pH of the solution (and therefore the protonation state of MAA) can be observed: Peaks at 800 and $1690\,\mathrm{cm^{-1}}$ (COOH and C=O group), which are related to the protonated form of MAA, decrease with increasing pH. While the peak at $850\,\mathrm{cm^{-1}}$ (COO^- group), which is related to the deprotonated form of MAA, increases with increasing pH. Moreover, the peaks for the COOH and COO^- group show equal intensity at pH=pKa. The peak at $1400\,\mathrm{cm^{-1}}$ shows a shift to higher wavenumbers and increases with increasing pH. While there are several additional minor peaks that show some sort of shifting or intensity changes, only the peaks mentioned above are also distinctive in the titration experiment with lower concentration of MAA ($0.05\,\mathrm{mol\,L^{-1}}$) as shown in Figure 5.3(b). Significant changes in the spectra of the $0.05\,\mathrm{mol\,L^{-1}}$ solution appear only at around $800\,\mathrm{cm^{-1}}$. However, in this spectral region multiple component peaks arise which impede an explicit allocation of components within the spectra. Thus, the spectral range considered for the IHM evaluation model in this work is truncated as a trade-off between a bigger spectral region with more information on the analyte versus a bigger spectral region containing unambiguous information. Further, the pH influence on the Raman spectra at ambient temperature and synthesis temperature of 70°C is examined. No differences in spectral expression between the two temperature regions are visible when comparing Figure 5.3(a) and 5.4. Overall, changes in peak position and intensity occur in the Raman spectra of MAA solutions upon pH variation. However, the spectral changes are insignificant for MAA solutions at synthesis concentrations. Thus, for the IHM evaluation model development, MAA and its dissociated species are considered as one model component.

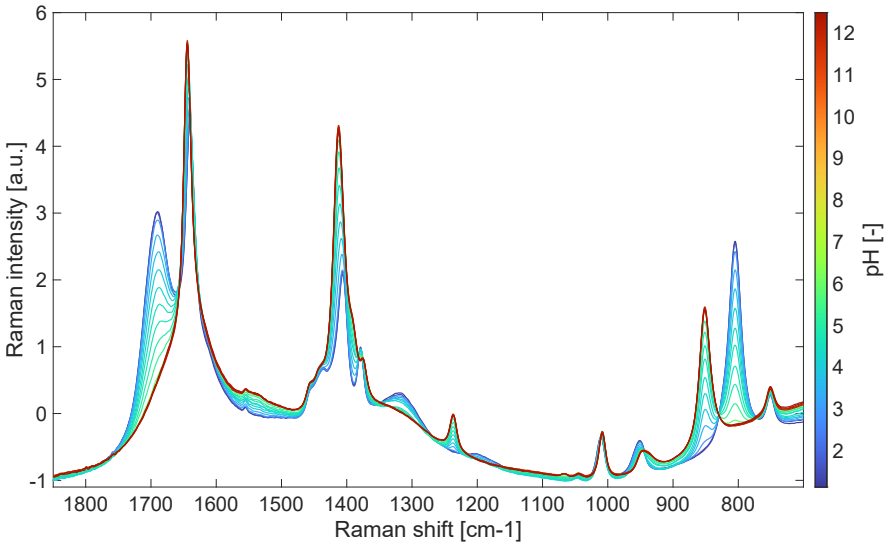

(a) $0.5\,\mathrm{mol\,L^{-1}}$ MAA: Initial $3.5\,\mathrm{mL}$ of $1\,\mathrm{mol\,L^{-1}}$ HCl to achieve full protonation.

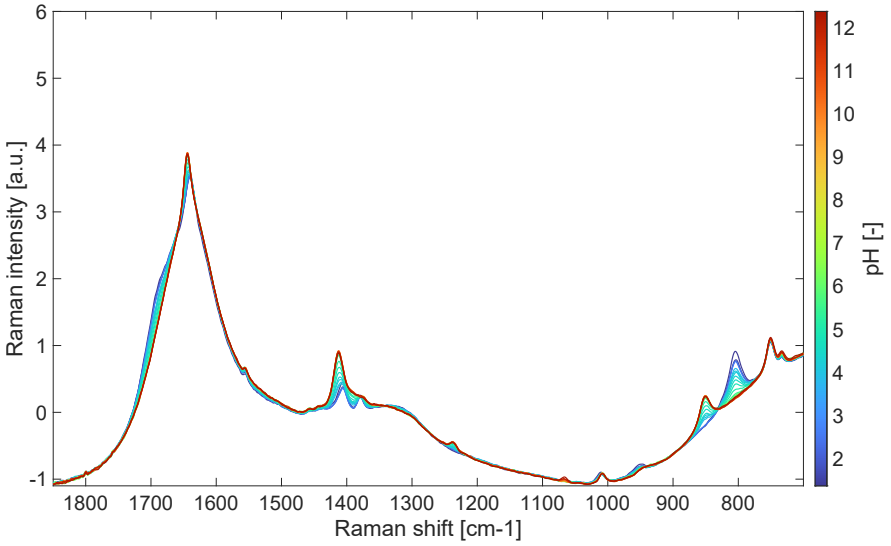

(b) $0.05\,\mathrm{mol\,L^{-1}}$ MAA: Initial $8.0\,\mathrm{mL}$ of $1\,\mathrm{mol\,L^{-1}}$ HCl to achieve full protonation.

Figure 5.3: Raman spectra of the titration experiment at 25°C: (a) 0.5 mol L^{-1} MAA, and (b) 0.05 mol L^{-1} MAA. Spectra are pretreated with linear fit baseline subtraction and SNV standardization for visualization.

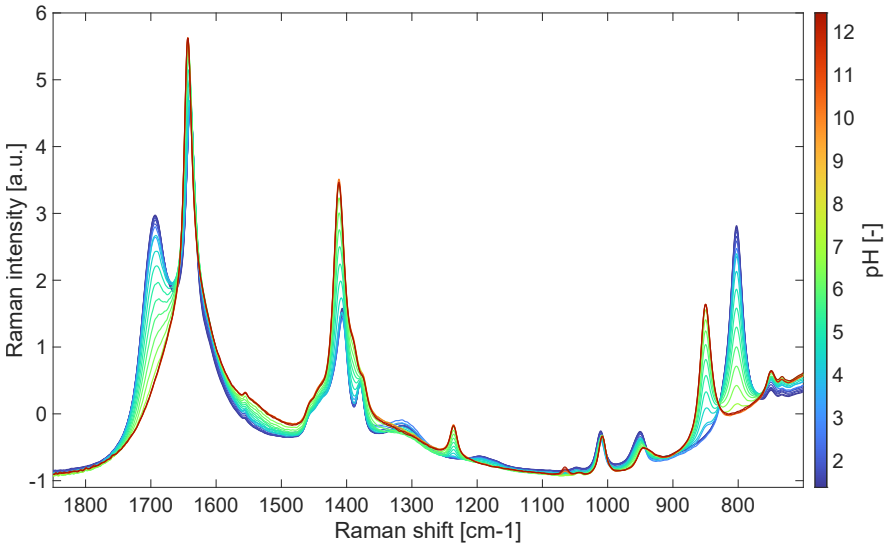

Figure 5.4: Raman spectra of the titration experiment of 0.5 mol L^{-1} MAA at 70°C. Initial 13.0 mL of 1 mol L^{-1} HCl to achieve full protonation. Spectra are pretreated with linear fit baseline subtraction and SNV standardization for visualization.

The analysis yields that the Raman signal of MAA varies with the degree of dissociation of the monomer. However, at the highly diluted conditions applied in the context of the aqueous microgel synthesis, the change in peak intensities due to the dissociation of the carboxylic group is negligible in the considered wavelength range. Hence, the carboxylic MAA monomers are included as one species comprising the charged and uncharged state for the evaluation model.

5.3.1.3 MAA-dependent IHM Evaluation Models

To model the produced microgel, the three different compositions of microgels with varying MAA compositions (5, 10, and 15 mol% of MAA) are considered. For improved visualization, linear fit subtraction and standard normal variate (SNV) standardization are applied as pretreatment to all spectral representations within this contribution. The Raman signal of microgels incorporating different amounts of MAA are shown in Figure 5.5. The Raman spectra of the NIPAM-*co*-MAA microgels change significantly depending on the content of MAA within the microgel. Exemplarily, in Figure 5.5, a spectral peak is visible at around 1300 cm^{-1} for microgels with a 5 mol% MAA content, but is not differentiable for 15 mol% MAA microgels. As the Raman signals of the microgels with different MAA amounts differ significantly, a different model is used for evaluating each synthesis separately. Hence, each model is calibrated with the corresponding microgel. The synthesized microgel is freeze-dried for calibration, and calibration samples are prepared accordingly.

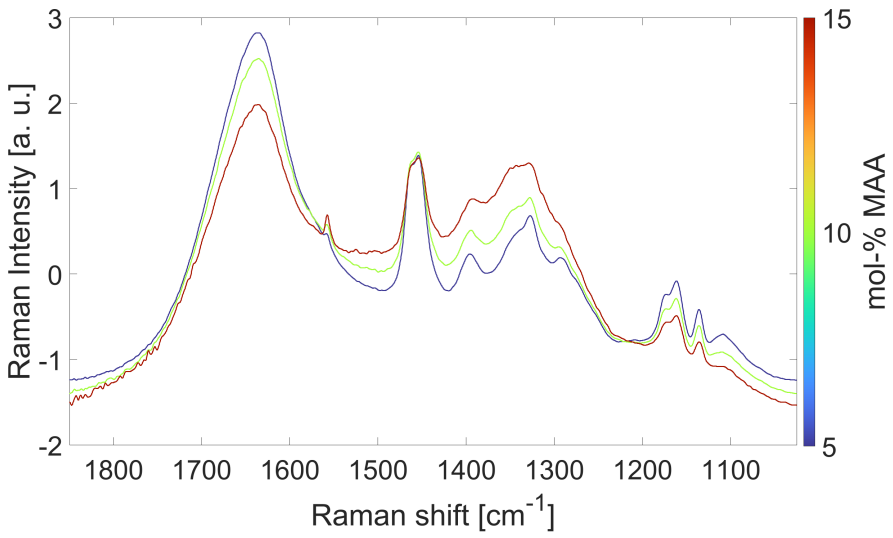

Figure 5.5: Raman spectra of NIPAM-*co*-MAA microgels in deionized water at 25°C with varying MAA composition. Spectra are pretreated with linear fit subtraction and SNV standardization for visualization.

The developed Raman evaluation model contains PCMs for water (6 peaks), NIPAM (21 peaks), KPS (1 peak), MAA (8 peaks), and the corresponding microgel NIPAM-*co*-MAA (14 peaks). Additional dummy PCMs are included for the oxygen peak (1 peak) and background noise (4 peaks).

5.3.1.4 Calibration Metrices

The results from the model calibration for the NIPAM-*co*-MAA containing different mol% of MAA are shown in Table 5.3 in the form of the coefficient of determination (R^2) value and the root mean squared error of cross-validation (RMSECV), respectively. The R^2 value and the RMSECV value all range in the same order of magnitude. Both calibration metrics show excellent model accuracy for the model training. Additionally, Figures 5.6(a) to 5.6(c) visualize the parity plots of the developed IHM models. The parity plots reflect the excellent model calibration, also indicated by the proper calibration metrics in Table 5.3.

5.3.2 Raman Spectroscopy of Reaction Samples

The spectra received by off-line Raman monitoring show the reaction progress explicitly. The resulting Raman spectra and the evaluation thereof for the remaining compositions are presented in the following. Figures 5.7 to 5.9 present the Raman signal during the NIPAM-*co*-MAA microgel synthesis with 5 to 15 mol-% MAA content. Here, the characteristic NIPAM monomer peaks at 1068 cm^{-1}, 1262 cm^{-1}, and 1415 cm^{-1} and the double peak at 1617 cm^{-1} and 1653 cm^{-1} (corresponding to the C=O bond and C=C bond, respectively) vanish with progressing reaction time. Also, MAA exhibits characteristic monomer peaks at 1379 cm^{-1}, 1407 cm^{-1}, and 1641 cm^{-1} which only contribute slightly to the spectral signal. Concurrently, the characteristic polymer peaks at 1392 cm^{-1} (CH_3 symmetric deformation) and 1636 cm^{-1} (amide I group) emerge. Also, the intensity of the common peak at 1452 cm^{-1} attributed to the C-H bending becomes more significant with longer reaction times.

Table 5.3: Calibration metrics for the NIPAM-*co*-MAA IHM evaluation models for different mol% of MAA co-monomer in the microgel.

	Component	R^2 [%]	RMSECV [wt%]
5 mol% MAA	Water	99.93	0.0153
	NIPAM	99.97	0.0098
	MAA	99.79	0.0066
	Microgel	99.97	0.0074
	KPS	99.87	0.0006
10 mol% MAA	Water	99.86	0.0219
	NIPAM	99.97	0.0100
	MAA	99.81	0.0063
	Microgel	99.83	0.0165
	KPS	99.92	0.0005
15 mol% MAA	Water	99.89	0.0192
	NIPAM	99.97	0.0104
	MAA	99.83	0.0059
	Microgel	99.88	0.0146
	KPS	99.80	0.0007

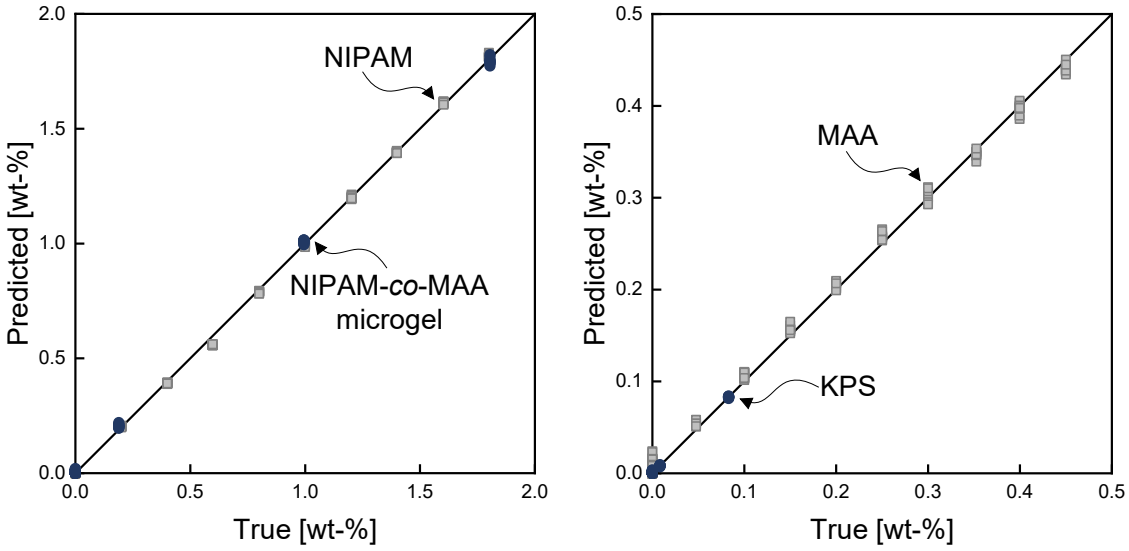

(a) 5 mol% of MAA

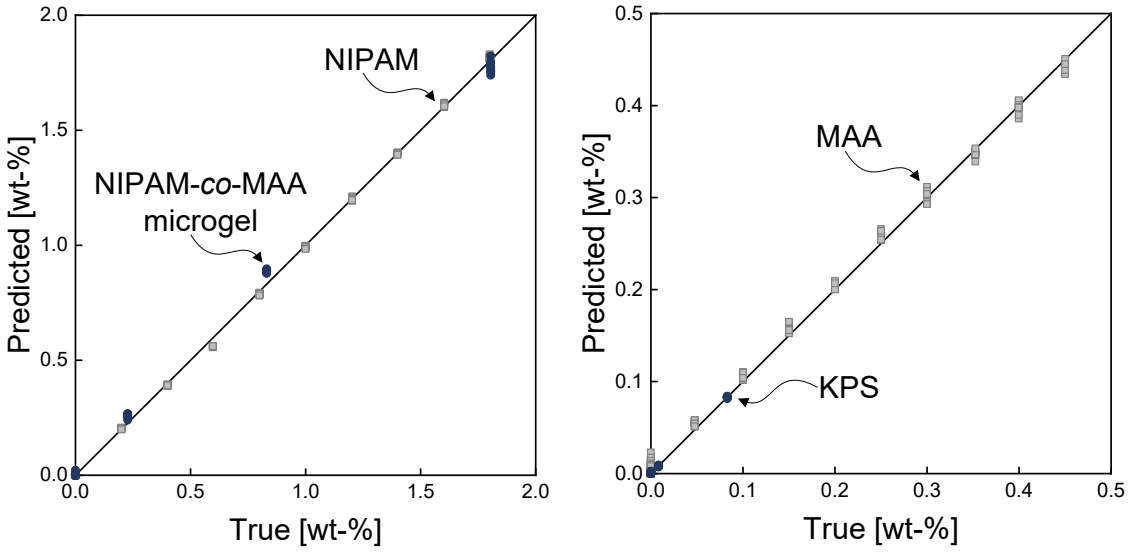

(b) 10 mol% of MAA

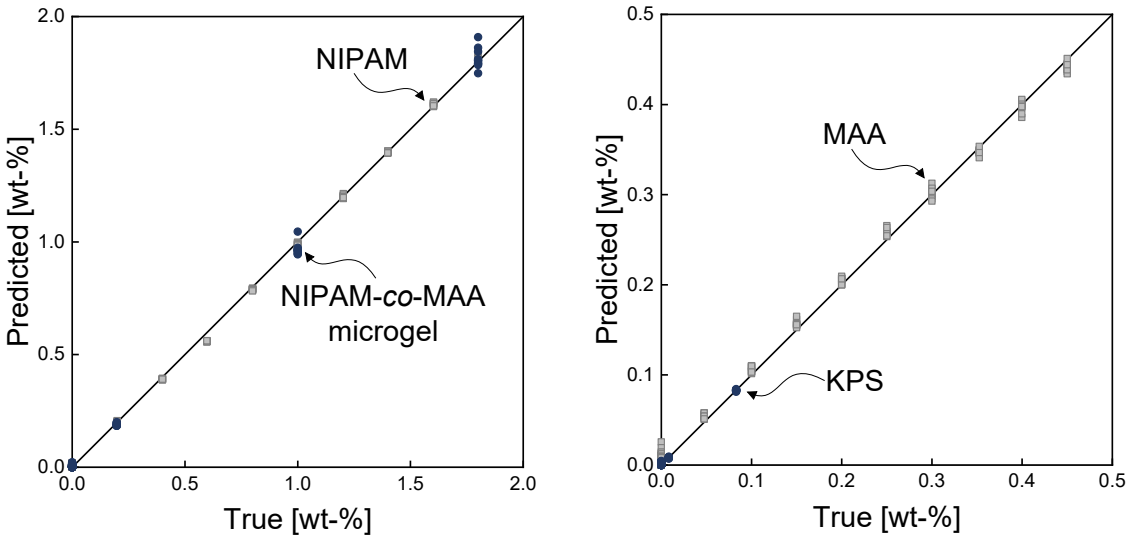

(c) 15 mol% of MAA

Figure 5.6: Parity plots for components of IHM prediction model for NIPAM-*co*-MAA synthesis with 5 mol% to 15 mol% MAA in the microgel.

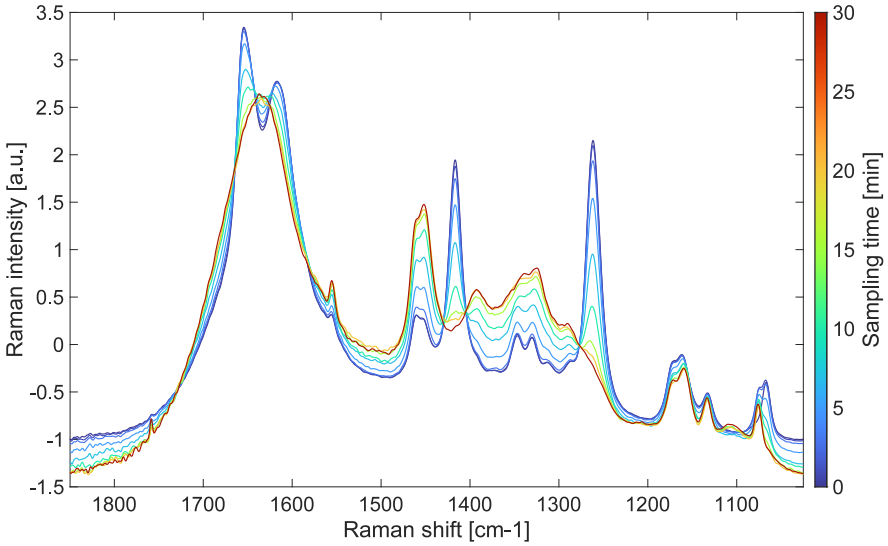

Figure 5.7: Raman spectra of the off-line samples during the 5 mol% NIPAM-*co*-MAA batch synthesis. Spectra are pretreated with a linear fit baseline subtraction and a SNV standardization for visualization.

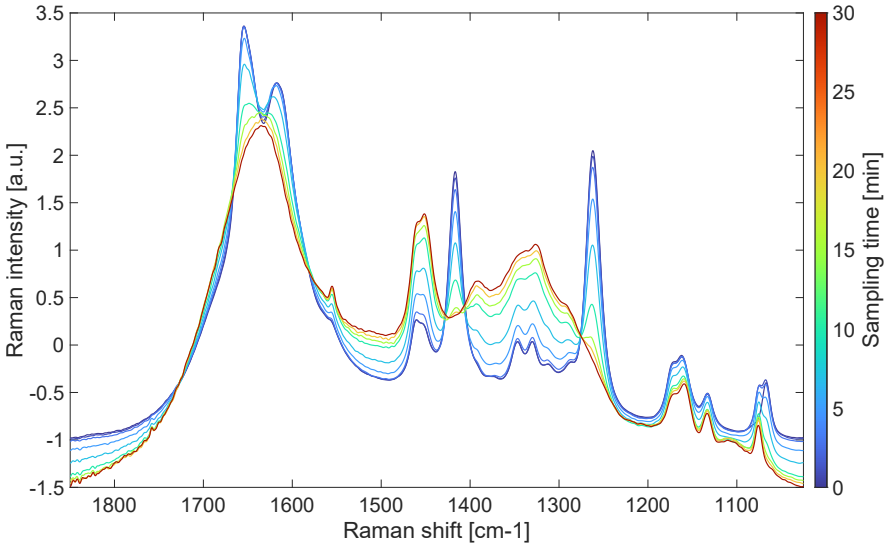

Figure 5.8: Raman spectra of the off-line samples during the 10 mol% NIPAM-*co*-MAA batch synthesis. Spectra are pretreated with a linear fit subtraction and SNV standardization for visualization.

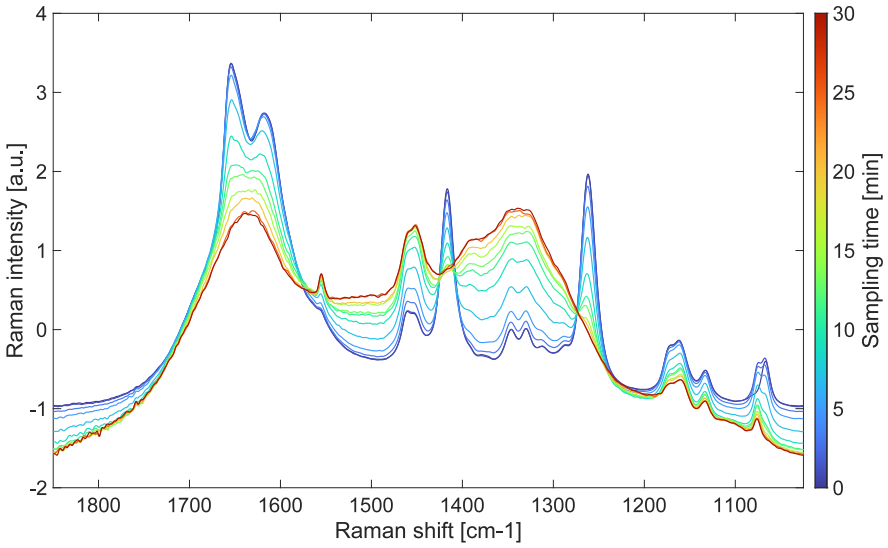

Figure 5.9: Raman spectra of the off-line samples during the 15 mol% NIPAM-*co*-MAA batch synthesis. Spectra are pretreated with a linear fit baseline subtraction and a SNV standardization for visualization.

When applying the developed IHM evaluation to the detected Raman spectra, the weight fractions of each component in the solution can be predicted over time. Figure 5.10 illustrates the predicted progression of NIPAM, MAA, KPS, and microgel over reaction time for the synthesis with different MAA content. The stars indicate the initial weighted weight fractions for NIPAM, MAA, and BIS, and the final weighted microgel weight fraction determined after dialysis and freeze-drying. The weight fractions of the monomers NIPAM and MAA decrease over time. While NIPAM is fully consumed after approximately 20 min, MAA is already depleted after 10 min. The initial weighted weight fractions of the monomers agree precisely with the predicted values from the Raman monitoring. The microgel formation arises inversely to the monomer consumption. Similar to the NIPAM progression, the microgel production reaches its final value after approximately 20 min. The final microgel weight

fraction determined by weighting is very similar to the predicted one but differs for example for the 10 mol% MAA synthesis by an absolute value of 0.134 wt%. The initiator weight fraction decreases steadily and reaches a value of 0.068 wt% after an hour of reaction (also examplarily for the 10 mol% MAA synthesis). Thus, the initiator KPS is not depleted during the synthesis. Generally, the IHM evaluation model tends to overestimate the content of the components in the solution. Altogether, this work shows that Raman spectroscopy and IHM evaluation are reliable methods for predicting the compositions during the microgel synthesis.

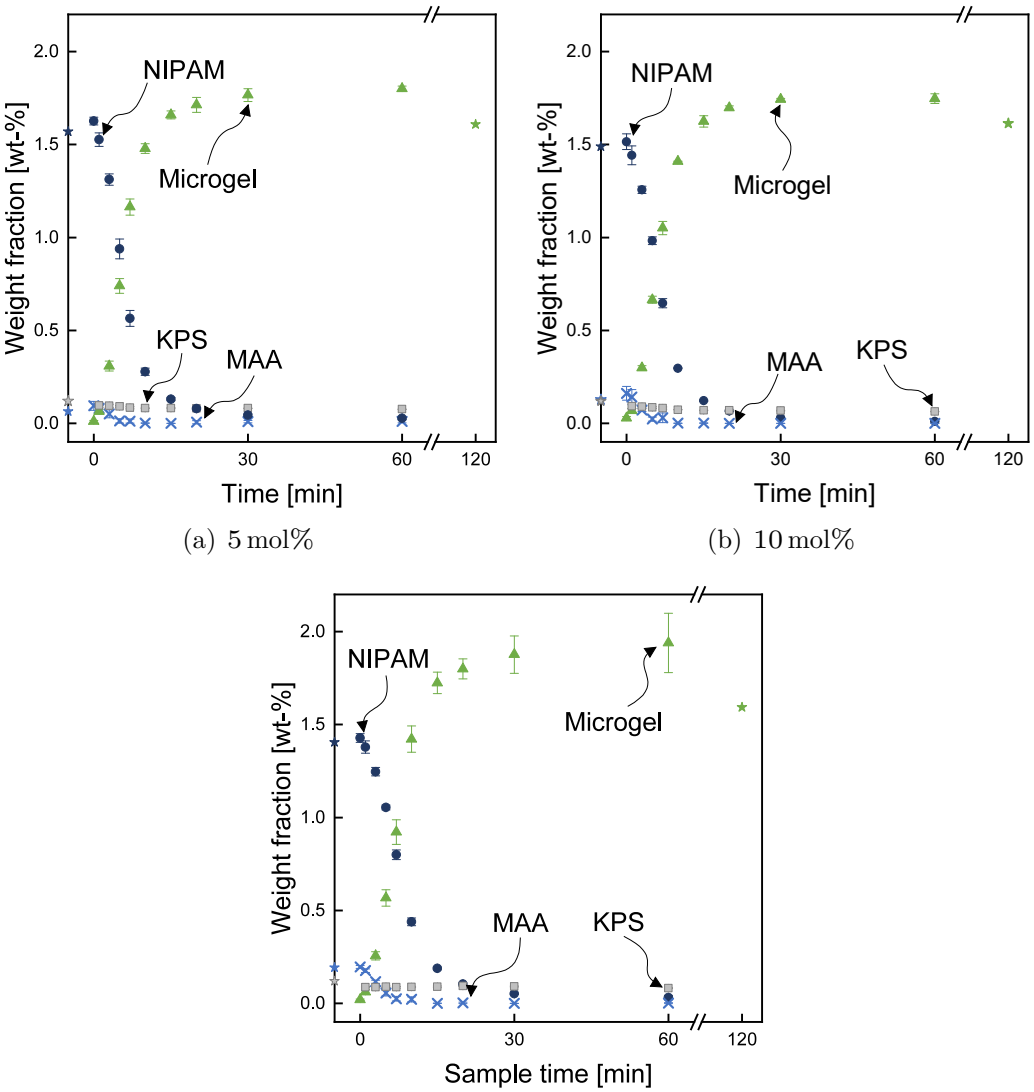

(a) 5 mol%

(b) 10 mol%

(c) 15 mol%

Figure 5.10: Predicted weight fractions of the off-line samples using IHM for the NIPAM-*co*-MAA batch synthesis with (a) 5 mol%, (b) 10 mol%, and (c) 15 mol% MAA content. The stars indicate the initial weighted weight fractions of the reactants and the weighted microgel weight fraction after dialysis and freeze-drying.

Based on the predicted weight fractions during the microgel synthesis, the conversion of the two monomers, NIPAM and MAA, can be calculated over time. Figure 5.11 shows the conversion of NIPAM and MAA over the reaction time for different content of MAA in the microgel. The conversion of NIPAM changes depending on the content of MAA in the synthesis. The more MAA is taking

part, the slower the conversion of NIPAM during the synthesis. Nevertheless, on average, a final NIPAM conversion of 0.985 is reached for every content of MAA considered. The conversion of MAA during the synthesis is challenging to monitor precisely. The acquired measurements and the evaluation thereof yield a high variance. Also, nonphysical values of the MAA conversion are derived (below zero conversion). Still, there is a trend that MAA is consumed much faster than NIPAM. Furthermore, the conversion of MAA is similar in every case considered.

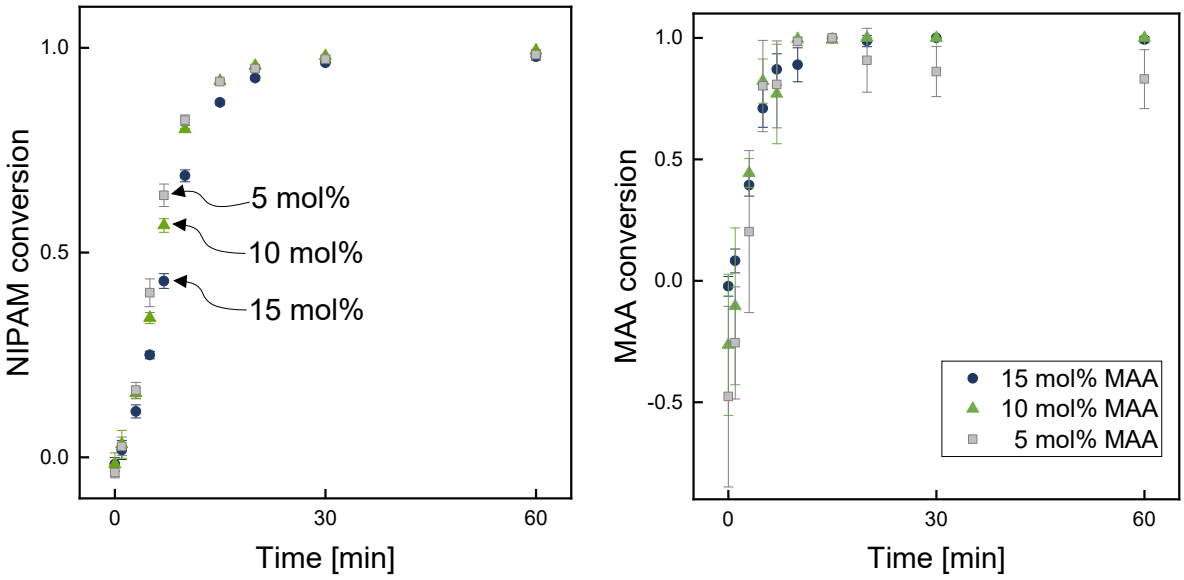

(a) NIPAM conversion

(b) MAA conversion

Figure 5.11: Conversion during the NIPAM-*co*-MAA synthesis with 5, 10, and 15 mol% MAA in the microgel: (a) NIPAM conversion, and (b) MAA conversion.

5.4 Conclusions

Process analytical analysis of multi-component solutions that occur in the turbid synthesis of microgels is challenging, especially when charged species such as MAA occur in dissociated and undissociated state. Raman spectroscopy is deployed to monitor the synthesis of charged NIPAM-*co*-MAA microgels. Applying indirect spectral hard modeling for spectra evaluation resolves the complexities caused by overlapping spectral peaks from multi-component solutions. The developed analytical procedure to determine the content of all participating components during the synthesis of charged microgels enables a sufficent concentration prediction. However, due to the low concentration of MAA in the system, the MAA prediction during the synthesis remains subject to high variance. Nevertheless, a detailed insight into the reaction phenomena during the charged microgel synthesis is enabled.

6 Identification of a Dynamic Model of the *N*-Vinylcaprolactam-*co*-Glycidyl Methacrylate Microgel Synthesis

6.1 Motivation for Modeling of *N*-Vinylcaprolactam-*co*-Glycidyl Methacrylate Microgel Synthesis

Microgels are crosslinked polymer networks with a reversible stimulus-specific swelling response to temperature, pH, or ionic strength. Microgels based on *N*-vinylcaprolactam (VCL) are temperature responsive and interesting due to their biocompatibility [72]. Incorporating co-monomers into PVCL microgels allows tuning their functionalities. Glycidyl methacrylate (GMA) is a promising co-monomer thanks to its reactive epoxy group that is versatile in subsequent reactions. Hence, PVCL microgels functionalized with GMA experience a wide range of applications [40, 44, 45].

GMA is more reactive than VCL in the co-polymerization leading to the heterogeneous composition of the resulting microgels, thus, the authors of [152] performed a gradual feeding technique to produce more homogeneous microgels. Under batch conditions, [153] also showed via high-magnification scanning electron microscopy (SEM) and transmission electron microscopy (TEM) images that the microgels inhibit a core-shell structure with a GMA-rich core surrounded by a VCL-rich shell. Due to the complexity of the reaction network during microgel synthesis, understanding the relationship between the synthesis conditions and the final composition of the microgels is challenging. Thus, for designing tailored microgels, detailed reaction models provide insights and assist with developing microgels with defined monomer distributions.

Previously, Janssen et al. [85] have developed a dynamic and mechanistic kinetic model for the aqueous microgel synthesis by precipitation polymerization. There, unknown parameter values were determined via quantum mechanical calculations [85, 154]. The model from Janssen et al. was simplified by Jung et al. [66] for improved parameter identifiabiliy. To estimate the model parameters, a combination of quantum mechanical calculations [154] and physical measurements [66] were used. Later, Schneider et al. [68] adjusted the dynamic model and applied it to predict and guide the synthesis of microgels based on monomer VCL, co-monomer vinylferrocene (VFc), and crosslinker N,N'-methylenebisacrylamide (BIS). In contrast to these monomer combinations, parameter values for the propagation rate coefficients and polymerization enthalpies of GMA/VCL and GMA/BIS systems in an aqueous solution remain unknown.

In previous work [14], a mechanistic model based on the model developed by Schneider et al. [68] was build for synthesizing VCL-based microgels functionalized with GMA. For the application to the VCL/GMA/BIS system, the model structure stayed identical but the parameter values have to be adjusted. Altogether, the model contains 14 unknown kinetic parameter values. For model identification in this chapter, a hybrid approach is pursued. First, parameter values for the propagation rate coefficients and polymerization enthalpies of the GMA/VCL and GMA/BIS systems in an aqueous

solution can be computed using transition state theory and quantum mechanical calculations [14]. These parameters account for 12 out of 14 parameters in total. Additionally, experiments with four different initial compositions and measurements of the enthalpy transfer rate during the synthesis using a calorimetric device are conducted [14]. Subsequently, the remaining parameter values of the five most sensitive propagation rate coefficients and the initiation and termination rates are estimated using the measured enthalpy transfer rate from the experiments. The quantum mechanically calculated values are incorporated as start values for the parameter estimation. Also, the computed error bounds from the quantum calculation are added as optimization constraints during the parameter estimation.

In this chapter, the focus is on a deeper analysis of parameter estimation that incorporate quantum mechanically calculated parameter values. Unknown parameter values are either set to the quantum mechanically calculated values or determined in a parameter estimation. In contrast to previous works that leveraged quantum mechanical computations [85], the present work developes a strategy to include quantum mechanically calculated values, while handling the arising trade-off between (*i*) using all available quantum mechanically calculated values with a significant computational error, and (*ii*) only estimating parameter values from experimental data, which necessitates high computational effort. Additionally, an identifiability analysis is conducted. Finally, the fully identified model of the VCL-*co*-GMA microgel synthesis is applied to predict feeding strategies for a homogeneous microgel composition.

6.2 Methods

In the following sections, first the experimental setup for the microgel synthesis monitored via real-time reaction calorimetry is described in Section 6.2.1. Subsequently, quantum mechanical calculations to determine propagation rate coefficients are briefly explained in Section 6.2.2. In Section 6.2.3, the assumptions of the model that is extended in this work is highlighted. Finally, the configurations for the parameter estimations and the identifiability analysis are explained in Section 6.2.4.

6.2.1 Microgel Synthesis and Real-Time Reaction Calorimetry

The precipitation polymerization of VCL crosslinked with BIS and functionalized with GMA is analyzed in the following. 2,2'-azobis(2-methylpropionamidine)dihydrochloride (AMPA) is considered as initiator. The previously measured enthalpy transfer rates during the reaction via real-time reaction calorimetry [14] are used as experimental data. Details on the setup and compositions of the conducted experiments can be found in previous works [14]. In Table 6.1, the variations between the experiments used in the current chapter are briefly outlined.

Table 6.1: Synthesis composition for experiments monitored via real-time reaction calorimetry.

Experiment	Molar ratio VCL:GMA	Molar amount of crosslinker BIS
1	90:10:00	2.0 mol%
2	90:10:00	2.6 mol%
3	93:07:00	2.0 mol%
4	95:05:00	2.6 mol%

6.2.2 Quantum Mechanical Calculations

The propagation rate coefficients of the VCL/GMA/BIS system that were calculated via quantum chemistry methods [14] are incorporated for the following work. There, conventional transition state theory was applied to determine propagation rate coefficients. Further, the enthalpies of reaction were calculated using the Gibbs-Helmholtz equation. Computational details can be found in [14].

6.2.3 Kinetic Model of Microgel Synthesis

The reaction system of the kinetic synthesis model is adapted from Schneider et al. [68] and the parameter values are changed according to the VCL/GMA/BIS system. The main model assumptions are briefly summarized in the following. The dispersed system is modeled in a pseudo-homogeneous phase. The occurring reactions include initiation, propagation, termination, and crosslinking. The efficiency of the initiator decomposition is assumed to be constant over the course of the synthesis and is set to 50% [69]. The kinetics of the propagation reactions depend only on the radical at the terminal end of the chain, and propagation reactions make up for to the enthalpy release. Termination only occurs due to disproportionation, and the kinetics of termination reactions do not depend on the terminal end of the active radical chains. The kinetics of the crosslinking reaction equals the kinetics of a propagation reaction with a BIS monomer.

6.2.4 Parameter Estimation and Identifiability Analysis

For the parameter estimation and identifiability analysis, the five reaction enthalpy values for the quantum mechanically calculated propagation including GMA are used without further considerations or treatment in the synthesis model. Then, a sensitivity analysis is performed to identify the most sensitive propagation rate coefficient (k_p) parameters. Subsequently, a parameter estimation is performed to determine different set of parameter values. For all estimations, the initiator decomposition (k_d) and the termination (k_t) rate coefficients are estimated as they remain unknown after the quantum mechanical calculations. The conducted estimations are split into the following sets:

1. Estimate all k_ps with arbitrary start values and bounds
2. Estimate all k_ps using the quantum calculations as start values and their error bounds as constraints
3. Estimate the five most sensitive k_ps using the quantum calculations as start values and their error bounds as constraints
4. Insert all k_ps into the model and only estimate k_t and k_d

The parameter estimation and the identifiability are conducted in Matlab, similar to [66], using the presented co-polymerization model and the calorimetric measurements. For part of the estimations, the calculated propagation rate coefficients act as start values and the calculation uncertainties derived from Gaussian error propagation analysis of the quantum mechanical method's uncertainty act as constraints in the optimization problem. For estimation (1) the start values for the propagation rate coefficients are 10, and the upper and lower bounds are 10^{-3} and 10^{5}, respectively. Within the identifiability analysis, the feasible parameter set is approximated for each parameter as a box constraint. The bounds of the box constraint are determined by solving multiple constrained parameter estimation problems [66]. By conducting the identifiability analysis, the confidence in the determined parameter values in the parameter estimation is established.

6.3 Results and Discussion

The results include the comparison of the propagation rate coefficient values calculated via quantum mechanically computations with the different parameter estimation configurations in Section 6.3.1. In addition, the results of the identifiability analysis are also presented in Section 6.3.1. Lastly, Section 6.3.2 shows process simulations for different feeding strategies of GMA to determine the optimal settings for a homogeneous GMA distribution within the microgel.

6.3.1 Quantum Mechanically Calculated and Estimated Kinetic Parameters

The calculated propagation rate coefficients for the VCL/GMA/BIS system in an ideally diluted aqueous solution at a temperature of 343 K are shown in the second column of Table 6.2. The applied bounds are presented in the third and fourth columns of Table 6.2. Using the optimized parameter values from estimation (3), the proposed model agrees to 97% on average to the measured enthalpy transfer rate from the experiments monitored via real-time reaction calorimetry.

The results in Table 6.2 show that the homopolymerizations of GMA and VCL are in the same order of magnitude when calculated, but the VCL reaction is approximately twice as fast after the optimization. The most significant reaction is between VCL-radical and GMA. The reaction between GMA-radical and VCL plays are negligible role in the polymerization system. All reactions consuming GMA occur relatively fast. Thus, the experimental observation of a GMA-rich microgel core for batch production fits the calculated findings.

The enthalpy transfer rate simulated via the synthesis model containing the respective parameter values is shown in Figure 6.1 exemplary for Experiment 3. The parameter sets from estimation (2) and (3) result in the best fit to the experimental data. Apparently, the estimation (1) with arbitrary start values and bounds gets stuck in a local minimum indicating the need for deterministic global optimization. The simulation of estimation (4) only has k_t and k_d as the degrees of freedom and does not sufficiently follow the experimental trend.

Table 6.2: propagation rate coefficients [$m^3mol^{-1}s^{-1}$] at 343 K calculated (Calc.) via quantum mechanical computations and optimized (Opt.) in the parameter estimations with corresponding upper and lower bound from the error of the quantum mechanical calculations.

Reactants	Calc. k_p [14]	Lower bound	Upper bound	Opt. k_p (1)	Opt. k_p (2)	Opt. k_p (3)	Opt. k_p (4)
VCL radical / VCL	86.8	10.4	727	28.7	23.8	116	-
VCL radical / GMA	516	61.6	4330	0.403	337	1300	-
GMA radical / GMA	65.5	7.8	549	10-3*	18.2	64.9	-
GMA radical / VCL	4.6	0.5	38.5	1.59	0.74	4.6	-
BIS radical / VCL	34.3	4.1	287	733	9.76	287	-
BIS radical / BIS	8.1	0.967	67.9	10-3*	67.9*	-	-
GMA radical / BIS	0.74	0.088	6.18	10-3*	2.44	-	-
BIS radical / GMA	129	15.4	1080	4210	15.4*	-	-
k_d [s^{-1}]	-	1×10^{-7}	1×10^{-3}	6.15×10^{-7}	3.48×10^{-5}	8.22×10^{-6}	8.97×10^{-7}
k_t [$m^3\,mol^{-1}\,s^{-1}$]	-	1×10^{-5}	105	1×10^{-5}*	244	1480	81.5

* denotes estimated parameter values at the bounds.

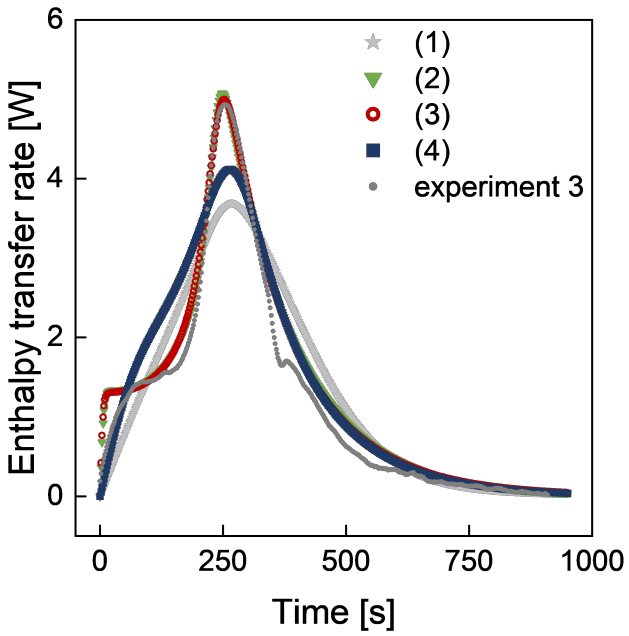

Figure 6.1: Enthalpy transfer rate for Experiment 3 and the simulations with the estimated parameter values from estimation (1) to (4).

In Figure 6.2, the result of the identifiability for the estimation with configuration (2) is shown. For visualization, only the parameters with the most significant variability are shown. Here, all parameters appear to be sufficiently identifiable except $k_{\mathrm{pBIS,BIS}}$. Hence, based on the real-time reaction calorimetry measurements all propagation rate coefficients can be identified except propagation rate coeffient of the BIS radical / BIS reaction. This finding is similar to previous identifiability studies considering microgel syntheses with cross-linker BIS [66].

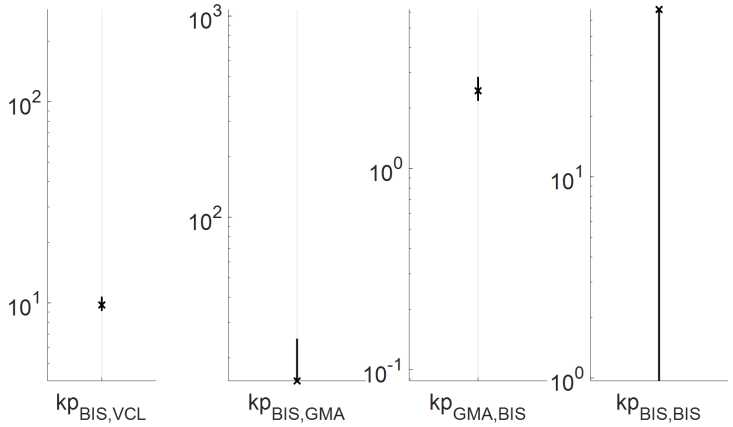

Figure 6.2: Identifiability analysis of selected parameters from estimation (2). The x indicates the optimal parameter value.

6.3.2 Process Simulations for Feeding Strategy

The identified model allows for assessment of feeding strategies. Optimization is conducted by leveraging synthesis simulations to find suitable strategies. However, in this context, no advanced com-

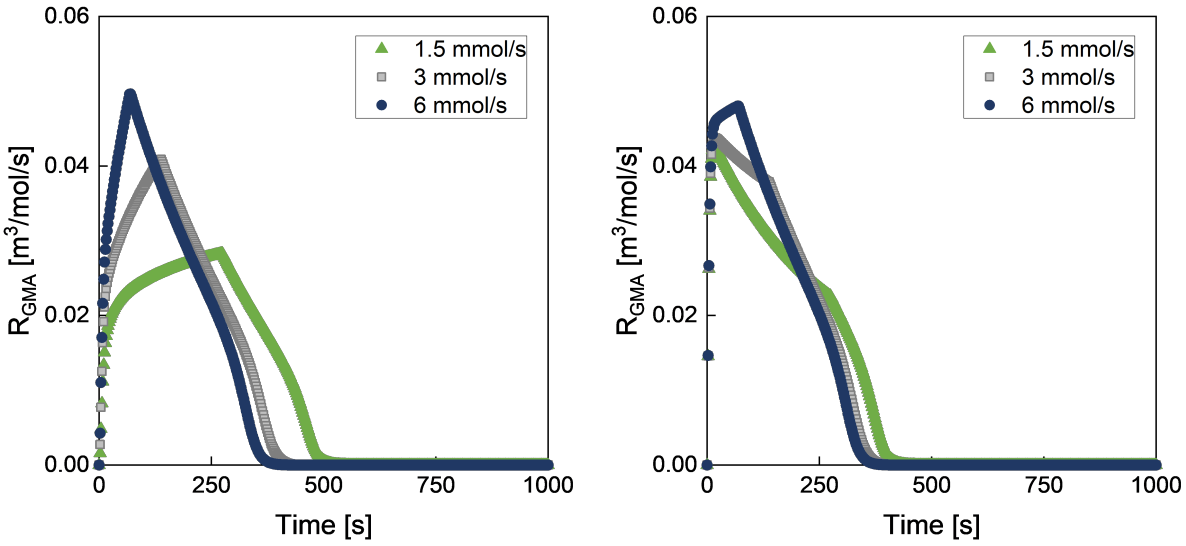

(a) 1:0 feeding

(b) 1:1 feeding

Figure 6.3: Simulation results of different GMA feeding strategies during the microgel synthesis: (a) Feeding strategy 1:0, all GMA is fed to the reactor, and the dosing flow rate varies. (b) Feeding strategy 1:1, half of the GMA is in the reactor at the start of the reaction, and half is fed at different dosing flow rates.

putational optimization methods, e.g., mathematical programming or numerical optimization, are applied. Therefore, different feeding strategies of GMA to the batch reaction are simulated in the following to analyze the distribution of functional GMA within the microgel. The focus is on two aspects, firstly the ratio of GMA initially in the reactor to in the dosing feed and secondly the dosing flow rate. The simulation includes the composition of Experiment 1 (see Table 6.1) and assumes that 7.5 mL of the total water volume is used for dosing. The ratio of GMA fed to GMA in the reactor varies from 0:1 (all GMA is initially in the reactor) to 1:1 and 1:0 (all GMA is fed to the reactor). Simultaneously, the dosing flow rate is set to 1.5, 3, and 6 $\mathrm{mmol\,s^{-1}}$.

In Figure 6.3, the results of the simulation scenarios are shown. Here, the combined reaction rate of GMA is depicted over time. The combined reaction rate comprises all reactions where GMA is consumed. When assuming monodisperse particle growth, the time of consumption of GMA correlates to the incorporated position in the microgel. Thus, the combined reaction rate of GMA represents its composition in the microgel. The progressions of Figure 6.3 indicate that adding all GMA at a dosing flow of 1.5 $\mathrm{mmol\,s^{-1}}$ is likely to achieve a homogeneous composition of GMA in the microgel.

6.4 Conclusions

In this contribution, the precipitation polymerization of microgels based on VCL/GMA/BIS in an aqueous solution is studied focusing on parameter estimation approaches. It is shown that incorporating quantum mechanically computed parameter values and their calculation error into the estimation problem improves the optimization result, while reducing the computational effort of the parameter estimation. Based on the fully identified synthesis model, it is possibel to derive an improved feeding strategy of GMA to the batch reaction to achieve a homogeneous GMA composition in the microgels by testing different scenarios. The proposed hybrid approach of quantum mechanical calculations and parameter estimation from experimental data shows the potential of integrating theoretical deriva-

tions and semi-empirical knowledge. Further, this contribution laid the ground to design and optimize the functionalization of VCL-based microgels with GMA in the future.

7 Dynamic Modeling and Identification of Microgel Synthesis with Charged Domains

Data Repository: *The mechanistic model developed in this chapter are published and available for free download via RWTH Publications [141].*

7.1 Motivation for Modeling of Charged Microgel Synthesis

By adding functional groups such as carboxylic acids to thermo-responsive microgels, these microgels are also attributed pH responsiveness [142–145]. Microgels with such dual stimulus swelling response find applications in drug delivery [33–36], catalysis [42, 43], sensing [46], and membranes [22]. Tan et al. [155] present a detailed review of pH-responsive microgel research.

Generally, it is possible to implement anionic (negatively charged) functional groups such as methacrylic acid (MAA) [143], or acrylic acid (AA) [144], or cationic (positively charged) functional groups such as amine N-(3-aminopropyl)methacrylamide hydrochloride (APMH) [156], or amine 2-aminoethylmethacrylate hydrochloride (AEMH) [157] into microgels. Ionic charges potentially allow the uptake of guest molecules based on electrostatic interactions [18], making pH-responsive microgels a proper material for drug delivery systems. Also, the different conditions of tumor tissue (pH 4.5) and physiological environments (pH 7.4) require pH-responsive drug delivery agents such as microgels for controlled release [158]. For biomedical applications, the toxicity of cationic particles is undesired [159, 160]. Thus, implementing anionic co-monomers such as AA or MAA is preferable. Therefore, the present study focuses on *N*-isopropylacrylamide (NIPAM)-based cross-linked microgels functionalized with MAA to represent a relevant case study.

In the past decades, modeling efforts regarding the synthesis of microgels have been presented and applied [14, 66–68, 76, 83–88]. With regard to the synthesis of NIPAM-BIS microgels cross-linked with *N*,*N*'-methylenebis(acrylamide) (BIS), Hoare et al. [83] derived a solely propagation-based steady-state terminal co-polymerization model accounting for the simultaneous reaction of four separate monomers. They applied the model to the synthesis of microgels containing NIPAM, cross-linker, and up to two functional monomers (among them MAA). To estimate the required reactivity ratios, they used the Price-Alfrey scheme [89]. Subsequently, Hoare et al. [84] observed a sufficient accuracy of their model prediction of the chain and radial functional group distribution with experimentally observed data.

For a complete model representation of the microgel synthesis, kinetic parameter values are crucial. As the kinetic rates involving carboxylic acids are temperature and pH-dependent, finding a complete set of coherent parameter values is challenging. Various experimental and theoretical studies regarding the kinetics of the homo- and co-polymerizations of NIPAM, BIS, and MAA are presented in the literature. However, no set of parameter values for consistent temperature, pH value, and dilute

aqueous conditions are available. For the system of NIPAM and BIS, Kröger et al. [154] used quantum mechanical calculations to determine the reaction enthalpies. Furthermore, Jung et al. [66, 67] estimated the kinetic rate coefficients of the NIPAM/BIS system, which were later used by Schneider et al. [68] in the synthesis model of NIPAM, BIS, and vinylferrocene (VFc). Thus, coherent parameter values for kinetic rate coefficients and reaction enthalpies for the NIPAM/BIS system are available.

Multiple experimental studies investigated the kinetics of the homopolymerization of aqueous MAA [161–166]. Recently, Buback et al. [167] reviewed the polymerization kinetics and modeling of ionized and non-ionized water-soluble monomers; among the studied monomers was MAA prominently. For a comprehensive review of propagation and termination rate coefficients regarding MAA, the reader is therefore directed to the work of Buback et al. [167]. In summary, the studies analyze the dependence on temperature and solvent [162], and the degree of ionization (which depends on the pH value of the solution) [164, 166]. Further, the propagation rate of MAA depends strongly on the weight fraction of MAA in the solution. For modeling the homopolymerization of MAA, a pseudo-co-polymerization of undissociated MAA and its ionized form is mainly applied, as introduced by Shoaf and Poehlein [161] to allow representing partially ionized MAA polymerization. Finally, non-ionized MAA at 50°C was chosen by Buback et al. [163] to study the effect that with lower monomer concentrations, the propagation rate is higher.

Brazel et al. [168] proposed experimentally determined reactivity ratios of NIPAM and MAA cross-linked with ethylene glycol dimethylacrylate (EGDMA) at 50°C. Regarding the linear co-polymerization of NIPAM and MAA, Xue et al. [169] calculated the reactivity ratios of NIPAM and MAA via the extended Kelen-Tüdös method. Their study explicitly omitted the reactivity ratios involving the cross-linker BIS. Finally, Hoare et al. [84] used the Price-Alfey scheme [89] to calculate missing parameter values of the synthesis involving NIPAM/BIS/MAA. Although the Price-Alfey scheme is a good approximation, it does not account for pH variations and does not generate precise parameter values, as it incorporates vague assumptions. All studies regarding the co-polymerization of NIPAM and MAA yield significantly different values for the reactivity ratios of the partaking monomers and even other qualitative trends [168–170]. Hence, the reliability of the reactivity values is questionable.

Herein, we present a dynamic model of the precipitation polymerization of pH- and thermo-responsive NIPAM-based microgels functionalized with MAA including pH dependency to predict the monomer conversion. The model extends previously developed models for the purley thermo-responsive microgel synthesis [66, 68]. To the authors knowledge, dynamic modeling is applied for the first time to the polymerization of microgels with charged domains. Moreover, missing reaction rate coefficients and reaction enthalpies for charged species are calculated by quantum mechanical computation or determined via parameter estimation based on experimental data from Raman spectra and real-time calorimetric measurements within this work.

The remaining chapter is structured as follows: Section 7.2 outlines the methods, encompassing experimental setup and settings and process analytical techniques. In Section 7.3, the modeling framework, structure of the quantum mechanical calculations, and parameter estimation approaches are introduced, outlining both theoretical assumptions and computational methods. Section 7.4 presents the results with respect to the evaluation of Raman monitoring, quantum mechanically calculated parameter values, and parameter estimation. Finally, Section 7.5 summarizes all findings, drawing conclusions and suggesting future research directions.

7.2 Experimental Microgel Synthesis with Real-Time Calorimetry

For real-time calorimetric measurements, microgel synthesis is carried out in a reaction calorimeter RC1e from Mettler Toledo using a 500 mL 3-wall AP01-0.5-RTCal reactor. The reactor is equipped with a Hastelloy stirrer, a baffle, and a Turbido turbidity probe from Solvias. The measurements are carried out in the isothermal mode, which means that the desired reaction temperature is set at a constant value, and the jacket temperature is changed automatically, such that the reaction temperature stays at the desired value. All experiments are performed at 70°C and ambient pressure. The reactor is filled with 0.185 L deionized water, the monomers NIPAM and MAA, the cross-linker BIS, and the surfactant sodium dodecyl sulfate (SDS) according to the previously stated compositions found in Table 5.1. The solution is stirred at 300 rpm, heated to 70°C, and subsequently degassed with nitrogen for 30 minutes. To generate a stable baseline, the solution is equilibrated for at least 60 minutes. The addition of dry potassium persulfate (KPS) initiates the reaction, and the synthesis lasts for 120 minutes. The experiments for the molar fractions of 5, 10, and 15 mol% are repeated three times. The software iControl RC1e 5.0 is used for data evaluation.

7.3 Dynamic Model of Charged-Microgel Synthesis and Parameter Determination

The structure and assumptions of the developed kinetic synthesis model of the NIPAM-*co*-MAA polymerization is presented in Section 7.3.1. Next, Section 7.3.2 describes the calculation of missing parameter values for the reaction enthalpies and the reaction rates via quantum mechanical calculations. Finally, Section 7.3.3 reports the setup of the parameter estimation problem based on the quantum mechanical calculations and experimental data.

7.3.1 Kinetic Synthesis Model

The presented dynamic model extends previous works on microgel synthesis modeling [66–69]. The assumptions derived therein are essentially:

- The dispersed system can be approximated by a pseudo-homogeneous phase.
- The kinetics of the initiator reaction are the same as the propagation reaction kinetics of an active polymer chain with the main monomer as the end type and the main monomer.
- The kinetics of the propagation reactions depend only on the type of radical at the end of the chain.
- The kinetics of the cross-linking reaction are as fast as the kinetics of a propagation reaction with a BIS monomer.
- The kinetics of termination reactions are diffusion-limited; thus, they do not depend on the terminal end of the active radical chains.
- Chain transfer reactions are negligible.
- The system is strongly diluted, which implies, that the volume, total mass, and heat capacity of the reactor content are equal to the corresponding properties of the solvent.

Table 7.1: Reaction mechanism with associated reaction rate coefficients (k_m), where m is the type of reaction and the partaking reactants. The indices i and j describe the reactants as NIPAM $i,j=1$, BIS $i,j=2$ MAA $i,j=3$, and MAA$^-$ $i,j=3\mathrm{d}$. PDB stands for pending double bond, and X denotes a completed cross-link.

Type of reaction	Mechanism
Decomposition	$\mathrm{I} \xrightarrow{k_\mathrm{d}} 2f\mathrm{R}^0_\bullet$
Chain initiation	$\mathrm{R}^0_\bullet + \mathrm{M}_j \xrightarrow{k_{\mathrm{p}1j}} \mathrm{R}^\mathrm{n}_\mathrm{j}$
Propagation of monomer ($i,j=\{1,3,3\mathrm{d}\}$)	$\mathrm{R}^n_i + \mathrm{M}_\mathrm{j} \xrightarrow{k_{\mathrm{p}ij}} \mathrm{R}^{n+1}_j$
	$\mathrm{R}^n_2 + \mathrm{M}_\mathrm{j} \xrightarrow{k_{\mathrm{p}2j}} \mathrm{R}^{n+1}_j$
Propagation of cross-linker ($i,j=\{1,3,3\mathrm{d}\}$)	$\mathrm{R}^n_i + \mathrm{M}_2 \xrightarrow{k_{\mathrm{p}i\mathrm{CL}}} \mathrm{R}^{n+1}_\mathrm{CL} + \mathrm{PDB}$
	$\mathrm{R}^n_2 + \mathrm{M}_2 \xrightarrow{k_{\mathrm{p}22}} \mathrm{R}^{n+1}_2 + \mathrm{PDB}$
Cross-linking	$\mathrm{R}^n_i + \mathrm{PDB} \xrightarrow{k_{\mathrm{p}i2}} \mathrm{R}^{n+1}_i + \mathrm{X}$
Termination	$\mathrm{R}^n_i + \mathrm{R}^m_\mathrm{j} \xrightarrow{k_\mathrm{t}} \mathrm{P}^n + \mathrm{P}^m$

The model presented in the current study includes the decomposition of the initiator, the propagation reactions between an active radical chain and the monomers, the cross-linking reaction between a pendant double bond (PDB) and an active radical chain, and a termination reaction between two active radical chains. The reaction system is shown in Table 7.1. Here, k_m (in $\mathrm{m^3\,mol^{-1}\,s^{-1}}$) generally represents the reaction rate coefficient in each type of reaction m.

Further assumptions are included regarding the functional co-monomer MAA:

- No secondary reactions such as backbiting occur with MAA polymerization [165, 166].
- The chain transfer to monomer MAA is negligible, as the constant $C_{\mathrm{tr,mon}} = \frac{k_{\mathrm{tr,mon}}}{k_\mathrm{p}} = 5.37 \times 10^{-5}$ [165] indicates that the kinetic rate of the transfer reaction is five orders of magnitude smaller than the propagation rate of MAA.
- The initiator efficiency is assumed to be constant over the course of the reaction, similarly to previous studies [69, 171, 172].

The kinetic model based on the listed assumptions is presented in Equations (7.1a) to (7.1g). Generally, the kinetic model equations presented by Jung et al. [66, 67] are extended to account for introducing the functional monomers MAA and its dissociated state MAA$^-$. The newly arising model equations are presented below, while the full model description is reported in Appendix B.2. Here, the time dependence (t) is omitted for improved readability.

Eq. (7.1a) describes the initiator decomposition rate k_d in form of the Arrhenius expression with $k_{\mathrm{d},0}$ (in $\mathrm{s^{-1}}$) as the pre-exponential factor, T (in K) as the temperature in the reactor, R_gas as the ideal gas constant ($8.3145\,\mathrm{J\,mol^{-1}\,K^{-1}}$), and E (in $\mathrm{J\,mol^{-1}}$) as the activation energy. The initiator decomposition depends on the temperature of the solution, while the pH dependency is negligible. This assumption is based on the insignificant change at 80°C from $k_\mathrm{d} = 6.9 \times 10^{-5}\,\mathrm{s^{-1}}$ at pH 7 to $k_\mathrm{d} = 9.2 \times 10^{-5}\,\mathrm{s^{-1}}$ at pH 13 [173]. Further, Lin et al. [174] could not observe a significant change in

polymerization rate with changing pH value for the solution polymerization of acrylamide using KPS as an initiator. Similarly, Preusser et al. [172] omitted the pH dependency of the initiator KPS in their kinetic model for the acrylamide polymerization. Further, the rate of propagation of the initiator radicals is equal to the rate of initiation in Equation (7.1b). Here, c_i represents the concentration (in $\mathrm{mol\,m^{-3}}$) of the respective component, f is the initiator efficiency, and R_i (in $\mathrm{mol\,m^{-3}\,s^{-1}}$) is the reaction rate.

A mass balance equation is derived for the total mass of MAA, including dissociated (M3d) and not dissociated MAA (M3) in Equation (7.1c). This pseudo-co-polymerization of dissociated and not dissociated MAA approach was originally introduced by Shoaf and Poehlein [161]. In the presented model, the amount of MAA radicals is balanced in Equation (7.1d). In Equation (7.1e), the total amount of MAA (dissociated and not dissociated) in the system is then calculated. The amount of dissociated MAA is calculated via the dissociation degree α^{diss} in Equation (7.1f). Here, α^{diss} depends on the pH value of the solution and the pKa value of MAA and is calculated in Equation (7.1g). Furthermore, an equilibrium of dissociation is assumed. As MAA has a pKa value of 4.65 [151], MAA is considered a weak acid. Furthermore, the concentration of MAA in the solution is very little (see Table 5.1). Thus, $\mathrm{Ka} = \frac{[\mathrm{H_3O^+}]\cdot[\mathrm{MAA^-}]}{[\mathrm{MAA_{total}}]}$ holds for the synthesis system. With the definition $\mathrm{pH} = -\log[\mathrm{H_3O^+}]$ and the correlation $\mathrm{Ka} = 10^{-\mathrm{pKa}}$, Equation (7.1g) is derived. Previously, it was found that the pKa value changes during the polymerization of MAA. For the pKa value of polymerized MAA, a value of 4.8 was reported by Singh et al. [36]. Buback et al. [167] explain the difference in pKa value of the polymerized MAA due to the "exchange of hydrogen cations as well as counterions during polymerization". For the kinetic model of the NIPAM-BIS-MAA synthesis in this chapter, the change in pKa is considered negligible, as the resulting model is insensitive to changes in the pKa parameter values.

The derived model equations include:

$$k_{\mathrm{d}} = k_{\mathrm{d},0} \cdot \exp\left(-\frac{E}{R_{\mathrm{gas}} \cdot T}\right) \tag{7.1a}$$

$$\dot{c}_{\mathrm{R}} = 2 f k_{\mathrm{d}} c_{\mathrm{I}} - R_{\mathrm{R1}} - R_{\mathrm{R2}} - R_{\mathrm{R3}} - R_{\mathrm{R3d}}, \tag{7.1b}$$

$$\begin{aligned}\dot{c}_{\mathrm{M3,tot}} = &- R_{\mathrm{p13}} - R_{\mathrm{p23}} - R_{\mathrm{p33}} - R_{\mathrm{p3d3}} - R_{\mathrm{p13d}} - R_{\mathrm{p23d}} \\ &- R_{\mathrm{p33d}} - R_{\mathrm{p3d3d}},\end{aligned} \tag{7.1c}$$

$$\begin{aligned}\dot{c}_{\mathrm{R3,total}} = &R_{\mathrm{R3}} + R_{\mathrm{R3d}} + R_{\mathrm{p13}} + R_{\mathrm{p23}} + R_{\mathrm{p13d}} + R_{\mathrm{p23d}} \\ &- R_{\mathrm{p31}} - R_{\mathrm{p32}} - R_{\mathrm{p3d1}} - R_{\mathrm{p3d2}} - k_{\mathrm{p32}} c_{\mathrm{R3}} c_{\mathrm{PDB}} \\ &- k_{\mathrm{p3d2}} c_{\mathrm{R3d}} c_{\mathrm{PDB}} - R_{\mathrm{t3}} - R_{\mathrm{t3d}},\end{aligned} \tag{7.1d}$$

$$c_{\mathrm{M3,total}} = c_{\mathrm{M3}} + c_{\mathrm{M3d}}, \tag{7.1e}$$

$$c_{\mathrm{M3d}} = c_{\mathrm{M3,total}} \cdot \alpha^{\mathrm{diss}}, \tag{7.1f}$$

$$\alpha^{\mathrm{diss}} = 10^{-\mathrm{pKa+pH}}. \tag{7.1g}$$

Here, $R_{\mathrm{p}ij}$ is defined as $k_{\mathrm{p}ij} c_{\mathrm{R}i} c_{\mathrm{M}j}$ and $R_{\mathrm{R}j}$ as $k_{\mathrm{p1}j} c_{\mathrm{R}} c_{\mathrm{M}j}$. Furthermore, $R_{\mathrm{t}i}$ is computed as $k_{\mathrm{t}} c_{\mathrm{R}i} \cdot \left(2 c_{\mathrm{R}i} + \sum c_{\mathrm{R}j}\right)$ with $j \neq i$.

7.3.2 Quantum Mechanical Calculations of Polymerization Enthalpies and Reaction Rates

To calculate parameter values for reaction rate coefficients $k_{\mathrm{p}ij}$, we use conventional transition state (TS) theory described in our previous works [14, 154]. We start by splitting the reaction rate coefficient

into two contributions, the gas and solution phase parts, which allows for separate calculations of gas-phase geometries and energies first, followed by incorporating solvation effects.

The gas phase reaction rates constants are obtained using the TAMkin software [175] with the rigid rotor harmonic oscillator (RRHO) approximation and Eckart tunneling correction. The molecular geometric structures and frequencies of TSs, reactants, and products are computed using the B3LYPD3/TZVP [176, 177] level of theory with an ultrafine grid and D3BJ [178] dispersion correction using GAUSSIAN16 [179], while the single-point energy calculations are performed at the B2PLYPD3/aug-cc-pVTZ level of theory using TURBOMOLE [180]. To investigate a wide range of TS conformations, dihedral scans around the new formed bond were conducted at the B3LYPD3/TZVP level of theory. Furthermore, intrinsic reaction coordinate (IRC) calculations were carried out at the B3LYPD3BJ/TZVP level to validate the connectivity of transition states between the desired reactants and products. For each reaction, all identified conformers of transition states are taken into consideration, and the final reaction rate is then obtained as the sum of the individual reaction rates.

To account for solvation effects, we estimate the solvation Gibbs free energies utilizing COSMO-RS theory [181–183]. Reactant and product geometries are optimized using COSMOconf [184], while transition state geometries are optimized using TURBOMOLE [180] at the BP-TZVP-COSMO level of theory. Once the geometries are determined, the solvation Gibbs free energies are calculated using COSMOtherm [185] at the reference state of a pure ideal gas at a concentration of $1\,\mathrm{mol\,L^{-1}}$, with the solute dissolved at infinite dilution and a reference concentration of $1\,\mathrm{mol\,L^{-1}}$.

Similarly to reaction rates, the reaction enthalpies are computed separately for the gas phase at B2PLYPD3BJ/aug-cc-pVTZ//B3LYPD3BJ/TZVP level of theory and solution phase at BP-TZVP-COSMO level of theory. The gas phase reaction enthalpies are calculated using TAMkin [175], and the solvation Gibbs free energies are obtained using COSMOtherm [185]. To approximate the derivative in the Gibbs-Helmholtz equation, we employ a first-order central finite difference scheme with a temperature step of 1 K. Finally, we use the Gibbs-Helmholtz equation, combining both gas and solution phase contributions, to calculate the missing parameter values for reaction enthalpies $\Delta H_{\mathrm{R}ij}$.

The method of Gaussian error propagation is employed to establish the confidence intervals for the $\Delta H_{\mathrm{R}ij}$ values. A detailed description of this methodology can be found in earlier studies [14, 154]. The method is based on the assumption that there are two primary independent contributions to the error, coming from the gas and solution calculations.

7.3.3 Determination of Parameter Values of the Dynamic Model

The model parameters of the proposed model (see Equations (7.1a) to (7.1g)) include $k_{\mathrm{d},0}$, E, f, pKa of MAA, $k_{\mathrm{p}ij}$, $\Delta H_{\mathrm{R}ij}$, and k_{t}. In the following paragraphs, the parameter values used in the model are outlined. The values are either derived from the literature, calculated via quantum mechanical calculations (Section 7.3.2), or estimated via regression (parameter estimation). For the estimation, the upper and lower bounds and the start values of the parameters in the estimation problem are highlighted.

The decomposition of the initiator KPS was studied extensively by Costa et al. [186]. Their work reports values for the decomposition rate coefficient $\mathrm{k_d}$ with $\ln\left(k_{\mathrm{d},0}\right) = 59 \pm 8$ for $k_{\mathrm{d},0}$ in $\mathrm{h^{-1}}$ and $E = 176 \pm 22\ \mathrm{kJ\,mol^{-1}}$. These parameter values are incorporated into the kinetic model for Equation (7.1a). For the initiator efficiency f, a value of 0.8 was previously proposed by Preusser et al. [172].

Table 7.2: Polymerization enthalpies $\Delta H_{\mathrm{R}ij}$ and kinetic rate coefficients $k_{\mathrm{p}ij}$ of the NIPAM/BIS system at 70°C [68].

Reaction	$\Delta H_{\mathrm{R}ij}$ ($\mathrm{kJ\,mol^{-1}}$) [154]	$k_{\mathrm{p}ij}$ ($\mathrm{m^3\,mol^{-1}\,s^{-1}}$) [68]
NIPAM radical / NIPAM	-87.5	1.69
NIPAM radical / BIS	-89.3	1.86
BIS radical / BIS	-77.8	338
BIS radical / NIPAM	-81.7	42.3

For the NIPAM/BIS system, parameter values for the kinetic rate coefficient and polymerization enthalpies are provided by Schneider et al. [68]. The system was extensively investigated in the past, and parameter values via quantum chemistry calculations [154] and parameter estimation [66] are generated. The parameter values are listed in Table 7.2 for a reactor temperature of 70°C.

The pKa value of MAA is well studied; thus, it is set to 4.65 [151] in the synthesis model. However, as stated previously, no reliable parameter values for the propagation reactions involving MAA (or even MAA$^-$) are available. The propagation rates of the NIPAM/MAA system have been analyzed by Ponratnam et al. [170], Brazel et al. [168], Xue et al. [169], and Hoare et al. [83, 84]. The provided values in the literature diverge significantly, as exemplified by the reactivity ratios presented in Table 7.3. Note that Ponratnam et al. [170] also provide reactivity ratios of the NIPAM/MAA system at different pH values. Here, the reactivity ratios of the NIPAM/MAA system are defined as

$$r_1 = \frac{k_{\mathrm{pNIPAM,NIPAM}}}{k_{\mathrm{pNIPAM,MAA}}}, \tag{7.2a}$$

$$r_2 = \frac{k_{\mathrm{pMAA,MAA}}}{k_{\mathrm{pMAA,NIPAM}}}. \tag{7.2b}$$

Due to the insufficient certainty of the parameter values regarding the NIPAM/MAA system, the literature values are not included in the proposed model.

The propagation rates of (non-)ionized MAA homopolymerization are studied extensively in the literature [163, 166, 167]. However, the derived parameter values for the MAA homopolymerization are not applicable for the microgel synthesis considered here, as the temperature and concentration range differ significantly.

Table 7.3: Reactivity ratios for the NIPAM/MAA system presented in the literature.

Reference	r_1	r_2
Ponratnam et al. [170]	0.20	2.8
Brazel et al. [168]	0.891	1.128
Xue et al. [169]	10.2±1.4	0.01± 0.03

The termination rate k_{t} in the homopolymerization of MAA has been studied experimentally in the past [163]. For the MAA homopolymerization, Buback et al. [167] found that k_{t} strongly depends on the degree of ionization. However, as previously stated, the presented model relies on the assumption of diffusion-limited termination; thus, the pH dependency is not included in the termination rate coefficient but influences the reaction outcome via the shift in equilibrium between MAA and MAA$^-$ (see Equation (7.1g)). Also, due to the assumption of diffusion-limitation, it is impossible to measure or explicitly calculate the termination rate k_{t} via quantum mechanical calculations. Hence, for the parameter estimation, arbitrary and relatively large bounds of $1.00 \times 10^{-5}\,\mathrm{m^3\,mol^{-1}\,s^{-1}}$ and $1.00 \times 10^{5}\,\mathrm{m^3\,mol^{-1}\,s^{-1}}$ and an initial value of $8.7967\,\mathrm{m^3\,mol^{-1}\,s^{-1}}$ based on previously estimated values for k_{t} in the context of the NIPAM/BIS synthesis [68] are included.

For the parameter estimation, the results of quantum mechanical calculations are incorporated to determine the parameter values of $\Delta H_{\mathrm{R}ij}$ and $k_{\mathrm{p}ij}$, as described in Section 7.3.2. Generally, polymerization models have multiple parameters which cannot be determined using the available measurements; the reader is referred to previous publications [66, 187] for discussion of this non-identifiable parameter estimation. Therefore, reducing the amount of parameter values to be estimated is beneficial. The reduction is achieved in terms of incorporation of parameter values of high certainty (e.g., well-studied parameters from the literature) or by using suitable measurement data to estimate sub-sets of the parameters. Furthermore, good start values and reasonable parameter bounds for the estimation problem are crucial. As shown in previous work [9, 14], it is beneficial to include parameters calculated via quantum mechanical calculations and the respective calculation confidence intervals as bounds in the parameter estimation to improve the fit between simulation and experiment.

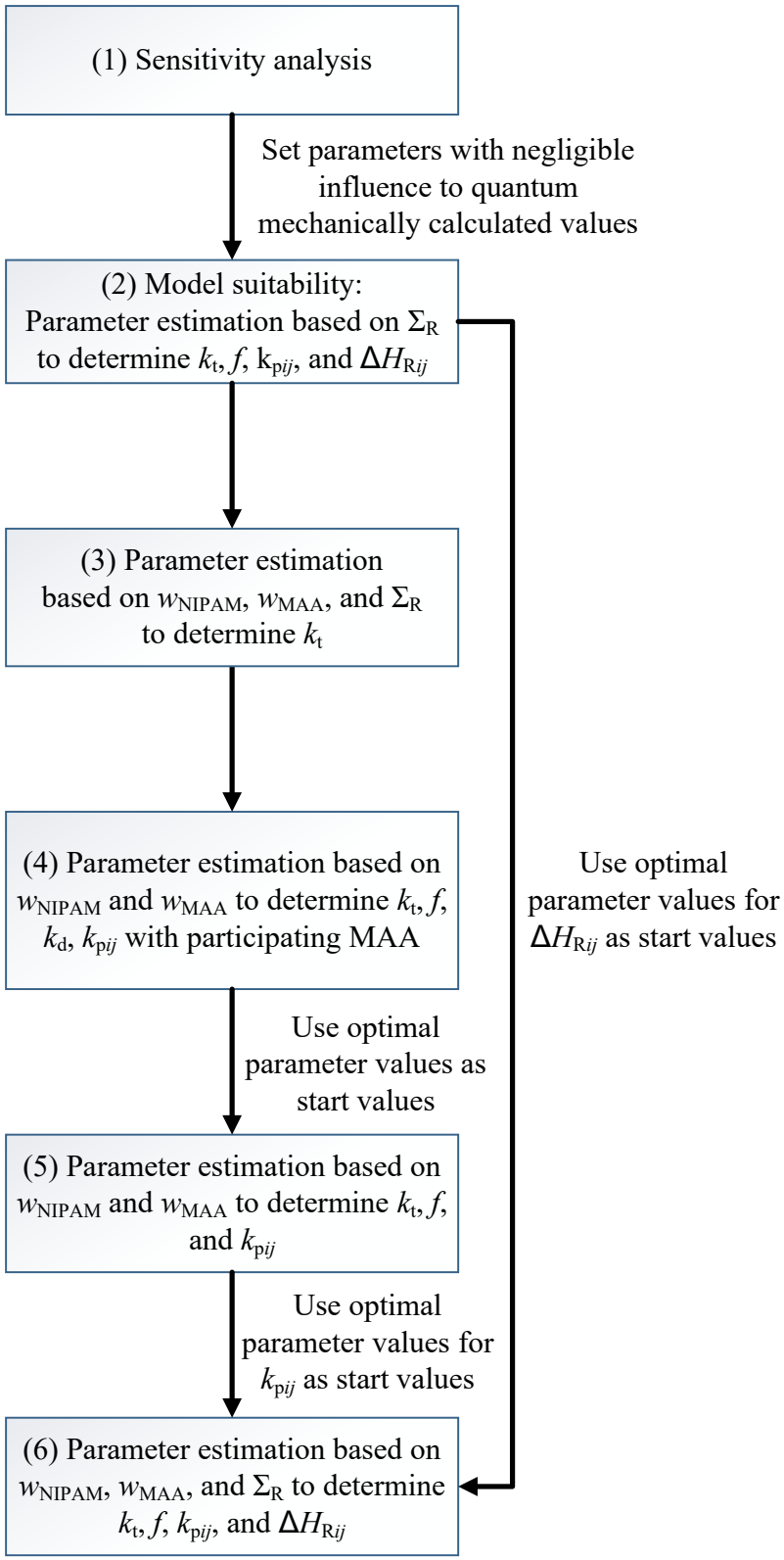

Figure 7.1: Schematic diagram of the conducted steps for estimating parameter values.

The procedure for including the quantum mechanically calculated values and estimating missing values meaningfully is outlined in Figure 7.1. The proposed procedure allows meaningful integration of well-studied and quantum mechanically calculated parameter values while deriving appropriate start values for the parameter estimation optimization problem. First, in Step 1, the parameter values that affect the model outcome most significantly are determined in a sensitivity analysis (Section 7.4.2.1). Propagation rates and enthalpies of polymerization that have a minor influence on the model outcome are set directly to the quantum mechanically calculated values. To assess the suitability of the proposed model structure to represent the experimental data (Step 2), a parameter estimation study is conducted, allowing all parameter values to change to suit the calorimetric measurements of the enthalpy transfer rate Σ_R (Section 7.4.2.2). For this suitability test,the parameter values for each experimental setting (5, 10, and 15 mol% content of MAA in the microgel) are estimated individually.

After the suitability of the model structure is established, a benchmark is determined in Step 3 by setting all parameters to the quantum mechanically determined values and solely estimating the remaining parameter k_t. For that, k_t is estimated first based on each experimental setting individually (5, 10, and 15 mol% MAA). After that, the results of the individual estimations are used for an estimation based on all experimental settings combined.

Next, the experimental data regarding the weight fractions of NIPAM and MAA (w_NIPAM and w_MAA) during the synthesis are used to estimate f, $k_{\mathrm{p}ij}$ of all reactions involving MAA, and k_t in Step 4 (Section 7.4.2.3). The upper and lower bounds of the $k_{\mathrm{p}ij}$ are based on the quantum mechanically calculated values and their respective uncertainty interval. Note that although Preusser et al. [172] provide a suitable value for f, they also reference the works of Kim et al. [171] suggesting to decrease the initiator efficiency of KPS to 0.2. Thus, the proposed values are included as upper and lower bound in the parameter estimation problem. In addition, the parameter values of the intensively studied NIPAM/BIS system are set to the values presented in Table 7.2 to reduce the number of parameter values to be estimated in Step 4.

In Step 5, the parameter values for k_t, f, and $k_{\mathrm{p}ij}$ are then estimated based on w_NIPAM and w_MAA for each experimental setting individually (Section 7.4.2.3). The start values are either derived from the previous estimation step or taken from the quantum mechanically calculated values. Next, the parameter values from the individual estimation are used as start values for the estimation based on all available experimental settings combined.

Finally, the outcome of the previously described estimation based on w_NIPAM and w_MAA and the model suitability study based on Σ_R are combined in Step 6 (Section 7.4.2.4). The previously derived optimal parameter values serve as starting points in the estimation. Based on all measurements, k_t, f, $k_{\mathrm{p}ij}$, and $\Delta H_{\mathrm{R}ij}$ are estimated.

Mathematically, the problem formulation of the parameter estimation in all cases is expressed as the weighted residual between model predictions and available measurements:

$$\min_{\mathbf{p}\in P} \quad \sum_{i=1}^{N^\mathrm{meas}} \sum_{j=1}^{N^\mathrm{t}} \frac{1}{s_{i,j}} \left| z_i^\mathrm{pred}\left(t_j;\mathbf{p}\right) - z_i^\mathrm{meas}\left(t_j\right) \right|. \tag{7.3}$$

Here, $\mathrm{z_i^{meas}}\left(t_j\right)$ is a measurement of all available measurements N^meas, e.g., Σ_R, w_NIPAM or w_MAA, with respective standard deviations $s_{i,j}$ at times $t_j \in [t_0, t_\mathrm{f}]$ with $j = 1, ..., N^\mathrm{t}$ (total number of discrete time points). The model predictions at times t_j are symbolized by z_i^pred and depend on the model parameters $\mathbf{p}$. For the parameter estimation, previously developed framework implemented in MATLAB [66] is used. Within this framework, the dynamic optimization tool DyOS [188] is used to integrate the system of differential-algebraic equations to compute z_i^pred. Specifically, the integrator NIXE [189] is applied with 1×10^{-6} absolute and relative tolerance. The synthesis model is implemented in the software Dymola [190] and is incorporated in DyOS as a functional mock-up unit

(FMU) [191]. By minimizing the weighted residual between the measurements and model (Equation (7.3)), an optimal set of parameter values is determined. This dynamic optimization problem involves a highly nonlinear synthesis model and multiple constraints on the parameter values. Therefore, the problem becomes challenging to solve. Furthermore, global optimization is essential to ensure optimal parameter values are found, providing the best alignment of simulated and experimental outcomes. The optimization problem is solved globally by incorporating the enhanced scatter-search method implemented in the open-source software for dynamic optimization MEIGO [192], similar to previous works [66]. In MEIGO, the dynamic hill climbing method [193] is implemented as a local solver. Altogether, the MEIGO-generated solutions are global but non-deterministic. Thus, global convergence is not secured but by allowing longer CPU times the likelihood of global optimality increases.

7.4 Results and Discussion

The results comprise the parameter values calculated via quantum mechanical calculations (Section 7.4.1) and the parameter estimation results (Section 7.4.2). The full model and the data gathered within this Chapter are published with open access [141].

7.4.1 Reaction Enthalpies and Rate Coefficients Calculated via Quantum Mechanical Calculations

Table 7.4 shows the values for reaction enthalpies and kinetic rate coefficients calculated via quantum mechanical computations. For the reaction enthalpies where only neutral molecules are involved, the total error is estimated to be are determined to be $3.49\,\mathrm{kJ\,mol^{-1}}$ after combining the $3.26\,\mathrm{kJ\,mol^{-1}}$ [194] for the liquid phase and $1.25\,\mathrm{kJ\,mol^{-1}}$ [195] for the gas phase (see Table 7.5). Regarding charged molecules, the total error is estimated to be $10.16\,\mathrm{kJ\,mol^{-1}}$ culminating the uncertainties $3.26\,\mathrm{kJ\,mol^{-1}}$ in the gas phase (assuming the same value from the neutral molecule in the gas phase) and $9.62\,\mathrm{kJ\,mol^{-1}}$ [196] in the liquid phase. For the kinetic rate coefficients where only neutral molecules are involved, the determined factor of the uncertainty interval is 8.379 at temperature 343 K [14, 154, 197]. This factor is estimated after combining the uncertainty of the solvation free energies predicted with COSMO-RS $1.25\,\mathrm{kJ\,mol^{-1}}$ [194] and of the gas phase energies predicted at double hybrid density functional theory (DFT) methods $3.26\,\mathrm{kJ\,mol^{-1}}$ [195]. In case of the reactions where charged species are involved, the factor is estimated at 478.5 since the error contribution of the solvation free energies is $9.62\,\mathrm{kJ\,mol^{-1}}$ [196].

Table 7.4 reveals that the absolute polymerization enthalpy values of reactions including MAA^- are smaller than for not dissociated MAA except for the reaction of an MAA^- with either species. Furthermore, all reactions including MAA^- have propagation rate coefficients in the order of magnitude between 1×10^{-6} to 1×10^{-20} and can thus be considered rather insignificant. Due to the slow reaction kinetics of MAA^-, the reaction of undissociated MAA is more likely to occur. The highest reaction rate coefficients are for MAA with a radical NIPAM or BIS end with $4.08 \times 10^{1}\,\mathrm{m^3\,mol^{-1}\,s^{-1}}$ and $1.56\,\mathrm{m^3\,mol^{-1}\,s^{-1}}$, respectively.

7.4.2 Parameter Estimation

From the quantum mechanical calculations in Section 7.4.1, it is derived that the propagation rate of the reaction between MAA^- and another MAA^- molecule is extremely slow ($1.16 \times 10^{-20}\,\mathrm{mol\,m^{-3}\,s^{-1}}$, see Table 7.4). Therefore, the reaction is considered negligible for the kinetic model and parameter

Table 7.4: Polymerization enthalpies and propagation rate coefficients at the B2PLYPD3BJ/aug-cc-pVTZ//B3LYPD3BJ/TZVP and BP-TZVP-COSMO level of theory in infinite diluted aqueous solution at T=343 K.

Reaction	$\Delta H_{\mathrm{R}ij}$ ($\mathrm{kJ\,mol^{-1}}$)	$k_{\mathrm{p}ij}$ ($\mathrm{m^3\,mol^{-1}\,s^{-1}}$)
MAA radical / BIS	-57.3 ± 3.49	3.54×10^{-2}
MAA radical / MAA	-63.7 ± 3.49	5.64×10^{-1}
MAA radical / MAA$^-$	-27.4 ± 10.16	6.48×10^{-10}
MAA radical / NIPAM	-57.7 ± 3.49	1.21×10^{-1}
MAA$^-$ radical / BIS	-16.2 ± 3.49	1.08×10^{-7}
MAA$^-$ radical / MAA	-37 ± 3.49	1.34×10^{-6}
MAA$^-$ radical / MAA$^-$	-65.8 ± 10.16	1.16×10^{-20}
MAA$^-$ radical / NIPAM	-42.9 ± 10.16	1.03×10^{-7}
NIPAM radical / MAA	-85.8 ± 3.49	4.08×10^{1}
NIPAM radical / MAA$^-$	-31.2 ± 10.16	3.76×10^{-8}
BIS radical / MAA	-76.5 ± 3.49	1.56
BIS radical / MAA$^-$	-27.5 ± 10.16	7.12×10^{-9}
NIPAM radical / BIS	-89.3 ± 3.49	1.03×10^{3}
NIPAM radical / NIPAM	-87,5 ± 3.49	5.99×10^{2}
BIS radical / NIPAM	-81.7 ± 3.49	9.99
BIS radical / BIS	-77.8 ± 3.49	8.10

estimation. Furthermore, the experimental analysis indicates that the pH value changes significantly during the reaction and can not be considered constant. The in-line pH measurements and the resulting dissociation degree during the synthesis of charged NIPAM-*co*-MAA microgels are shown in Appendix B.1. The varying measured pH values are included as piecewise constant input to the model for the parameter estimation.

7.4.2.1 Sensitivity Analysis

The sensitivity analysis of the parameter values in the model reveals that the propagation rate coefficients and the polymerization enthalpies involving the dissociated MAA exhibit a negligible impact on the model predictions (see Appendix B.3). This finding is attributed to the low concentration of dissociated MAA under the studied conditions. Consequently, only the parameters without the participation of dissociated MAA are included in the parameter estimation study. In the subsequent estimations, the propagation rate coefficient and polymerization enthalpy parameter values, including dissociated MAA, are fixed to the value calculated via quantum mechanical methods (see Table 7.4).

Table 7.5: Error of polymerization enthalpies.

	Error of $\Delta H_{\mathrm{R}ij}$			
	neutral	Ref.	charged	Ref.
gas	3.26	[198]	3.26*	[198]
liquid	1.25	[194]	9.62	[196]
	3.49		**10.16**	

* Assuming error in gas phase is the same for gas and liquid conditions.

7.4.2.2 Model Suitability

The model suitability study reveals that the model structure can cover the progression of the enthalpy transfer rate during the synthesis (see Figure 7.2). The underlying optimal parameter values are tabulated in Appendix B.4.1. For the suitability analysis, all parameter values (k_t, k_d, f, all propagation rate coefficients k_{pij} and polymerization enthalpies ΔH_{Rij} excluding dissociated MAA) are allowed to change. Note that the parameter bounds for $\Delta H_{NIPAM\text{-}NIPAM}$ and $\Delta H_{BIS\text{-}BIS}$ have to be adjusted to allow a suitable fit (see Appendix B.4.1). Further, the parameter estimation is conducted solely based on the enthalpy transfer rates Σ_R, as this progression is more challenging to cover than the weight fractions of the monomers. In the process, each experimental setting (5, 10, or 15 mol%) is individually used in the estimation. The resulting fit of experimentally and computationally determined Σ_R indicates that the model structure can cover the general trends qualitatively and quantitatively with adjusted parameter values. Furthermore, the experimental Σ_R progressions (see Figure 7.2) reveal that with increasing MAA content in the synthesis, the second peak in time and the overall enthalpy transfer diminish.

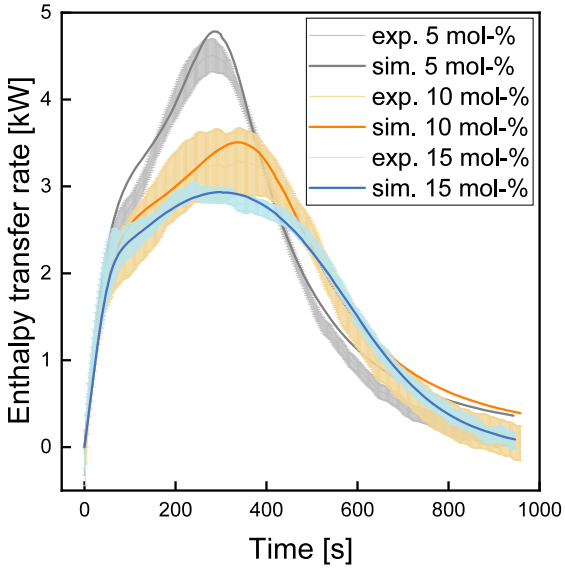

Figure 7.2: Simulation and experimental results for the synthesis of microgels with 5 mol% to 15 mol% MAA content.

7.4.2.3 Estimation Based on Weight Fractions

The available measurements are split and only the weight fraction predictions of NIPAM and MAA are used for estimating kinetic rates in the subsequent studies. The parameter values for each experimental setup are estimated first individually and then for all experiments together. Note that due to the significant difference in quantum mechanically calculated parameter values for the NIPAM/BIS system in this work and previous works [68], the upper and lower bounds for the respective parameter values are increased for the parameter estimations here. Furthermore, the conducted parameter estimation study in Step 4 serves for the determination of suitable start values exclusively and is not elaborated on in detail here.

When estimating the parameter values based on each experimental setup (5 mol% to 15 mol% of MAA in the microgel) individually (see Figure 7.3), the resulting fit is appropriate. Also, when estimating based on all experimental setups combined (see Figure 7.4 for estimation with start values

from the 10 mol% individual estimation, or Appendix B.4.3 for the remaining cases) the fit is satisfying. Note that for the combined case, different estimation runs are conducted by changing the start values of the estimation to the values obtained in the estimation of each individual setup. Although the allowed CPU time is set to 200 000 s, the estimated optimal parameter values differ slightly depending on the start values incorporated (see Appendix Table B.5). Furthermore, Figures 7.3(b) and 7.4(b) reveal that the model prediction lacks to cover the progression of w_{MAA} during the 5 mol% MAA microgel synthesis. The small amount of MAA present during this synthesis setting complicates the Raman monitoring (as indicated by the high measurement standard deviation in Figure 5.11) and hinders a better fit. Thus, although the fit of the experiment and simulation does not fully agree, the model prediction is considered sufficient.

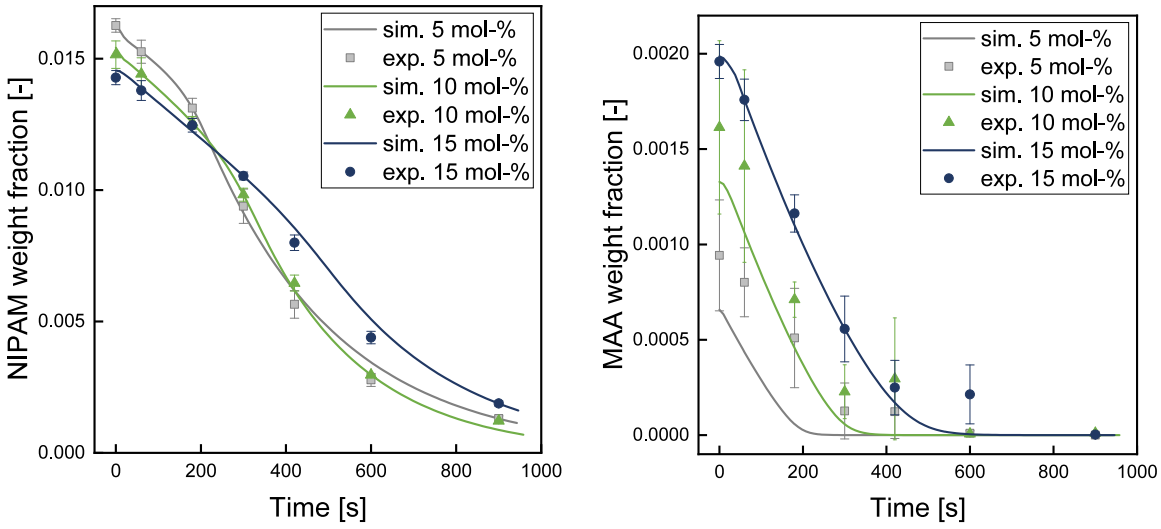

(a) Weight fraction NIPAM (w_{NIPAM})

(b) Weight fraction MAA (w_{MAA})

Figure 7.3: Results of estimation using only the weight fractions and estimating based on each experiment individually.

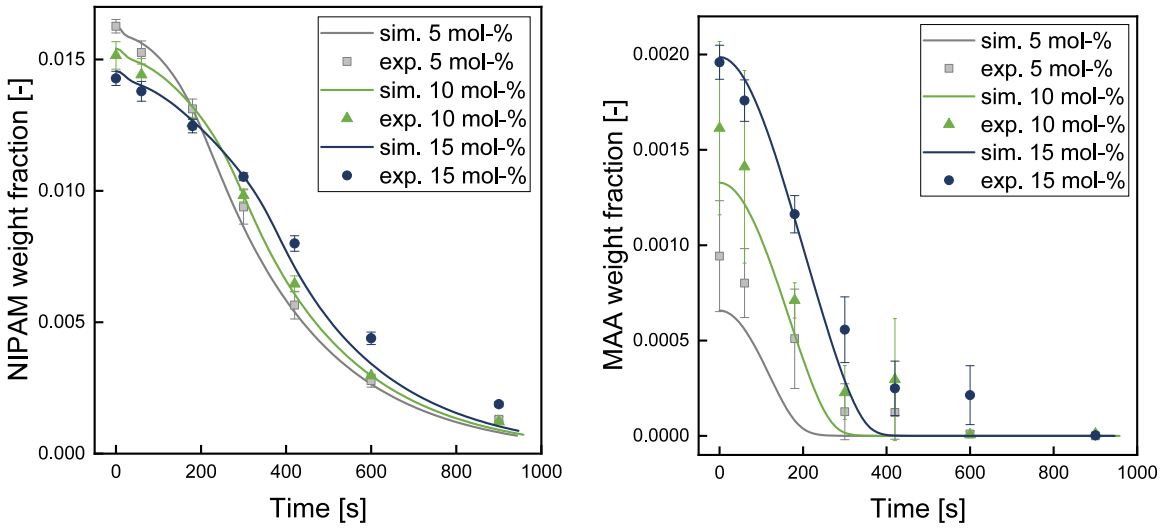

(a) Weight fraction NIPAM (w_{NIPAM})

(b) Weight fraction MAA (w_{MAA})

Figure 7.4: Results of estimation using only the weight fractions and estimating based on all experiments together, using the results of the individual estimation with 10 mol% MAA as the start values.

7.4.2.4 Estimation Based on Enthalpy Transfer Rates and Weight Fractions

The polymerization enthalpies and kinetic rate coefficients are estimated within the bounds obtained by the quantum mechanical calculations (see Section 7.4.1). Exceptions are the reaction enthalpies of NIPAM radical / NIPAM and BIS radical / BIS, as in the suitability analysis it was determined that the bounds must be adapted (see Section 7.4.2.2). Also, the bounds on the propagation rate coefficient of the NIPAM/BIS system are adjusted as the kinetic rates from different studies diverge significantly. The numeric values for all parameter bounds are included in Table 7.6. The initial values for the kinetic rate coefficients are taken from the results of the estimation based on the weight fractions altogether (see Section 7.4.2.3). For the polymerization enthalpies, the initial values are taken from the suitability study.

Figure 7.5 presents the results of the estimation based on the measured enthalpy transfer rates and weight fractions, using the results of the previous estimation that used start values of 10 wt% (figures showing the results for the remaining start values are shown in Appendix B.4.4). The determined optimal parameter values for all start values are presented in Table 7.6. In comparison, the experimental data is shown, and the result of the estimation when only k_{t} is estimated, and all other parameter values are taken from quantum mechanical calculations or the literature. The resulting progressions in Figure 7.5 indicate that by using the error estimates from the quantum mechanical calculations, the fit can be significantly improved compared to the benchmark case (indicated by *ref.*). Especially the enthalpy transfer rate can not be sufficiently covered when only allowing k_{t} to change, as is demonstrated in Figure 7.5(c). The model is capable of predicting the progression of the enthalpy transfer rate during the microgel synthesis with 5 mol% MAA accurately. However, for the synthesis with higher amounts of MAA (10 and 15 mol%), the model over-predicts the enthalpy transfer rates at higher reaction times.

Table 7.6: Parameter estimation setup and optimal parameter values for estimation based on enthalpy transfer rate and weight fraction measurements combined from all experimental setups for the synthesis of microgels containing 5 mol% to 15 mol% MAA. Termination rate coefficient and propagation rate coefficients are provided in [$m^3mol^{-1}s^{-1}$].

Parameter	Optimization setup		Optimal parameter values		
	Lower bound	Upper bound	Start value 5 mol%	Start value 10 mol%	Start value 15 mol%
k_t	1.00E-05	1.00E+05	2.26E-01	2.29E-01	2.29E-01
f	2.00E-01	8.00E-01	2.18E-01	2.15E-01	2.16E-01
Propagation rate coefficients k_{pij}:					
NIPAM radical / MAA	4.87E+00	3.42E+02	8.52E+00	8.63E+00	8.63E+00
BIS radical / MAA	1.86E-01	1.31E+01	1.86E-01	1.86E-01	1.86E-01
MAA radical / NIPAM	1.44E-02	1.01E+00	1.79E-01	1.81E-01	1.81E-01
MAA radical / BIS	4.22E-03	2.97E-01	2.97E-01	2.97E-01	2.97E-01
MAA radical / MAA	6.73E-02	4.73E+00	6.73E-02	6.73E-02	6.73E-02
BIS radical / BIS	9.67E-01	2.83E+03	9.67E-01	9.67E-01	9.67E-01
BIS radical / NIPAM	1.19E+00	3.54E+02	3.54E+02	3.54E+02	3.54E+02
NIPAM radical / BIS	2.22E-01	8.63E+03	6.35E+01	6.43E+01	6.43E+01
NIPAM radical / NIPAM	2.02E-01	5.02E+03	8.78E-01	8.89E-01	8.89E-01
Polymerization enthalpies ΔH_{Rij}:					
MAA radical / MAA	6.02E+04	6.72E+04	6.72E+04	6.72E+04	6.72E+04
NIPAM radical / MAA	8.23E+04	8.93E+04	8.23E+04	8.23E+04	8.23E+04
MAA radical / NIPAM	5.42E+04	6.12E+04	5.42E+04	5.42E+04	5.42E+04
BIS radical / MAA	7.30E+04	8.00E+04	8.00E+04	8.00E+04	8.00E+04
MAA radical / BIS	5.38E+04	6.08E+04	6.08E+04	6.08E+04	6.08E+04
BIS radical / BIS	7.43E+04	9.13E+04	9.13E+04	9.13E+04	9.13E+04
BIS radical / NIPAM	7.82E+04	8.52E+04	8.52E+04	8.52E+04	8.52E+04
NIPAM radical / BIS	8.58E+04	9.28E+04	9.28E+04	9.28E+04	9.28E+04
NIPAM radical / NIPAM	5.38E+04	9.10E+04	6.10E+04	6.10E+04	6.10E+04

Notably, during parameter estimation, the parameter values for the polymerization enthalpies all reach the allowable bounds except for the NIPAM radical / NIPAM reaction. Together with the low sensitivity of the model overall concerning the polymerization enthalpies, this phenomenon indicates that the identifiability of these parameter values is deficient. Furthermore, the initiator efficiency is relatively low, with values around 0.22. A closer analysis of the derived propagation rate coefficients is presented in the following Section 7.4.2.5, including the comparison to literature values.

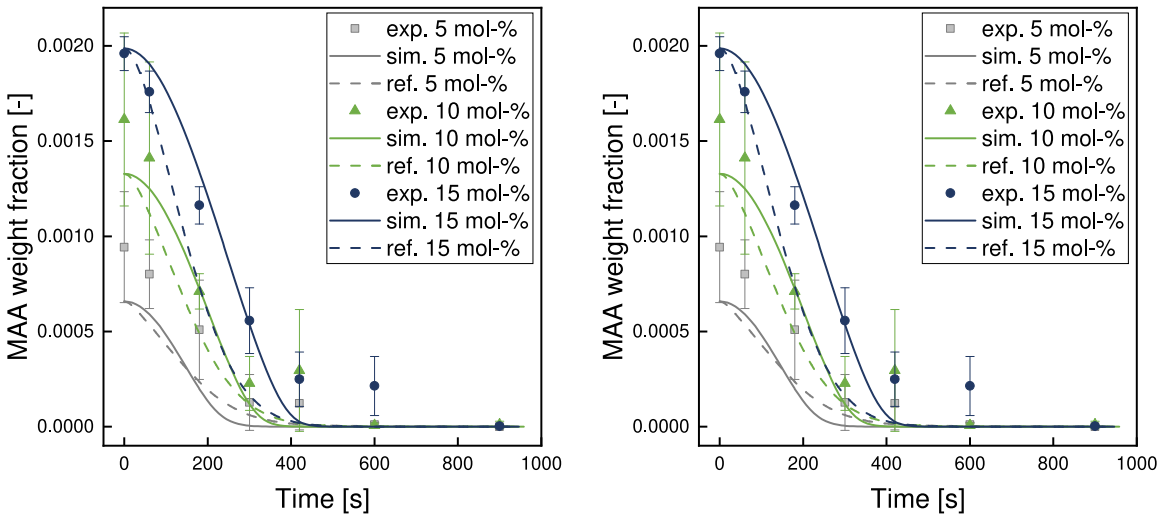

(a) Weight fraction NIPAM (w_{NIPAM})

(b) Weight fraction MAA (w_{MAA})

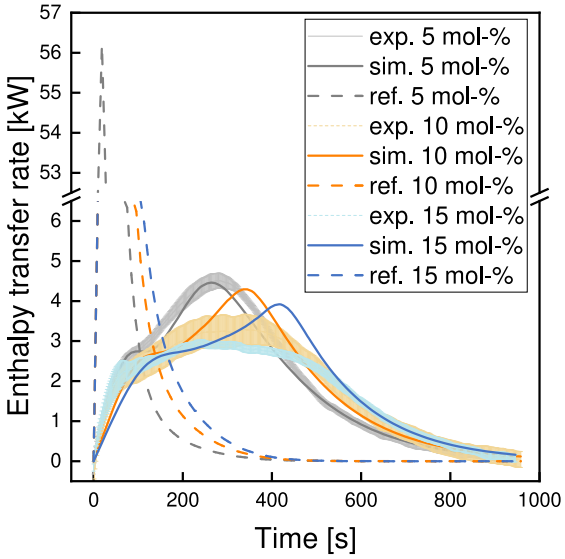

(c) Enthalpy transfer rate (Σ_{R})

Figure 7.5: Results of estimation using the weight fraction and enthalpy transfer measurements and estimating based on all experiment together. Using the start values from estimation based on 10 mol% MAA experiment start values.

7.4.2.5 Comparison to Literature Reactivity Values

When calculating the reactivity ratios for the NIPAM/MAA system based on Equations (7.2a) and (7.2b), the values $r_1 = 0.74$ and $r_2 = 1.24$ agree the most with the values proposed by Brazel et al. [168] (see Table 7.3). Thus, MAA will be favored in comparison to NIPAM during the polymerization. Furthermore, now the reactivity ratios can be calculated also for the BIS-MAA system. The reactivity ratios for the BIS-MAA system yield $r_1 = 1.14$ and $r_2 = 1.11$. Because of the similar reactivity ratios, MAA and BIS will be incorporated equally during the reaction.

7.5 Conclusions

This chapter provides valuable insights into the synthesis of charged microgels through a comprehensive approach of experimental and modeling studies. A dynamic synthesis model is extended to account for the pH dependence of the reaction kinetics. Combining experimental approaches and quantum mechanical computations allows estimating unknown parameter values based on the derived synthesis model. The systematic approach provides clariyfing insight into the reactivity ratios of NIPAM, MAA, and BIS, improving the system knowledge significantly.

Furthermore, the developed computational model presents a robust framework for predicting and optimizing the performance of charged microgels in diverse scenarios, paving the way for designing more efficient and tailored microgel-based systems for innovative applications, e.g., in drug-delivery systems. Future investigations face the extension of the dynamic synthesis model to also cover the particle growth of the charged microgels to enhance the predictive capabilities of the existing model. Also, experimental validation of the developed synthesis model will involve the synthesis of charged microgels with pH control to leverage the developed model.

8 Data-Driven Product-Process Optimization of *N*-isopropylacrylamide Microgel Flow-Synthesis

Data Repository: *The Raman spectra and polymer size predictions acquired in this chapter are published and available for free download via RWTH Publications [199].*

8.1 Motivation for Data-Driven Multi-Objective Optimization of Microgel Flow-Synthesis

The microgels' size and their ability to react reversibly to external stimuli of temperature, pH, or electrical potential in the surrounding medium [50] is highly relevant for their application. By definition microgels of any form exhibit an equivalent diameter between 0.1 µm to 100 µm in the swollen state [15]. The relevance of the microgel size has been studied for biomedical [37–39], phase separation [47–49], and catalysis [41] applications. Especially smaller microgels (diameters between 0.1 µm to 0.2 µm in the swollen state) have previously been applied for biomedical purposes, e.g., for drug delivery agents for medical uptake and release [38, 39] or implant coating [37]. In biomedical applications, microgels are particularly relevant, as their small size allows them to pass the human cell boundary [38]. For the cellular uptake, it was found that microgels of a hydrodynamic radius in the swollen state (at 20°C) above 400 nm and a cross-linker content above 10 mol % prevent microgel internalization.

The synthesis of microgels in flow reactors can overcome shortcomings of batch reactors, e.g., limited production capacity and downtime between batches, and enhances product development, intensifies production, and facilitates reaction scale-up [1, 51, 54, 55]. Furthermore, including process analytical technology in flow reactors allows in-line monitoring and process control under highly reproducible conditions [1, 55, 56]. Thus, continuous production enables the reliable synthesis of microgels.

To unfold the full potential of microgels, accelerating the development of tailor-made microgels is desirable. A faster development can be achieved by producing microgels in a continuous reactor mode, as it simplifies up-scaling to large-scale industrial production. Furthermore, model-based approaches facilitate the optimization of microgels with tailored properties. Computational models for describing microgel growth during the synthesis are very sparse and comprise mechanistic models suited for batch reaction exclusively [66, 67, 76, 84–86]. The findings from Chapter 3 revealed significant deviations between the reaction progress in batch and flow reactors in the microgel synthesis. In particular, the batch model equations cannot be transferred straight to a plug-flow model, but rather diffusion effects, temperature distribution, and rheological aspects must be considered. The physical properties such as diffusivity coefficient and viscosity are not known during the microgel synthesis, so mechanistic modeling of the flow process is restricted.

To address this gap, in this chapter, a data-driven hardware-in-the-loop optimization for *N*-

isopropylacrylamide (NIPAM)-based microgels, one of the most widely studied thermo-responsive microgel systems, is proposed. The data-driven approach facilitates the reaction optimization of the microgel synthesis in flow. Here, Thompson sampling efficient multi-objective optimization (TS-EMO) [200] is applied to enhance the experimental synthesis design iteratively. The TS-EMO solver is based on the Thompson sampling [201] algorithm, a popular approach in Bayesian optimization. In the following, a concise introduction to Bayesian optimization focusing on the TS-EMO algorithm is presented. For a more comprehensive elaboration of the methodology, the interested reader is kindly direct to consult the relevant literature [202, 203].

Bayesian optimization searches for a (global) optimum with a focus on efficiency, i.e., aiming for small number of function evaluations. Efficiency is crucial when function evaluations are costly, e.g., require experimentation or extensive computation. In Bayesian optimization, a probabilistic model (also called surrogate or digital twin) of the objective function is constructed and iteratively updated as new data points are evaluated. The surrogate models are constructed via Gaussian Processes (GPs). GPs are considered an effective surrogate model as they provide predictions and variance estimates while relying on relatively few data points [204]. Black-box optimization involving GPs for chemical synthesis has been successfully applied for various reactions [205], including pharmaceutical product development [206], electrochemical reductive carboxylation [207], and polymerization [208]. Based on the surrogate model, a new set of input conditions is proposed for the next experimentation while considering the exploration-exploitation trade-off. The goal is to find the input variable values that minimize the objective function. TS-EMO extends the Thompson sampling algorithm to the multi-objective optimization setting. The promising performance of TS-EMO concerning data efficiency, capacity to handle noise, and the ability for batch-sequential usage [200] makes the algorithm suitable for the optimization of microgel synthesis.

As the microgel size is a highly relevant product characteristic in the mentioned applications, the aim is to produce microgels of a targeted size (product feature). Simultaneously, the product flow and energy demand (process features) are optimized because the synthesis has to meet economic and ecological requirements. The synthesis procedure highly influences the characteristics of microgels, and multiple influences on the microgel size have been discovered experimentally. The surfactant [48, 54, 75, 209–212], monomer [213], cross-linker [52, 87, 210, 214], and initiator [213, 215, 216] concentration in the synthesis impact the microgel size. Also, the process conditions, including reactor temperature [210, 213] and flow profile [51, 213], determine the microgel size. For the synthesis of microgels with constant cross-linking fraction, the reaction temperature, initiator and monomer flow, and the surfactant concentration are included as variable inputs in the data-driven study.

Since TS-EMO is a stochastic optimization algorithm, it does not guarantee finding the global optimum. Therefore a computational validation step is conducted via global deterministic optimization using the open-source software MAiNGO (McCormick-based algorithm for mixed-integer nonlinear global optimization) [217]. MAiNGO has been demonstrated to be very suitable for optimization with GPs embedded [218]. The global deterministic optimization ensures that for a given GP and acquisition function the optimal solution is found. The computed Pareto-optimal solutions are computed based on the GPs trained on the experimental data. Thus, the Pareto-optimal points are estimates and need to be validated experimentally to show that indeed it is possible to synthesize the desired microgel and to ensure that computational prediction and real experiment agree. Therefore, in addition, the optimization results are validated experimentally. The proposed synthesis of a selection of Pareto-optimal points are conducted and the experimental outcome is compared to the computed findings.

The remaining chapter is structured as follows. Section 8.2 describes the experimental setup of the microgel synthesis in the flow reactor. Section 8.3 reports the optimization approach, including the TS-EMO algorithm, the initial data set, and the problem setup using MAiNGO. Section 8.4 presents

the results of the optimization studies and the computational and experimental validation. Finally, the contributions are concluded in Section 8.5.

8.2 Experimental Microgel Synthesis in Flow Reactor

Microgels are synthesized via precipitation polymerization inside a tubular glass reactor setup, as described in detail in Chapter 3. In the following, a brief summary of this experimental setup is provided. Two feed solutions are created, where the monomer and initiator are dissolved in water. The monomer solution contains deionized water with 110.6 mmol L^{-1} of NIPAM, 2.7 mmol L^{-1} of cross-linker *N,N'*-methylenebis(acrylamide) (BIS), and 0.41 mmol L^{-1} of surfactant hexadecyltrimethylammonium bromide (CTAB). Thus, the resulting microgels contain a cross-linker fraction of 2.5 mol%. The initiator solution comprises deionized water with 1.5 mmol L^{-1} of initiator 2,2'-azobis(2-methylpropionamidine)dihydrochloride (AMPA). Both solutions (initiator and monomer) and constantly degassed using nitrogen. The flow rates of the monomer and initiator solution can be controlled between 2 mL min^{-1} to 18 mL min^{-1} and 0.1 mL min^{-1} to 0.9 mL min^{-1}, respectively. Hence, the overall flow rate and the ratio between both feed flows can be adapted. An external heating bath heats the reactor to reaction temperature. The reactor temperature is adjusted between 60°C to 80°C. The produced microgels exit the reactor, and the solution is cooled to stop the reaction. During the continuous synthesis, Raman spectroscopy is used to determine the weight fraction of the remaining NIPAM (w_{NIPAM}) via in-line measurements. Raman spectra are recorded in HoloGRAMS (Kaiser Optical Systems, Ann Arbor, Michigan, USA) with cosmic ray correction using an RXN2 Raman Analyzer (Kaiser Optical Systems) and an acquisition time of 40 s. More details on the Raman measurement configuration are described in Chapter 3. The Raman spectra are assessed using an evaluation model based on indirect hard modeling [80], which is presented in Chapter 3 as well. The calibration measurements for the model development are published for transparency and reproducibility [93]. In an off-line step, a Zetasizer Ultra (Malvern Panalytical, Malvern, UK) is used to determine the hydrodynamic diameter (D_H) of the collapsed microgels via dynamic light scattering (DLS). The microgel samples are diluted in ultrapure water and prepared in a disposable capillary cell of the type DTS0012 for the DLS measurements. The measurements are carried out at 50°C with an angle of 90°(side scatter). For consistency, microgel size measurements are acquired in the collapsed state above the volume phase transition temperature (approximately 32° C [50]), as the in-line Raman measurements are also conducted at reaction temperature (between 60°C to 80°C). For the sake of completeness, DLS measurements are taken at 20°C and also provided in the data publication to this work [199]. Each DLS measurement is repeated four times, and the software ZS Xplorer analyzes the results. Experimental data points are excluded when the DLS measurements are unreliable due to a high relative error of the microgel size or an increased polydispersity index, indicating that no microgels formed.

8.3 Computational

The following section is structured as follows. First, the optimization problem is formulated considering the goals and limitations of the experimental setup, see Section 8.3.1. In Section 8.3.2, the procedure for generating a set of experiments to initialize the iterative optimization study is described. Next, the conducted optimization studies are outlined in a high-level description in Section 8.3.3. Further, details are provided on the basic operating principle of the employed TS-EMO algorithm in the

hardware-in-the-loop setup and the validation approach via global deterministic optimization and the optimization problem definition therein in Section 8.3.3.1 and 8.3.3.2, respectively.

8.3.1 Optimization Problem Definition

The optimization aims to find optimal settings for the synthesis to generate a high product output at short residence times and precise, targeted microgel sizes while minimizing the reaction temperature at steady-state. Bayesian optimization designs the best combination of input values to optimize these objectives efficiently. Furthermore, the objectives must be determined from outputs quantifiable via established monitoring techniques.

The reaction system has four optimization variables as inputs $\mathbf{x}$: reaction temperature T, surfactant concentration c_{CTAB}, and flow rates of the initiator F_{I} and monomer F_{M} solution. The bounds on the inputs are presented in Table 8.1. The range of T comprises the minimum of 60°C when the initiator decomposition effectively sets in [173] and the maximum of 80°C when solvent evaporation becomes an issue. The bounds on c_{CTAB} are based on the reaction experience that no colloidal stability sets in below the lower limit. Generally, a higher c_{CTAB} causes a smaller microgel size. Thus, the upper limit for c_{CTAB} is determined based on preliminary experiments. The pump's capacity defines the limits for the monomer and initiator solution flow rates. Furthermore, at the minimum $F_{\mathrm{M}} = 2\,\mathrm{mL\,min^{-1}}$, which entails the maximum residence time in the reactor (approximately 1800 s), the final conversion is reached, as discovered previously (see Chapter 3). The employed upper bounds allow for achieving the desired microgel size range, as is concluded from empirical knowledge. The concentration of the monomer NIPAM ($c_{\mathrm{NIPAM}} = 110.6\,\mathrm{mmol\,L^{-1}}$) in the stock solution, and the ratio of monomer to cross-linker BIS are kept constant for the reaction optimization to maintain a cross-linking fraction of 2.5 mol% within the microgel.

Table 8.1: Bounds on input variable values.

Variable	Unit	Lower bound	Upper bound
F_{I}	$\mathrm{mL\,min^{-1}}$	0.1	0.9
F_{M}	$\mathrm{mL\,min^{-1}}$	2	18
c_{CTAB}	$\mathrm{mmol\,L^{-1}}$	0.14	0.41
T	°C	60	80

Two quantities of the system are measured at the end of the reaction: The weight fraction of the monomer NIPAM w_{NIPAM} and the microgel's hydrodynamic radius r_{H}. From the measurements, two quantities $\mathbf{y}$ are derived for the surrogate model data set: The product flow (F_{Product}) and the squared deviation from the targeted microgel size (Δr_{H}^2). The product flow characterizes the reactor efficiency and is computed via:

$$F_{\mathrm{Product}} = \frac{w_{\mathrm{NIPAM,0}} - w_{\mathrm{NIPAM,f}}}{w_{\mathrm{NIPAM,0}}} \cdot (F_{\mathrm{I}} + F_{\mathrm{M}}),$$

where $w_{\mathrm{NIPAM,0}}$ and $w_{\mathrm{NIPAM,f}}$ denote the initial and final NIPAM weight fraction.

The output Δr_{H}^2 is calculated as the squared difference between the measured and targeted hydrodynamic radius:

$$\Delta r_{\mathrm{H}}^2 = (r_{\mathrm{H}}^{\mathrm{meas}} - r_{\mathrm{H}}^{\mathrm{target}})^2.$$

The targeted microgel size in this chapter is a hydrodynamic radius of 100 nm in the collapsed state at 50° C, as the size range is relevant in medical applications to pass the human cell boundary. Previously, it was found that microgels with a hydrodynamic diameter above 800 nm in the swollen

state are unsuitable for cellular uptake [38]. This size corresponds to a hydrodynamic radius of approximately 222 nm at the collapsed state. Thus, microgels of a hydrodynamic radius of 100 nm are expected to achieve fast cellular uptake kinetics.

The efficient microgel production targets a low reaction temperature as heating contributes significantly to energy consumption. The reaction temperature T is an input to the reactor system; hence, no additional measurement technology is needed. The difference to the minimum allowable temperature (see Table 8.1) is defined as another objective function:

$$\Delta T = T - T^{\min}.$$

Technically, the input temperature can be used as an objective function directly. However, the temperature difference is used as the objective to scale the temperature values to a similar magnitude as the flow rates and to underline the generality of the method.

The resulting multi-objective optimization problem is summarized in the following:

$$\min_{\mathbf{x}\in[\mathbf{x}^{\mathrm{L}},\mathbf{x}^{\mathrm{U}}]} \; -F_{\mathrm{Product}},\, \Delta r_{\mathrm{H}}^2,\, \Delta T,$$

where, $\mathbf{x} = [F_{\mathrm{I}}, F_{\mathrm{M}}, c_{\mathrm{CTAB}}, T]$, and $\mathbf{x}^{\mathrm{L}}$ and $\mathbf{x}^{\mathrm{U}}$ denote their corresponding lower and upper bounds as presented in Table 8.1.

8.3.2 Initial Data Set

Effective initial values are important to initialize the data-driven optimization algorithm. Often random choices are taken as initial guesses, without distinguishing between variables. However, efficient usage of experimental resources is desired and accordingly the following tailored initialization is devised. Three groups of experiments are configured, each comprising five experimental settings. The division is visualized in Figure 8.1. It is distinguished between input variables T and c_{CTAB} that are at a fixed value for each group and inputs F_{M} and F_{I} that vary simultaneously within one group. A group size of five experimental settings per session is adopted, as this quantity aligns with the capacity of a day's work in the laboratory.

Furthermore, three groups of experiments are considered as a trade-off between covering the input space of T and c_{CTAB} sufficiently and conducting a reasonable size of initial experiments in total.

Changing T between experimental runs relates to long transition times. Thus, T is kept at a fixed value for each group of experiments for an efficient proceeding. Also, c_{CTAB} is fixed for an experimental group, as preparing the monomer solution with different content of CTAB for each experiment execution is laborious and increases the risks of inserting air into the reactor system (oxygen inhibits the reaction) while decreasing the flexibility of the reaction setup. Therefore, keeping c_{CTAB} fixed constitutes a trade-off between effort for the synthesis preparation, risk of contamination, and loss of flexibility in synthesis execution.

The `lhsdesign` function for latin hypercube sampling (LHS) is employed in MATLAB 2019b to determine the input values for the initial experiments. In the first step, the values for T and c_{CTAB} are set for each of the three groups via LHS. Subsequently, LHS is performed again for F_{I} and F_{M} within each group for five settings. In total, an amount of 15 initial experiments is derived.

8.3.3 General Approach

A hardware-in-the-loop optimization study involving TS-EMO and a validation study including computational and experimental validation are conducted. In the hardware-in-the-loop approach, TS-EMO is employed to determine the next group of experiments based on an initial experimental data

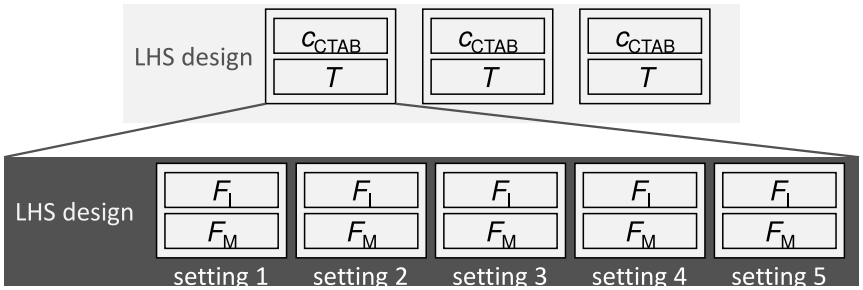

Figure 8.1: Grouping of initial experiments designed via LHS.

set. The Bayesian optimization algorithm TS-EMO iteratively suggests new experimental conditions based on the results of previous experiments. After the suggested group conditions are experimentally tested, the optimization process and subsequent experimentation are repeated until eleven iterations have been reached. Finally, the results from the TS-EMO study are validated computationally via global deterministic optimization using the software MAiNGO and experimentally with reaction settings from Pareto optimal points.

8.3.3.1 TS-EMO Algorithm

TS-EMO [200] is applied to the product-process optimization of the continuous microgel synthesis. The schematic setup of the reactor combined with the algorithm is shown in Figure 8.2. TS-EMO

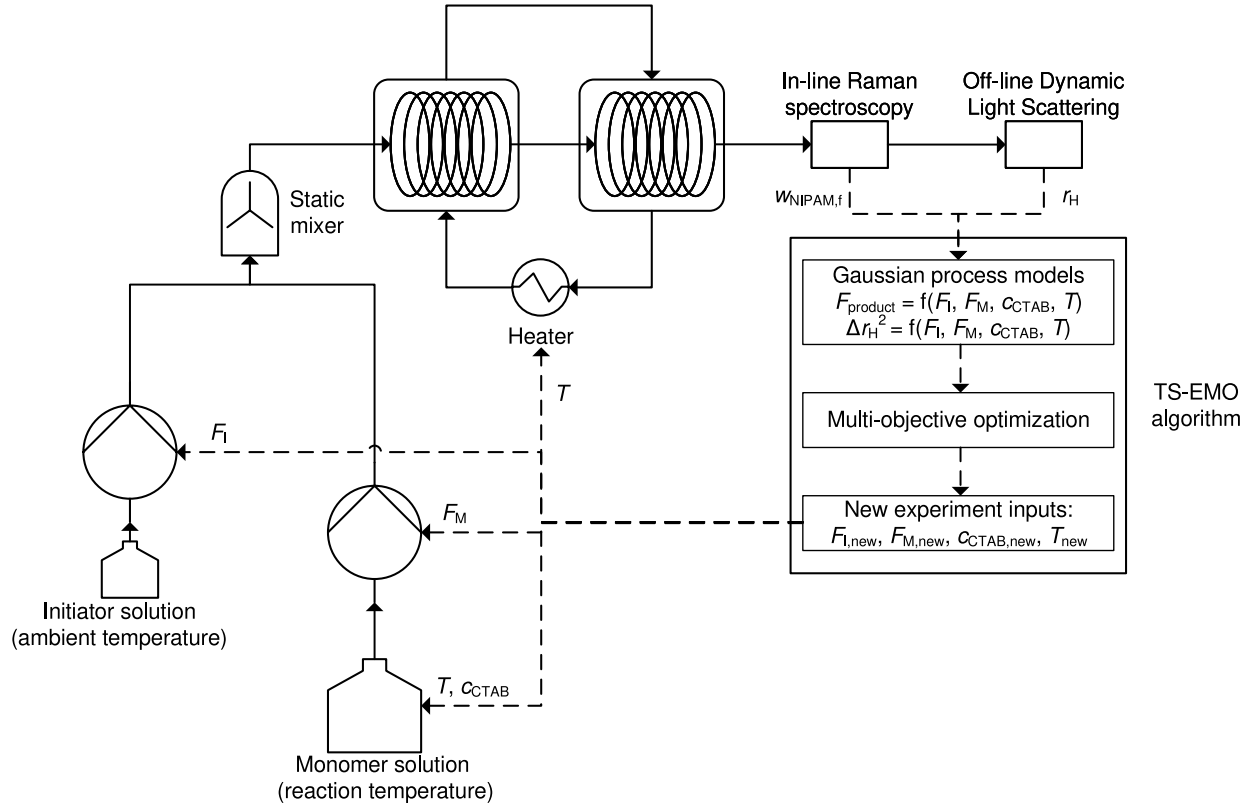

Figure 8.2: Overview of the iterative multi-objective optimization of the microgel synthesis in flow using the TS-EMO algorithm. Solid arrows indicate material flow, dotted arrows represent information transfer.

uses experimental data points $\mathbf{x}^{(i)} = [F_\mathrm{I}, F_\mathrm{M}, c_\mathrm{CTAB}, T]$ and $\mathbf{y}^{(i)} := [F_\mathrm{product}, \Delta r_\mathrm{H}^2]$ to create an approximation via a GP surrogate model of the unknown function f. For the training of the GPs, Matérn type 1 is applied as the function kernel. The third objective can directly be calculated from the input variables. In the multi-objective optimization step, Thompson sampling allows approximating the Pareto set of the optimal solutions. Here, the number of spectral sampling points is set to 4.000. Lastly, an optimal candidate set of input conditions $\mathbf{x}^{(i+1)} = [F_\mathrm{I,new}, F_\mathrm{M,new}, c_\mathrm{CTAB,new}, T_\mathrm{new}]$ is calculated to continue in the next experimental iteration loop. The settings incorporate a genetic algorithm with 1.000 generations for optimization.

In conclusion, the TS-EMO algorithm is provided with an initial experimental data set designed via LHS. The algorithm then provides a new set of experiments to be conducted in the following experimental round. Subsequently, in each optimization round, a set of the following five experiments at one fixed T and c_CTAB with varying F_I and F_M is determined. Here, atch-sequential optimization is chosen, meaning evaluating multiple points in each iteration, as off-line DLS measurements are conducted more efficiently in batch preparation. In addition, five experimental settings are chosen, as this quantity can adequately be conducted within one day of synthesis experimentation. The TS-EMO calculation and the experimentation are repeated in multiple iterations. Meanwhile, searching for the optimal recipe should take as few iterations as possible to decrease the experimental effort and expense of chemicals used. Thus, the hardware-in-the-loop procedure ends when a certain number of iterations have been performed or the executor decides that sufficient reaction knowledge has been gathered. In the presented study, the procedure ends after eleven iterations.

8.3.3.2 Global Deterministic Optimization

For the computational validation, MAiNGO [217] is used to conduct a global deterministic optimization. MAiNGO is employed as an alternative approach to the non-deterministic optimization included in the TS-EMO algorithm. Validation using MAiNGO does not require conducting new experiments but leverages the data collected during the Bayesian optimization. For the validation study, F_Product acts as the single objective. Additionally, the ϵ-constraint method [219] is applied to restrict the objective Δr_H^2. As the remaining objective ΔT is directly proportional to the input T, the upper bound of the input variable T is step-wise restricted. For the global optimization, the experimental data received in the TS-EMO study is used and no further experiments in the form of a hardware-in-the-loop approach are performed. The starting point and the ϵ values for the optimization are set based on the results derived from the hardware-in-the-loop study.

The optimization problem is re-written to a single-objective formulation in reduced space:

$$\begin{aligned} \min_{\mathbf{x}\in[\mathbf{x}^\mathrm{L},\mathbf{x}^\mathrm{U}]} \quad & -F_\mathrm{Product} \\ \text{s.t. } & \Delta r_\mathrm{H}^2 \leq \epsilon \end{aligned} \tag{8.1}$$

As stated above, the values for ϵ, $\mathbf{x}^\mathrm{U}$ of T, and the starting point are derived from the results of the TS-EMO study.

8.4 Results and Discussion

The results and discussion are organized as follows. First, the findings from the study involving TS-EMO with four inputs and three objectives are presented in Section 8.4.1. There, the Pareto optimal solutions for the three-dimensional objective system, the progression of the experimental outcome with accumulating experimentation, the error analysis of the measurements, and the Pareto optimal

solutions for each of the four inputs are shown. Subsequently, the results of the validation studies are displayed in Section 8.4.2. The computational validation via global deterministic optimization is shown in Section 8.4.2.1. The optimization problem is re-formualted to a single objective with four input variables for the final study. In Section 8.4.2.2, the experimental validation of three Pareto optimal points is additionally exhibited. All experimental data [199] is provided open-source. The data includes the raw Raman measurements and an evaluation of the DLS measurements. In addition, data points underlying the graphical representation of the results are made available in Section C.2 in the Appendix. The data points include the experimental data (Appendix C.2.1) and the Pareto optimal solutions calculated via global deterministic optimization in the validation step (Appendix C.2.2). As the Pareto optimal solutions calculated via TS-EMO are exhaustive, the data is not provided explicitly. The results can be re-constructed by applying TS-EMO on the experimental data provided. The software employed in this chapter is available open-source: TS-EMO [220] and MAiNGO [221] with MeLOn [222], the interface for embedded machine-learning models.

8.4.1 Hardware-in-the-Loop Involving TS-EMO

Eleven iterations are conducted for the hardware-in-the-loop optimization. The Pareto optimal solutions are analyzed in detail regarding the feasible space of the objective values in Section 8.4.1.1. Next, the progression of the experimentation outcome, an analysis of the errors from the experimental measurements, and the computational uncertainty of the calculated Pareto front are presented in Section 8.4.1.2. Lastly, the input variable values at the Pareto optimal points are evaluated to derive suitable reactor settings for the desired microgel product in Section 8.4.1.3.

8.4.1.1 Pareto Optimal Solutions

In the hardware-in-the-loop study, F_I, F_M, c_CTAB, and T are varied as the inputs to the reactor, and F_Product, Δr_H^2, and ΔT are the objectives. Figure 8.3 shows the resulting Pareto front of the study calculated using TS-EMO (marked with colored circles) and the experimental data points obtained during the hardware-in-the-loop optimization (marked with 'x' symbols). Later, in Section 8.4.1.2, also the progression of experimental outcomes for each iteration are shown separately (see Figure 8.4). For the TS-EMO calculations in Figure 8.3, a population size of 5,000 is used to represent the three-dimensional Pareto front sufficiently. As visualizing three objectives is challenging, a two-dimensional plot and add a color scale for the third objective are employed to visualize the estimated Pareto front for better interpretation. However, it is crucial to remember that the optimization results are three-dimensional for the meaningful interpretation of the two-dimensional plots.

For the two-dimensional Pareto fronts, the desired outcome in Figure 8.3, the utopia point, of the multi-objective optimization regarding the product flow and the squared radius deviation is located in the bottom left corner of the plot. Equally, small temperature deviations (depicted in dark blue) indicate the location of the utopia point in the third dimension. Looking at the results, it appears that the three objective functions are conflicting; thus, reaching the utopia point is impossible. In other words: the product flow rate becomes lower for microgels closer to the targeted size, and higher temperatures are needed for high product flow rates. In addition, the shaded area around a squared radius deviation accounts for a difference of $\pm 5\,\mathrm{nm}$ or 5% to the desired size.

The analysis of the estimated Pareto front in Figure 8.3 yields that up to $6.0\,\mathrm{mL\,min^{-1}}$ of product flow, a microgel size sufficiently close ($\pm 5\,\mathrm{nm}$) to the desired size is achievable. The microgel size deviation begins to diverge more strongly from the targeted value after a product flow rate of approximately $6.5\,\mathrm{mL\,min^{-1}}$ is reached. This deviation shows that product flow rates above a value of around $6.5\,\mathrm{mL\,min^{-1}}$ are incompatible with the targeted microgel size.

The temperature influences the optimal product flow more significantly than the optimal microgel size. This trend is represented by the color indicated temperature change that is more substantial along the x-axis than the y-axis. The underlying GPs (depicted in Appendix C.1) show that an increase in temperature generally accompanies an increase in product flow. Still, the product flow converges towards approximately $6.5\,\mathrm{mL\,min^{-1}}$ for temperatures above approximately 70°C (corresponding to 10 K temperature deviation). Thus, low temperatures (below 70°C) are sufficient considering the trade-off between maximizing product flow and achieving the targeted microgel size, as above approximately 70°C only the product flow improves. Overall, the optimal temperature input spans the entire allowable range between 60°C to 80°C. Furthermore, the GP for the squared radius deviation (Appendix C.1) shows an increase with rising temperatures. However, the correlation between reaction temperature and microgel size deviation appears highly nonlinear and subject to inherent variance. Lastly, the underlying GP for the temperature deviation (Appendix C.1) confirms the successful training of the GPs, as the temperature deviation shows no correlation to F_I, F_M, or c_CTAB, and is directly proportional to the input temperature values with little variance.

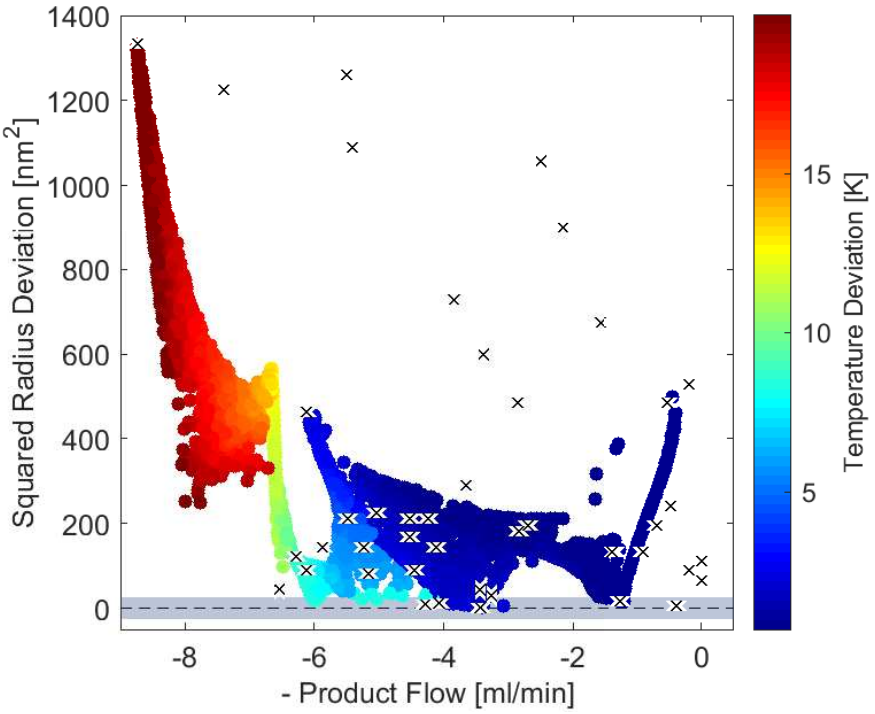

Figure 8.3: Estimated Pareto front of the hardware-in-the-loop study using TS-EMO: Squared radius deviation over product flow. The color scale indicates the temperature deviation. The x symbols mark the experimental data points. The shaded area maps the deviation of ± 5 nm to the desired microgel radius.

In conclusion, the results concerning a suitable microgel size at a high product flow and medium reactor temperatures are promising. The underlying GPs confirm the apriori reaction knowledge; thus, the functionality of the applied method is validated elementarily. However, the GPs are occasionally subject to high variance, and the available data points are limited. Nevertheless, meaningful information about the synthesis can be derived, e.g., limiting the temperature to 70°C is sufficient for successful synthesis. Furthermore, a maximum product flow of $6.0\,\mathrm{mL\,min^{-1}}$ is achievable when restricting the allowable microgel size deviation to ±5 nm.

8.4.1.2 Experiment Progression and Error Analysis

In Figure 8.4, the calculated Pareto front is shown with the progression of the experimentation. The temperature and the surfactant concentration for each experimental group are listed in addition to the order of experiment progression on the color scale. In the graph, the stars mark the results from the initial experiments designed via LHS. The LHS ensures a good distribution over the input space. The initial experimental results also cover the output space adequately, indicating that the initial data set already provides a reasonable basis for information on the reaction.

Furthermore, the triangles depicted in a color scale represent the experimentally determined data points and their progression in the hardware-in-the-loop approach. In each set of experiments, five data points are received. Some data points must be neglected due to DLS measurement showing a high size distribution index (indicating that no real microgel is formed) or a high relative measurement error. Thus, a reduced amount of experimental data points is shown. There is no clear trend visible in the experiment progression, as the algorithm tries to balance exploitation and exploration in the design of the next experiment. The listed temperature and surfactant concentration values along the experimental progression show that the algorithm mostly explores temperature regions below 70°C. While the surfactant concentration is varied over the entire allowed input space. Also, for the conducted experiments in this study, the algorithm does not repeat in any iteration the suggested experimental conditions regarding the combination of temperature and surfactant concentration. Although output measurements are sometimes excluded without further information to the algorithm, the algorithm does not try to re-evaluate the correlated input space. The batch-sequential procedure presumably achieves that the algorithm carries on without going back to previously tested conditions where no information is received. In other words: although no input information is gathered at certain input conditions within one experimental group, the information from the remaining input conditions within the group supports the algorithm enough.

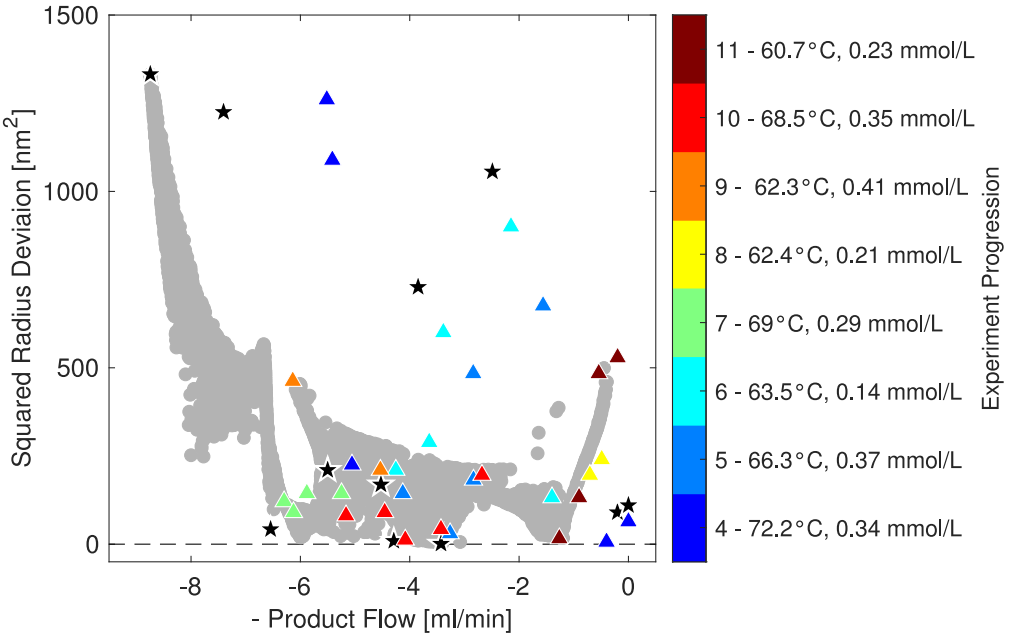

Figure 8.4: Estimated Pareto front of the hardware-in-the-loop study using TS-EMO: Squared radius deviation over product flow. The gray circles represent the estimated Pareto optimal solutions based on the GPs. The stars indicate the initial experimental data set and the triangles the subsequent experimental data points, while the color of the triangles shows the experimental progression.

In Figure 8.5, the calculated Pareto front is shown with the computational standard deviation of the optimal points. Also, the experimental data points are depicted with the according experimental error bars. The magnitude of the experimental error is derived from the measurement technology. The evaluation model of the Raman measurements has an inherent root mean squared error of cross-validation (RMSECV) of 0.037 wt%. The error propagation, including the RMSECV, is considered for the uncertainty of the product flow. For the DLS measurement, the Zetasizer Ultra internally evaluates the standard deviation over the four conducted measurements. This error value is also propagated for the uncertainty of the experimental squared particle size deviation.

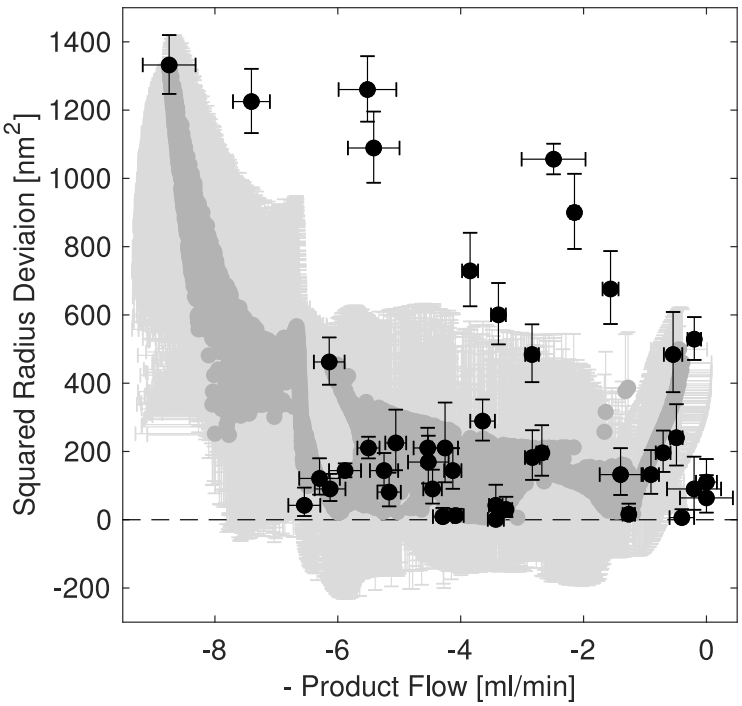

Figure 8.5: Estimated Pareto front of the hardware-in-the-loop study using TS-EMO: Squared radius deviation over product flow. The gray circles represent the estimated Pareto optimal solutions based on the GPs and the according standard deviation. The black circles indicate the experimental outcomes and the according measurement uncertainty.

Some experimental data points lie slightly below the estimated Pareto front. This phenomenon becomes visible in a three-dimensional analysis. However, the considered experimental data points lie within the calculated standard deviation of the estimated Pareto front for the squared radius deviation. Furthermore, the experimental error bars resulting from the DLS and Raman measurement errors are displayed to underline the magnitude of uncertainty inherent in the real-life experimental setup.

8.4.1.3 Pareto Optimal Solutions for Different Inputs

In Figure 8.6(a) to 8.6(c), the Pareto front for the objectives Δr_{H}^2 and F_{Product} and three out of the four applied inputs is shown. The color scale indicates the associated input configuration. The inputs pictured include the surfactant concentration, the monomer, and the initiator flow rate. The Pareto front with the according input temperature is not depicted explicitly, as Figure 8.3 contains information on the input temperature.

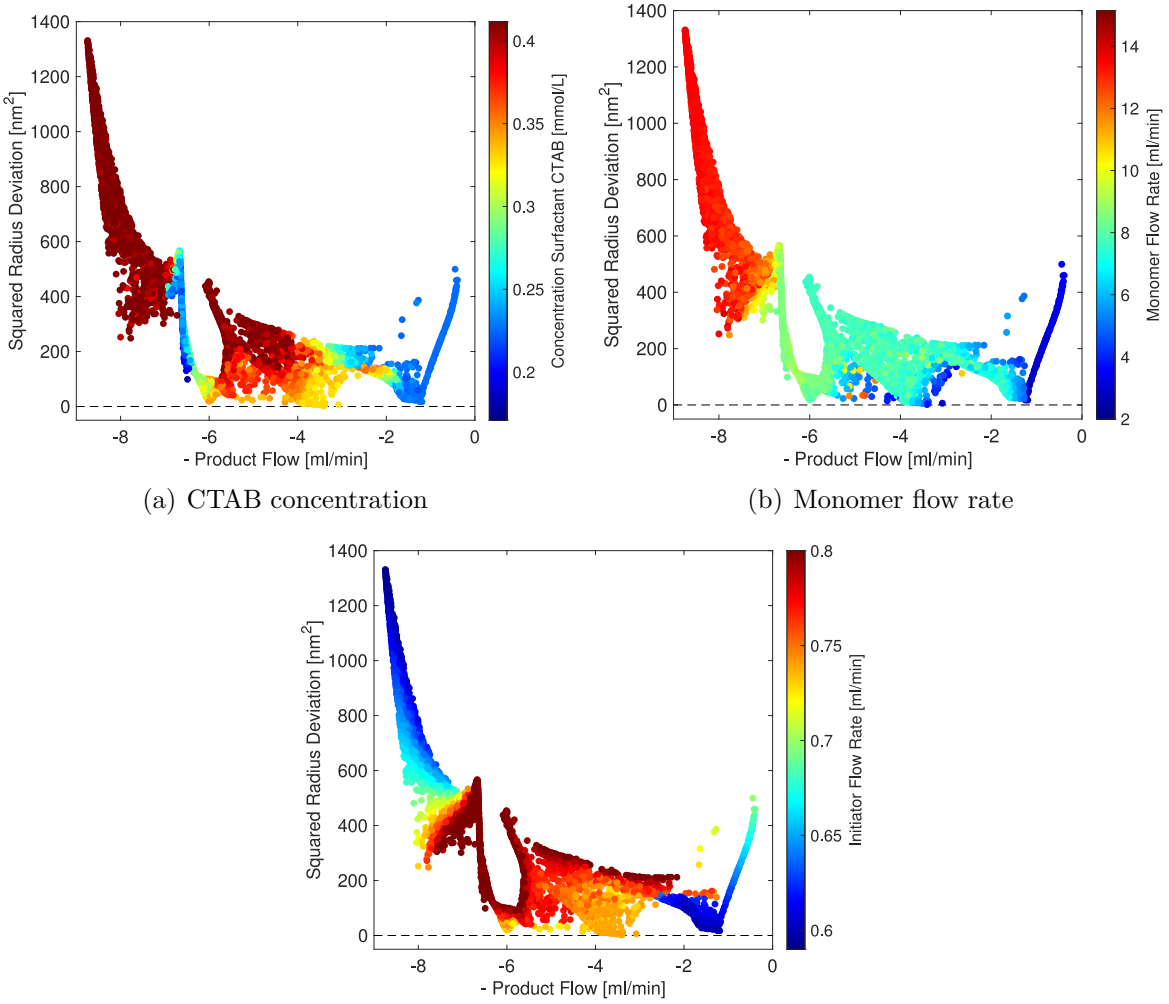

(a) CTAB concentration

(b) Monomer flow rate

(c) Initiator flow rate

Figure 8.6: Estimated Pareto front of main study: Squared radius deviation over product flow for the input variables (a) CTAB concentration, (b) monomer flow rate, and (c) initiator flow rate. The circles represent the estimated Pareto optimal solutions based on the GPs, while the color scale indicates the magnitude of the respective input variable.

Figure 8.6(a) shows that the microgel size deviates strongly from the desired size for higher c_{CTAB} values. Overall, c_{CTAB} ranges only between $0.22\,\mathrm{mmol\,L^{-1}}$ to $0.41\,\mathrm{mmol\,L^{-1}}$. The underlying GP (depicted in Appendix C.1) indicates that the product flow can be considered independent of c_{CTAB}. In contrast, the correlation between squared radius deviation and c_{CTAB} is impaired by high variance. The finding that the product flow is unaffected by c_{CTAB} follows the expected outcome, as a change in stabilizer should not impact the conversion kinetics of the reaction system.

In Figure 8.6(b), the monomer flow rate ranges between $2.75\,\mathrm{mL\,min^{-1}}$ to $14.2\,\mathrm{mL\,min^{-1}}$ and mainly correlates to the product flow. The relation between monomer flow rate and product flow is defined in Equation (8.3.1) stating that generally, the monomer flow and product flow are directly proportional (second term in Equation (8.3.1)). However, the monomer flow rate is also related to the conversion (first term of Equation (8.3.1)). A higher monomer flow can cause a smaller conversion, as not all monomer can be consumed in the smaller residence time. The underlying GP (depicted in Appendix C.1) shows the trade-off between high monomer flow rates associated with an increased overall flow and a lower conversion and low monomer flow rates with a low overall flow but higher

conversion. Furthermore, the monomer flow rate has little to no influence on the microgel size deviation according to the underlying GP.

Finally, Figure 8.6(c) shows the Pareto front for different initiator flow rates. Here, the initiator flow rate ranges between $0.59\,\mathrm{mL\,min^{-1}}$ to $0.8\,\mathrm{mL\,min^{-1}}$ with a clear tendency to the upper bound. Similar to the monomer flow rate, the initiator flow rate is directly proportional to the product flow as defined in Equation (8.3.1). However, the initiator flow is a maximum of a third of the total flow rate and thus less significant for the overall change in residence time. As expected, the underlying GP (depicted in Appendix C.1) also shows a highly linear correlation between initiator flow rate and product flow. In addition, the GP for the squared radius deviation shows no clear trend depending on the initiator flow rate.

8.4.2 Validation

The validation conducted within this chapter includes a computational and experimental part. The computational validation is global deterministic optimization of the final GP, Section 8.4.2.1. The experimental validation is carried out for three calculated Pareto optimal solutions, and the results are shown in Section 8.4.2.2.

8.4.2.1 Computational Validation via Global Deterministic Optimization

A final deterministic global optimization is conducted using MAiNGO. The results from the hardware-in-the-loop study are incorporated into the final optimization for validation. First, the data points from the TS-EMO study are used to train GPs for F_{Product} and Δr_{H}^2. The training settings are the same as for the GPs used in the hardware-in-the-loop approach including TS-EMO. Second, the identified optimal point close to the targeted microgel size and a sufficient product flow at a reasonably low temperature is embedded as the starting point of the optimization: $F_I = 0.73\,\mathrm{mL\,min^{-1}}$, $F_M = 8.1\,\mathrm{mL\,min^{-1}}$, $c_{CTAB} = 0.34\,\mathrm{mmol\,L^{-1}}$, and $T = 68.5°\mathrm{C}$. The calculated outcome for these input variables yields a microgel size deviation of $21.1\,\mathrm{nm^2}$ and a product flow of $6.0\,\mathrm{mL\,min^{-1}}$. Also, the visualization of the TS-EMO study (see Figure 8.3) allows setting reasonable values for the ϵ constraint method.

For the deterministic global optimization, the results including the ϵ constraint method, are presented in Figure 8.7 for each input separately. Here, the squared radius deviation is constrained step-wise with a maximum of $25\,\mathrm{nm^2}$. The problem becomes infeasible, meaning under the specified conditions no solution meets all the constraints and still optimizes the objective, for squared radius deviations below $2\,\mathrm{nm^2}$. The global deterministic optimization (MAiNGO) is compared with the optimization results for two objectives (product flow and squared radius deviation) using TS-EMO.

Overall, the Figs. 8.7(a) to 8.7(d) show that the experimental data points, the Pareto front generated via TS-EMO, and the Pareto front obtained from MAiNGO agree correctly above a product flow of approximately $4.3\,\mathrm{mL\,min^{-1}}$. TS-EMO finds a feasible Pareto optimal solution only down to $12.6\,\mathrm{nm^2}$ at a product flow of $4.0\,\mathrm{mL\,min^{-1}}$. In this region, the calculated solution via MAiNGO diverges and includes feasible solutions in the product flow range around $4.3\,\mathrm{mL\,min^{-1}}$ with squared radius deviations between $10\,\mathrm{nm^2}$ to $12\,\mathrm{nm^2}$.

The experimental data is obtained through hardware-in-the-loop optimization, balancing exploration and exploitation strategies. Consequently, the experimental data only partly aligns with the computed Pareto curve, as the algorithm also ventures into uncharted regions. Particularly at low product flows with high radius deviations, the experimental points are not part of the Pareto optimal set. However, the calculated Pareto optimal curve relies on the experimental data points. Hence, it becomes imperative that in the region of multi-objective optima, the experimental data points

agree with the calculated Pareto front. As illustrated in Figure 8.7, the experimental values agree with the calculated results along the estimated Pareto front, implying qualitatively that the result is trustworthy.

Within the Pareto optimal solutions calculated via MAiNGO, three regimes can be differentiated most visible for the CTAB concentration and the reaction temperature. These regimes range at a product flow of $3.4\,\mathrm{mL\,min^{-1}}$ to $3.8\,\mathrm{mL\,min^{-1}}$, around $4.3\,\mathrm{mL\,min^{-1}}$, and $4.5\,\mathrm{mL\,min^{-1}}$ to $6\,\mathrm{mL\,min^{-1}}$. In each regime, the CTAB concentration, the initiator flow rate, and the reaction temperature are approximately constant, and only the monomer flow rate varies.

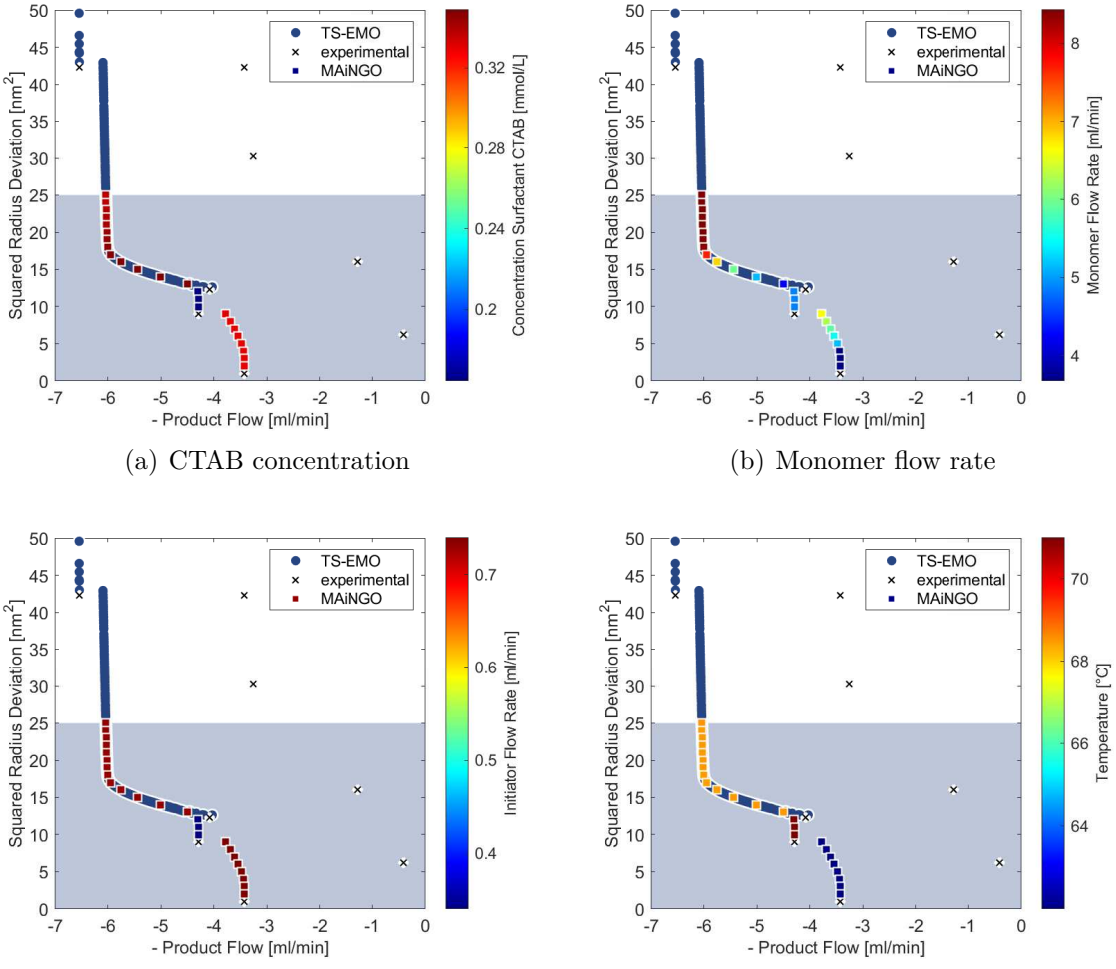

(a) CTAB concentration

(b) Monomer flow rate

(c) Initiator flow rate

(d) Reaction temperature

Figure 8.7: Estimated Pareto front of global deterministic optimization: squared radius deviation over product flow for the input variables (a) CTAB concentration, (b) monomer flow rate, (c) initiator flow rate and, (d) reaction temperature. The squares represent the estimated Pareto optimal solutions based on the GPs, while the color scale indicates the magnitude of the respective input variable. The x symbols mark the experimental data points. The blue circles indicate the estimated Pareto front via TS-EMO for two objectives only.

Further, the upper bound of the reactor temperature input variable value is changed to 61°C, 62°C, and 70°C. The results of the TS-EMO optimization with two objectives compared to global deterministic optimization results via MAiNGO are shown in Figure 8.8. The problem becomes infeasible for squared radius deviations below $2\,\mathrm{nm^2}$ for temperatures 62°C and higher, and below

16 nm^2 for 61°C. In other words, based on the optimization results it is not possible to synthesize microgels with a squared radius deviation below 2 nm^2 when restricting the reaction temperature to a maximum of 62°C or higher. Similarly, for a maximum temperature of 61°C, the smallest achievable squared radius deviation is 16 nm^2.

In Figure 8.8, the Pareto optimal points generated via TS-EMO and MAiNGO agree mostly. Only for a maximum input temperature of 61°C the global deterministic optimization via MAiNGO finds slightly better Pareto optimal points for squared radius deviations above 23 nm^2. However, the product flow range between 1.3 mL min^{-1} to 1.6 mL min^{-1} and a minimum squared radius deviation of 16.4 nm^2 for the associated temperature are undesirable. Thus, temperatures above 61°C are more relevant. For a maximum input temperature of 62°C, the Pareto optimal product flow is limited to 4 mL min^{-1} even for substantial deviations in squared radius at 25 nm^2. The Pareto optimal points for squared radius deviations below 13 nm^2 overlap for the MAiNGO and TS-EMO optimization for 62°C and 70°C. For a maximum input temperature of 70°C, a notable improvement of the product flow up to approximately 6 mL min^{-1} is achievable when allowing squared radius deviations starting at 18 nm^2 and above. The TS-EMO Pareto optimal points only cover squared radius deviations above 12.5 nm^2 for a maximum temperature of 70°C. The Pareto optimal points for the MAiNGO optimization with a maximum temperature of 70°C (see Figure 8.8) and 80°C (see Figure 8.7) agree except for the regime around 4.3 mL min^{-1} and squared radius deviations of 10 nm^2 to 12 nm^2 indicating that temperatures above 70°C are irrelevant for optimized reactor settings.

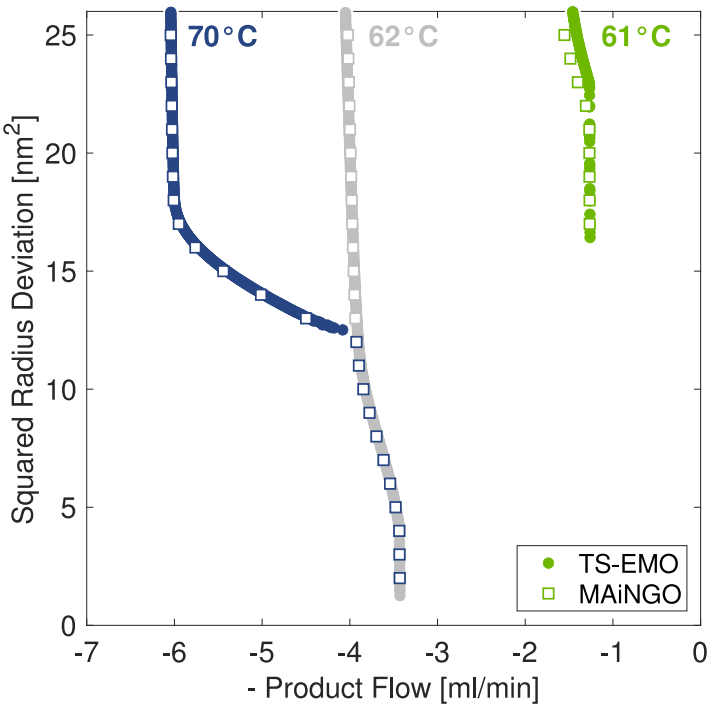

Figure 8.8: Comparison of TS-EMO and MAiNGO results for different bounds on input temperature. The filled circles represent the Pareto optimal points calculated via TS-EMO, while the squares show the Pareto optimal points calculated via MAiNGO.

Overall, the Pareto optimal solutions of TS-EMO and MAiNGO agree very well. Hence, the hardware-in-the-loop procedure using TS-EMO is validated sufficiently. However, the global deterministic optimization finds feasible Pareto optimal solutions beyond TS-EMO. The global deterministic optimization of the multi-objective synthesis problem is beneficial because little data is available,

and thus guaranteeing a reliable and reproducible solution is crucial. However, the surrogate models represented by GPs are subject to significant variance. Thus, a solution representing the actual reality remains challenging. Also, it is demonstrated that the deterministic single-objective formulation is advantageous here to focus on the output space of interest and reduce computational effort.

8.4.2.2 Experimental Validation

Three experiments are conducted along the deterministically estimated Pareto front for an experimental validation step to determine if the computed estimate based on the trained GPs can be verified experimentally. The inputs, the estimated, and experimentally determined values are presented in Table 8.2. The experimental and calculated values agree very well for the product flow. The most significant difference regarding the product flow occurs in Experiment 3 with an absolute divergence of $0.03\,\mathrm{mL\,min^{-1}}$ (or approximately 2.8%) to the calculated value. Generally, the agreement of calculated and experimental values is higher for the product flow than for the squared radius deviation. The most notable difference regarding the squared radius deviation arises for Experiment 1, where the absolute divergence is $83\,\mathrm{nm^2}$. This significant divergence can be attributed to the high variation in the GP prediction for the squared radius deviation. At the same time, the estimated and experimental value for Experiments 2 and 3 agree sufficiently. Experiment 3 shows that microgels with a radius of 101.5 nm can be efficiently synthesized, which is acceptable in terms of accuracy.

Overall, the experimental validation indicates that the obtained data is enough to enable an adequate prediction via a GP surrogate model. The agreement between estimated and calculated data is good, although the underlying GPs are subject to significant variance. The applied procedure is successful with an absolute deviation of 1.5 nm to the desired microgel radius.

Table 8.2: Experimental validation of global deterministic optimization.

Experiment	Input	Value	Output	Estimated value	Experimental value
1	T	68.5°C	F_{Product}	$5.95\,\mathrm{mL\,min^{-1}}$	$5.93\,\mathrm{mL\,min^{-1}}$
	c_{CTAB}	$0.35\,\mathrm{mmol\,L^{-1}}$	Δr_{H}^2	$17\,\mathrm{nm^2}$	$100\,\mathrm{nm^2}$
	F_{I}	$0.73\,\mathrm{mL\,min^{-1}}$			
	F_{M}	$7.69\,\mathrm{mL\,min^{-1}}$			
2	T	71.0°C	F_{Product}	$4.29\,\mathrm{mL\,min^{-1}}$	$4.20\,\mathrm{mL\,min^{-1}}$
	c_{CTAB}	$0.16\,\mathrm{mmol\,L^{-1}}$	Δr_{H}^2	$10\,\mathrm{nm^2}$	$12.25\,\mathrm{nm^2}$
	F_{I}	$0.34\,\mathrm{mL\,min^{-1}}$			
	F_{M}	$4.87\,\mathrm{mL\,min^{-1}}$			
3	T	62.0°C	F_{Product}	$3.43\,\mathrm{mL\,min^{-1}}$	$3.53\,\mathrm{mL\,min^{-1}}$
	c_{CTAB}	$0.33\,\mathrm{mmol\,L^{-1}}$	Δr_{H}^2	$2\,\mathrm{nm^2}$	$2.25\,\mathrm{nm^2}$
	F_{I}	$0.74\,\mathrm{mL\,min^{-1}}$			
	F_{M}	$3.68\,\mathrm{mL\,min^{-1}}$			

8.5 Conclusions

Polymerization reactions in flow reactors play an essential role in precise polymer production. The efficient, accurate, reproducible synthesis of polymers such as microgels is important. Data-driven optimization supports the microgel development effectively. The multi-objective optimization algorithm

TS-EMO is incorporated to optimize the synthesis of tailored microgels ecologically and economically. The proposed synthesis settings enable a product flow of maximum $6.0\,\mathrm{mL\,min^{-1}}$ while remaining in an acceptable range of $\pm 5\,\mathrm{nm}$ to the targeted hydrodynamic radius. The global deterministic optimization software MAiNGO is used to prove the reliability and reproducibility of the results. In addition, the usefulness of global deterministic solutions for problems with little data availability is demonstrated.

From the experimental side, including Raman spectroscopy constitutes a powerful in-line process analytical tool that has the potential to be incorporated into automated reaction optimization setups. Limitations of the proposed work include the non-automated reactor system due to off-line DLS measurements. Dependable in-line size determination remains a critical shortcoming on the road to autonomous reaction optimization. Furthermore, the DLS data is occasionally unreliable or shows a high polydispersity (indicating no real microgel is produced). At the moment, these data points are discarded but could be meaningfully included as valuable information for the algorithm in the future. The reliability of DLS data and the challenging interpretation of the GP predictions shows that expert knowledge is still crucial in the optimization procedure and limits a potentially autonomous process based on machine learning. Generally, data-driven optimization is limited to a specific reactor setup. However, the proposed framework can be quickly adapted to other desired microgel properties and reactor setups. Thus, this work supports and enhances the development of suitable microgels for size-specific applications. The presented method efficiently explores new microgel synthesis recipes that facilitate tailor-made microgel production.

9 Conclusions and Perspectives

This thesis systematically enhances the production of functional microgels through a multifactorial approach. The main emphasis encompasses three aspects of microgel synthesis: process monitoring, mechanistic modeling, and data-driven hardware-in-the-loop optimization. Monitoring via Raman spectroscopy is amplified in three ways: conversion monitoring in continuous flow reactors, conversion monitoring of charged microgels, and microgel size determination. Additionally, dynamic mechanistic modeling approaches are extended to include pH influence during the synthesis and forecast the course of reactions involving novel functional co-monomers, specifically glycidyl methacrylate (GMA) and methacrylic acid (MAA). Ultimately, a data-driven approach is implemented to execute product-process optimization of microgel synthesis, leveraging Bayesian optimization. The following paragraphs present conclusive thoughts on each aspect of microgel synthesis enhancement. As each aspect exhibits links to future works, perspective next steps are also described, respectively.

Regarding conversion monitoring in continuous flow reactors, the main challenge was to transfer the measurement accuracy from batch to continuous production mode. This challenge is resolved by establishing a successive protocol to rule out potential sources of measurement interference, thereby deriving the maximum allowable measurement deviation as a quality criterion. Applying the derived quality criterion enables high-quality measurements and allows the functional detection of outliers during the synthesis. Identifying and excluding outliers eliminates several potential errors that cause the difference in measurement results from the flow and batch reactor. Furthermore, outlier detection allows reliable process monitoring. Therefore, the contribution serves as a guideline for transferring in-line monitoring from batch to flow reactors at the example of precipitation polymerization. The next steps include the model-based validation of the experimental outcomes regarding the continuous microgel synthesis. A model-based approach allows advanced process control of the continuous flow reactor. Consequently, flexible production modes and accelerated process start-up are facilitated.

Considering microgel size prediction from Raman spectra, the main challenges were reducing the large input spectral dimension and robust size prediction from untreated spectra. These challenges are overcome by applying the diffusion maps (DMAPs) algorithm for dimensionality and conformal autoencoder neural network (CANN) for size prediction. The developed workflow is applied to a data set of Raman spectra with associated size measured via dynamic light scattering of 47 microgel samples in a diameter range of 208 nm to 483 nm. The CANN approach substantially outperforms state-of-the-art methods and results for the first time in a promising prediction of polymer size from Raman spectra. Opportunities to continue the work on size prediction (or other characteristics, e.g., morphologies) from Raman spectra are manifold and range beyond the application to microgels or even polymers in general. Concerning microgel synthesis, future work focuses on the workflow extension to simultaneously predict concentrations and microgel sizes from Raman spectra and analysis of extrapolation for size prediction beyond the capabilities of established process analytics.

With respect to conversion determination of charged microgels, the main challenge arose from the multitude of components in the system with dissociated and undissociated states. At the same time, the synthesis kinetics are in the order of magnitude challenging to acquire with low-frequency measurements, and the synthesis conditions are turbid due to precipitation. The challenges are tackled by applying indirect hard modeling (IHM) spectral evaluation and successively analyzing components with relevant influence on the Raman spectra during the synthesis. Although the prediction of MAA

concentration during the synthesis remains subject to significant variance, Raman measurements allow detailed insight into the reaction phenomena during the charged microgel synthesis. Furthermore, the procedure involving Raman measurements and the evaluation using IHM thereof can be easily applied to other charged microgel systems. Future research also directs towards enabling in-line monitoring via Raman spectroscopy of the charged synthesis.

Dynamic mechanistic modeling and parameter estimation for microgel synthesis with functional co-monomer GMA is challenging due to the high number of unknown parameter values and identifiability issues. The obstacles are overcome by systematically including parameter values computed via quantum mechanical calculations. The results show that the estimation approach enables a sufficient accuracy of parameter values of the *N*-vinylcaprolactam-*co*-glycidyl methacrylate (VCL-*co*-GMA) system. Further, the distribution of functional groups within the microgel is predicted with the fully identified model for multiple fed-batch scenarios. Future considerations should focus on experimental validation of the model predictions but face the challenge of lacking experimental methods for determining the position of functional GMA groups within the microgel.

Synthesizing charged microgels entails the challenging tasks of unreliable kinetic parameter values and, at the same time, a large reaction system with many parameters. This complexity is dealt with by including pH dependency in the dynamic synthesis model and estimating unknown parameter values in a structured procedure. Based on the reaction monitoring results from Raman spectroscopy and calorimetry and quantum chemical computations, missing parameter values are estimated to obtain a complete set of reaction parameter values for synthesizing *N*-isopropylacrylamide-*co*-methacrylic (NIPAM-*co*-MAA) microgels. The proposed model allows simulating the microgel synthesis with respect to changes in pH and its implications. Thus, this work represents an important step towards the model-based production of multi-responsive microgels. The subsequent steps address various aspects, including the model extension to additionally predict sizes of charged microgels, transfer of the charged microgel synthesis to continuous flow production, and model application and adaptation to other charged microgel systems.

Holistic optimization of the microgel synthesis with a focus on product and process objectives entails the inherent challenge of conflicting objectives and necessitating either mechanistic model-based approaches or many experiments for validation. The hardware-in-the-loop framework based on Bayesian optimization developed in this thesis enables the resource-efficient and effective synthesis of microgels with tailored properties regarding the polymer size. The results from the experiment-driven hardware-in-the-loop study are validated via global deterministic optimization. The proposed framework can be applied to other desired microgel properties and reactor setups and has the potential for efficient development by minimizing the number of experiments and modeling efforts needed. Perspective work develops methods to include mechanistic modeling knowledge into the data-driven approach for a hybrid concept and incorporates global deterministic optimization already in the hardware-in-the-loop optimization steps.

In conclusion, this thesis amalgamates progress in process analytical technology, computational mechanistic modeling, and data-driven optimization concatenating experimental real-world advancement with theoretical considerations. Consequently, the findings of this thesis represent a significant advance toward synthesizing tailor-made microgels with specific compositions or functionalities at an augmented production scale. Lastly, numerous insights derived from this thesis bear relevance to methodological advancements in spectroscopy-based size prediction and hardware-in-the-loop optimization for diverse (chemical) systems.

Appendix A

Supplemental Material Regarding In-line Monitoring of Continuous Flow Microgel Synthesis

A.1 Calibration Samples and Raman Measurements

The compositions of the calibration samples used for regression are presented in Tables A.1 and A.2. For the *in cell* calibration (see Table A.1), all samples are prepared in conventional glass flasks and subsequently filled in the measurement cell to conduct calibration measurements via Raman spectroscopy. For these measurements, the cell is sealed at the entrance and the exit to keep the calibration sample inside the cell. The compositions of the calibration samples used for regression of the *in glass* and *multiple in glass* indirect hard models (IHMs) are presented in Table A.2. These samples are prepared in glass flasks and afterward measured via Raman spectroscopy.

In Figure 3.4, the Raman measurements of calibration samples in the measurement cell containing water and *N*-isopropylacrylamide (NIPAM) are shown. For the monomer NIPAM, characteristic peaks occur at $1653\,\mathrm{cm^{-1}}$ corresponding to the C=C bond and $1617\,\mathrm{cm^{-1}}$ corresponding to the C=O bond [101]. The NIPAM spectra also show characteristic peaks at $977\,\mathrm{cm^{-1}}$, $1068\,\mathrm{cm^{-1}}$, $1262\,\mathrm{cm^{-1}}$, and $1415\,\mathrm{cm^{-1}}$. The NIPAM and the poly *N*-isopropylacrylamide (PNIPAM) spectra display similar peaks at approximately $850\,\mathrm{cm^{-1}}$ representing the C–C stretching, $1133\,\mathrm{cm^{-1}}$ representing CH_3 rocking, $1160\,\mathrm{cm^{-1}}$ representing C–O–C stretching, between $1244\,\mathrm{cm^{-1}}$ and $1367\,\mathrm{cm^{-1}}$ representing amide III groups, and $1452\,\mathrm{cm^{-1}}$ representing the C–H bending [223]. The broad peak at $1452\,\mathrm{cm^{-1}}$ is present in the NIPAM and the PNIPAM spectrum, but contributes more substantially to the polymer spectrum. Most visibly, the two C=O peaks disappear in the polymer spectrum; instead, a characteristic peak at around $1636\,\mathrm{cm^{-1}}$ emerges, which corresponds to the amide I group. The PNIPAM spectra shown in Figure 6 exhibit further peaks between $900\,\mathrm{cm^{-1}}$ to $970\,\mathrm{cm^{-1}}$ representing C–C skeletal stretching, and at $1392\,\mathrm{cm^{-1}}$ representing CH_3 symmetric deformation [223].

Figure A.1 illustrates the spectra of *N*,*N*'-methylenebis(acrylamide) (BIS), 2,2'-azobis(2-methylpropionamidine)dihydrochloride (AMPA), and hexadecyltrimethylammonium bromide (CTAB) in water at the concentrations used for the microgel synthesis. The spectra are acquired at 60 s acquisition time interval. In the significant spectral range used for the quantification of the reactant composition between $800\,\mathrm{cm^{-1}}$ to $1850\,\mathrm{cm^{-1}}$, the three components are unidentifiable. All components are present at small weight fractions of below 0.04 wt% during the synthesis. Due to the small weight fractions, the Raman signatures of the substances cannot be detected. Hence, a quantitative determination of the composition of these substances in the reaction solution is not feasible. Therefore, the components are not included in the IHM evaluation model for quantitative analysis.

Table A.1: Composition of the samples used for calibration inside the measurement cell in weight fraction.

	Water	NIPAM	PNIPAM
C1	1.00	-	-
C2	0.9981	-	0.0019
C3	0.9965	-	0.0035
C4	0.9949	-	0.0051
C5	0.9929	-	0.0071
C6	0.9911	-	0.0089
C7	0.9867	-	0.0133
C8	0.9825	-	0.0175
C9	0.9735	-	0.0265
C10	0.9899	0.0055	0.0046
C11	0.9785	0.0058	0.0157
C12	0.9852	0.0101	0.0047
C13	0.9806	0.0104	0.0090
C14	0.9782	0.0150	0.0068
C15	0.9715	0.0151	0.0134
C16	0.9763	0.0215	0.0022
C17	0.9973	0.0027	-
C18	0.9945	0.0055	-
C19	0.9917	0.0083	-
C20	0.9889	0.0111	-
C21	0.9861	0.0139	-

A.2 Measurement Cell

In Figure A.2, reference Raman spectra from conventional measurements inside a 3 ml glass flask (solid line) are compared to measurements conducted inside the novel measurement cell. The cell material (polyamide) has a considerable influence on the overall intensity even when using a short focal length (0 mm). For polyamide, additional characteristic peaks emerge in the considered spectral range of the Raman shift (dotted line). In particular, a characteristic peak at wavenumbers of approximately $1400\,\mathrm{cm}^{-1}$ to $1500\,\mathrm{cm}^{-1}$ occurs. This effect is suppressed by covering the inside of the measurement cell channel with aluminum foil (dashed line). This material is reaction-inert and, at the same time, very reflective. Therefore, it amplifies the intensity of the detected Raman signal in the measurement cell while preventing characteristic peaks of the cell material in the spectral range considered.

A.3 Raman Synthesis Measurements

For the synthesis measurements shown in Figure 3.9, the predicted weight fractions of NIPAM and PNIPAM are presented in Table A.3.

A.4 Mean Residence Time Measurements

The experimental determination of the mean residence time allows comparing the flow reactor with the mean residence time in a batch reactor. The volume flow rates are experimentally related to mean

Table A.2: Composition of the samples used for calibration inside conventional glass flasks in weight fraction.

	Water	NIPAM	PNIPAM
G1	1.00	-	-
G2	0.9970	-	0.0030
G3	0.9939	-	0.0061
G4	0.9909	-	0.0091
G5	0.9879	-	0.0121
G6	0.9849	-	0.0151
G7	0.9898	0.0051	0.0051
G8	0.9799	0.0051	0.0150
G9	0.9799	0.0151	0.0051
G10	0.9791	0.0102	0.0108
G11	0.9844	0.0105	0.0051
G12	0.9842	0.0051	0.0108
G13	0.9970	0.0030	-
G14	0.9939	0.0061	-
G15	0.9910	0.0090	-
G16	0.9879	0.0121	-
G17	0.9849	0.0151	-

residence times at Position 1 and 2 by conducting pulse injections of a fluid with a strong Raman signal. Here, water flows inside the reactor, and a pulse of 0.5 mL ethanol is injected right in front of the Y-connector. The use of ethanol allows short acquisition time intervals of 1 s. The constant volume flow rates range from $2.5\,\mathrm{mL\,min^{-1}}$ to $20\,\mathrm{mL\,min^{-1}}$ and $4.8\,\mathrm{mL\,min^{-1}}$ to $32.4\,\mathrm{mL\,min^{-1}}$ to evaluate mean residence times at Position 1 and 2. The continuous Raman measurements start once the pulse is injected and end when no more ethanol signal is detected. The mean residence time is defined as the time when half of the tracer material has exited the reactor.

The relation between total volume flow rate and the mean residence time in the reactor is presented in Figure A.3. The solid lines represent the equation fit to:

$$\tau = \frac{V}{F}. \tag{A.1}$$

Here, τ denotes the mean residence time, V the reactor volume, and F the volumetric flow rate. The flow rates result in Reynolds numbers between 16 and 128 and mean residence times of 65 s to 1465 s. Thus, the set range of volumetric flow rates provokes a laminar flow regime.

A.5 Impact of Raman Focus Depth

Analyzing the measurement accuracy necessitates the discussion of the captured signal of the focus of the Raman probe. The integrated Raman focus has a focus depth of 0 mm. In theory, the analyte in the focus point will have the most decisive influence on the Raman signal. In a flow reactor with a reigning laminar flow regime, the short focus would cause that the Raman probe captures the edge of the laminar velocity profile and thus not the average of the analyte content at the measurement position. However, the visualization of the background influence of the measurement in Figure A.2 and the experiences show that the probe captures Raman signals within a longer distance than 0 mm. The actual change in signal intensity over the distance to the Raman probe head is not this

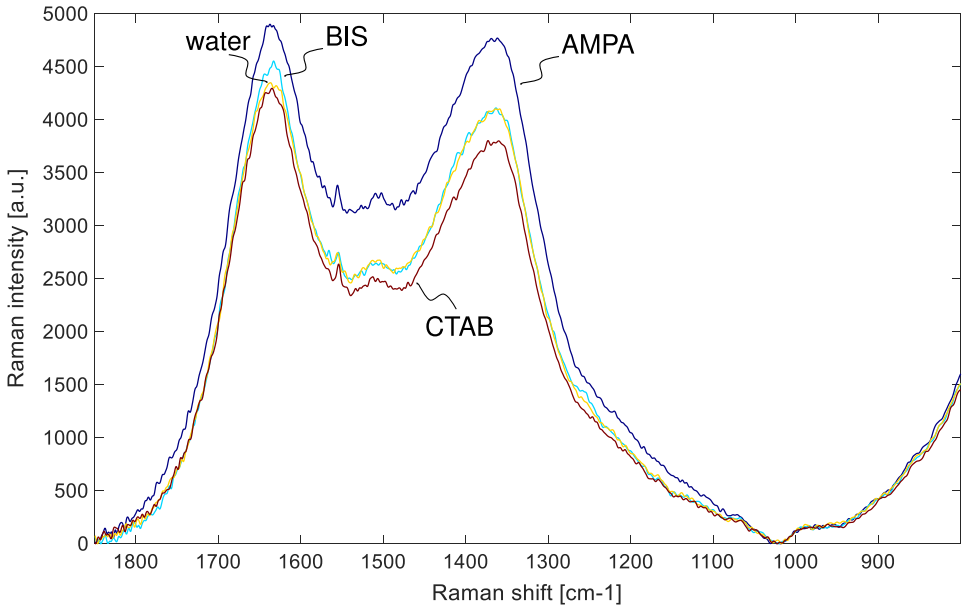

Figure A.1: Raman spectra of samples containing water with AMPA, BIS, and CTAB, respectively. The spectra are treated with a linear fit subtraction.

Table A.3: NIPAM and PNIPAM microgel weight fractions for different volumetric flow rates during the synthesis.

Volumetric flow rate [mL min^{-1}]	NIPAM weight fraction [wt%]	PNIPAM microgel weight fraction [wt%]
2.5	0.126	0.950
3.4	0.195	0.853
5.0	0.381	0.639
6.0	0.500	0.455
7.9	0.718	0.131
12.0	0.981	2.3×10^{-13}
14.0	1.061	1.9×10^{-13}
18.0	1.106	1.8×10^{-13}

study's topic. Yet, to exclude that the flow regime combined with the focus depth results in flawed measurements, two aspects are considered. First, an additional static mixer is integrated right before the installed position of the measurement cell. The second mixer causes a nearly homogeneously mixed reactor fluid to enter the measurement cell. The comparison of the synthesis measurements with and without the mixer is shown in Figure A.4. Hence, the difference between the measurements with and without the additional static mixer is insignificant. The additional mean residence time caused by the length of the static mixer is not taken into account, though. The additional time is not expected to contradict the matching results, as the red triangles in Figure A.4 would be slightly shifted to the right.

Secondly, the immersion depth of the Raman probe head into the reactor is varied. Here, the exact immersion depth is challenging to determine, as the depth is changed manually. However, an approximate analysis is still possible under these conditions. The standard deviations of the NIPAM content during the microgel synthesis at 70° C for varying immersion depths of the Raman probe head at Position 2 are calculated from measurements at volumetric flow rates of 2.5 mL min^{-1} and

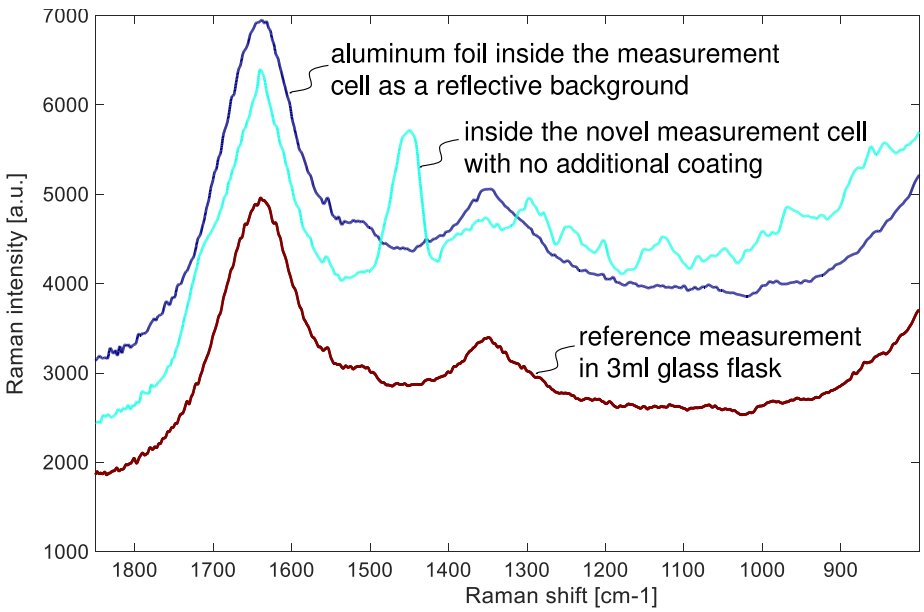

Figure A.2: Raw spectra of Raman intensity of pure water of 30 s acquisition time interval for different configurations.

$20\,\mathrm{mL\,min^{-1}}$. The values for the standard deviation are $0.0052\,\mathrm{wt\%}$ and $0.0097\,\mathrm{wt\%}$, respectively. These values range in the order of magnitude as the standard deviation from repeated experiments (see Table 3.2). Compared to the root mean squared error (RMSE) of flowing PNIPAM (see Figure 3.7(c)), the standard deviation of varying immersion depths is very small. Hence, the small standard deviation from changing the immersion depth is another indicator that the exact signal path of the focus is insignificant compared to the influence of larger molecules in the flow reactor.

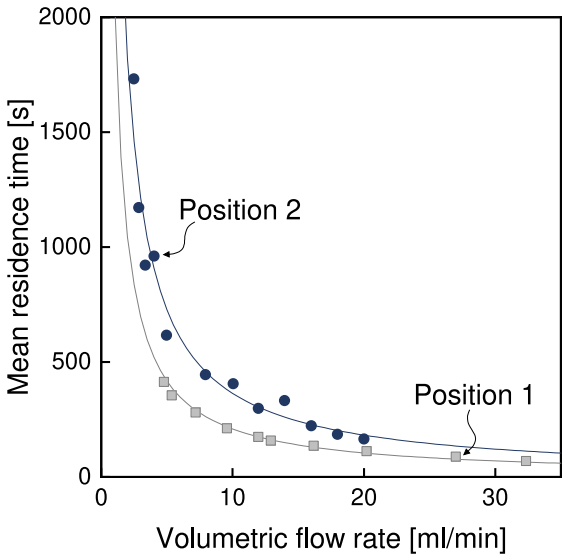

Figure A.3: Mean residence time measurements for Position 1 (grey boxes) and Position 2 (blue circles). Bold lines indicate the respective equation fit to Equation (A.1).

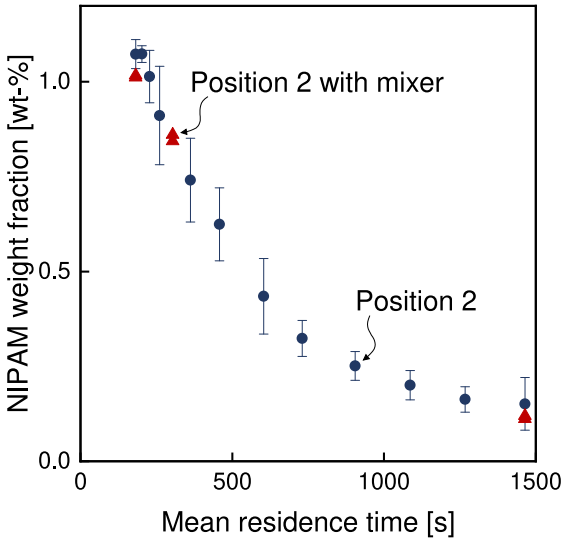

Figure A.4: Comparison NIPAM content during reaction inside the flow reactor at Position 2: Red triangles and blue circles indicate measurements with and without static mixer before the measurement cell, respectively.

Appendix B

Supplemental Material Regarding Modeling of the *N*-isopropylacrylamide-co-Methacrylic Acid Microgel Synthesis

B.1 Influence of pH Value during Synthesis

The pH value is measured during the synthesis of microgels with a methacylic acid (MAA) content of 5, 10 and 15 mol% using a pH and temperature sensor (SenTix 940 from WTW). The measured pH values are presented in Figure B.1(a). Based on the measured pH values the degree of dissociation can be calculated via:

$$\alpha^{\text{diss}} = 10^{-\text{pKa}+\text{pH}}. \tag{B.1}$$

The according degree of dissociation is pictured in Figure B.1(b). Here, it is visible that the pH value ranges between 2.8 and 4.4 over the course of the reaction. Accordingly, the degree of dissociation reaches a minimum and maximum value of 1.3 % and 54.5 %, respectively.

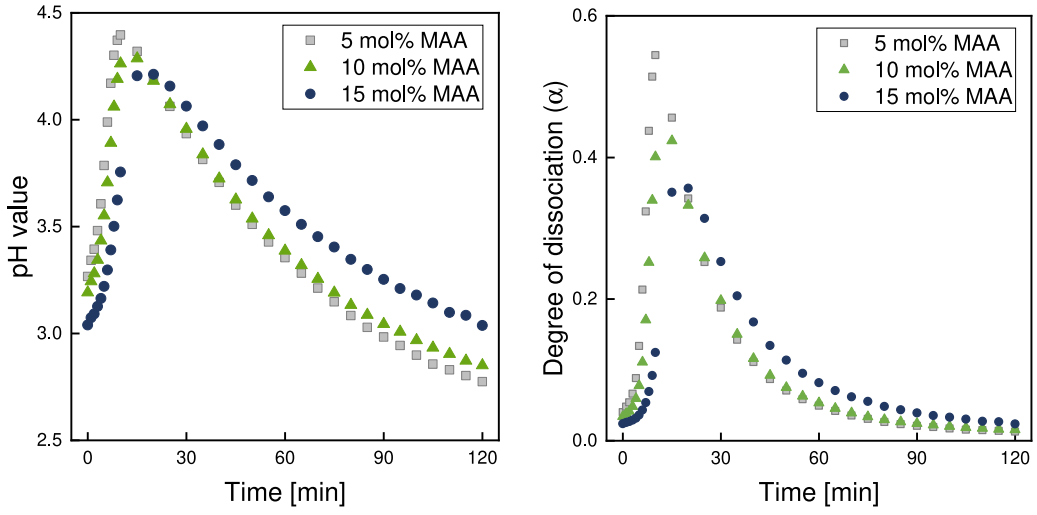

(a) pH value

(b) Degree of dissociation (α^{diss})

Figure B.1: pH value and resulting degree of dissociation during the synthesis of microgels with 5, 10, and 15 mol% MAA content.

Using the developed synthesis model, it is found that the pH value significantly influences the system outputs, namely the enthalpy transfer rate and the weight fractions of the monomers *N*-isopropylacrylamide (NIPAM) and MAA. By simulating the model for different pH values, the significance of the pH value on the synthesis outcome is demonstrated. Figure B.2 shows the enthalpy transfer rate and the weight fractions of the monomers NIPAM and MAA predicted by the kinetic synthesis model for different pH values. The parameter values for the propagation rates and reaction enthalpies are taken directly from the quantum mechanical calculations (see Section 7.3.2). The initiator efficiency f is set to 0.8, the decomposition rate k_d is set to $1 \times 10^{-5}\,\mathrm{s}^{-1}$, and the termination rate k_t is set to $1 \times 10^{-2}\,\mathrm{m}^3\,\mathrm{mol}^{-1}\,\mathrm{s}^{-1}$. The pH value is varied between 2.8 to 4.4, which corresponds to the lowest and highest pH values measured during the syntheses (see Figure B.1(a)).

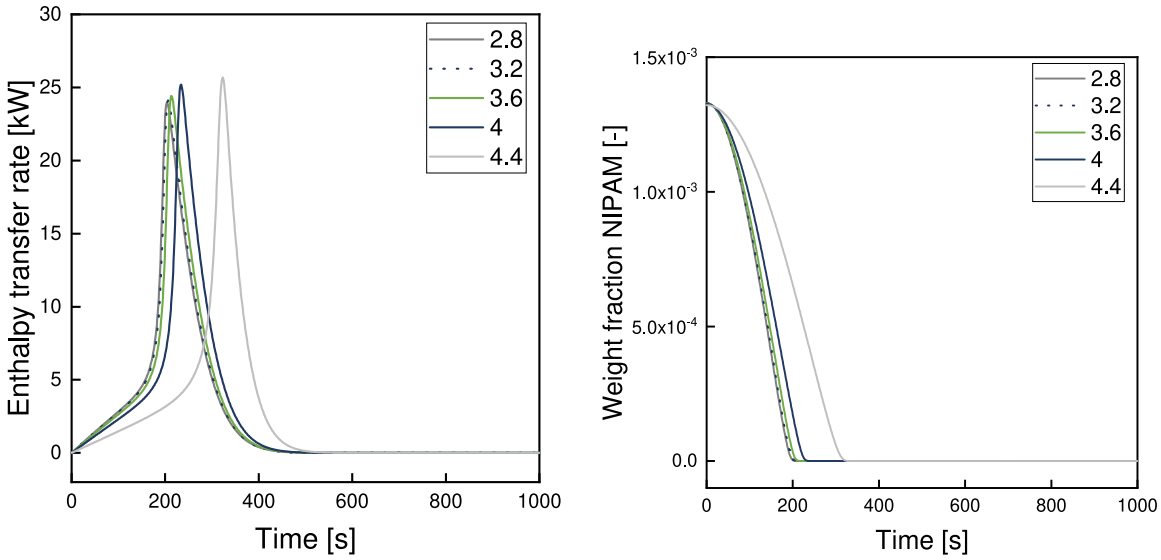

(a) Enthalpy transfer rate

(b) Weight fraction NIPAM

Figure B.2: Simulation results for the synthesis of microgels with 10 mol% MAA for different pH values.

Figure B.2 demonstrates that differences in the pH value in the range below 4.0 result in insignificantly different progression of the enthalpy transfer rate and monomer weight fractions. However, above a pH of 4.0 the pH value influences the output quantities substantially. Thus, the pH value cannot be assumed to be constant during the synthesis.

B.2 Synthesis Model

The model equations presented by Jung et al. [66] (marked in gray) are extended to account for the integration of functional monomer MAA. Time dependence (t) is omitted for improved readability.

$$\begin{aligned}
0 =& 2fk_{\mathrm{d}}c_{\mathrm{I}} - k_{\mathrm{p}11}c_{\mathrm{R}}c_{\mathrm{M}1} - k_{\mathrm{p}12}c_{\mathrm{R}}c_{\mathrm{M}2} \\
& - k_{\mathrm{p}13}c_{\mathrm{R}}c_{\mathrm{M}3} - k_{\mathrm{p}13\mathrm{d}}c_{\mathrm{R}}c_{\mathrm{M}3\mathrm{d}}, && \text{(B.2a)} \\
\dot{c}_{\mathrm{M}1} =& -k_{\mathrm{p}11}c_{\mathrm{R}1}c_{\mathrm{M}1} - k_{\mathrm{p}21}c_{\mathrm{R}2}c_{\mathrm{M}1} - k_{\mathrm{p}3\mathrm{d}1}c_{\mathrm{R}3}c_{\mathrm{M}1} \\
& - k_{\mathrm{p}31}c_{\mathrm{R}3\mathrm{d}}c_{\mathrm{M}1}, && \text{(B.2b)} \\
\dot{c}_{\mathrm{M}2} =& -k_{\mathrm{p}12}c_{\mathrm{R}1}c_{\mathrm{M}2} - k_{\mathrm{p}22}c_{\mathrm{R}2}c_{\mathrm{M}2} - k_{\mathrm{p}32}c_{\mathrm{R}3}c_{\mathrm{M}2} \\
& - k_{\mathrm{p}3\mathrm{d}2}c_{\mathrm{R}3\mathrm{d}}c_{\mathrm{M}2}, && \text{(B.2c)} \\
\dot{c}_{\mathrm{R}1} =& +k_{\mathrm{p}11}c_{\mathrm{R}}c_{\mathrm{M}1} - k_{\mathrm{t}}\left(2c_{\mathrm{R}1}^2 + c_{\mathrm{R}1}\left(c_{\mathrm{R}2} + c_{\mathrm{R}3} + c_{\mathrm{R}3\mathrm{d}}\right)\right) \\
& - k_{\mathrm{p}12}c_{\mathrm{R}1}c_{\mathrm{M}2} - k_{\mathrm{p}13}c_{\mathrm{R}1}c_{\mathrm{M}3} - k_{\mathrm{p}12}c_{\mathrm{R}1}c_{\mathrm{PDB}} - k_{\mathrm{p}13\mathrm{d}}c_{\mathrm{R}1}c_{\mathrm{M}3\mathrm{d}} \\
& + k_{\mathrm{p}21}c_{\mathrm{R}2}c_{\mathrm{M}1} + k_{\mathrm{p}31}c_{\mathrm{R}3}c_{\mathrm{M}1} + k_{\mathrm{p}3\mathrm{d}1}c_{\mathrm{R}3\mathrm{d}}c_{\mathrm{M}1}, && \text{(B.2d)} \\
\dot{c}_{\mathrm{R}2} =& +k_{\mathrm{p}12}c_{\mathrm{R}}c_{\mathrm{M}2} - k_{\mathrm{t}}\left(2c_{\mathrm{R}2}^2 + c_{\mathrm{R}2}\left(c_{\mathrm{R}1} + c_{\mathrm{R}3} + c_{\mathrm{R}3\mathrm{d}}\right)\right) \\
& + k_{\mathrm{p}12}c_{\mathrm{R}1}c_{\mathrm{M}2} + k_{\mathrm{p}32}c_{\mathrm{R}3}c_{\mathrm{M}2} + k_{\mathrm{p}3\mathrm{d}2}c_{\mathrm{R}3\mathrm{d}}c_{\mathrm{M}2} \\
& + k_{\mathrm{p}12}c_{\mathrm{R}1}c_{\mathrm{PDB}} + k_{\mathrm{p}32}c_{\mathrm{R}3}c_{\mathrm{PDB}} + k_{\mathrm{p}3\mathrm{d}2}c_{\mathrm{R}3\mathrm{d}}c_{\mathrm{PDB}} \\
& - k_{\mathrm{p}21}c_{\mathrm{R}2}c_{\mathrm{M}1} - k_{\mathrm{p}23}c_{\mathrm{R}2}c_{\mathrm{M}3} - k_{\mathrm{p}23\mathrm{d}}c_{\mathrm{R}2}c_{\mathrm{M}3\mathrm{d}}, && \text{(B.2e)} \\
\dot{c}_{\mathrm{PDB}} =& +k_{\mathrm{p}12}c_{\mathrm{R}1}c_{\mathrm{M}2} + k_{\mathrm{p}22}c_{\mathrm{R}2}c_{\mathrm{M}2} + k_{\mathrm{p}32}c_{\mathrm{R}3}c_{\mathrm{M}2} + k_{\mathrm{p}3\mathrm{d}2}c_{\mathrm{R}3\mathrm{d}}c_{\mathrm{M}2} \\
& - k_{\mathrm{p}12}c_{\mathrm{R}1}c_{\mathrm{PDB}} - k_{\mathrm{p}22}c_{\mathrm{R}2}c_{\mathrm{PDB}} \\
& - k_{\mathrm{p}32}c_{\mathrm{R}3}c_{\mathrm{PDB}} - k_{\mathrm{p}3\mathrm{d}2}c_{\mathrm{R}3\mathrm{d}}c_{\mathrm{PDB}} && \text{(B.2f)}
\end{aligned}$$

where c_{I}, $c_{\mathrm{M}1}$, and $c_{\mathrm{M}2}$ are the molar concentrations of initiator (I) 2,2'-azobis(2-methylpropionamidine)dihydrochloride (AMPA), monomer NIPAM (M_1), and cross-linker (M_2) *N*,*N*'-methylenebis(acrylamide) (BIS), respectively. $c_{\mathrm{R}i}$ are the molar concentrations of active radical chains with a corresponding terminal end; they are equivalent to the zeroth order moments of the radical chains.

The enthalpy transfer rate Σ_{R}, which is the enthalpy flow rate due to the exothermic polymerization reaction, is modeled based on the assumption that the major contributor to the enthalpy release are the propagation reactions. Hence, the enthalpy transfer rate can be determined as

$$\Sigma_{\mathrm{R}} = -V \cdot \left(\sum_i \sum_j \Delta H_{\mathrm{R}ij} k_{\mathrm{p}ij} c_{\mathrm{R}i} c_{\mathrm{M}j} + \sum_i \Delta H_{\mathrm{R}i2} k_{\mathrm{p}i2} c_{\mathrm{R}i} c_{\mathrm{PDB}} \right), \tag{B.3}$$

for $i,j = \{1,2,3,3\mathrm{d}\}$. There, c_i is the molar concentration of component $i \in$ [1=NIPAM, 2=BIS, 3=MAA, 3d=MAA$^-$], $\Delta H_{\mathrm{R}ij}$ is the enthalpy of reaction of respective reactions. V denotes the volume of the solvent water in the reactor.

The weight fraction of monomer can be determined based on the concentration by

$$w_{\mathrm{NIPAM}} = \frac{c_{\mathrm{M}1} M_{\mathrm{M}1} \cdot V}{m_{\mathrm{H_2O}}}, \tag{B.4a}$$

$$w_{\mathrm{MAA}} = \frac{(c_{\mathrm{M}3} M_{\mathrm{M}3} + c_{\mathrm{M}3\mathrm{d}} M_{\mathrm{M}3\mathrm{d}}) \cdot V}{m_{\mathrm{H_2O}}} \tag{B.4b}$$

where $M_{\mathrm{M}1}$, $M_{\mathrm{M}3}$, and $M_{\mathrm{M}3\mathrm{d}}$ are the molecular weights of NIPAM, MAA, and MAA$^-$, and $m_{\mathrm{H_2O}}$ is the mass of solvent in the reactor. The weight fraction of the cross-linker w_{BIS} cannot be measured with Raman spectroscopy due to the low amounts of cross-linker present in the reactor.

Table B.1: Sensitivity of changes in $\Delta H_{\mathrm{R}ij}$ on Σ_{R}.

Reaction	Relative sensitivity [%]
MAA radical / BIS	0.34
MAA radical / MAA	39.38
MAA radical / MAA$^-$	0.00
MAA radical / NIPAM	95.42
MAA$^-$ radical / BIS	0.00
MAA$^-$ radical / MAA	0.00
MAA$^-$ radical / MAA$^-$	0.00
MAA$^-$ radical / NIPAM	0.00
NIPAM radical / MAA	100.00
NIPAM radical / MAA$^-$	0.00
BIS radical / MAA	0.00
BIS radical / MAA$^-$	0.00

B.3 Sensitivity Analysis

For the sensitivity analysis, parameter values calculated from quantum mechanical computations and initial concentration values from the synthesis of microgels containing 10 mol% MAA are incorporated. Each parameter is varied by ±10% and simulate the output variables: weight fraction of NIPAM (w_{NIPAM}) and MAA (w_{MAA}), and enthalpy transfer rate (Σ_{R}). The deviation in output prediction for changes in parameter (p) is calculated, e.g., for the change in Σ_{R}, summarized for each time point (t_i) as follows:

$$\Delta\Sigma_{\mathrm{R},p} = \sum_{t_0}^{t_{\mathrm{f}}} \left(\frac{|\Sigma_{\mathrm{R},0}(t_i) - \Sigma_{R,\pm 10\%}(t_i)|}{\Sigma_{\mathrm{R},0}(t_i)} \right) \tag{B.5a}$$

$$\sigma_p = \frac{\Delta\Sigma_{\mathrm{R},p}}{\max(\Delta\Sigma_{\mathrm{R},p})}. \tag{B.5b}$$

The sensitivity (σ) based on the parameter p change is calculated in Equation (B.5b). Here, the maximum output change is used to normalize the resulting sensitivity. Based on the model structure, the enthalpies of polymerization ($\Delta H_{\mathrm{R}ij}$) only impact Σ_{R}. The resulting sensitivities of Σ_{R} for changes in $\Delta H_{\mathrm{R}ij}$ are summarized in Table B.1. Similarly, the sensitivities of Σ_{R}, w_{NIPAM}, and w_{MAA} for changes in kinetic rate parameters are shown in Table B.1.

Table B.2: Sensitivity of changes in reaction rate coefficients on Σ_R, w_{NIPAM}, and w_{MAA}.

Parameter	Relative sensitivity [%]		
	Σ_R	w_{NIPAM}	w_{MAA}
k_t	100.00	100.00	100.00
k_d	22.91	90.52	36.35
f	25.59	1.03	39.96
Propagation rate coefficients:			
MAA radical / BIS	1.13	0.00	0.99
MAA radical / MAA	31.18	0.00	29.37
MAA radical / MAA^-	0.00	0.00	0.00
MAA radical / NIPAM	57.70	38.68	70.72
MAA^- radical / BIS	0.00	0.00	0.00
MAA^- radical / MAA	0.00	0.00	0.00
MAA^- radical / MAA^-	0.00	0.00	0.00
MAA^- radical / NIPAM	0.00	0.00	0.00
NIPAM radical / MAA	19.16	3.79	11.27
NIPAM radical / MAA^-	0.00	0.00	0.00
BIS radical / MAA	0.00	0.00	0.00
BIS radical / MAA^-	0.00	0.00	0.00

B.4 Parameter Estimations

B.4.1 Model Suitability

Table B.3: Parameter estimation setup and optimal parameter values for estimation based on individual Σ_{R} for the synthesis of microgels containing 5 mol% to 15 mol% MAA. Termination rate coefficient and propagation rate coefficients are provided in [$m^3mol^{-1}s^{-1}$], decomposition rate in [s^{-1}] and polymerization enthalpies in [J].

Parameter	Optimization setup				Optimal parameter values		
	Start value (5 and 10 mol%)	Start value (15 mol%)	Lower bound	Upper bound	5 mol%	10 mol%	15 mol%
k_{t}	8.80	1.00×10^{-5}	1.00×10^{-5}	1.00×10^{5}	1.55×10^{1}	1.54×10^{2}	1.32
k_{d}	1.89×10^{-5}	1.37×10^{-5}	2.84×10^{-12}	1.26×10^{2}	4.57×10^{-6}	2.69×10^{-7}	5.24×10^{-6}
f	8.00×10^{-1}	7.97×10^{-1}	2.00×10^{-1}	8.00×10^{-1}	3.52×10^{-1}	5.17×10^{-1}	4.73×10^{-1}
Propagation rate coefficients $k_{\mathrm{p}ij}$:							
NIPAM radical / MAA	4.08×10^{1}	1.19×10^{2}	4.87	3.42×10^{2}	1.23×10^{1}	6.57	2.71×10^{2}
BIS radical / MAA	1.56	1.86×10^{-1}	1.86×10^{-1}	1.31×10^{1}	1.03×10^{1}	1.31×10^{1}	1.86×10^{-1}
MAA radical / NIPAM	1.21×10^{-1}	1.54×10^{-2}	1.44×10^{-2}	1.01	9.88×10^{-2}	1.40×10^{-1}	8.03×10^{-2}
MAA radical / BIS	3.54×10^{-2}	2.97×10^{-1}	4.22×10^{-3}	2.97×10^{-1}	4.22×10^{-3}	4.63×10^{-3}	2.97×10^{-1}
MAA radical / MAA	5.64×10^{-1}	1.04×10^{-1}	6.73×10^{-2}	4.73	6.73×10^{-2}	6.73×10^{-2}	2.01
BIS radical / BIS	8.10	9.67×10^{-1}	9.67×10^{-1}	2.83×10^{3}	1.04	1.04×10^{3}	2.83×10^{3}
BIS radical / NIPAM	9.99	8.37×10^{1}	1.19	3.54×10^{2}	1.19	1.97×10^{1}	2.30×10^{1}
NIPAM radical / BIS	1.03×10^{3}	2.14×10^{3}	2.22×10^{-1}	8.63×10^{3}	7.14×10^{2}	5.59×10^{3}	8.63×10^{3}
NIPAM radical / NIPAM	5.99×10^{2}	1.72×10^{2}	2.02×10^{-1}	5.02×10^{3}	8.06×10^{1}	9.37×10^{2}	3.23×10^{2}
Polymerization enthalpies $\Delta H_{\mathrm{R}ij}$:							
MAA radical / MAA	6.37×10^{4}	6.02×10^{4}	6.02×10^{4}	6.72×10^{4}	6.02×10^{4}	6.02×10^{4}	6.72×10^{4}
NIPAM radical / MAA	8.58×10^{4}	8.23×10^{4}	8.23×10^{4}	8.93×10^{4}	8.23×10^{4}	8.23×10^{4}	8.93×10^{4}
MAA radical / NIPAM	5.77×10^{4}	5.42×10^{4}	5.42×10^{4}	6.12×10^{4}	5.42×10^{4}	5.42×10^{4}	6.12×10^{4}
BIS radical / MAA	7.65×10^{4}	7.30×10^{4}	7.30×10^{4}	8.00×10^{4}	7.30×10^{4}	7.30×10^{4}	8.00×10^{4}
MAA radical / BIS	5.73×10^{4}	5.43×10^{4}	5.38×10^{4}	6.08×10^{4}	5.38×10^{4}	5.38×10^{4}	6.08×10^{4}
BIS radical / BIS	7.78×10^{4}	9.13×10^{4}	7.43×10^{4}	8.13×10^{4}*	7.43×10^{4}	7.43×10^{4}	9.13×10^{4}
BIS radical / NIPAM	8.17×10^{4}	8.49×10^{4}	7.82×10^{4}	8.52×10^{4}	7.82×10^{4}	7.82×10^{4}	8.52×10^{4}
NIPAM radical / BIS	8.93×10^{4}	9.28×10^{4}	8.58×10^{4}	9.28×10^{4}	8.58×10^{4}	8.58×10^{4}	9.28×10^{4}
NIPAM radical / NIPAM	8.75×10^{4}	5.38×10^{4}	8.40×10^{4}**	9.10×10^{4}	8.40×10^{4}	8.40×10^{4}	5.43×10^{4}

* For 15 mol% this value is 9.22×10^{4}. ** For 15 mol% this value is 5.38×10^{4}.

B.4.2 Estimation Based on Weight Fractions Individually

Table B.4: Parameter estimation setup and optimal parameter values for estimation based on individual weight fraction measurements for the synthesis of microgels containing 5 mol% to 15 mol% MAA. Termination rate coefficient and propagation rate coefficients are provided in $[m^3mol^{-1}s^{-1}]$.

	Optimization setup			Optimal parameter values		
Parameter	Start value	Lower bound	Upper bound	5 mol%	10 mol%	15 mol%
k_t	2.47	1.00×10^{-5}	1.00×10^{5}	2.64×10^{2}	2.81×10^{1}	6.29×10^{1}
f	2.28×10^{-1}	2.00×10^{-1}	8.00×10^{-1}	6.17×10^{-1}	4.67×10^{-1}	5.43×10^{-1}
NIPAM radical / MAA	2.50×10^{1}	4.87	3.42×10^{2}	1.63×10^{2}	4.64×10^{1}	3.81×10^{1}
BIS radical / MAA	1.86×10^{-1}	1.86×10^{-1}	1.31×10^{1}	1.86×10^{-1}	1.87×10^{-1}	2.88
MAA radical / NIPAM	3.28×10^{-1}	1.44×10^{-2}	1.01	1.01	5.68×10^{-1}	8.68×10^{-1}
MAA radical / BIS	1.88×10^{-1}	4.22×10^{-3}	2.97×10^{-1}	1.30×10^{-2}	1.38×10^{-2}	1.44×10^{-1}
MAA radical / MAA	6.73×10^{-2}	6.73×10^{-2}	4.73	7.04×10^{-2}	6.73×10^{-2}	6.73×10^{-2}
BIS radical / BIS	3.38×10^{2}	9.67×10^{-1}	2.83×10^{3}	5.68	2.32	1.12×10^{1}
BIS radical / NIPAM	4.23×10^{1}	1.19	3.54×10^{2}	1.96×10^{2}	4.16×10^{1}	1.19
NIPAM radical / BIS	1.86	2.22×10^{-1}	8.63×10^{3}	3.80×10^{3}	8.35×10^{3}	8.61×10^{3}
NIPAM radical / NIPAM	1.69	2.02×10^{-1}	5.02×10^{3}	8.99	4.23	4.80

B.4.3 Estimation Based on Weight Fraction Combined

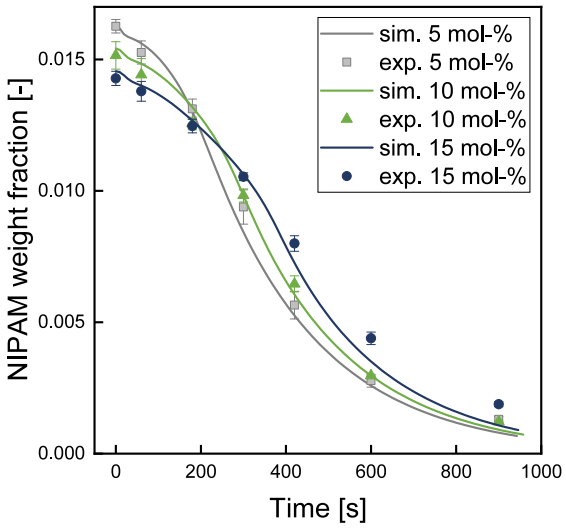

(a) Weight fraction NIPAM (w_{NIPAM})

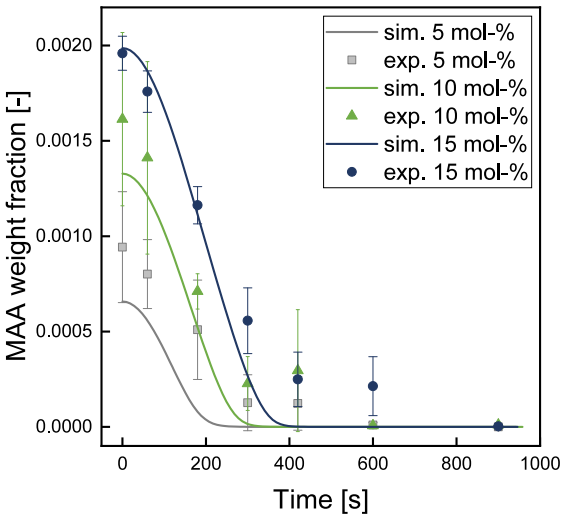

(b) Weight fraction MAA (w_{MAA})

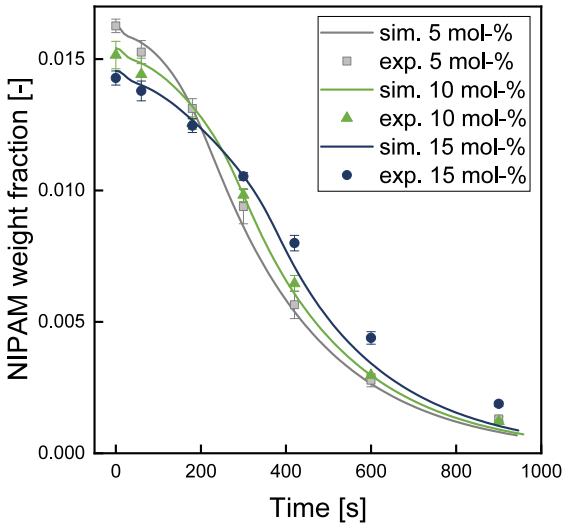

(c) Weight fraction NIPAM (w_{NIPAM})

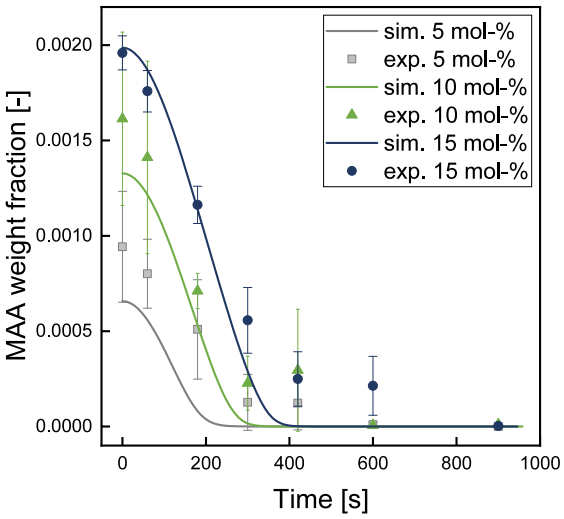

(d) Weight fraction MAA (w_{MAA})

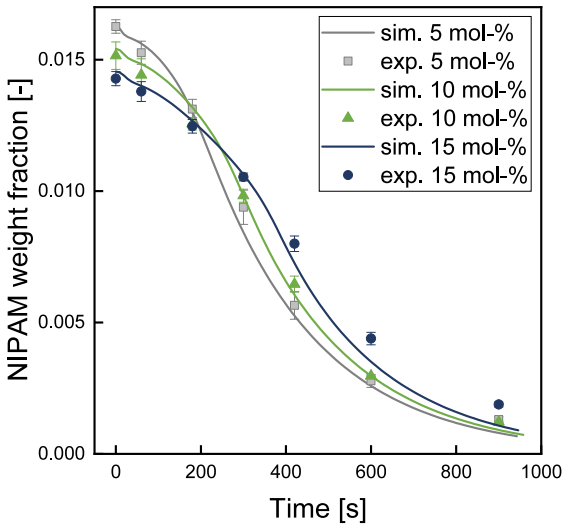

(e) Weight fraction NIPAM (w_{NIPAM})

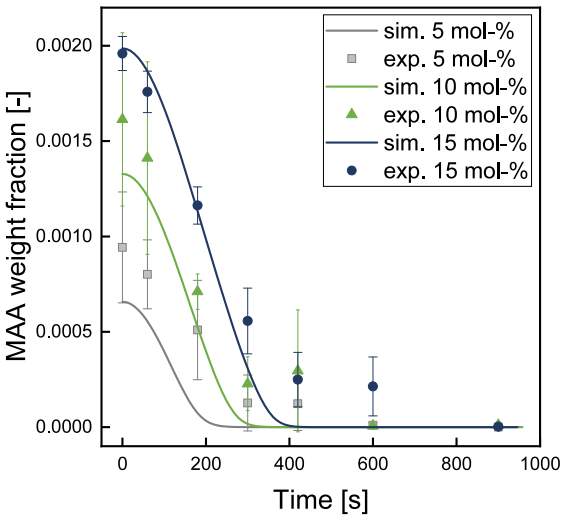

(f) Weight fraction MAA (w_{MAA})

Figure B.3: Results of estimation using only the weight fractions and estimating based all experiment combined with start values from estimation based on: (a),(b) 5 mol% MAA, (c), (d) 10 mol% MAA, and (e), (f) 15 mol% MAA experiment individually.

Table B.5: Parameter estimation setup and optimal parameter values for estimation based on weight fraction measurements combined from all experimental setups for the synthesis of microgels containing 5 mol% to 15 mol% MAA. Termination rate coefficient and propagation rate coefficients are provided in [$m^3mol^{-1}s^{-1}$].

	Optimization setup		Optimal parameter values		
Parameter	Lower bound	Upper bound	start values 5 mol%	start values 10 mol%	start values 15 mol%
k_t	1.00×10^{-5}	1.00×10^{5}	2.99×10^{-1}	5.48×10^{-1}	5.39×10^{-1}
f	2.00×10^{-1}	8.00×10^{-1}	5.58×10^{-1}	2.92×10^{-1}	3.74×10^{-1}
NIPAM radical / MAA	4.87	3.42×10^{2}	5.93	1.11×10^{1}	9.60
BIS radical / MAA	1.86×10^{-1}	1.31×10^{1}	1.86×10^{-1}	1.86×10^{-1}	1.86×10^{-1}
MAA radical / NIPAM	1.44×10^{-2}	1.01	1.02×10^{-1}	1.96×10^{-1}	1.56×10^{-1}
MAA radical / BIS	4.22×10^{-3}	2.97×10^{-1}	4.22×10^{-3}	4.22×10^{-3}	4.22×10^{-3}
MAA radical / MAA	6.73×10^{-2}	4.73	6.73×10^{-2}	6.73×10^{-2}	6.73×10^{-2}
BIS radical / BIS	9.67×10^{-1}	2.83×10^{3}	9.67×10^{-1}	9.67×10^{-1}	9.67×10^{-1}
BIS radical / NIPAM	1.19	3.54×10^{2}	3.54×10^{2}	3.54×10^{2}	3.54×10^{2}
NIPAM radical / BIS	2.22×10^{-1}	8.63×10^{3}	7.96×10^{2}	1.54×10^{3}	1.32×10^{3}
NIPAM radical / NIPAM	2.02×10^{-1}	5.02×10^{3}	3.87×10^{-1}	7.24×10^{-1}	6.32×10^{-1}

B.4.4 Estimation Based on All Enthalpy Transfer Rates and Weight Fractions

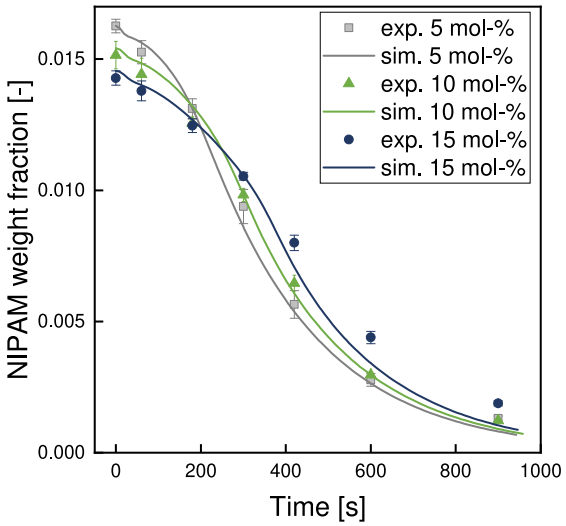

(a) Weight fraction NIPAM (w_{NIPAM})

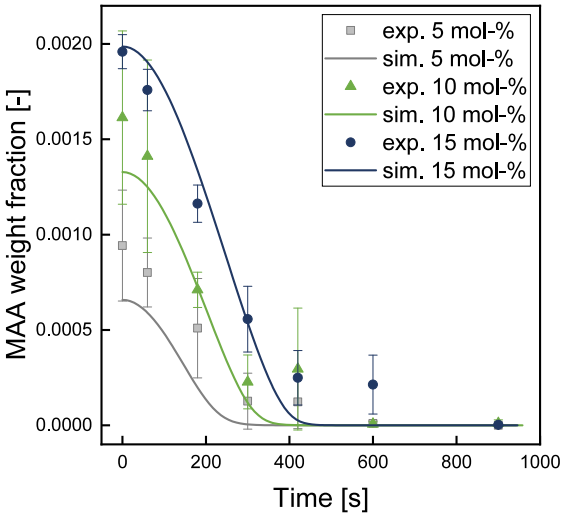

(b) Weight fraction MAA (w_{MAA})

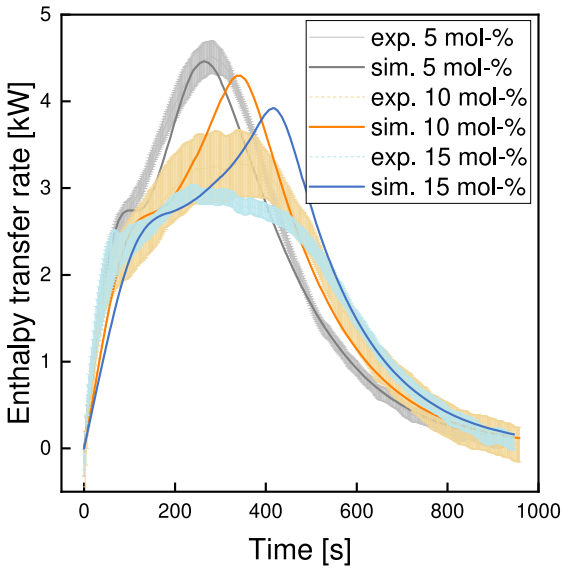

(c) Enthalpy transfer rate (Σ_{R})

Figure B.4: Results of estimation using the weight fraction and enthalpy transfer measurements and estimating based on all experiment together. Using the start values from estimation based on 5 mol% MAA experiment start values.

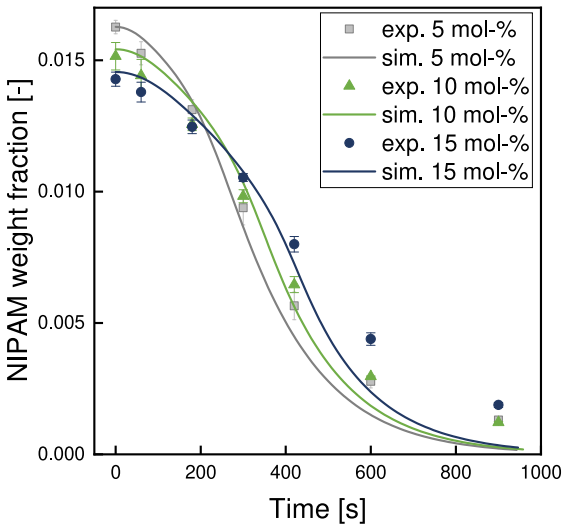

(a) Weight fraction NIPAM (w_{NIPAM})

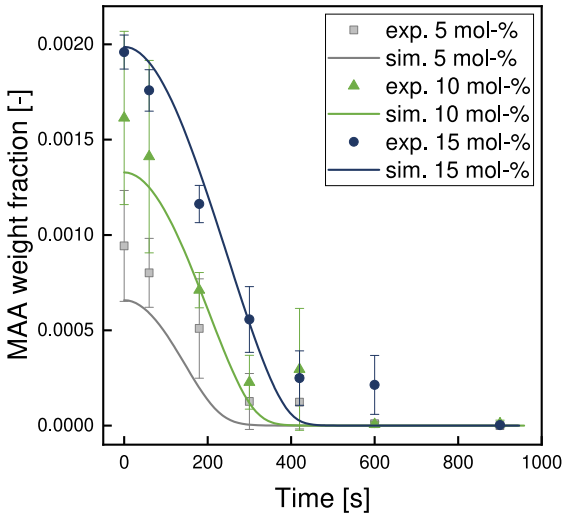

(b) Weight fraction MAA (w_{MAA})

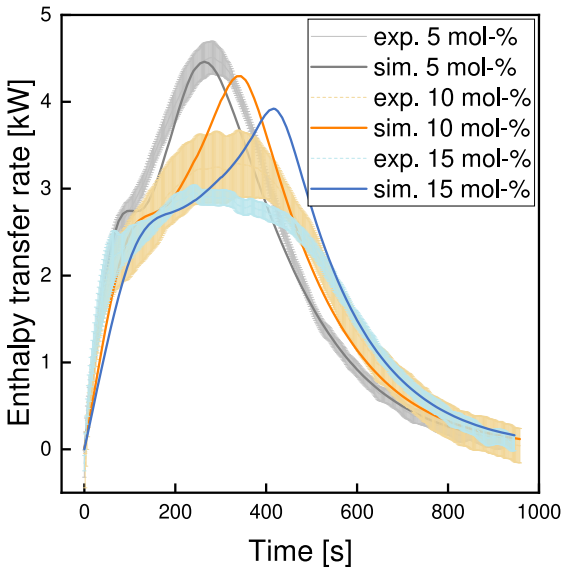

(c) Enthalpy transfer rate (Σ_{R})

Figure B.5: Results of estimation using the weight fraction and enthalpy transfer measurements and estimating based on all experiment together. Using the start values from estimation based on 15 mol% MAA experiment start values.

Appendix C

Supplemental Material Regarding Data-Driven Product-Process Optimization of *N*-isopropylacrylamide Microgel Flow-Synthesis

C.1 Gaussian Processes

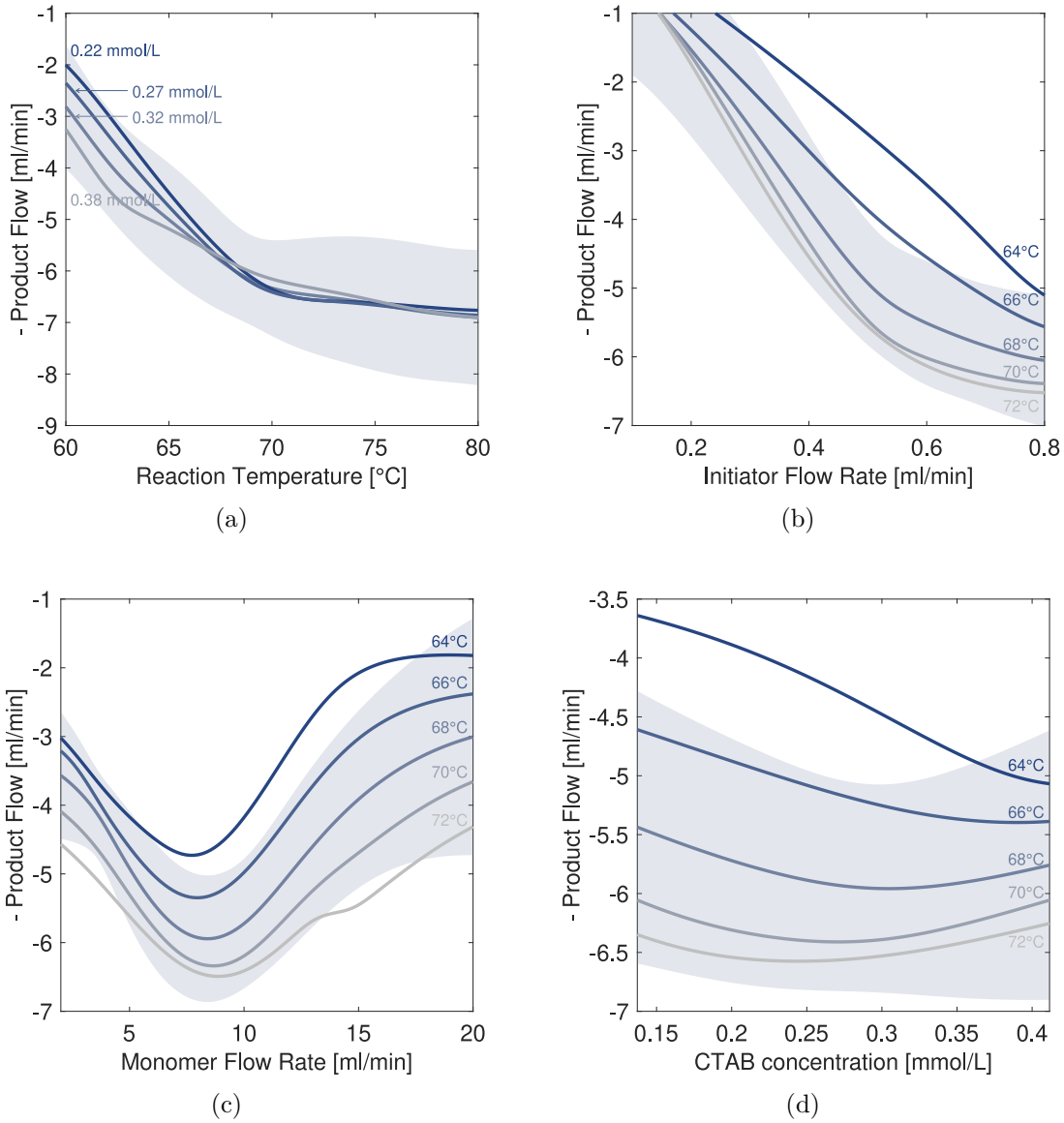

Figure C.1: GP prediction of product flow as a function of: (a) reaction temperature, (b) initiator flow rate, (c) monomer flow rate, and (d) surfactant concentration. The GP is trained on data points generated in the hardware-in-the-loop study involving TS-EMO. The shaded are represents the variance of the prediction at 0.32 mmol L^{-1} for (a). For (b), (c), and (d), the shaded area denotes the variance of the prediction at 68°C.

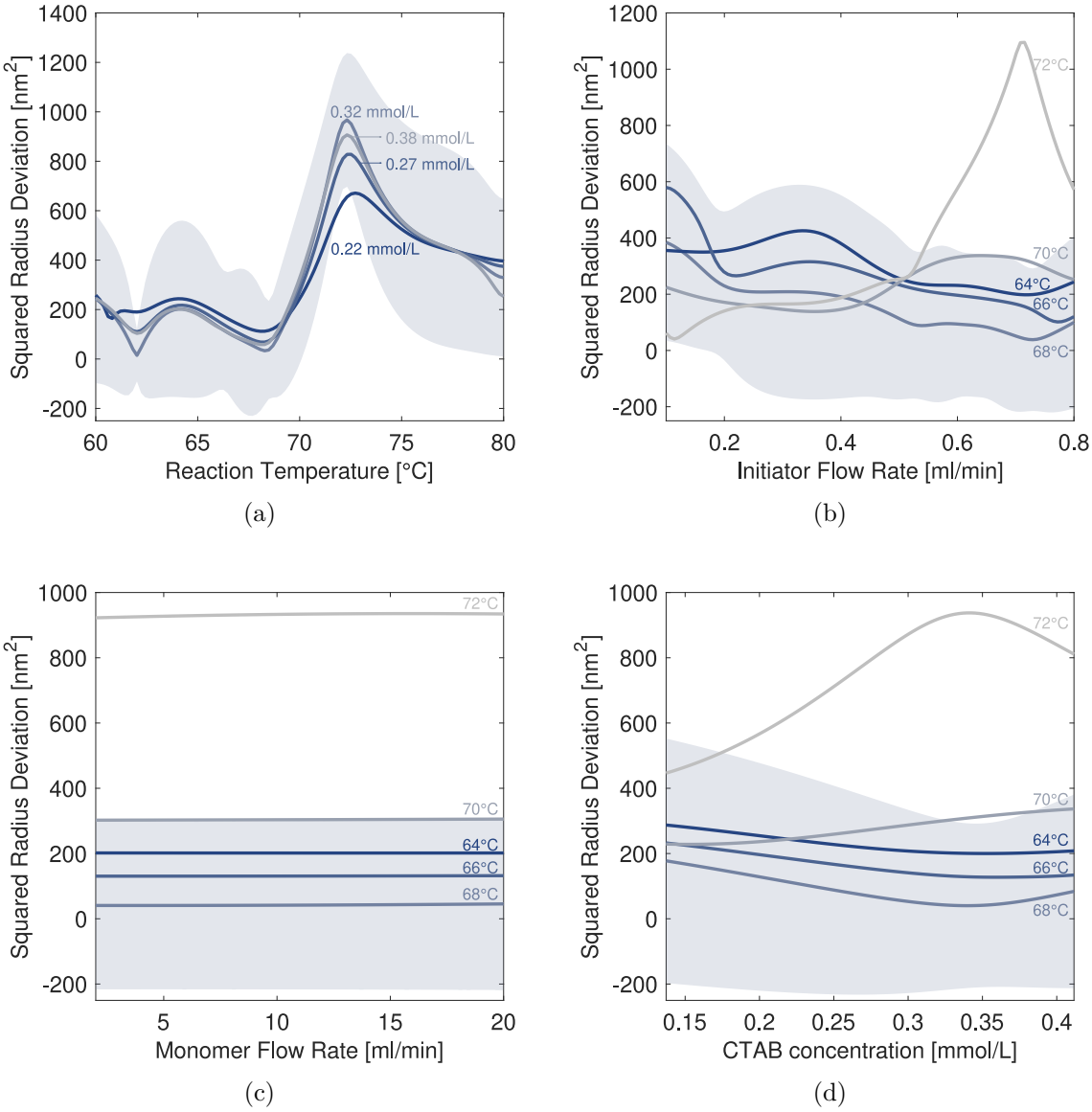

Figure C.2: GP prediction of squared radius deviation as a function of: (a) reaction temperature, (b) initiator flow rate, (c) monomer flow rate, and (d) surfactant concentration. The GP is trained on data points generated in the hardware-in-the-loop study involving TS-EMO. The shaded are represents the variance of the prediction at 0.32 mmol L^{-1} for (a). For (b), (c), and (d), the shaded area denotes the variance of the prediction at 68°C.

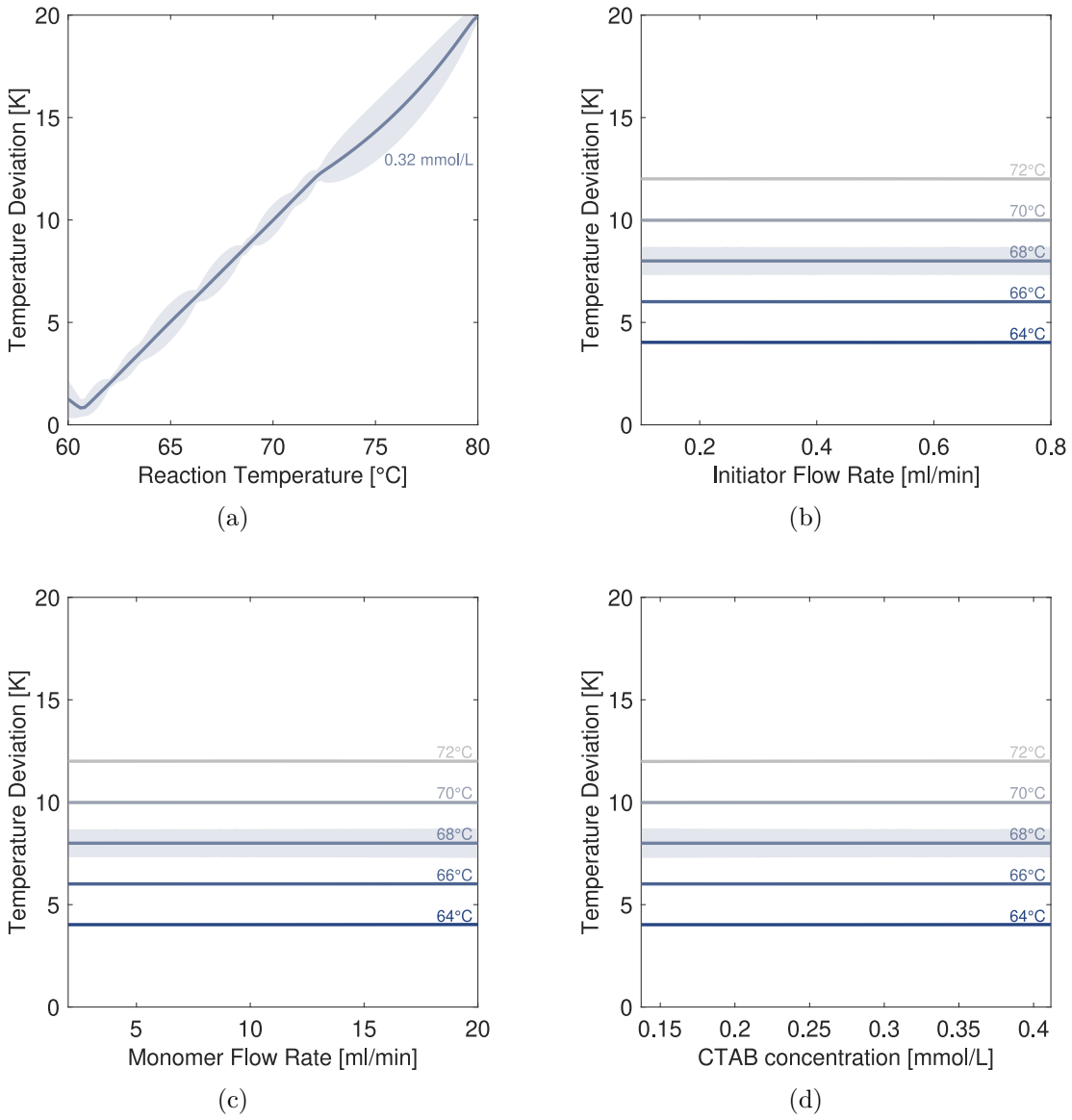

Figure C.3: GP prediction of temperature deviation as a function of: (a) reaction temperature, (b) initiator flow rate, (c) monomer flow rate, and (d) surfactant concentration. The GP is trained on data points generated in the hardware-in-the-loop study involving TS-EMO. The shaded are represents the variance of the prediction at 0.32 mmol L^{-1} for (a). For (b), (c), and (d), the shaded area denotes the variance of the prediction at 68°C.

C.2 Data Tables

C.2.1 Data Regarding Hardware-in-the-loop Study Involving TS-EMO

The data presented in Table C.1 enables the reconstruction of Figures 3, 4, and 6.

Table C.1: Hardware-in-the-loop input and output data.

# iteration	F_{I} [mL min^{-1}]	F_{M} [mL min^{-1}]	T [°C]	c_{CTAB} [mmol L^{-1}]	Δr_{H}^2 [nm^2]	F_{product} [mL min^{-1}]
0	0.34	4.86	71	0.16	9.00	-4.29
0	0.46	10.46	71	0.16	169.00	-4.53
0	0.8	7.80	71	0.16	42.25	-6.54
0	0.52	16.42	71	0.16	1,056.25	-2.49
0	0.44	9.45	80	0.41	1,225.00	-7.41
0	0.59	13.58	80	0.41	1,332.25	-8.75
0	0.21	4.04	80	0.41	729.00	-3.85
0	0.73	5.23	80	0.41	210.25	-5.50
0	0.74	3.67	62	0.33	1.00	-3.43
0	0.65	13.76	62	0.33	90.25	-0.20
0	0.11	5.51	62	0.33	110.25	0.00
1	0.70	13.12	72.2	0.34	1089.00	-5.42
1	0.11	6.51	72.2	0.34	6.25	-0.40
1	0.71	14.77	72.2	0.34	1260.25	-5.52
1	0.52	5.14	72.2	0.34	225.00	-5.06
1	0.10	14.03	72.2	0.34	64.00	0.00
2	0.77	2.60	66.3	0.37	30.25	-3.26
2	0.18	3.90	66.3	0.37	182.25	-2.83
2	0.73	3.80	66.3	0.37	144.00	-4.13
2	0.10	4.00	66.3	0.37	676.00	-1.56
2	0.17	3.30	66.3	0.37	484.00	-2.84
3	0.36	2.02	63.5	0.14	900.00	-2.15
3	0.58	5.96	63.5	0.14	289.00	-3.64
3	0.59	3.40	63.5	0.14	600.25	-3.39
3	0.56	10.64	63.5	0.14	132.25	-1.40
3	0.56	6.24	63.5	0.14	210.25	-4.25
4	0.80	9.91	69	0.29	121.00	-6.30
4	0.67	7.52	69	0.29	90.25	-6.13
4	0.46	6.97	69	0.29	144.00	-5.25
4	0.53	7.98	69	0.29	144.00	-5.88
5	0.44	3.58	62.4	0.21	196.00	-0.71
5	0.44	2.94	62.4	0.21	240.25	-0.49
6	0.77	6.70	62.3	0.41	210.25	-4.54
6	0.80	7.52	62.3	0.41	462.25	-6.14
7	0.61	5.53	68.5	0.35	81.00	-5.16
7	0.65	4.22	68.5	0.35	90.25	-4.46
7	0.19	2.68	68.5	0.35	196.00	-2.68
7	0.73	3.63	68.5	0.35	12.25	-4.08
7	0.53	3.06	68.5	0.35	42.25	-3.43
8	0.70	4.22	60.7	0.23	484.00	-0.54
8	0.60	2.66	60.7	0.23	16.00	-1.26
8	0.74	3.67	60.7	0.23	132.25	-0.90
8	0.70	3.03	60.7	0.23	529.00	-0.20

C.2.2 Data Regarding Global Deterministic Optimization Including MAiNGO

The data presented in Tables C.2 to C.5 enables the reconstruction of Figures 7 and 8.

Table C.2: Pareto optimal solutions calculated via MAiNGO for a upper bound on the input temperature of 80°C.

F_I [mL min^{-1}]	F_M [mL min^{-1}]	T [°C]	c_CTAB [mmol L^{-1}]	Δr_H^2 [nm^2]	F_product [mL min^{-1}]
0.73	8.44	68.52	0.34	25	-6.04
0.73	8.44	68.51	0.34	24	-6.04
0.73	8.44	68.50	0.34	23	-6.04
0.73	8.44	68.50	0.34	22	-6.03
0.73	8.43	68.49	0.34	21	-6.03
0.73	8.43	68.49	0.34	20	-6.02
0.73	8.42	68.48	0.34	19	-6.02
0.73	8.38	68.46	0.35	18	-6.01
0.73	7.69	68.46	0.35	17	-5.95
0.73	6.84	68.47	0.35	16	-5.76
0.73	5.98	68.48	0.35	15	-5.44
0.73	5.13	68.49	0.35	14	-5.01
0.73	4.27	68.49	0.35	13	-4.50
0.34	4.88	71.00	0.16	12	-4.30
0.34	4.87	71.00	0.16	11	-4.30
0.34	4.87	71.00	0.16	10	-4.29
0.74	6.63	62.00	0.33	9	-3.78
0.74	6.26	62.00	0.33	8	-3.70
0.74	5.88	62.00	0.33	7	-3.62
0.74	5.51	62.00	0.33	6	-3.54
0.74	5.14	62.00	0.33	5	-3.48
0.74	3.70	62.01	0.33	4	-3.44
0.74	3.69	62.01	0.33	3	-3.43
0.74	3.68	62.00	0.33	2	-3.43

Table C.3: Pareto optimal solutions calculated via MAiNGO for a upper bound on the input temperature of 70°C.

F_I $[\mathrm{mL\,min^{-1}}]$	F_M $[\mathrm{mL\,min^{-1}}]$	T [°C]	c_CTAB $[\mathrm{mmol\,L^{-1}}]$	Δr_H^2 $[\mathrm{nm^2}]$	F_product $[\mathrm{mL\,min^{-1}}]$
0.73	8.45	68.51	0.34	25	-6.04
0.73	8.44	68.51	0.34	24	-6.04
0.73	8.44	68.51	0.34	23	-6.04
0.73	8.44	68.50	0.34	22	-6.03
0.73	8.44	68.50	0.34	21	-6.03
0.73	8.43	68.49	0.34	20	-6.02
0.73	8.42	68.48	0.34	19	-6.02
0.73	8.36	68.47	0.35	18	-6.01
0.73	7.69	68.46	0.35	17	-5.95
0.73	6.84	68.47	0.35	16	-5.76
0.73	5.98	68.48	0.35	15	-5.44
0.73	5.13	68.49	0.35	14	-5.01
0.73	4.27	68.49	0.35	13	-4.50
0.74	7.57	62.01	0.33	12	-3.92
0.74	7.35	62.00	0.33	11	-3.90
0.74	7.00	62.00	0.33	10	-3.85
0.74	6.63	62.00	0.33	9	-3.78
0.74	6.26	62.00	0.33	8	-3.70
0.74	5.88	62.00	0.33	7	-3.62
0.74	5.51	62.00	0.33	6	-3.54
0.74	5.14	62.00	0.33	5	-3.48
0.74	3.70	62.01	0.33	4	-3.44
0.74	3.69	62.01	0.33	3	-3.43
0.74	3.68	62.00	0.33	2	-3.43

Table C.4: Pareto optimal solutions calculated via MAiNGO for a upper bound on the input temperature of 62°C.

F_I $[\mathrm{mL\,min^{-1}}]$	F_M $[\mathrm{mL\,min^{-1}}]$	T [°C]	c_CTAB $[\mathrm{mmol\,L^{-1}}]$	Δr_H^2 $[\mathrm{nm^2}]$	F_product $[\mathrm{mL\,min^{-1}}]$
0.74	7.78	62.00	0.34	25	-4.02
0.74	7.77	62.00	0.34	24	-4.02
0.74	7.77	62.00	0.34	23	-4.01
0.74	7.77	62.00	0.34	22	-4.00
0.74	7.76	62.00	0.34	21	-4.00
0.74	7.76	62.00	0.34	20	-3.99
0.74	7.75	62.00	0.34	19	-3.99
0.74	7.75	62.00	0.33	18	-3.98
0.74	7.74	62.00	0.33	17	-3.97
0.74	7.73	62.00	0.33	16	-3.96
0.74	7.72	62.00	0.33	15	-3.96
0.74	7.70	62.00	0.33	14	-3.95
0.74	7.67	62.00	0.33	13	-3.94
0.74	7.59	62.00	0.33	12	-3.92
0.74	7.35	62.00	0.33	11	-3.89
0.74	7.00	62.00	0.33	10	-3.84
0.74	6.63	62.00	0.33	9	-3.77
0.74	6.25	62.00	0.33	8	-3.69
0.74	5.88	62.00	0.33	7	-3.61
0.74	5.51	62.00	0.33	6	-3.54
0.74	5.14	62.00	0.33	5	-3.48
0.74	3.70	62.00	0.33	4	-3.43
0.74	3.69	62.00	0.33	3	-3.43
0.74	3.68	62.00	0.33	2	-3.43

Table C.5: Pareto optimal solutions calculated via MAiNGO for a upper bound on the input temperature of 61°C.

F_I $[\mathrm{mL\,min^{-1}}]$	F_M $[\mathrm{mL\,min^{-1}}]$	T [°C]	c_CTAB $[\mathrm{mmol\,L^{-1}}]$	Δr_H^2 $[\mathrm{nm^2}]$	F_product $[\mathrm{mL\,min^{-1}}]$
0.60	6.44	60.71	0.23	25	-1.55
0.60	6.01	60.71	0.23	24	-1.48
0.60	5.59	60.70	0.23	23	-1.40
0.60	5.16	60.70	0.23	22	-1.31
0.60	2.66	60.73	0.23	21	-1.27
0.60	2.66	60.72	0.23	20	-1.27
0.60	2.66	60.72	0.23	19	-1.27
0.60	2.66	60.71	0.23	18	-1.27
0.60	2.66	60.71	0.23	17	-1.26

Bibliography

[1] L. F. **Kaven**, H. J. M. Wolff, L. Wille, M. Wessling, A. Mitsos, and J. Viell. In-line Monitoring of Microgel Synthesis: Flow versus Batch Reactor. *Organic Process Research & Development*, 25(9):2039–2051, 2021. ISSN 1083-6160. doi: 10.1021/acs.oprd.1c00087.

[2] L. **Bering**, H. Wolff, M. Wessling, A. Mitsos, and J. Viell. Monitoring of Continuous Microgel Synthesis via In-line Raman Spectroscopy. *Conference presentation*, 13$^{\text{th}}$ International Workshop on Polymer Reaction Engineering, Hamburg, Germany, 2019.

[3] L. F. **Bering**, A. Mitsos, and J. Viell. Measurement Cells for In-line Raman Spectroscopy in Continuous Flow Reactors. *Conference poster*, 13$^{\text{th}}$ Interdisciplinary Ph.D. Seminar, Berlin, Germany, 2019.

[4] L. F. **Kaven**, H. J. Wolff, L. Wille, M. Wessling, , A. Mitsos, and J. Viell. Transfer of In-line Raman Spectroscopy in Precipitation Polymerization from Batch to Flow Reactor. *Conference poster*, EuroPACT2021, Online Event, 2021.

[5] E. D. Koronaki, L. F. **Kaven**, J. M. M. Faust, I. G. Kevrekidis, and A. Mitsos. Nonlinear Manifold Learning Determines Microgel Size from Raman Spectroscopy. *AIChE Journal*, page e18494, 2024. doi: 10.1002/aic.18494.

[6] L. F. **Kaven**, J. Keil, A. Mitsos, and J. Viell. Particle Size Determination from Indirect Hard Modeling Parameters. *Conference poster*, 15$^{\text{th}}$ Interdisciplinary Ph.D. Seminar, Online Event, 2021.

[7] L. F. **Kaven**, J. Keil, N. Wolter, T. Nevolianis, A. Pich, K. Leonhard, A. Mhamdi, and A. Mitsos. Dynamic modeling for synthesis of tailored microgels with charged domains. *Industrial & Engineering Chemistry Research*, 63(17):7727–7742, 2024. doi: 10.1021/acs.iecr.3c04433.

[8] L. F. **Kaven**, T. Nevolianis, N. Wolter, A. Mhamdi, A. Pich, A. Mitsos, and K. Leonhard. Identification of a dynamic model of the N-vinylcaprolactam-co-glycidyl methacrylate microgel synthesis. In A. C. Kokossis, M. C. Georgiadis, and S. Pistikopoulos, editors, *33rd European Symposium on Computer Aided Process Engineering*, volume 52 of *Computer-aided chemical engineering*, pages 807–812, Amsterdam, 2023. Elsevier. ISBN 978-0-443-23553-5. doi: 10.1016/B978-0-443-15274-0.50129-3.

[9] L. F. **Kaven**, T. Nevolianis, N. Wolter, A. Mhamdi, A. Pich, A. Mitsos, and K. Leonhard. Identification of a dynamic model of the N-vinylcaprolactam-co-glycidyl methacrylate microgel synthesis. In A. C. Kokossis, M. C. Georgiadis, and S. Pistikopoulos, editors, *33rd European Symposium on Computer Aided Process Engineering*, volume 52 of *Computer-aided chemical engineering*, pages 807–812. Elsevier, Amsterdam, 2023. ISBN 978-0-443-23553-5. doi: 10.1016/B978-0-443-15274-0.50129-3.

[10] L. F. **Kaven**, A. M. Schweidtmann, J. Keil, J. Israel, N. Wolter, and A. Mitsos. Data-driven Product-Process Optimization of N-isopropylacrylamide Microgel Flow-Synthesis. *Chemical Engineering Journal*, 479:147567, 2024. doi: 10.1016/j.cej.2023.147567.

[11] L. F. **Kaven**, J. Keil, A. M. Schweidtmann, N. Wolter, and A. Mitsos. Bayesian optimization of continuous microgel synthesis in the loop. *Conference presentation*, 14$^{\text{th}}$ International Workshop on Polymer Reaction Engineering, Potsdam, Germany, 2023.

[12] A. N. Ksiazkiewicz, L. **Bering**, F. Jung, N. A. Wolter, J. Viell, A. Mitsos, and A. Pich. Closing the 1–µm size gap: Temperature-programmed, fed-batch synthesis of µm-sized microgels. *Chemical Engineering Journal*, 379:122293, 2020. ISSN 13858947. doi: 10.1016/j.cej.2019.122293.

[13] P. Schäfer, L. F. **Bering**, A. Caspari, A. Mhamdi, and A. Mitsos. Nonlinear dynamic optimization for improved load-shifting agility of cryogenic air separation plants. In M. R. Eden, M. G. Ierapetritou, and G. P. Towler, editors, *13th International Symposium on Process Systems Engineering (PSE 2018)*, volume 44 of *Computer Aided Chemical Engineering*, pages 547–552. Elsevier, 2018. doi: https://doi.org/10.1016/B978-0-444-64241-7.50086-0. URL `https://www.sciencedirect.com/science/article/pii/B9780444642417500860`.

[14] T. Nevolianis, N. Wolter, L. F. **Kaven**, L. Krep, C. Huang, A. Mhamdi, A. Mitsos, A. Pich, and K. Leonhard. Kinetic Modeling of a Poly(N-vinylcaprolactam-co-glycidyl methacrylate) Microgel Synthesis: A Hybrid In Silico and Experimental Approach. *Industrial & Engineering Chemistry Research*, 62(2):893–902, 2023. ISSN 0888-5885. doi: 10.1021/acs.iecr.2c03291.

[15] J. V. Alemán, A. V. Chadwick, J. He, M. Hess, K. Horie, R. G. Jones, P. Kratochvíl, I. Meisel, I. Mita, G. Moad, S. Penczek, and R. F. T. Stepto. Definitions of terms relating to the structure and processing of sols, gels, networks, and inorganic-organic hybrid materials (IUPAC Recommendations 2007). *Pure and Applied Chemistry*, 79(10):1801–1829, 2007. ISSN 0033-4545. doi: 10.1351/pac200779101801.

[16] E. Daly and B. R. Saunders. Temperature–dependent electrophoretic mobility and hydrodynamic radius measurements of poly(N-isopropylacrylamide) microgel particles: Structural insights. *Physical Chemistry Chemical Physics*, 2(14):3187–3193, 2000. ISSN 14639076. doi: 10.1039/b002678f.

[17] R. Tiwari, T. Heuser, E. Weyandt, B. Wang, and A. Walther. Polyacid microgels with adaptive hydrophobic pockets and ampholytic character: synthesis, solution properties and insights into internal nanostructure by cryogenic-TEM. *Soft matter*, 11(42):8342–8353, 2015. doi: 10.1039/c5sm01327e.

[18] A. P. H. Gelissen, A. Scotti, S. K. Turnhoff, C. Janssen, A. Radulescu, A. Pich, A. A. Rudov, I. I. Potemkin, and W. Richtering. An anionic shell shields a cationic core allowing for uptake and release of polyelectrolytes within core-shell responsive microgels. *Soft matter*, 14(21):4287–4299, 2018. doi: 10.1039/c8sm00397a.

[19] O. Mergel, S. Schneider, R. Tiwari, P. T. Kühn, D. Keskin, M. C. A. Stuart, S. Schöttner, M. de Kanter, M. Noyong, T. Caumanns, J. Mayer, C. Janzen, U. Simon, M. Gallei, D. Wöll, P. van Rijn, and F. A. Plamper. Cargo shuttling by electrochemical switching of core-shell microgels obtained by a facile one-shot polymerization. *Chemical science*, 10(6):1844–1856, 2019. ISSN 2041-6520. doi: 10.1039/c8sc04369h.

[20] K. Marcisz, M. Mackiewicz, J. Romanski, Z. Stojek, and M. Karbarz. Significant, reversible change in microgel size using electrochemically induced volume phase transition. *Applied Materials Today*, 13:182–189, 2018. ISSN 23529407. doi: 10.1016/j.apmt.2018.09.006.

[21] X. Sui, L. Shui, J. Cui, Y. Xie, J. Song, A. van den Berg, M. A. Hempenius, and G. J. Vancso. Redox-responsive organometallic microgel particles prepared from poly(ferrocenylsilane)s generated using microfluidics. *Chemical communications (Cambridge, England)*, 50(23):3058–3060, 2014. doi: 10.1039/c3cc49501a.

[22] L. Zhang, M. W. Spears, and L. A. Lyon. Tunable swelling and rolling of microgel membranes. *Langmuir*, 30(26):7628–7634, 2014. ISSN 0743-7463. doi: 10.1021/la500860t.

[23] Q. M. Zhang, X. Li, M. R. Islam, M. Wei, and M. J. Serpe. Light switchable optical materials from azobenzene crosslinked poly(N-isopropylacrylamide)-based microgels. *J. Mater. Chem. C*, 2(34):6961–6965, 2014. ISSN 2050-7526. doi: 10.1039/C4TC00653D.

[24] Q. M. Zhang, W. Wang, Y.-Q. Su, E. J. M. Hensen, and M. J. Serpe. Biological Imaging and Sensing with Multiresponsive Microgels. *Chemistry of Materials*, 28(1):259–265, 2016. ISSN 0897-4756. doi: 10.1021/acs.chemmater.5b04028.

[25] A. Garcia, M. Marquez, T. Cai, R. Rosario, Z. Hu, D. Gust, M. Hayes, S. A. Vail, and C.-D. Park. Photo-, thermally, and pH-responsive microgels. *Langmuir*, 23(1):224–229, 2007. ISSN 0743-7463. doi: 10.1021/la061632n.

[26] R. Pelton. Temperature-sensitive aqueous microgels. *Advances in Colloid and Interface Science*, 85(1):1–33, 2000. ISSN 00018686. doi: 10.1016/S0001-8686(99)00023-8.

[27] M. Karg and T. Hellweg. New "smart" poly(NIPAM) microgels and nanoparticle microgel hybrids: Properties and advances in characterisation. *Current Opinion in Colloid & Interface Science*, 14(6):438–450, 2009. ISSN 13590294. doi: 10.1016/j.cocis.2009.08.002.

[28] A. Imaz and J. Forcada. New Biocompatible Microgels. *Macromolecular Symposia*, 281(1): 85–88, 2009. ISSN 1022-1360. doi: 10.1002/masy.200950711.

[29] N. A. Cortez-Lemus and A. Licea-Claverie. Poly(N-vinylcaprolactam), a comprehensive review on a thermoresponsive polymer becoming popular. *Progress in Polymer Science*, 53:1–51, 2016. ISSN 00796700. doi: 10.1016/j.progpolymsci.2015.08.001.

[30] M. Heskins and J. E. Guillet. Solution Properties of Poly(N-isopropylacrylamide). *Journal of Macromolecular Science: Part A - Chemistry*, 2(8):1441–1455, 1968. ISSN 0022-233X. doi: 10.1080/10601326808051910.

[31] G. Li, I. Varga, A. Kardos, I. Dobryden, and P. M. Claesson. Nanoscale Mechanical Properties of Core-Shell-like Poly-NIPAm Microgel Particles: Effect of Temperature and Cross-Linking Density. *The journal of physical chemistry. B*, 125(34):9860–9869, 2021. ISSN 1520-6106. doi: 10.1021/acs.jpcb.1c04173.

[32] A. Laukkanen, L. Valtola, F. M. Winnik, and H. Tenhu. Formation of Colloidally Stable Phase Separated Poly(N-vinylcaprolactam) in Water: A Study by Dynamic Light Scattering, Microcalorimetry, and Pressure Perturbation Calorimetry. *Macromolecules*, 37(6):2268–2274, 2004. ISSN 0024-9297. doi: 10.1021/ma035124l.

[33] M. Das, S. Mardyani, W. C. W. Chan, and E. Kumacheva. Biofunctionalized pH-Responsive Microgels for Cancer Cell Targeting: Rational Design. *Advanced Materials*, 18(1):80–83, 2006. ISSN 0935-9648. doi: 10.1002/adma.200501043.

[34] Y. Gao, A. Ahiabu, and M. J. Serpe. Controlled drug release from the aggregation-disaggregation behavior of pH-responsive microgels. *ACS applied materials & interfaces*, 6 (16):13749–13756, 2014. doi: 10.1021/am503200p.

[35] N. M. B. Smeets and T. Hoare. Designing responsive microgels for drug delivery applications. *Journal of Polymer Science Part A: Polymer Chemistry*, 51(14):3027–3043, 2013. ISSN 0887624X. doi: 10.1002/pola.26707.

[36] J. Singh and P. Nayak. pH –responsive polymers for drug delivery: Trends and opportunities. *Journal of Polymer Science*, 2023. ISSN 2642-4150. doi: 10.1002/pol.20230403.

[37] D. Keskin, O. Mergel, H. C. van der Mei, H. J. Busscher, and P. van Rijn. Inhibiting Bacterial Adhesion by Mechanically Modulated Microgel Coatings. *Biomacromolecules*, 20(1):243–253, 2019. doi: 10.1021/acs.biomac.8b01378.

[38] V. K. Switacz, S. K. Wypysek, R. Degen, J. J. Crassous, M. Spehr, and W. Richtering. Influence of Size and Cross-Linking Density of Microgels on Cellular Uptake and Uptake Kinetics. *Biomacromolecules*, 21(11):4532–4544, 2020. doi: 10.1021/acs.biomac.0c00478.

[39] C. Zhang, E. Gau, W. Sun, J. Zhu, B. M. Schmidt, A. Pich, and X. Shi. Influence of size, crosslinking degree and surface structure of poly(N-vinylcaprolactam)-based microgels on their penetration into multicellular tumor spheroids. *Biomaterials science*, 7(11):4738–4747, 2019. doi: 10.1039/c9bm01132c.

[40] P. Li, R. Xu, W. Wang, X. Li, Z. Xu, K. W. K. Yeung, and P. K. Chu. Thermosensitive poly(N-isopropylacrylamide-co-glycidyl methacrylate) microgels for controlled drug release. *Colloids and surfaces. B, Biointerfaces*, 101:251–255, 2013. doi: 10.1016/j.colsurfb.2012.07.009.

[41] S. R. Khan, S. Ali, B. Ullah, S. Jamil, and T. Zanib. Synthesis of iron nanoparticles in poly(N-isopropylacrylamide-acrylic acid) hybrid microgels for catalytic reduction of series of organic pollutants: A first approach. *Journal of Nanoparticle Research*, 22(7):72, 2020. ISSN 1388-0764. doi: 10.1007/s11051-020-04924-5.

[42] M. Hashaam, S. Ali, T. Khan, M. Salman, S. R. Khan, A. I. Aqib, T. Zaheer, S. Bibi, S. Jamil, M. S. Al-Sharif, S. F. Mahmoud, and W. Yao. Assembly of Smart Microgels and Hybrid Microgels on Graphene Sheets for Catalytic Reduction of Nitroarenes. *Catalysts*, 12(10):1172, 2022. doi: 10.3390/catal12101172.

[43] Z. H. Farooqi, K. Naseem, A. Ijaz, and R. Begum. Engineering of silver nanoparticle fabricated poly (N-isopropylacrylamide-co-acrylic acid) microgels for rapid catalytic reduction of nitrobenzene. *Journal of Polymer Engineering*, 36(1):87–96, 2016. ISSN 0334-6447. doi: 10.1515/polyeng-2015-0082.

[44] D. Schäfer, F. Fink, D. Kleinschmidt, K. Keisers, F. Thomas, A. Hoffmann, A. Pich, and S. Herres-Pawlis. Enhanced catalytic activity of copper complexes in microgels for aerobic oxidation of benzyl alcohols. *Chemical communications (Cambridge, England)*, 56(42):5601–5604, 2020. doi: 10.1039/d0cc02433c.

[45] Z. Zou, E. Gau, I. El-Awaad, F. Jakob, A. Pich, and U. Schwaneberg. Selective Functionalization of Microgels with Enzymes by Sortagging. *Bioconjugate chemistry*, 30(11):2859–2869, 2019. doi: 10.1021/acs.bioconjchem.9b00568.

[46] Y. Zhang, Y. Guan, and S. Zhou. Synthesis and volume phase transitions of glucose-sensitive microgels. *Biomacromolecules*, 7(11):3196–3201, 2006. doi: 10.1021/bm060557s.

[47] M. Faulde, E. Siemes, D. Wöll, and A. Jupke. Fluid Dynamics of Microgel-Covered Drops Reveal Impact on Interfacial Conditions. *Polymers*, 10(8), 2018. doi: 10.3390/polym10080809.

[48] M. Destribats, M. Eyharts, V. Lapeyre, E. Sellier, I. Varga, V. Ravaine, and V. Schmitt. Impact of pNIPAM microgel size on its ability to stabilize Pickering emulsions. *Langmuir : the ACS journal of surfaces and colloids*, 30(7):1768–1777, 2014. doi: 10.1021/la4044396.

[49] W. Richtering. Responsive emulsions stabilized by stimuli-sensitive microgels: Emulsions with special non-Pickering properties. *Langmuir : the ACS journal of surfaces and colloids*, 28(50): 17218–17229, 2012. doi: 10.1021/la302331s.

[50] A. Pich and W. Richtering. Microgels by Precipitation Polymerization: Synthesis, Characterization, and Functionalization. In A. Pich and W. Richtering, editors, *Chemical Design of Responsive Microgels*, volume 234, pages 1–37. Springer Berlin Heidelberg, Berlin, Heidelberg, 2011. doi: 10.1007/12$\backslash$textunderscore.

[51] M. Kather, F. Ritter, and A. Pich. Surfactant-free synthesis of extremely small stimuli-responsive colloidal gels using a confined impinging jet reactor. *Chemical Engineering Journal*, 344:375–379, 2018. ISSN 13858947. doi: 10.1016/j.cej.2018.03.082.

[52] F. Schneider, A. Balaceanu, A. Feoktystov, V. Pipich, Y. Wu, J. Allgaier, W. Pyckhout-Hintzen, A. Pich, and G. J. Schneider. Monitoring the internal structure of poly(N-vinylcaprolactam) microgels with variable cross-link concentration. *Langmuir : the ACS journal of surfaces and colloids*, 30(50):15317–15326, 2014. doi: 10.1021/la503830w.

[53] R. Acciaro, T. Gilányi, and I. Varga. Preparation of Monodisperse Poly(N-isopropylacrylamide) Microgel Particles with Homogenous Cross-Link Density Distribution. *Langmuir*, 27(12):7917–7925, 2011. ISSN 0743-7463. doi: 10.1021/la2010387.

[54] H. J. M. Wolff, M. Kather, H. Breisig, W. Richtering, A. Pich, and M. Wessling. From Batch to Continuous Precipitation Polymerization of Thermoresponsive Microgels. *ACS applied materials & interfaces*, 10(29):24799–24806, 2018. doi: 10.1021/acsami.8b06920.

[55] P. Fandrich, L. Wiehemeier, M. Dirksen, O. Wrede, T. Kottke, and T. Hellweg. Acrylamide precipitation polymerization in a continuous flow reactor: An in situ FTIR study reveals kinetics. *Colloid and Polymer Science*, 299(2):221–232, 2020. ISSN 0303-402X. doi: 10.1007/s00396-020-04762-w.

[56] P. Fandrich, J. Esteban Vázquez, R. Haverkamp, and T. Hellweg. Growth of Smart Microgels in a Flow Reactor Scrutinized by In-Line SAXS. *Langmuir : the ACS journal of surfaces and colloids*, 2023. doi: 10.1021/acs.langmuir.2c02796.

[57] J. Meyer-Kirschner, M. Kather, A. Pich, D. Engel, W. Marquardt, J. Viell, and A. Mitsos. Inline monitoring of monomer and polymer content during microgel synthesis using precipitation polymerization via raman spectroscopy and indirect hard modeling. *Applied spectroscopy*, 70 (3):416–426, 2016. doi: 10.1177/0003702815626663.

[58] J. Meyer-Kirschner, A. Mitsos, and J. Viell. Polymer particle sizing from Raman spectra by regression of hard model parameters. *Journal of Raman Spectroscopy*, 49(8):1402–1411, 2018. ISSN 0377-0486. doi: 10.1002/jrs.5387.

[59] B. Boldrini, W. Kessler, K. Rebner, and R. W. Kessler. Hyperspectral Imaging: A Review of Best Practice, Performance and Pitfalls for in-line and on-line Applications. *Journal of Near Infrared Spectroscopy*, 20(5):483–508, 2012. ISSN 0967-0335. doi: 10.1255/jnirs.1003.

[60] M. M. Reis, P. H. Araújo, C. Sayer, and R. Giudici. Evidences of correlation between polymer particle size and Raman scattering. *Polymer*, 44(20):6123–6128, 2003. ISSN 00323861. doi: 10.1016/S0032-3861(03)00669-4.

[61] M. van den Brink, M. Pepers, and A. M. van Herk. Raman spectroscopy of polymer latexes. *Journal of Raman Spectroscopy*, 33(4):264–272, 2002. ISSN 0377-0486. doi: 10.1002/jrs.834.

[62] K. Ito, T. Kato, and T. Ona. Non-destructive method for the quantification of the average particle diameter of latex as water-based emulsions by near-infrared Fourier transform Raman spectroscopy. *Journal of Raman Spectroscopy*, 33(6):466–470, 2002. ISSN 0377-0486. doi: 10.1002/jrs.860.

[63] C. Houben, G. Nurumbetov, D. Haddleton, and A. A. Lapkin. Feasibility of the Simultaneous Determination of Monomer Concentrations and Particle Size in Emulsion Polymerization Using in Situ Raman Spectroscopy. *Industrial & Engineering Chemistry Research*, 54(51):12867–12876, 2015. ISSN 0888-5885. doi: 10.1021/acs.iecr.5b02759.

[64] P. M. N. Ambrogi, M. M. E. Colmán, and R. Giudici. Miniemulsion Polymerization Monitoring Using Off-Line Raman Spectroscopy and In-Line NIR Spectroscopy. *Macromolecular Reaction Engineering*, 11(4):1600013, 2017. ISSN 1862832X. doi: 10.1002/mren.201600013.

[65] F. A. Plamper and W. Richtering. Functional Microgels and Microgel Systems. *Accounts of chemical research*, 50(2):131–140, 2017. doi: 10.1021/acs.accounts.6b00544.

[66] F. Jung, F. A. L. Janssen, A. Ksiazkiewicz, A. Caspari, A. Mhamdi, A. Pich, and A. Mitsos. Identifiability analysis and parameter estimation of microgel synthesis: A set-membership approach. *Industrial & Engineering Chemistry Research*, 58(30):13675–13685, 2019. ISSN 0888-5885. doi: 10.1021/acs.iecr.8b05274.

[67] F. Jung, A. Ksiazkiewicz, A. Mhamdi, A. Pich, and A. Mitsos. Model-based Prediction of the Hydrodynamic Radius of Collapsed Microgels and Experimental Validation. *Chemical Engineering Journal*, 378(8):121740, 2019. ISSN 13858947. doi: 10.1016/j.cej.2019.05.101.

[68] S. Schneider, F. Jung, O. Mergel, J. Lammertz, A. C. Nickel, T. Caumanns, A. Mhamdi, J. Mayer, A. Mitsos, and F. A. Plamper. Model-based design and synthesis of ferrocene containing microgels. *Polymer Chemistry*, 11(2):315–325, 2020. ISSN 1759-9954. doi: 10.1039/C9PY00494G.

[69] F. Jung, A. Ksiazkiewicz, A. Mhamdi, A. Pich, and A. Mitsos. Model-Based Optimization of Microgel Synthesis in the µm Size Range. *Industrial & Engineering Chemistry Research*, 59 (46):20437–20446, 2020. ISSN 0888-5885. doi: 10.1021/acs.iecr.0c04286.

[70] P. W. Zhu and D. H. Napper. Light scattering studies of poly(N-isopropylacrylamide) microgel particles in mixed water-acetic acid solvents. *Macromolecular Chemistry and Physics*, 200(8):1950–1955, 1999. ISSN 10221352. doi: 10.1002/(SICI)1521-3935(19990801)200:8{\textless}1950::AID-MACP1950{\textgreater}3.0.CO;2-R.

[71] S. Nikolov, A. Fernandez-Nieves, and A. Alexeev. Mesoscale modeling of microgel mechanics and kinetics through the swelling transition. *Applied Mathematics and Mechanics*, 39(1):47–62, 2018. ISSN 0253-4827. doi: 10.1007/s10483-018-2259-6.

[72] B. R. Saunders, N. Laajam, E. Daly, S. Teow, X. Hu, and R. Stepto. Microgels: From responsive polymer colloids to biomaterials. *Advances in Colloid and Interface Science*, 147-148:251–262, 2009. ISSN 00018686. doi: 10.1016/j.cis.2008.08.008.

[73] M. Brugnoni, A. C. Nickel, L. C. Kröger, A. Scotti, A. Pich, K. Leonhard, and W. Richtering. Synthesis and structure of deuterated ultra-low cross-linked poly(N-isopropylacrylamide) microgels. *Polymer Chemistry*, 10(19):2397–2405, 2019. ISSN 1759-9954. doi: 10.1039/C8PY01699B.

[74] R. Keidel, A. Ghavami, D. M. Lugo, G. Lotze, O. Virtanen, P. Beumers, J. S. Pedersen, A. Bardow, R. G. Winkler, and W. Richtering. Time-resolved structural evolution during the collapse of responsive hydrogels: The microgel-to-particle transition. *Science advances*, 4(4): eaao7086, 2018. doi: 10.1126/sciadv.aao7086.

[75] M. Andersson and S. L. Maunu. Structural studies of poly(N–isopropylacrylamide) microgels: Effect of SDS surfactant concentration in the microgel synthesis. *Journal of Polymer Science Part B: Polymer Physics*, 44(23):3305–3314, 2006. ISSN 08876266. doi: 10.1002/polb.20971.

[76] F. A. L. Janssen, M. Kather, A. Ksiazkiewicz, A. Pich, and A. Mitsos. Synthesis of Poly(N-vinylcaprolactam)-Based Microgels by Precipitation Polymerization: Pseudo-Bulk Model for Particle Growth and Size Distribution. *ACS omega*, 4(9):13795–13807, 2019. doi: 10.1021/acsomega.9b01335.

[77] R. Hidalgo-Alvarez. *Structure and Functional Properties of Colloidal Systems*. CRC Press, 2009. doi: 10.1201/9781420084474.

[78] C. V. Raman. A new radiation. *Proceedings of the Indian Academy of Sciences - Section A*, 37 (3):333–341, 1953. ISSN 0370-0089. doi: 10.1007/BF03052651.

[79] F. Alsmeyer, H.-J. Koss, and W. Marquardt. Indirect Spectral Hard Modeling for the Analysis of Reactive and Interacting Mixtures. *Applied spectroscopy*, 58(8):975–985, 2004. doi: 10.1366/0003702041655368.

[80] E. Kriesten, F. Alsmeyer, A. Bardow, and W. Marquardt. Fully automated indirect hard modeling of mixture spectra. *Chemometrics and Intelligent Laboratory Systems*, 91(2):181–193, 2008. ISSN 01697439. doi: 10.1016/j.chemolab.2007.11.004.

[81] A. Echtermeyer, C. Marks, A. Mitsos, and J. Viell. Inline Raman Spectroscopy and Indirect Hard Modeling for Concentration Monitoring of Dissociated Acid Species. *Applied spectroscopy*, 75(5):506–519, 2021. doi: 10.1177/0003702820973275.

[82] A. W. W. Echtermeyer. *Inline spectroscopy with model-based spectra evaluation for biorefinery unit operations*. PhD thesis, RWTH Aachen University, 2022.

[83] T. Hoare and D. McLean. Multi-Component Kinetic Modeling for Controlling Local Compositions in Thermosensitive Polymers. *Macromolecular Theory and Simulations*, 15(8):619–632, 2006. ISSN 1022-1344. doi: 10.1002/mats.200600031.

[84] T. Hoare and D. McLean. Kinetic prediction of functional group distributions in thermosensitive microgels. *The journal of physical chemistry. B*, 110(41):20327–20336, 2006. ISSN 1520-6106. doi: 10.1021/jp0643451.

[85] F. A. L. Janssen, M. Kather, L. C. Kröger, A. Mhamdi, K. Leonhard, A. Pich, and A. Mitsos. Synthesis of Poly(N-vinylcaprolactam)-Based Microgels by Precipitation Polymerization: Process Modeling and Experimental Validation. *Industrial & Engineering Chemistry Research*, 56 (49):14545–14556, 2017. ISSN 0888-5885. doi: 10.1021/acs.iecr.7b03263.

[86] F. A. Janssen, A. Ksiazkiewicz, M. Kather, L. C. Kröger, A. Mhamdi, K. Leonhard, A. Pich, and A. Mitsos. Kinetic Modeling of Precipitation Terpolymerization for Functional Microgels. In *28th European Symposium on Computer Aided Process Engineering*, volume 43 of *Computer Aided Chemical Engineering*, pages 109–114. Elsevier, 2018. ISBN 9780444642356. doi: 10.1016/B978-0-444-64235-6.50021-8.

[87] O. L. J. Virtanen, M. Kather, J. Meyer-Kirschner, A. Melle, A. Radulescu, J. Viell, A. Mitsos, A. Pich, and W. Richtering. Direct Monitoring of Microgel Formation during Precipitation Polymerization of N-Isopropylacrylamide Using in Situ SANS. *ACS omega*, 4(2):3690–3699, 2019. doi: 10.1021/acsomega.8b03461.

[88] Y. Nishizawa, H. Minato, T. Inui, T. Uchihashi, and D. Suzuki. Nanostructures, Thermoresponsiveness, and Assembly Mechanism of Hydrogel Microspheres during Aqueous Free-Radical Precipitation Polymerization. *Langmuir*, 37(1):151–159, 2021. ISSN 0743-7463. doi: 10.1021/acs.langmuir.0c02654.

[89] T. Alfrey and C. C. Price. Relative reactivities in vinyl copolymerization. *Journal of Polymer Science*, 2(1):101–106, 1947. ISSN 2642-4150. doi: 10.1002/pol.1947.120020112.

[90] G. Odian. *Principles of Polymerization*. Wiley, 2004. doi: 10.1002/047147875X.

[91] F. R. Mayo and F. M. Lewis. Copolymerization. I. A Basis for Comparing the Behavior of Monomers in Copolymerization; The Copolymerization of Styrene and Methyl Methacrylate. *Journal of the American Chemical Society*, 66(9):1594–1601, 1944. doi: 10.1021/ja01237a052.

[92] C. Kiparissides. Polymerization reactor modeling: A review of recent developments and future directions. *Chemical Engineering Science*, 51(10):1637–1659, 1996. ISSN 00092509. doi: 10.1016/0009-2509(96)00024-3.

[93] L. **Kaven**, H. Wolff, L. Wille, M. Wessling, A. Mitsos, and J. Viell. Dataset to: In-line Monitoring of Microgel Synthesis: Flow Versus Batch Reactor, 2021. doi:10.18154/RWTH-2021-09666.

[94] M. H. Reis, F. A. Leibfarth, and L. M. Pitet. Polymerizations in Continuous Flow: Recent Advances in the Synthesis of Diverse Polymeric Materials. *ACS Macro Letters*, 9(1):123–133, 2020. ISSN 2161-1653. doi: 10.1021/acsmacrolett.9b00933.

[95] C. Minnich, S. Hardy, and S. Krämer. Stopping the Babylonian Confusion: An Updated Nomenclature for Process Analyzers in PAT Applications. *Chemie Ingenieur Technik*, 88(6):694–697, 2016. ISSN 0009286X. doi: 10.1002/cite.201500188.

[96] X. Chen, K. Laughlin, J. R. Sparks, L. Linder, V. Farozic, H. Masser, and M. Petr. In Situ Monitoring of Emulsion Polymerization by Raman Spectroscopy: A Robust and Versatile Chemometric Analysis Method. *Organic Process Research & Development*, 19(8):995–1003, 2015. ISSN 1083-6160. doi: 10.1021/acs.oprd.5b00045.

[97] E. Dropsit, S. Hoppe, D. Chapron, A. Durand, and P. Bourson. In situ conversion monitoring of styrene emulsion polymerization by deconvolution of a single reference band near 1,000 cm −1. *Journal of Raman Spectroscopy*, 50(12):1938–1948, 2019. ISSN 0377-0486. doi: 10.1002/jrs.5738.

[98] O. Elizalde, J. R. Leiza, and J. M. Asua. On-line monitoring of all-acrylic emulsion polymerization reactors by Raman spectroscopy. *Macromolecular Symposia*, 206(1):135–148, 2004. ISSN 1022-1360. doi: 10.1002/masy.200450211.

[99] M. Gheghiani, N. Caillol, S. Henrot, T. F. L. McKenna, and N. Sheibat-Othman. Monitoring of polymer content in an emulsion polymerization using spatially resolved spectroscopy in the near infrared region and Raman spectroscopy. *Polymer Engineering & Science*, 34:1188, 2020. ISSN 0032-3888. doi: 10.1002/pen.25467.

[100] C. Houben and A. A. Lapkin. Automatic discovery and optimization of chemical processes. *Current Opinion in Chemical Engineering*, 9:1–7, 2015. ISSN 22113398. doi: 10.1016/j.coche.2015.07.001.

[101] J. Meyer-Kirschner, A. Mitsos, and J. Viell. Reliable Spectroscopic Process Monitoring using an Optimal Acquisition Time Procedure Determined by Signal-to-Noise Ratio. *Measurement*, pages 100–105, 2018. ISSN 02632241. doi: 10.1016/j.measurement.2018.02.061.

[102] S. Mozharov, A. Nordon, D. Littlejohn, C. Wiles, P. Watts, P. Dallin, and J. M. Girkin. Improved method for kinetic studies in microreactors using flow manipulation and noninvasive Raman spectrometry. *Journal of the American Chemical Society*, 133(10):3601–3608, 2011. doi: 10.1021/ja1102234.

[103] V. Sans and L. Cronin. Towards dial-a-molecule by integrating continuous flow, analytics and self-optimisation. *Chemical Society reviews*, 45(8):2032–2043, 2016. doi: 10.1039/c5cs00793c.

[104] S. Mozharov, A. Nordon, J. M. Girkin, and D. Littlejohn. Non-invasive analysis in microreactors using Raman spectrometry with a specially designed probe. *Lab on a chip*, 10(16):2101–2107, 2010. ISSN 1473-0197. doi: 10.1039/c004248j.

[105] S.-A. Leung, R. F. Winkle, R. C. R. Wootton, and A. J. deMello. A method for rapid reaction optimisation in continuous-flow microfluidic reactors using online Raman spectroscopic detection. *The Analyst*, 130(1):46–51, 2005. ISSN 0003-2654. doi: 10.1039/b412069h.

[106] S. Schwolow, F. Braun, M. Rädle, N. Kockmann, and T. Röder. Fast and Efficient Acquisition of Kinetic Data in Microreactors Using In-Line Raman Analysis. *Organic Process Research & Development*, 19(9):1286–1292, 2015. ISSN 1083-6160. doi: 10.1021/acs.oprd.5b00184.

[107] G. Rinke, A. Ewinger, S. Kerschbaum, and M. Rinke. In situ Raman spectroscopy to monitor the hydrolysis of acetal in microreactors. *Microfluidics and Nanofluidics*, 10(1):145–153, 2011. ISSN 1613-4982. doi: 10.1007/s10404-010-0654-8.

[108] E. Cao, M. Sankar, S. Firth, K. F. Lam, D. Bethell, D. K. Knight, G. J. Hutchings, P. F. McMillan, and A. Gavriilidis. Reaction and Raman spectroscopic studies of alcohol oxidation on gold–palladium catalysts in microstructured reactors. *Chemical Engineering Journal*, 167 (2-3):734–743, 2011. ISSN 13858947. doi: 10.1016/j.cej.2010.08.082.

[109] S. E. Barnes, Z. T. Cygan, J. K. Yates, K. L. Beers, and E. J. Amis. Raman spectroscopic monitoring of droplet polymerization in a microfluidic device. *The Analyst*, 131(9):1027–1033, 2006. ISSN 0003-2654. doi: 10.1039/b603693g.

[110] T. A. Hamlin and N. E. Leadbeater. Raman spectroscopy as a tool for monitoring mesoscale continuous-flow organic synthesis: Equipment interface and assessment in four medicinally-relevant reactions. *Beilstein journal of organic chemistry*, 9:1843–1852, 2013. ISSN 1860-5397. doi: 10.3762/bjoc.9.215.

[111] T. A. Hamlin and N. E. Leadbeater. Real-time Monitoring of Reactions Performed Using Continuous-flow Processing: The Preparation of 3-Acetylcoumarin as an Example. *Journal of visualized experiments : JoVE*, 105:e52393, 2015. doi: 10.3791/52393.

[112] G. Chaplain, S. J. Haswell, P. D. I. Fletcher, S. M. Kelly, and A. Mansfield. Development and Evaluation of a Raman Flow Cell for Monitoring Continuous Flow Reactions. *Australian Journal of Chemistry*, 66(2):208, 2013. ISSN 0004-9425. doi: 10.1071/CH12379.

[113] F. Feidl, S. Garbellini, S. Vogg, M. Sokolov, J. Souquet, H. Broly, A. Butté, and M. Morbidelli. A new flow cell and chemometric protocol for implementing in-line Raman spectroscopy in chromatography. *Biotechnology progress*, 35(5):e2847, 2019. doi: 10.1002/btpr.2847.

[114] J. Huang, S. Romero-Torres, and M. Moshgbar. Practical considerations in data pre-treatment for NIR and Raman spectroscopy. *American Pharmaceutical Review*, (13):116–127, 2010.

[115] A. Balaceanu, V. Mayorga, W. Lin, M.-P. Schürings, D. E. Demco, A. Böker, M. A. Winnik, and A. Pich. Copolymer microgels by precipitation polymerisation of N-vinylcaprolactam and N-isopropylacrylamides in aqueous medium. *Colloid and Polymer Science*, 291(1):21–31, 2013. ISSN 0303-402X. doi: 10.1007/s00396-012-2659-1.

[116] C. G. Malmberg and A. A. Maryott. Dielectric constant of water from 0°to 100°C. *Journal of Research of the National Bureau of Standards*, 56(1):1–8, 1956.

[117] C. G. Malmberg. Dielectric constant of deuterium oxide. *Journal of Research of the National Bureau of Standards*, 60(6):609–612, 1958.

[118] L. F. **Kaven** and A. Mitsos. Dataset to: "Nonlinear Manifold Learning Determines Microgel Size from Raman Spectroscopy", 2023. doi:10.18154/RWTH-2023-05604.

[119] W. Chew and P. Sharratt. Trends in process analytical technology. *Analytical Methods*, 2(10): 1412, 2010. ISSN 1759-9660. doi: 10.1039/c0ay00257g.

[120] T. de Beer, A. Burggraeve, M. Fonteyne, L. Saerens, J. P. Remon, and C. Vervaet. Near infrared and Raman spectroscopy for the in-process monitoring of pharmaceutical production processes. *International journal of pharmaceutics*, 417(1-2):32–47, 2011. ISSN 0378-5173. doi: 10.1016/j.ijpharm.2010.12.012.

[121] A. L. Pomerantsev and O. Y. Rodionova. Process analytical technology: a critical view of the chemometricians. *Journal of Chemometrics*, 26(6):299–310, 2012. ISSN 08869383. doi: 10.1002/cem.2445.

[122] L. L. Simon, H. Pataki, G. Marosi, F. Meemken, K. Hungerbühler, A. Baiker, S. Tummala, B. Glennon, M. Kuentz, G. Steele, H. J. M. Kramer, J. W. Rydzak, Z. Chen, J. Morris, F. Kjell, R. Singh, R. Gani, K. V. Gernaey, M. Louhi-Kultanen, J. O'Reilly, N. Sandler, O. Antikainen, J. Yliruusi, P. Frohberg, J. Ulrich, R. D. Braatz, T. Leyssens, M. von Stosch, R. Oliveira, R. B. H. Tan, H. Wu, M. Khan, Des O'Grady, A. Pandey, R. Westra, E. Delle-Case, D. Pape, D. Angelosante, Y. Maret, O. Steiger, M. Lenner, K. Abbou-Oucherif, Z. K. Nagy, J. D. Litster, V. K. Kamaraju, and M.-S. Chiu. Assessment of Recent Process Analytical Technology (PAT) Trends: A Multiauthor Review. *Organic Process Research & Development*, 19(1):3–62, 2015. ISSN 1083-6160. doi: 10.1021/op500261y.

[123] A. Beer. Bestimmung der Absorption des rothen Lichts in farbigen Flüssigkeiten. *Annalen der Physik und Chemie*, 162(5):78–88, 1852. ISSN 00033804. doi: 10.1002/andp.18521620505.

[124] F. Marini, R. Bucci, A. L. Magrì, and A. D. Magrì. Artificial neural networks in chemometrics: History, examples and perspectives. *Microchemical Journal*, 88(2):178–185, 2008. ISSN 0026265X. doi: 10.1016/j.

[125] M. Garrido, F. X. Rius, and M. S. Larrechi. Multivariate curve resolution-alternating least squares (MCR-ALS) applied to spectroscopic data from monitoring chemical reactions processes. *Analytical and bioanalytical chemistry*, 390(8):2059–2066, 2008. doi: 10.1007/s00216-008-1955-6.

[126] C. F. Bohren and D. R. Huffman. *Absorption and Scattering of Light by Small Particles*. Wiley, 1998. doi: 10.1002/9783527618156.

[127] R. R. Coifman and S. Lafon. Diffusion maps. *Applied and Computational Harmonic Analysis*, 21(1):5–30, 2006.

[128] B. Nadler, S. Lafon, R. R. Coifman, and I. G. Kevrekidis. Diffusion maps, spectral clustering and reaction coordinates of dynamical systems. *Applied and Computational Harmonic Analysis*, 21(1):113–127, 2006.

[129] R. R. Coifman, I. G. Kevrekidis, S. Lafon, M. Maggioni, and B. Nadler. Diffusion maps, reduction coordinates, and low dimensional representation of stochastic systems. *Multiscale Modeling & Simulation*, 7(2):842–864, 2008.

[130] N. Evangelou, N. J. Wichrowski, G. A. Kevrekidis, F. Dietrich, M. Kooshkbaghi, S. McFann, and I. G. Kevrekidis. On the parameter combinations that matter and on those that do not: data-driven studies of parameter (non)identifiability. *PNAS Nexus*, 1(4):pgac154, 09 2022. ISSN 2752-6542. doi: 10.1093/pnasnexus/pgac154. URL `https://doi.org/10.1093/pnasnexus/pgac154`.

[131] E. D. Koronaki, N. Evangelou, Y. M. Psarellis, A. G. Boudouvis, and I. G. Kevrekidis. From partial data to out-of-sample parameter and observation estimation with diffusion maps and geometric harmonics. *Computers & Chemical Engineering*, 178:108357, 2023. ISSN 0098-1354. doi: https://doi.org/10.1016/j.compchemeng.2023.108357. URL `https://www.sciencedirect.com/science/article/pii/S0098135423002272`.

[132] N. Evangelou, F. Dietrich, E. Chiavazzo, D. Lehmberg, M. Meila, and I. G. Kevrekidis. Double Diffusion Maps and their Latent Harmonics for Scientific Computations in Latent Space. *arXiv preprint arXiv:2204.12536*, 2022.

[133] Y. M. Psarellis, S. Lee, T. Bhattacharjee, S. S. Datta, J. M. Bello-Rivas, and I. G. Kevrekidis. Data-driven discovery of chemotactic migration of bacteria via machine learning. *arXiv preprint arXiv:2208.11853*, 2022.

[134] R. R. Coifman and S. Lafon. Geometric harmonics: a novel tool for multiscale out-of-sample extension of empirical functions. *Applied and Computational Harmonic Analysis*, 21(1):31–52, 2006.

[135] E. Chiavazzo, C. W. Gear, C. J. Dsilva, N. Rabin, and I. G. Kevrekidis. Reduced models in chemical kinetics via nonlinear data-mining. *Processes*, 2(1):112–140, 2014.

[136] E. J. Nyström. *Über die praktische Auflösung von linearen Integralgleichungen mit Anwendungen auf Randwertaufgaben der Potentialtheorie*. Akademische Buchhandlung, 1929.

[137] C. Fowlkes, S. Belongie, and J. Malik. Efficient spatiotemporal grouping using the Nystrom method. In *Proceedings of the 2001 IEEE Computer Society Conference on Computer Vision and Pattern Recognition. CVPR 2001*, volume 1, pages I–I. IEEE, 2001.

[138] C. J. Dsilva, R. Talmon, R. R. Coifman, and I. G. Kevrekidis. Parsimonious representation of nonlinear dynamical systems through manifold learning: A chemotaxis case study. *Applied and Computational Harmonic Analysis*, 44(3):759–773, 2018.

[139] E. Koronaki, L. F. **Kaven**, J. M. M. Faust, I. G. Kevrekidis, and A. Mitsos. Code to: Nonlinear Manifold Learning Determines Microgel Size from Raman Spectroscopy, 2023. https://gitlab.com/eleni.koronaki/mlforpolymersizeraman.git.

[140] M. I. Ltd. Zetasizer Nano technical note MRK728-01 - The accuracy and precision expected from dynamic light scattering measurements, 2006. `https://kdsi.ru/upload/iblock/357/be4ecfa4fcce215f870e4acb8eb229d6.pdf`.

[141] L. F. **Kaven**, J. Keil, and A. Mitsos. Dataset to: "Monitoring and Modeling of the N-isopropylacrylamide-co-Methacrylic Acid Microgel Synthesis", 2023. doi:`10.18154/RWTH-2023-09503`.

[142] M. J. Snowden, B. Z. Chowdhry, B. Vincent, and G. E. Morris. Colloidal copolymer microgels of N-isopropylacrylamide and acrylic acid: pH, ionic strength and temperature effects. *Journal of the Chemical Society, Faraday Transactions*, 92(24):5013, 1996. ISSN 0956-5000. doi: 10.1039/FT9969205013.

[143] S. Zhou and B. Chu. Synthesis and Volume Phase Transition of Poly(methacrylic acid-co-N-isopropylacrylamide) Microgel Particles in Water. *The journal of physical chemistry. B*, 102 (8):1364–1371, 1998. ISSN 1520-6106. doi: 10.1021/jp972990p.

[144] A. Khan. Preparation and characterization of N-isopropylacrylamide/acrylic acid copolymer core-shell microgel particles. *Journal of Colloid and Interface Science*, 313(2):697–704, 2007. ISSN 00219797. doi: 10.1016/j.jcis.2007.05.027.

[145] X. Xing, Z. Li, and T. Ngai. pH-Controllable Depletion Attraction Induced by Microgel Particles. *Macromolecules*, 42(19):7271–7274, 2009. ISSN 0024-9297. doi: 10.1021/ma901130x.

[146] C. E. Belman-Flores, W. Herrera-Kao, R. F. Vargas-Coronado, A. May-Pat, A. I. Oliva, N. Rodríguez-Fuentes, H. Vázquez-Torres, J. V. Cauich-Rodríguez, and J. M. Cervantes-Uc. Synthesis and characterization of pH sensitive hydrogel nanoparticles based on poly(N-isopropyl acrylamide-co-methacrylic acid). *Journal of Materials Science: Materials in Medicine*, 31(8): 61, 2020. ISSN 1573-4838. doi: 10.1007/s10856-020-06400-x.

[147] S. R. Khan, S. Jamil, S. Li, and A. Sultan. Acrylic Acid and Methacrylic Acid Based Microgel Catalysts for Reduction of 4-Nitrophenol. *Russian Journal of Physical Chemistry A*, 92(13): 2656–2664, 2018. ISSN 1531-863X. doi: 10.1134/S003602441901014X.

[148] J. P. Pinheiro, L. Moura, R. Fokkink, and J. P. S. Farinha. Preparation and Characterization of Low Dispersity Anionic Multiresponsive Core-Shell Polymer Nanoparticles. *Langmuir*, 28 (13):5802–5809, 2012. doi: 10.1021/la2045477.

[149] D. V. Subotic and X. Y. Wu. Interactions of poly(n-isopropylacrylamide-co-methacrylic acid) with poly(n-vinylpyrrolidone). *Industrial & Engineering Chemistry Research*, 36(4):1302–1309, 1997. doi: 10.1021/ie9604987.

[150] M. Martinez-Moro, J. Jenczyk, J. M. Giussi, S. Jurga, and S. E. Moya. Kinetics of the thermal response of poly(N-isopropylacrylamide co methacrylic acid) hydrogel microparticles under different environmental stimuli: A time-lapse NMR study. *Journal of Colloid and Interface Science*, 580:439–448, 2020. ISSN 00219797. doi: 10.1016/j.jcis.2020.07.049.

[151] N. A. Pérez-Chávez, A. G. Albesa, and G. S. Longo. Thermodynamic Theory of Multiresponsive Microgel Swelling. *Macromolecules*, 2021. ISSN 0024-9297. doi: 10.1021/acs.macromol.0c02885.

[152] X. Qiu and S. A. Sukhishvili. Copolymerization of N-vinylcaprolactam and glycidyl methacrylate: Reactivity ratio and composition control. *Journal of Polymer Science Part A: Polymer Chemistry*, 44(1):183–191, 2006. ISSN 0887-624X. doi: 10.1002/pola.21153.

[153] N. Häntzschel, F. Zhang, F. Eckert, A. Pich, and M. A. Winnik. Poly(N-vinylcaprolactam-co-glycidyl methacrylate) aqueous microgels labeled with fluorescent LaF3:Eu nanoparticles. *Langmuir : the ACS journal of surfaces and colloids*, 23(21):10793–10800, 2007. doi: 10.1021/la701691g.

[154] L. C. Kröger, W. A. Kopp, and K. Leonhard. Prediction of Chain Propagation Rate Constants of Polymerization Reactions in Aqueous NIPAM/BIS and VCL/BIS Systems. *The journal of physical chemistry. B*, 121(13):2887–2895, 2017. ISSN 1520-6106. doi: 10.1021/acs.jpcb.6b09147.

[155] B. H. Tan and K. C. Tam. Review on the dynamics and micro-structure of pH-responsive nano-colloidal systems. *Advances in Colloid and Interface Science*, 136(1-2):25–44, 2008. ISSN 00018686. doi: 10.1016/j.cis.2007.07.002.

[156] M. Annegarn, M. Dirksen, and T. Hellweg. Importance of pH in Synthesis of pH-Responsive Cationic Nano- and Microgels. *Polymers*, 13(5), 2021. doi: 10.3390/polym13050827.

[157] F. Meunier, A. Elaïssari, and C. Pichot. Preparation and characterization of cationic poly(N-isopropylacrylamide) copolymer latexes. *Polymers for Advanced Technologies*, 6(7):489–496, 1995. ISSN 10427147. doi: 10.1002/pat.1995.220060710.

[158] F. Avalos Belmontes, F. J. González, and M. Á. López-Manchado. *Green-Based Nanocomposite Materials and Applications*. Springer International Publishing, Cham, 2023. ISBN 978-3-031-18427-7. doi: 10.1007/978-3-031-18428-4.

[159] L. Chen, J. D. Simpson, A. V. Fuchs, B. E. Rolfe, and K. J. Thurecht. Effects of Surface Charge of Hyperbranched Polymers on Cytotoxicity, Dynamic Cellular Uptake and Localization, Hemotoxicity, and Pharmacokinetics in Mice. *Molecular pharmaceutics*, 14(12):4485–4497, 2017. doi: 10.1021/acs.molpharmaceut.7b00611.

[160] E. Fröhlich. The role of surface charge in cellular uptake and cytotoxicity of medical nanoparticles. *International journal of nanomedicine*, 7:5577–5591, 2012. doi: 10.2147/IJN.S36111.

[161] G. L. Shoaf and G. W. Poehlein. Solution and emulsion polymerization with partially neutralized methacrylic acid. *Journal of Applied Polymer Science*, 42(5):1239–1257, 1991. ISSN 00218995. doi: 10.1002/app.1991.070420507.

[162] F.-D. Kuchta, A. M. van Herk, and A. L. German. Propagation Kinetics of Acrylic and Methacrylic Acid in Water and Organic Solvents Studied by Pulsed-Laser Polymerization. *Macromolecules*, 33(10):3641–3649, 2000. ISSN 0024-9297. doi: 10.1021/ma990906t.

[163] M. Buback, P. Hesse, R. A. Hutchinson, P. Kasák, I. Lacík, M. Stach, and I. Utz. Kinetics and Modeling of Free-Radical Batch Polymerization of Nonionized Methacrylic Acid in Aqueous Solution. *Industrial & Engineering Chemistry Research*, 47(21):8197–8204, 2008. ISSN 0888-5885. doi: 10.1021/ie800887v.

[164] I. Lacík, L. Učňová, S. Kukučková, M. Buback, P. Hesse, and S. Beuermann. Propagation Rate Coefficient of Free-Radical Polymerization of Partially and Fully Ionized Methacrylic Acid in Aqueous Solution. *Macromolecules*, 42(20):7753–7761, 2009. ISSN 0024-9297. doi: 10.1021/ma9013516.

[165] N. F. G. Wittenberg, M. Buback, and R. A. Hutchinson. Kinetics and Modeling of Methacrylic Acid Radical Polymerization in Aqueous Solution. *Macromolecular Reaction Engineering*, 7(6): 267–276, 2013. ISSN 1862832X. doi: 10.1002/mren.201200089.

[166] E. Fischer, G. Storti, and D. Cuccato. Aqueous Free-Radical Polymerization of Non-Ionized and Fully Ionized Methacrylic Acid. *Processes*, 5(2):23, 2017. ISSN 2227-9717. doi: 10.3390/pr5020023.

[167] M. Buback, R. A. Hutchinson, and I. Lacík. Radical polymerization kinetics of water-soluble monomers. *Progress in Polymer Science*, 138:101645, 2023. ISSN 00796700. doi: 10.1016/j.progpolymsci.2022.101645.

[168] C. S. Brazel and N. A. Peppas. Synthesis and Characterization of Thermo- and Chemomechanically Responsive Poly(N-isopropylacrylamide-co-methacrylic acid) Hydrogels. *Macromolecules*, 28(24):8016–8020, 1995. ISSN 0024-9297. doi: 10.1021/ma00128a007.

[169] W. Xue, S. Champ, and M. B. Huglin. Observations on some copolymerisations involving N-isopropylacrylamide. *Polymer*, 41(20):7575–7581, 2000. ISSN 00323861. doi: 10.1016/S0032-3861(00)00171-3.

[170] S. Ponratnam and S. L. Kapur. Reactivity ratios of ionizing monomers in aqueous solution. Copolymerization of acrylic and methacrylic acids with acrylamide. *Die Makromolekulare Chemie*, 178(4):1029–1038, 1977. ISSN 0025-116X. doi: 10.1002/macp.1977.021780408.

[171] C. J. Kim and A. E. Hamielec. Polymerization of acrylamide with diffusion-controlled termination. *Polymer*, 25(6):845–849, 1984. ISSN 00323861. doi: 10.1016/0032-3861(84)90016-8.

[172] C. Preusser, A. Chovancová, I. Lacík, and R. A. Hutchinson. Modeling the Radical Batch Homopolymerization of Acrylamide in Aqueous Solution. *Macromolecular Reaction Engineering*, 10(5):490–501, 2016. ISSN 1862832X. doi: 10.1002/mren.201500076.

[173] Sigma-Aldrich Chemie GmbH. Safety data sheet 440914. version 7.2, 2023. URL `https://www.sigmaaldrich.com/DE/en/sds/aldrich/440914`.

[174] H.-R. Lin. Solution polymerization of acrylamide using potassium persulfate as an initiator: kinetic studies, temperature and pH dependence. *European Polymer Journal*, 37(7):1507–1510, 2001. ISSN 00143057. doi: 10.1016/S0014-3057(00)00261-5.

[175] A. Ghysels, T. Verstraelen, K. Hemelsoet, M. Waroquier, and V. van Speybroeck. TAMkin: A Versatile Package for Vibrational Analysis and Chemical Kinetics. *Journal of Chemical Information and Modeling*, 50:1736–1750, 2010. ISSN 1549-9596. doi: 10.1021/ci100099g.

[176] P. Stephens, F. Devlin, C. Chabalowski, and M. J. Frisch. Ab Initio Calculation of Vibrational Absorption and Circular Dichroism Spectra Using Density Functional Force Fields. *The Journal of Physical Chemistry*, 98(45):11623–11627, 1994.

[177] A. Schäfer, C. Huber, and R. Ahlrichs. Fully Optimized Contracted Gaussian-Basis Sets of Triple Zeta Valence Quality for Atoms Li to Kr. *Journal of Chemical Physics*, 100:5829–5835, 1994. doi: 10.1063/1.467146.

[178] S. Grimme. Semiempirical GGA-type density functional constructed with a long-range dispersion correction. *Journal of Computational Chemistry*, 27(15):1787–1799, NOV 30 2006. ISSN 0192-8651. doi: 10.1002/jcc.20495.

[179] M. J. Frisch, G. W. Trucks, H. B. Schlegel, G. E. Scuseria, M. A. Robb, J. R. Cheeseman, G. Scalmani, V. Barone, G. A. Petersson, H. Nakatsuji, X. Li, M. Caricato, A. Marenich, J. Bloino, B. G. Janesko, R. Gomperts, B. Mennucci, H. P. Hratchian, J. V. Ortiz, A. F. Izmaylov, J. L. Sonnenberg, D. Williams-Young, F. Ding, F. Lipparini, F. Egidi, J. Goings, B. Peng, A. Petrone, T. Henderson, D. Ranasinghe, V. G. Zakrzewski, J. Gao, N. Rega, G. Zheng, W. Liang, M. Hada, M. Ehara, K. Toyota, R. Fukuda, J. Hasegawa, M. Ishida, T. Nakajima, Y. Honda, O. Kitao, H. Nakai, T. Vreven, K. Throssell, J. A. M. Jr., J. E. Peralta, F. Ogliaro, M. Bearpark, J. J. Heyd, E. Brothers, K. N. Kudin, V. N. Staroverov, T. Keith, R. Kobayashi, J. Normand, K. Raghavachari, A. Rendell, J. C. Burant, S. S. Iyengar, J. Tomasi, M. Cossi, J. M. Millam, M. Klene, C. Adamo, R. Cammi, J. W. Ochterski, R. L. Martin, K. Morokuma, O. Farkas, J. B. Foresman, and D. J. Fox. Gaussian 09, Revision D.01, 2013.

[180] TURBOMOLE V7.0.1 2015, a development of University of Karlsruhe and Forschungszentrum Karlsruhe GmbH, 1989-2007, TURBOMOLE GmbH, since 2007. URL `http://www.turbomole.com`.

[181] A. Klamt. Conductor-Like Screening Model for Real Solvents: A New Approach to the Quantitative Calculation of Solvation Phenomena. *Journal of Physical Chemistry*, 99:2224–2235, 1995. doi: 10.1021/j100007a062.

[182] A. Klamt, V. Jonas, T. Bürger, and J. C. W. Lohrenz. Refinement and Parametrization of COSMO-RS. *Journal of Physical Chemistry A*, 102:5074–5085, 1998. doi: 10.1021/jp980017s.

[183] A. Klamt, F. Eckert, and W. Arlt. COSMO-RS: an alternative to simulation for calculating thermodynamic properties of liquid mixtures. *Annual Review of Chemical and Biomolecular Engineering*, 1:101–122, 2010. doi: 10.1146/annurev-chembioeng-073009-100903.

[184] COSMOconf, 4.2, COSMOlogic GmbH & Co KG, 2013. URL `http://www.cosmologic.de`.

[185] COSMOtherm, C3.0, release 19, COSMOlogic GmbH & Co KG, Leverkusen, 2019. URL `http://www.cosmologic.de`.

[186] C. Costa, A. L. Alberton, A. F. Santos, M. Fortuny, P. H. H. Araújo, C. Sayer, and J. C. Pinto. Kinetic Parameters of the Initiator Decomposition in Microwave and in Conventional Batch Reactors - KPS and V50-Case Studies. *Macromolecular Reaction Engineering*, 9(4):366–373, 2015. ISSN 1862832X. doi: 10.1002/mren.201500013.

[187] P. J. Joy, A. Mhamdi, and A. Mitsos. Identifiability Analysis and Model Reduction of a Semi-batch Emulsion Polymerization Process Model. In A. E. na, M. Graells, and L. Puigjaner, editors, *27th European Symposium on Computer Aided Process Engineering*, volume 40 of *Computer Aided Chemical Engineering*, pages 295–300. Elsevier, 2017. doi: https://doi.org/10.1016/B978-0-444-63965-3.50051-9.

[188] DyOS RWTH Aachen University (AVT.SVT). `http://permalink.avt.rwth-aachen.de/?id=295232`. Accessed: 2023-10-08.

[189] J. Lotz, U. Naumann, R. Hannemann-Tamás, T. Ploch, and A. Mitsos. Higher-order Discrete Adjoint ODE Solver in C++ for Dynamic Optimization. *Procedia Computer Science*, 51:256–265, 2015. ISSN 18770509. doi: 10.1016/j.procs.2015.05.237.

[190] Dassault Systems. `https://www.3ds.com/products-services/catia/products/dymola/`. Accessed: 2023-10-08.

[191] FMI standard - Functional mock-up interface for model exchange and co-simulation. `http://fmi-standard.org`. Accessed: 2023-10-08.

[192] J. Egea, D. Henriques, T. Cokelaer, A. Villaverde, A. MacNamara, D. Danciu, J. Banga, and J. Saez-Rodriguez. MEIGO: An Open-source Software Suite based on Metaheuristics for Global Optimization in Systems Biology and Bioinformatics. *BMC Bioinformatics*, 15:136, 2014.

[193] D. Yuret and M. de La Maza, editors. *Dynamic Hill Climbing: Overcoming the Limitations of Optimization Techniques*, 1993.

[194] T. M. Letcher. *Development and Applications in Solubility*. Royal Society of Chemistry, 2007. URL `https://books.google.de/books?hl=de&lr=&id=0VMd-M2KbuYC&oi=fnd&pg=PA188&dq=cosmo-rs+henry+constant+rms&ots=jefz1mETmY&sig=70FNRPYcGbqgVFadvrMYMztjNvE#v=onepage&q&f=false`.

[195] J. Zheng, Y. Zhao, and D. G. Truhlar. The DBH24/08 Database and Its Use to Assess Electronic Structure Model Chemistries for Chemical Reaction Barrier Heights. *Journal of Chemical Theory and Computation*, 5(4):808–821, 2009. doi: 10.1021/ct800568m.

[196] L. C. Kröger, S. Müller, I. Smirnova, and K. Leonhard. Prediction of Solvation Free Energies of Ionic Solutes in Neutral Solvents. *The journal of physical chemistry. A*, 124(20):4171–4181, 2020. doi: 10.1021/acs.jpca.0c01606.

[197] C. Gertig, L. Kröger, L. Fleitmann, J. Scheffczyk, A. Bardow, and K. Leonhard. Rx-COSMO-CAMD: Computer-Aided Molecular Design of Reaction Solvents Based on Predictive Kinetics from Quantum Chemistry. *Industrial & Engineering Chemistry Research*, 58(51):22835–22846, 2019. doi: 10.1021/acs.iecr.9b03232.

[198] J. Zheng, Y. Zhao, and D. G. Truhlar. The DBH24/08 Database and Its Use to Assess Electronic Structure Model Chemistries for Chemical Reaction Barrier Heights. *Journal of chemical theory and computation*, 5(4):808–821, 2009. ISSN 1549-9618. doi: 10.1021/ct800568m.

[199] L. **Kaven**, A. M. Schweidtmann, J. Keil, J. Israel, N. Wolter, and A. Mitsos. Dataset to: Data-driven Product-Process Optimization of N-isopropylacrylamide Microgel Flow-Synthesis, 2023. doi:10.18154/RWTH-2023-05551.

[200] E. Bradford, A. M. Schweidtmann, and A. Lapkin. Efficient multiobjective optimization employing Gaussian processes, spectral sampling and a genetic algorithm. *Journal of Global Optimization*, 71(2):407–438, 2018. ISSN 0925-5001. doi: 10.1007/s10898-018-0609-2.

[201] W. R. Thompson. On the Likelihood that One Unknown Probability Exceeds Another in View of the Evidence of Two Samples. *Biometrika*, 25(3/4):285, 1933. ISSN 00063444. doi: 10.2307/2332286.

[202] J. Snoek, H. Larochelle, and R. P. Adams. Practical Bayesian Optimization of Machine Learning Algorithms. In F. Pereira, C.J. Burges, L. Bottou, and K.Q. Weinberger, editors, *Advances in Neural Information Processing Systems*, volume 25. Curran Associates, Inc, 2012.

[203] R. Garnett. *Bayesian Optimization*. Cambridge University Press, 2023.

[204] B. J. Shields, J. Stevens, J. Li, M. Parasram, F. Damani, J. I. M. Alvarado, J. M. Janey, R. P. Adams, and A. G. Doyle. Bayesian reaction optimization as a tool for chemical synthesis. *Nature*, 590(7844):89–96, 2021. doi: 10.1038/s41586-021-03213-y.

[205] A. M. Schweidtmann, A. D. Clayton, N. Holmes, E. Bradford, R. A. Bourne, and A. A. Lapkin. Machine learning meets continuous flow chemistry: Automated optimization towards the Pareto front of multiple objectives. *Chemical Engineering Journal*, 352(1–9):277–282, 2018. ISSN 13858947. doi: 10.1016/j.cej.2018.07.031.

[206] S. Sano, T. Kadowaki, K. Tsuda, and S. Kimura. Application of Bayesian Optimization for Pharmaceutical Product Development. *Journal of Pharmaceutical Innovation*, 15(3):333–343, 2020. ISSN 1872-5120. doi: 10.1007/s12247-019-09382-8.

[207] Y. Naito, M. Kondo, Y. Nakamura, N. Shida, K. Ishikawa, T. Washio, S. Takizawa, and M. Atobe. Bayesian optimization with constraint on passed charge for multiparameter screening of electrochemical reductive carboxylation in a flow microreactor. *Chemical communications (Cambridge, England)*, 58(24):3893–3896, 2022. doi: 10.1039/d2cc00124a.

[208] A. Mogilicharla, P. Mittal, S. Majumdar, and K. Mitra. Kriging Surrogate Based Multi-objective Optimization of Bulk Vinyl Acetate Polymerization with Branching. *Materials and Manufacturing Processes*, 30(4):394–402, 2015. ISSN 1042-6914. doi: 10.1080/10426914.2014.921709.

[209] W. McPhee, K. C. Tam, and R. Pelton. Poly(N-isopropylacrylamide) Latices Prepared with Sodium Dodecyl Sulfate. *Journal of Colloid and Interface Science*, 156(1):24–30, 1993. ISSN 00219797. doi: 10.1006/jcis.1993.1075.

[210] X. Wu, R. H. Pelton, A. E. Hamielec, D. R. Woods, and W. McPhee. The kinetics of poly(N-isopropylacrylamide) microgel latex formation. *Colloid and Polymer Science*, 272(4):467–477, 1994. ISSN 0303-402X. doi: 10.1007/BF00659460.

[211] B. Wedel, T. Brändel, J. Bookhold, and T. Hellweg. Role of Anionic Surfactants in the Synthesis of Smart Microgels Based on Different Acrylamides. *ACS omega*, 2(1):84–90, 2017. doi: 10.1021/acsomega.6b00424.

[212] K. von Nessen, M. Karg, and T. Hellweg. Thermoresponsive poly-(N-isopropylmethacrylamide) microgels: Tailoring particle size by interfacial tension control. *Polymer*, 54(21):5499–5510, 2013. ISSN 00323861. doi: 10.1016/j.polymer.2013.08.027.

[213] O. L. J. Virtanen and W. Richtering. Kinetics and particle size control in non-stirred precipitation polymerization of N-isopropylacrylamide. *Colloid and Polymer Science*, 292(8):1743–1756, 2014. ISSN 0303-402X. doi: 10.1007/s00396-014-3208-x.

[214] A. Balaceanu, D. E. Demco, M. Möller, and A. Pich. Microgel Heterogeneous Morphology Reflected in Temperature-Induced Volume Transition and 1 H High-Resolution Transverse Relaxation NMR. The Case of Poly(N-vinylcaprolactam) Microgel. *Macromolecules*, 44(7):2161–2169, 2011. ISSN 0024-9297. doi: 10.1021/ma200103y.

[215] A. Imaz and J. Forcada. N-vinylcaprolactam-based microgels: Synthesis and characterization. *Journal of Polymer Science Part A: Polymer Chemistry*, 46(7):2510–2524, 2008. ISSN 0887-624X. doi: 10.1002/pola.22583.

[216] Y. Y. Chiu and L. J. Lee. Microgel formation in the free radical crosslinking polymerization of ethylene glycol dimethacrylate (EGDMA). I. Experimental. *Journal of Polymer Science Part A: Polymer Chemistry*, 33(2):257–267, 1995. ISSN 0887-624X. doi: 10.1002/pola.1995.080330208.

[217] D. Bongartz, J. Najman, S. Sass, and A. Mitsos. MAiNGO - McCormick-based Algorithm for mixed-integer Nonlinear Global Optimization. Technical Report. URL `https://www.avt.rwth-aachen.de/global/show_document.asp?id=aaaaaaaaabclahw`.

[218] A. M. Schweidtmann, D. Bongartz, D. Grothe, T. Kerkenhoff, X. Lin, J. Najman, and A. Mitsos. Deterministic global optimization with Gaussian processes embedded. *Mathematical Programming Computation*, 13(3):553–581, 2021. ISSN 1867-2949. doi: 10.1007/s12532-021-00204-y.

[219] M. Ehrgott. Multiobjective Optimization. *AI Magazine*, 29(4):47, 2009. ISSN 0738-4602. doi: 10.1609/aimag.v29i4.2198.

[220] E. Bradford. TS-EMO algorithm. `https://github.com/Eric-Bradford/TS-EMO`, last updated 2020-06.

[221] D. Bongartz. MAiNGO - McCormick-based Algorithm for mixed-integer Nonlinear Global Optimization. `https://git.rwth-aachen.de/avt-svt/public/maingo`, last updated 2021-06.

[222] A. Schweidtmann. MeLOn - Machine Learning Models for Optimization. `https://git.rwth-aachen.de/avt-svt/public/MeLOn`, last updated 2021-06.

[223] V. Nigro, F. Ripanti, R. Angelini, A. Sarra, M. Bertoldo, E. Buratti, P. Postorino, and B. Ruzicka. Molecular mechanisms driving the microgels behaviour: A Raman spectroscopy and dynamic light scattering study. *Journal of Molecular Liquids*, 284:718–724, 2019. ISSN 01677322. doi: 10.1016/j.molliq.2019.04.024.

DOI: 10.18154/RWTH-2024-06268

Aachener
Verfahrenstechnik

RWTH AACHEN
UNIVERSITY